



UiT The Arctic University of Norway

FACULTY OF SCIENCE AND TECHNOLOGY

Department of Geosciences

Fluid flow and faulting along the northern margin of the Loppa High

Cornelia Mentzoni Binde

Master's thesis in Geology, GEO-3900

May 2020



Abstract

The Barents Sea is a large epicontinental sea and petroliferous basin, which is fairly unexplored compared to other regions of the Norwegian Continental Shelf (NCS). The structural configuration of the SW Barents Sea is characterized by a complex mosaic of structural highs, platforms and basins, reflecting the interplay between multiple tectonic phases. Late Cenozoic glacially induced subsidence and uplift, and extensive differential erosion, may have had a major impact on the petroleum systems in the area, causing a reconfiguration of the fluid flow systems by gas expansion, oil-spill, migration and remigration of hydrocarbons into the shallower subsurface. Subsequent accumulations of shallow gas may represent significant drilling hazards, potential commercial hydrocarbon resources or be indicative of deeper prospective reservoirs, and are as such important exploration targets. Identification and analysis of fluid flow indications and their relationship to the structural development and denudation history of the Loppa High will provide a better insight to the controlling mechanisms of fluid flow systems on both a local and regional scale.

Seismic interpretation, spatial visualization and analysis of 2D and 3D data from the northern margin of the Loppa High have revealed numerous fluid flow indications such as leaking faults, gas chimneys, shallow gas accumulations and buried and exposed depressions. The complex structural development of the Loppa High has led to the development of several sets of faults, which have been classified as deep-seated Permian, vertically extensive Permian-Triassic and shallow Triassic. The larger-scale structural geology of the study area encompasses narrow grabens and extensive horsts, believed to reflect Carboniferous-Permian rifting, extensional faulting related to the proto-Atlantic rift system and later rifting events associated with the opening of the Norwegian-Greenland Sea. The numerous faults identified may constitute a larger network of potential fluid conduits, connecting deeper reservoirs with shallower, suggesting a structural control on the fluid flow systems in the study area. Gas chimneys and high-amplitude anomalies occurring at several levels within the subsurface strata, and the presence of both buried and exposed seabed depressions, testifies to vertical and lateral migration from deeper source rock intervals, gas accumulations along faults and URU, and episodes of potential gas release at the seabed. Observations and results largely correspond to similar studies carried out in the SW Barents Sea region, supporting the theory that fluid flow systems in the area are at least partially structurally controlled and that the distribution of fluid flow systems may have been altered by Late Cenozoic tectonic readjustments through extensive uplift and erosion.

Acknowledgement

Fem år på Universitetet i Tromsø avsluttes med innlevering av en veldig spennende og lærerik masteroppgave. Innspurten og avslutningen har vært utfordrende og ikke minst annerledes, med lockdown av UiT og Norge, og en hverdag snudd på hodet. Til tross for mange nye utfordringer, har vi på mirakuløst vis allikevel kommet oss igjennom det.

Jeg vil først og fremst gjerne takke mine veiledere, professor Stefan Bünz (CAGE) og Sunil Vadakkepuliambatta (CAGE), for muligheten til og datagrunnlaget for å skrive denne oppgaven, og for god veiledning gjennom det siste året.

Jeg vil også gjerne takke min bedre halvdel og svært tålmodige samboer, Tord, for utrolig god støtte og oppmuntring – jeg hadde nok ikke kommet meg igjennom dette uten deg. Min familie i Asker, særlig mine foreldre, skal også ha en stor takk for all hjelp, og ikke minst for motiverende og støttende ord. Herlige medstudenter og sparrepартnere har gjort de siste årene utrolig fine, og jeg setter enormt stor pris på alle (etter hvert også digitale) kaffepauser og samtaler, både akademiske og ikke fullt så akademiske.

Cornelia Mentzoni Binde

Tromsø, Mai 2020

Content

1	INTRODUCTION	1
1.1	MOTIVATION AND OBJECTIVES	1
2	THEORETICAL FRAMEWORK	2
2.1	THE PETROLEUM SYSTEM	2
2.1.1	SOURCE ROCK	2
2.1.2	RESERVOIR ROCK	3
2.1.3	TRAPS AND SEALS.....	3
2.1.4	MIGRATION	4
2.2	FAULTS.....	9
2.2.1	FAULT ANATOMY AND TYPES.....	9
2.2.2	FAULT INITIATION AND REACTIVATION	10
2.2.3	POLYGONAL FAULTS	13
2.2.4	MIGRATION THROUGH FAULTS.....	13
2.3	SEISMIC REFLECTION THEORY.....	14
2.3.1	BASIC PRINCIPLES.....	14
2.3.2	SEISMIC RESPONSE AND POLARITY.....	15
2.3.3	RESOLUTION	16
2.4	FLUID FLOW FEATURES.....	20
2.4.1	SURFACE INDICATORS	20
2.4.2	SUBSURFACE INDICATORS.....	22
2.5	GAS HYDRATES	25
3	GEOLOGICAL FRAMEWORK	27
3.1	TECTONIC AND STRUCTURAL DEVELOPMENT OF THE SW BARENTS SEA	29
3.1.1	PALEOZOIC	29
3.1.2	MESOZOIC.....	30
3.1.3	CENOZOIC.....	31
3.2	STRATIGRAPHY AND PALEOENVIRONMENT OF THE SW BARENTS SEA	32
3.2.1	PALEOZOIC	32
3.2.2	MESOZOIC.....	34
3.2.3	CENOZOIC.....	35
3.3	LOPPA HIGH	36
3.4	STRATIGRAPHIC UNITS	37
3.4.1	TEMPELFJORDEN GROUP.....	37
3.4.2	SASSENDALEN GROUP	38
3.4.3	KAPP TOSCANA GROUP.....	39
3.4.4	NORDLAND GROUP	39
3.5	PETROLEUM SYSTEMS IN THE SW BARENTS SEA.....	40
3.5.1	PLAYS AND SOURCE ROCKS	40
3.5.2	EFFECTS OF UPLIFT ON MATURITY AND MIGRATION.....	41

4	<u>DATA AND METHODS.....</u>	<u>43</u>
4.1	DATASETS AND WELLS	43
4.1.1	FREQUENCIES	44
4.1.2	VELOCITIES	46
4.1.3	RESOLUTION	46
4.2	SEISMIC ARTEFACTS	48
4.3	METHODS	48
4.3.1	SOFTWARE.....	48
4.3.2	SEISMIC INTERPRETATION.....	49
4.3.3	SEISMIC ATTRIBUTES.....	50
4.3.4	INTEGRATED INTERPRETATION.....	51
5	<u>RESULTS</u>	<u>52</u>
5.1	SEISMIC STRATIGRAPHY	52
5.2	FAULTS	55
5.2.1	PERMIAN FAULTS	57
5.2.2	PERMIAN-TRIASSIC FAULTS.....	57
5.2.3	TRIASSIC FAULTS	60
5.3	FLUID FLOW INDICATIONS.....	62
5.3.1	AMPLITUDE ANOMALIES.....	62
5.3.2	LARGER ZONES OF ACOUSTIC MASKING	73
5.3.3	MORPHOLOGICAL FEATURES ON THE SEABED.....	75
6	<u>DISCUSSION.....</u>	<u>87</u>
6.1	FAULTS AND CORRELATION WITH TECTONIC EVENTS	87
6.1.1	PERMIAN FAULTS	87
6.1.2	PERMIAN-TRIASSIC FAULTS.....	88
6.1.3	TRIASSIC FAULTS	89
6.2	FLUID ORIGIN	90
6.3	FLUID MIGRATION AND ACCUMULATION	91
6.3.1	VERTICAL MIGRATION ALONG FAULTS	91
6.3.2	LATERAL MIGRATION IN RESERVOIR INTERVALS.....	95
6.3.3	LATERAL MIGRATION IN DIPPING STRATA.....	97
6.4	MORPHOLOGICAL INDICATIONS OF GAS SEEPAGE	98
6.4.1	DEPRESSION/POCKMARK DISTRIBUTION.....	98
6.4.2	DEPRESSION/POCKMARK ORIGIN	100
6.5	CONCEPTUAL MODEL AND PETROLEUM SYSTEM EVENT CHART	102
7	<u>CONCLUSION</u>	<u>105</u>
8	<u>FURTHER RESEARCH.....</u>	<u>106</u>
	<u>REFERENCES.....</u>	<u>107</u>

TABLE OF FIGURES.....113

TABLE OF EQUATIONS118

1 Introduction

1.1 Motivation and objectives

Proven accumulations of hydrocarbons in the Barents Sea demonstrates the region's prolific nature. The complex geological development of the region, characterized by multiple tectonic phases during the Paleozoic and Mesozoic and extensive uplift and glacial erosion during the Late Cenozoic, has left the Barents Sea a very peculiar exploration target. Late Cenozoic denudation and accompanied processes are thought to have affected the petroleum systems in the Barents Sea, possibly triggering fluid flow and expulsion from deeper reservoirs to shallower, or causing the complete escape of fluids from the subsurface (Doré & Jensen, 1996; Henriksen, Bjørnseth, et al., 2011). These processes might explain the many shallow gas accumulations and large vertical fluid flow structures identified in the region (e.g. Andreassen, Nilssen, et al. (2007), Chand et al. (2012) and Vadakkepuliymbatta et al. (2013)), and possibly why gas discoveries appear to outnumber oil discoveries (Nyland et al., 1992).

Fluid flow anomalies and shallow gas accumulations may represent significant drilling hazards, potential commercial hydrocarbon resources, or be indicative of deeper prospective reservoirs (Andreassen, Nilssen, et al., 2007; Heggland, 1998). These aspects emphasize the need to improve the understanding of their exact distribution and controlling mechanisms, on both a local and regional scale. Interpretation of newly released seismic from the northern margin of the Loppa High provides new insight on the processes and mechanisms involved in fluid leakage and accumulation in the Barents Sea. The main objective of this thesis is thus two-fold:

- Gain better understanding of the controlling mechanisms for the occurrence and development of focused fluid flow features (i.e. faults and/or gas chimneys), as well as shallow gas accumulations
- Try to infer the relationship between focused fluid flow features/gas accumulations and the structural development and denudation history of the area

The study is based on interpretation of three newly released 3D seismic datasets, five 2D datasets and well data from well 7222/1-1 on the northern Loppa High, of which stratigraphic delineation and structural interpretation constitute the basis for further analysis. Mapping, visualization and spatial analysis of fluid flow structures (leakage features, shallow/deep gas accumulations and potential reservoirs) and amplitude anomalies in Petrel E&P will be essential tools for the development of geological models for focused fluid flow in the area, accounting for the potential relationship to structural elements, migration mechanisms, potential fluid sources and timing of fluid flow.

2 Theoretical framework

2.1 The petroleum system

For a petroleum accumulation to occur, there are several essential elements and processes required prior to accumulation and preservation of hydrocarbons. The term *petroleum system* refers to a naturally occurring system encompassing all the crucial elements and processes for generation, migration and accumulation of hydrocarbons, such as oil and gas (Magoon & Beaumont, 1999; Selley & Sonnenberg, 2015). The interdependent processes and elements include (1) an active *source rock*, (2) a *reservoir rock* of sufficient porosity and permeability, (3) a *sealing rock* preventing leakage and further migration, (4) an *overburden rock* providing sufficient pressure and burial, (5) a *trapping mechanism* and (6) *migration pathways* facilitating the movement of hydrocarbons from source to trap (Magoon & Beaumont, 1999). Not only must they be present, but they must also occur in time and space so that organic matter generated by the source rock may be converted into a petroleum accumulation in a trap (Magoon & Beaumont, 1999). The ideal course of events is presented in fig. 2.1, in terms of a Petroleum System Event Chart.

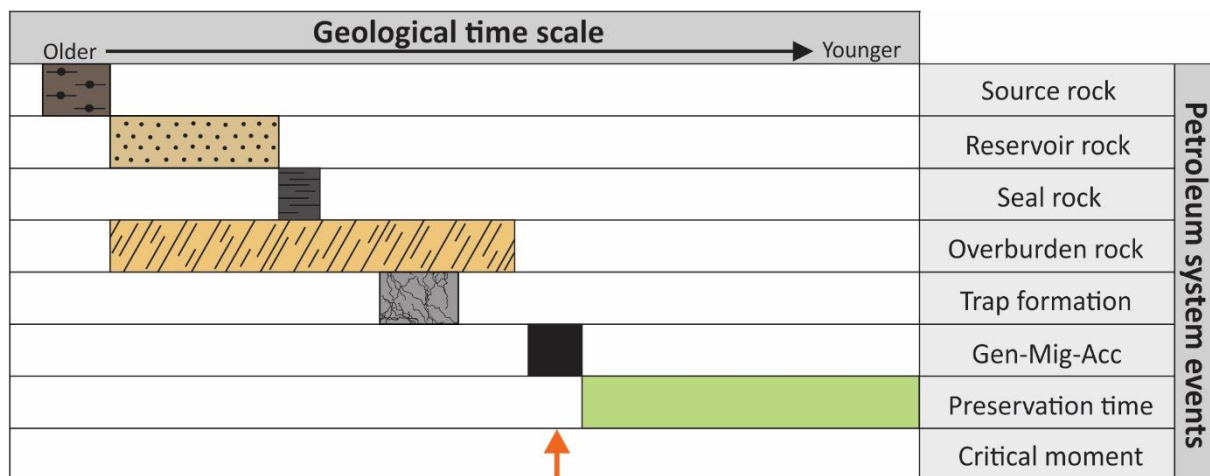


Figure 2.1: Petroleum System Event Chart, showing the ideal course of events and processes resulting in a hydrocarbon accumulation. Critical moment refers to the time of generation, migration and accumulation, preferentially occurring after trap formation. Inspired by fig. 3-6 in Magoon and Beaumont (1999).

2.1.1 Source rock

A source rock is defined as an organic-rich rock which, given the right temperature and pressure conditions, generates oil and/or gas. Organic matter is produced by the process of photosynthesis, and the accumulated amount is directly related to the ratio between the production and degradation of the material. Preservation of organic matter is favored by anoxic conditions, i.e. oxygen depletion, in environments such as lakes, barred basins, continental shelves with upwelling and deep ocean basins (Selley & Sonnenberg, 2015). Following deposition, there are three phases in the evolution of organic matter in response to increasing

pressure and temperature, with respect to increasing burial depth; (1) *diagenesis*, in which degradation of the material by microbial processes leaves a complex hydrocarbon termed *kerogen*, (2) *catagenesis*, in which petroleum is released from kerogen as it matures (oil at 75-170°C and gas at 170-230°C) and (3) *metagenesis*, in which the last hydrocarbons are expelled (Selley & Sonnenberg, 2015). Depending on the origin and the chemical composition of the organic matter, four types of kerogen may be produced and distinguished from one another (illustrated in fig. 2.2). These components in turn determine whether oil and/or gas is generated (Selley & Sonnenberg, 2015; Speight, 2012).

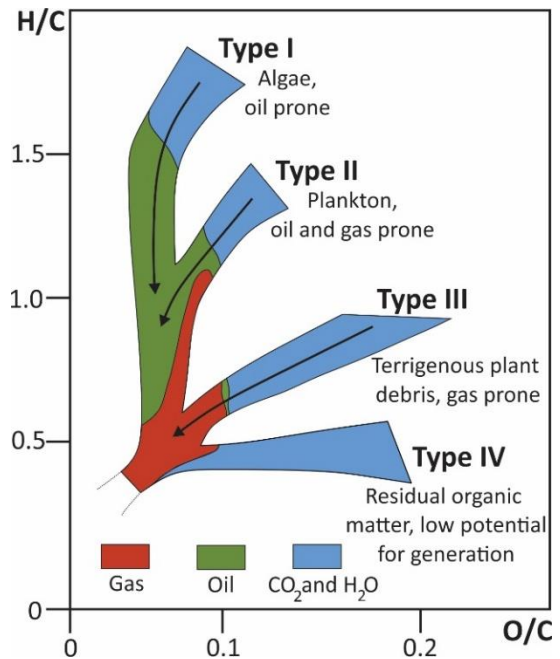


Figure 2.2: Van Krevelen Diagram, showing the origin of the main kerogen types and their potential for generating oil and/or gas. Inspired by fig. 5.15 in Selley and Sonnenberg (2015).

2.1.2 Reservoir rock

A reservoir rock is a porous rock with the potential to store fluids (Selley & Sonnenberg, 2015). Even though any rock may act as a reservoir, there are two essential properties defining the integrity of a reservoir rock; porosity and permeability. Porosity quantifies the amount of open pore space that have the potential to be filled with fluids, whereas permeability refers to the ability of a rock to transmit fluids through connected pore space (Selley & Sonnenberg, 2015). The quality of the reservoir is defined by its porosity and permeability, which tend to decrease during burial due to increased overburden load and the effects of diagenesis. Thus, there are specific subsurface conditions favoring the accumulation of hydrocarbons within a reservoir, also known as the Golden Zone (Buller et al., 2005). The Golden Zone refers to the temperature interval between 60°C to 120°C and is not only dependent on reservoir quality, but also the rates and risks of overpressure, oil generation and biodegradation as a function of increasing temperatures. In terms of reservoir quality, porosities and permeabilities are still sufficient within the Golden Zone; at lower temperatures, loss is related to compaction, whereas at higher temperatures, loss is related to cementation (Buller et al., 2005).

2.1.3 Traps and seals

A trap is an area in which hydrocarbons may accumulate and becomes barred from further movement (Selley & Sonnenberg, 2015). There is a given set of conditions required in order

for hydrocarbons to accumulate in a trap and the most important aspects are illustrated in fig. 2.3. The integrity of a trap is largely defined by the presence of an overlying and effective seal. The sealing lithologies are commonly porous, and in some cases hydrocarbon saturated, but must be essentially impermeable (Selley & Sonnenberg, 2015).

Traps may be classified according to their origin, and there are thus five main groups of traps; (1) *structural traps*, formed by post-depositional tectonic processes such as folding and faulting (e.g. anticlines and faults), (2) *stratigraphic traps*, formed by depositional or post-depositional non-tectonic processes (e.g. pinch-outs and channel deposits), (3) *diapiric traps*, caused by upwards doming of overlying strata, produced by moving salt or mud, (4) *hydrodynamic traps*, produced when the downward movement of water prevents the upward movement of hydrocarbons, and (5) *combination traps*, which are formed by a combination of two or more of the previously defined genetic processes (Selley & Sonnenberg, 2015).

2.1.4 Migration

2.1.4.1 Primary, secondary and tertiary migration

Migration refers to the process of subsurface hydrocarbon relocation or movement. As a result of burial, source rocks become subjected to increasing pressures and temperatures, ultimately resulting in the fracturing of the rock and the expulsion of hydrocarbons (Henriet et al., 1991). Hydrocarbon migration can be subdivided into three processes based on where in the petroleum system migration occurs, as illustrated in fig. 2.3.

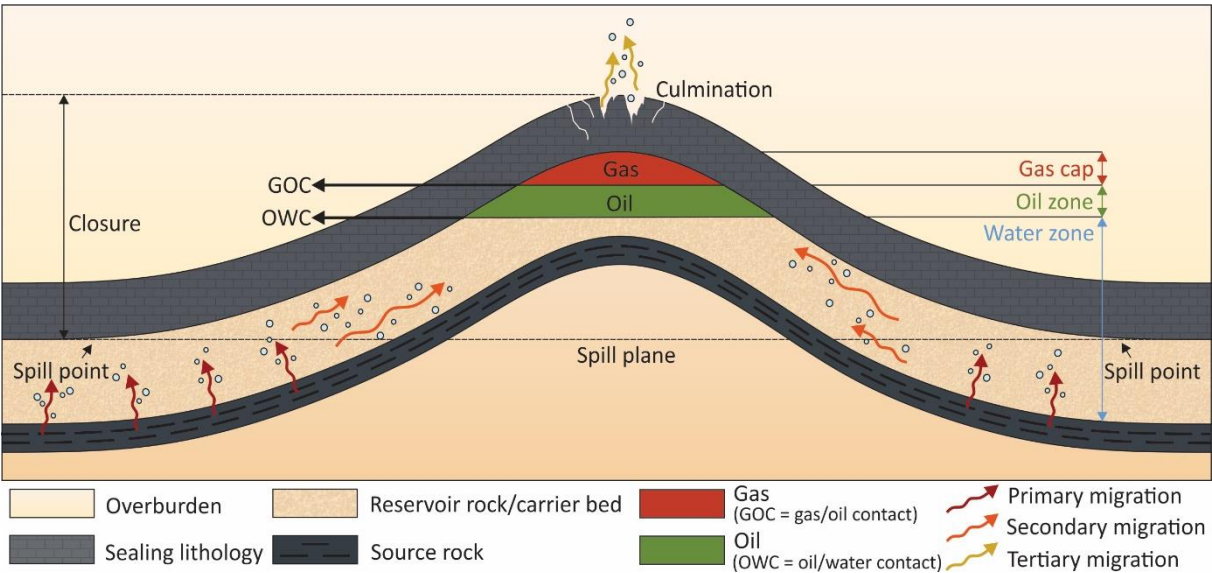


Figure 2.3: The most essential elements and processes of a trap, represented by the simplest anticlinal trap. Inspired by fig. 7.1 in Selley and Sonnenberg (2015).

Migration from the source rock into permeable carrier beds is known as *primary migration*. The subsequent movement of hydrocarbons within these carrier beds and towards and into a

reservoir is known as *secondary migration* (England et al., 1987; Selley & Sonnenberg, 2015). Although less common, migration occurring out of the reservoir through the cap rock (leakage or remigration) is termed *tertiary migration* (Judd & Hovland, 2007; Magoon & Beaumont, 1999). Depending on the properties of the subsurface strata, hydrocarbon migration occurs both vertically and horizontally, of which structural and/or lithological barriers may slow down or cause complete cessation of migration (Selley & Sonnenberg, 2015).

2.1.4.2 Fluid flow dynamics

2.1.4.2.1 Subsurface pressures

The overburden pressure is the sum of the vertical forces exerted by formation pore fluids (pore pressure) and by the solid rock matrix (lithostatic pressure). Selley and Sonnenberg (2015) thus defines the overburden pressure as:

Eq. 2.1: Overburden pressure

$$S = P + O$$

where S = overburden pressure (Pa), P = lithostatic pressure (Pa) and O = pore pressure (Pa). The interplay between the lithostatic pressure and the pore pressure largely affects the diagenetic properties and hence the porosity and permeability of formations. With increasing lithostatic pressure, formation fluids are usually forced out of the pores and the grains are rearranged in a tighter array, causing the porosity to decrease. Increasing pore pressure may cause a weakening of the forces acting on the grain contacts, and the sediments may transform into an unstable plastic state (Selley & Sonnenberg, 2015).

The lithostatic pressure increases along the lithostatic gradient (fig. 2.4), which usually varies according to depth, density of the overburden and to the extent to which grain contacts are supported by pore pressure (Selley & Sonnenberg, 2015). The pore pressure can be further subdivided into hydrostatic or hydrodynamic; the former imposed by a fluid at rest, the latter imposed by fluids in motion (Selley & Sonnenberg, 2015). The hydrostatic pressure gradient is the pressure that would be exerted by a continuous column of static fluid (Osborne & Swarbrick, 1997) and can be expressed as:

Eq. 2.2: Hydrostatic pressure

$$P_{hs} = \rho gh + P_a$$

Where P_{hs} = pore pressure (hydrostatic, Pa), ρ = density of pore fluid (kg/m^3), g = gravitational constant (m/s^2), h = height of fluid column (m) and P_a = atmospheric pressure (atm) (Judd & Hovland, 2007). The hydrodynamic pressure gradient, also known as the fluid potential

gradient, is caused by fluids in motion (Selley & Sonnenberg, 2015), and can be related to the potential energy of hydrocarbons at two different points or levels in the subsurface (England et al., 1987).

Pore pressures equal to the hydrostatic pressure are termed normal, but deviations are frequently occurring in the subsurface. Pressures less than the hydrostatic are termed subnormal pressures (abnormally low, underpressure), whereas pressures greater than the hydrostatic are termed supernormal pressures (abnormally high, overpressure). Sub- and supernormal pressures (fig. 2.4) occur in environments of which pressure equilibrium is not

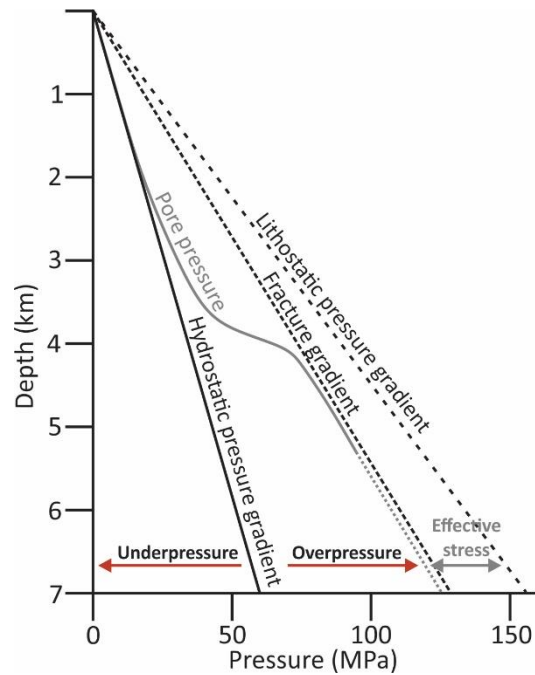


Figure 2.4: Relationship between the hydrostatic, lithostatic, pore and fracture pressures. Inspired by fig. 4.13 in Selley and Sonnenberg (2015) and fig. on p. 4 in Buller et al. (2005).

achieved, mainly due to lithological or structural permeability barriers impairing out- or inflow of fluids (Beaumont & Fiedler, 1999; Berndt, 2005; Selley & Sonnenberg, 2015). Overpressured environments are rather normal in the subsurface, and the most common cause of overpressure can be attributed to increases in compressive stress, resulting in reduction of formation pore volume by disequilibrium compaction. This may occur due to increased vertical compression in response to burial or increased horizontal compression in response to tectonic movements. In any case, rapid decrease in pore volume requires an equally rapid expulsion of formation fluids if pressure is to remain hydrostatic. If expulsion is impaired, overpressure occurs. Other causes may be attributed to hydrocarbon buoyancy and gas volume expansion during ascension, as well as reduced permeability and slowed migration resulting from diagenetic effects (e.g. cementation)(Osborne & Swarbrick, 1997).

2.1.4.2.2 Darcy's Law

Assuming constant fluid properties, the amount of fluids transmitted through a porous and permeable material depend on the materials ability to conduct fluids and the pore-water pressure difference between two ends of the flow (Berndt, 2005). This relationship can be quantified in terms of Darcy's Law:

Eq. 2.3: Darcy's Law

$$Q = \frac{kA(P_1 - P_2)}{\mu L}$$

where Q = rate of flow (m^3/s), k = permeability (m^2), $P_1 - P_2$ = pressure drop (Pa), A = cross-sectional area through which flow is possible (m^2), L = horizontal distance of flow (m) and μ = viscosity of the fluid ($\text{Pa}\cdot\text{s}$) (Selley & Sonnenberg, 2015). From eq. 2.3 it follows that fluid flow will continue until the pressure drop approaches zero; the pressure thus becomes hydrostatic, and migration slows down and eventually ceases. Short migration distances coupled with a high permeability and pressure drop are thus favorable for a more effective fluid flow.

2.1.4.2.3 Buoyancy and capillary pressure

Fluid flow is also governed by the fluids ability to overcome the capillary entry pressure of the overlying formation. Under hydrostatic conditions, buoyancy is the main driving force for vertical hydrocarbon migration, resulting from the density contrast between two immiscible fluids (i.e. the hydrocarbon phase and the water phase) (Schowalter, 1979). Based on eq. 7.7 in Judd and Hovland (2007) and adapted to fluid buoyancy, the buoyancy pressure can be defined as:

Eq. 2.4: Buoyancy pressure

$$P_b = (\rho_w - \rho_h)gh$$

where P_b = buoyant pressure (Pa), ρ_w = density of water (kg/m^3), ρ_h = density of hydrocarbons (kg/m^3), g = gravitational constant (m/s^2) and h = thickness of hydrocarbon column (m). It follows from eq. 2.4 that a greater density difference causes a greater buoyant force for a given length of a hydrocarbon column (Hindle, 1997; Schowalter, 1979). However, if hydrocarbons are required to move through a water-saturated formation, the relationship between the buoyant force and the capillary pressure of the formation will determine whether the fluids may migrate through the material (Hindle, 1997). The capillary pressure is the pressure difference across the interface between two immiscible fluids (Selley & Sonnenberg, 2015), and can be expressed as:

Eq. 2.5: Capillary pressure

$$P_{cap} = p_{wetting} - p_{non\ wetting}$$

where P_{cap} = capillary pressure, $p_{wetting}$ = pressure of the wetting phase and $p_{non\ wetting}$ = pressure of the non-wetting phase. The wetting phase is the fluid of which preferentially adhere to the capillary walls before the non-wetting phase, and in the case of a water-saturated formation, water is usually the wetting phase (fig. 2.5). The wettability of a fluid depends on its

surface tension, the contact angle of the fluid and the radius of the pore throat, so that capillary pressure (in dyn/cm²) can alternatively be expressed as:

Eq. 2.6: Capillary pressure

$$P_{cap} = \frac{2\gamma \times \cos \theta}{r}$$

where γ = interfacial tension between two fluids (dyn/cm), θ = wetting angle (degrees) and r = effective radius of the pore throats (cm)(Beaumont & Fiedler, 1999; Schowalter, 1979). In order for the non-wetting phase to enter the formation, the displacement pressure of the hydrocarbons must exceed the capillary pressure of the formation

(Schowalter, 1979; Selley & Sonnenberg, 2015). It follows from eq. 2.6 that decreasing pore diameter, greater interfacial tension and smaller wetting angle causes an increase in the capillary pressure and hence the displacement pressure required for migration to occur (Hindle, 1997; Schowalter, 1979).

2.1.4.3 Vertical and lateral migration

As oil, gas and water have different densities ($\rho_{gas} < \rho_{oil} < \rho_{water}$), they occur stratified in porous and permeable reservoirs, usually accumulated in the highest point of a trap (structural or stratigraphic culmination). These facts imply that fluids have been free to migrate within the reservoir, and that migration has included both a vertical and a horizontal component (Selley & Sonnenberg, 2015). Furthermore, hydrocarbon accumulations occurring in stratigraphic levels above prolific source rocks suggests vertical migration, whereas accumulations with no obvious adjacent source rocks usually indicate lateral migration (Selley & Sonnenberg, 2015).

Fluids move according to the path of least resistance and in response to differential pressures, of which migration occur from high to low pressure environments (Selley & Sonnenberg, 2015). Under hydrodynamic conditions, the fluid potential largely determines the migration direction, and may vary considerably between two points in the subsurface. Migration occurs from high to low fluid potential (deep to shallow stratigraphic levels) along the fluid potential gradient, which is affected by variations in excess water pressure, the buoyancy pressure of hydrocarbons and variations in the capillary pressure of the surrounding formations (England et al., 1987). Fluids thus tend to move in the same direction updip due to the nature of the gradient and the buoyancy of the hydrocarbons (England et al., 1987). In areas of which the areal extent of the sealing lithology is large, this may cause long-range lateral migration, which

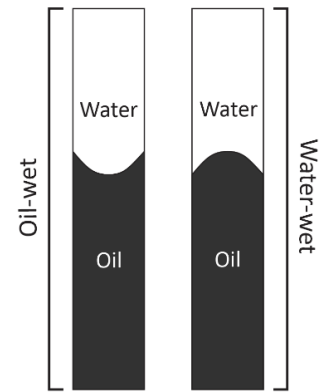


Figure 2.5: The concept of capillarity and the meniscus effect of an oil-wet and water-wet reservoir in a capillary tube. Inspired by fig. 6.17 in Selley and Sonnenberg (2015).

is common in basins that are tectonically inactive and the extent of the seal has been preserved (Hindle, 1997). Hydrocarbons will continue to migrate laterally until the capillary pressure of overlying formations is exceeded, thus facilitating vertical migration, or structural/stratigraphic permeability barriers are encountered. If no barriers are encountered, lateral migration distances may be large, exceeding 150 km (Hindle, 1997; Selley & Sonnenberg, 2015).

Under hydrostatic conditions, the only forces acting on hydrocarbons are the vertical buoyancy and capillary pressures. The process of vertical migration thus occurs whenever the buoyancy or displacement pressure exceeds the capillary pressure of the overlying formation, and will continue until the fluids reach a virtually impermeable seal (Selley & Sonnenberg, 2015). Vertical migration is also governed by the relationship between the pore pressure and fracture pressure of the formation. The fracture pressure (fig. 2.4) is the amount of pore pressure the formation can withstand before fracturing occurs, and is usually 70-90% of the overburden pressure (Osborne & Swarbrick, 1997). In overpressured environments, fluid migration is prevented so that the formation pore pressure consequently builds up. If the fracture gradient is less than the lithostatic gradient, pore pressures approaching the fracture pressure may cause disintegration of the formation. This will consequently increase the porosity and permeability of the formation, ultimately resulting in enhanced fluid migration (Osborne & Swarbrick, 1997).

2.2 Faults

Faults are complex deformational features, characterized by shear displacement confined along a surface or a narrow zone (Fossen, 2016). Faulting and fracturing of rocks occur when the stress applied to the rock exceeds its internal strength, and by displacing the surrounding material, faults form discontinuities in the subsurface by brittle or plastic deformation (Fossen, 2016). The complex structural development of the SW Barents Sea has resulted in the development of extensive fault zones, reaching both deeper and shallower stratigraphic levels. As faults may act as fluid conduits or impair fluid movement, the structural setting and development of the SW Barents Sea and Loppa High (accounted for in chap. 3) may have had a significant impact on both fluid flow and prospective reservoirs in the area.

2.2.1 Fault anatomy and types

The complexity of a fault is attributed to its many structural features, such as multiple slip surfaces and subsidiary fractures. However, the general anatomy of a fault can be divided into a central *fault core* or *surface*, characterized by intense shearing, and the *fault damage zone*, representing the zone of deformed material surrounding the fault core (Fossen, 2016). A

common feature of the fault zone is the presence of fault gouge (for crystalline rocks) or smear (for sedimentary rocks), acting as low-permeability barriers for fluid flow (Fossen, 2016).

The largest fault in a faulted area is commonly called the *master fault*. The master fault is often associated with minor faults that are antithetic (dipping towards the master fault) or synthetic (dipping away from the master fault). Faults are generally classified based on the relative displacement of fault blocks and their angle of dip. For non-vertical faults, it is common to distinguish between the hanging wall (above the fault plane) and the footwall (below the fault plane), and the relative displacement between them give rise to three types of faults (illustrated in fig. 2.6); *normal* (hanging wall downthrown), *reverse* (hanging wall upthrown) and *strike-slip* (lateral displacement). Faults with dip angles less than 30° are termed *low-angle faults*, whereas faults with dips exceeding 60° are termed *steep faults*. Faults that tend to flatten downwards (decreasing dip) are known as *listric faults*. A common result of normal faulting is the development of *horst-and-graben structures*. Horsts (upthrown block) and grabens (downthrown block) develop whenever two normal faults are dipping away or towards each other, respectively (Fossen, 2016).

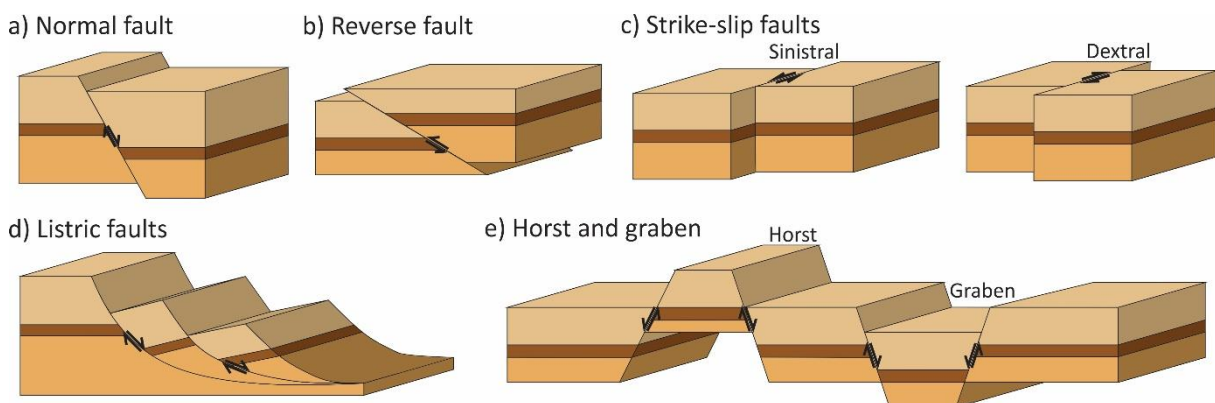


Figure 2.6: The main fault types.

2.2.2 Fault initiation and reactivation

The stress applied on a surface is a vector (σ), defined as force (F) per unit area (A). A stress vector can be resolved into a normal stress component (σ_n) and a shear stress component (σ_s), acting perpendicular and parallel to the surface, respectively. At any point in the subsurface, rocks will experience stress from all directions, and the stress state can be described by three principle stress vectors that are orthogonal to each other: σ_1 , σ_2 and σ_3 , of which $\sigma_1 > \sigma_2 > \sigma_3$. The principal stresses and their inherent normal and shear stress components contribute to the normal and shear stress acting on a given plane (Fossen, 2016). If the stress is equal in all directions, the stress is termed lithostatic and $\sigma_1 = \sigma_2 = \sigma_3$. However, directional tectonic

stresses give rise to differential stress, which is defined as the difference between maximum stress (σ_1) and the minimum stress (σ_3); $d = \sigma_1 - \sigma_3$ (Fossen, 2016).

When the differential stress exceeds the internal yield strength of the rock, fracturing and faulting results, and the manner in which this occurs depends on the magnitude of the different principle stresses. Anderson (1951) proposed a classification of tectonic stress regimes into normal, thrust and strike-slip regimes based on which of the three principle stresses is vertical (illustrated in fig. 2.7); (1) σ_1 is vertical for normal-fault regime, (2) σ_3 is vertical for reverse-fault regime and (3) σ_2 is vertical for strike-slip regime (Fossen, 2016).

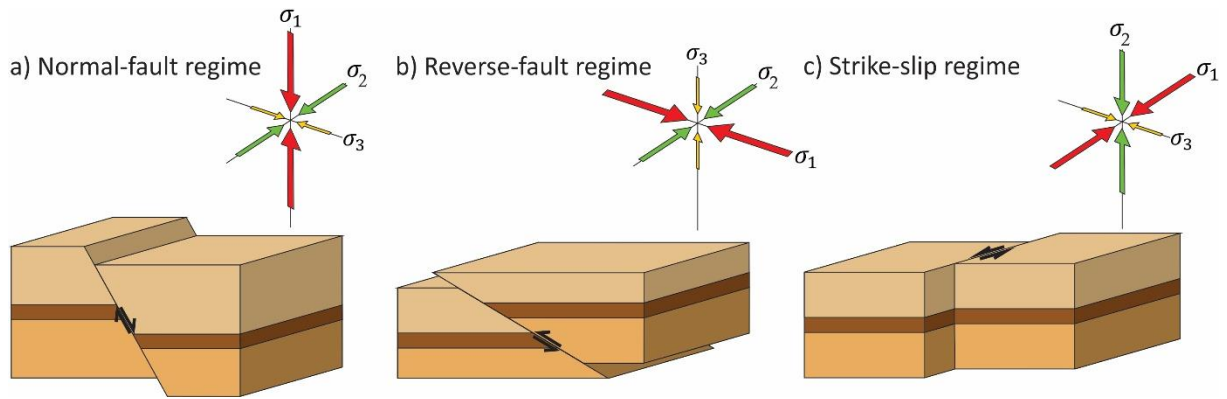


Figure 2.7: Anderson's (1951) classification of tectonic regimes, showing the relationship between the three principle stresses and the relative magnitude of stresses. Inspired by fig. 5.13 in Fossen (2016).

The normal and shear stresses acting on planes of all possible orientations through a point in a rock can be described by Mohr's circle (illustrated in fig. 2.8). The horizontal and vertical axes correspond to normal (σ_n) and shear (σ_s) stresses acting on a plane through a given point, and the value of the maximum (σ_1) and minimum (σ_3) principal stresses are plotted on the horizontal axis. Thus, at any point on Mohr's circle, the normal and shear stress values acting on a plane can be obtained. The distance between σ_1 and σ_3 , i.e. the differential stress, constitutes the diameter of the circle (Fossen, 2016).

As mentioned, the initiation of a fracture occurs whenever the differential stress exceeds the internal strength of the rock. The Coulomb fracture criterion accounts for the critical shear stress and normal stress acting on a potential fracture at the moment of failure, and thus describes the condition at which a rock fractures (Fossen, 2016). Accounting for the normal (σ_n) and shear (σ_s) stresses, the internal strength of the rock (C) and the angle of internal friction (ϕ), the fracture criterion can be defined as:

Eq. 2.7: Coulomb fracture criterion

$$\sigma_s = C + \sigma_n \tan \phi$$

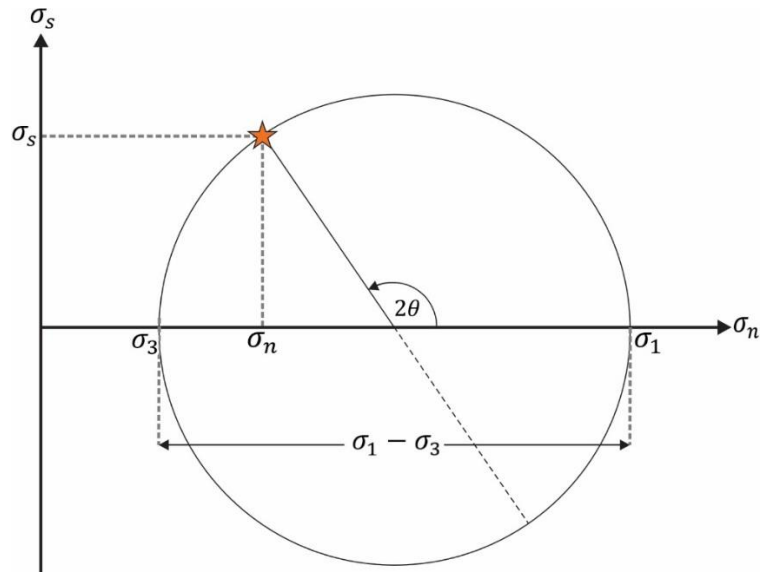


Figure 2.8: Mohr's circle. Star represents the fault plane orientation, of which both shear and normal stresses can be obtained. Note that the angles in Mohr's space are doubled. Inspired by fig. 4.7 in Fossen (2016).

The Coulomb fracture criterion is expressed as a straight line in Mohr's space, and defines the Coulomb failure envelope (illustrated in fig. 2.9). The stress state of the rock is determined by the position of Mohr's circle relative to the failure envelope. The state of stress is stable if the circle lies well outside the envelope. If the envelope is tangent to the circle, the state of stress is critical, and if the circle intersects or crosses, the state of stress becomes unstable and results in fracturing. Rocks containing fluids may be forced into an unstable state if the pore pressure increases (Fossen, 2016).

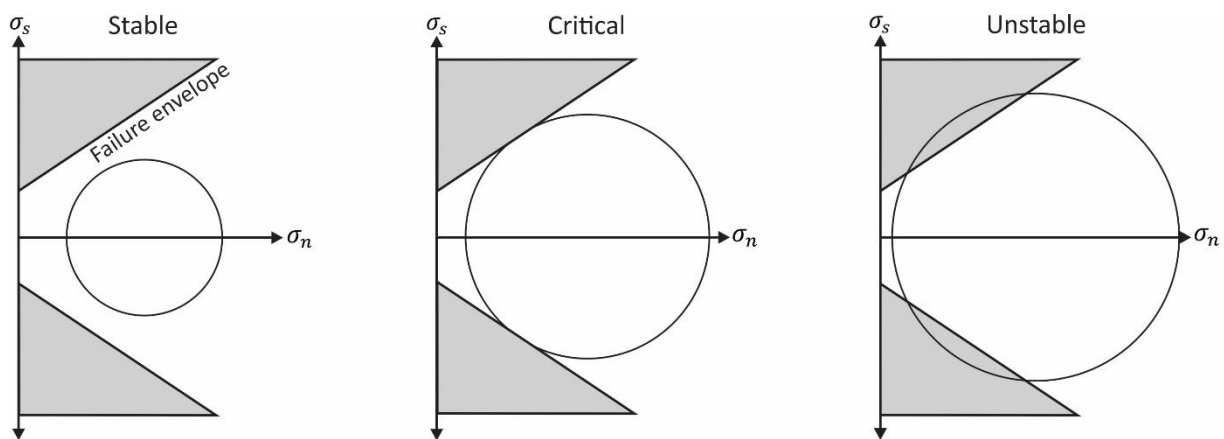


Figure 2.9: Mohr's circle and Coulomb failure envelope, and corresponding states of stress. Inspired by fig. 7.13 in Fossen (2016).

Fault and fracture formation is a process encompassing the growth and linkage of smaller structural features such as minor fractures. Once a fault or fracture has developed, it represents a zone or plane of weakness. The stress required to reactivate such a zone is much less than that

required to develop new ones, and reactivation of older fractures and faults is thus more likely if stress were to build up again (Fossen, 2016).

2.2.3 Polygonal faults

Polygonal fault systems are extensive arrays of normal dip-slip faults confined to a specific stratigraphic interval in the subsurface, observed in passive margin basins, abyssal basins and some foreland and intracratonic basins (Cartwright & Dewhurst, 1998). Very fine-grained (clay size) sediments exclusively characterize these intervals, of which host sediments may range from claystones to chalks (Cartwright, 2011; Cartwright & Dewhurst, 1998). The propagation of individual faults causes them to have a wide range of strikes, resulting in a characteristic polygonal planform geometry suggesting a non-tectonic origin (Cartwright, 2007, 2011).

The stratigraphic units hosting the polygonal faults are usually referred to as tiers (Cartwright, 2011). Within these tiers, individual faults are planar to gently listric with increasing depth or thickness of the tier. Shallow faults have dips ranging from 50° to 80°, whereas deeper-seated faults have dips ranging from 20° to 50° (Cartwright, 2011). Even though there are good indications that the development of polygonal fault systems begins at shallow burial depths, their exact origin is still a matter of debate. Several theories have been proposed for the mechanisms responsible for their development, including syneresis of colloidal sediments, density inversion, volumetric contraction and low coefficients of residual friction (Cartwright & Dewhurst, 1998; Cartwright & Lonergan, 2003; Davies & Ireland, 2011; Davies et al., 2009; Dewhurst et al., 1999; Goult, 2008).

Polygonal faults may be of great importance for petroleum geologists. The manner of faulting may compartmentalize intervals of interbedded sandstones (Cartwright, 2011; Goult, 2008), juxtaposing sealing lithologies towards permeable lithologies and thus creating local and potentially closed reservoirs. Fluid escape features observed in association with polygonal fault systems may also suggest that the faults have been or are acting as fluid conduits (Goult, 2008). Given that these faults may transmit fluids, the relatively shallow depths may facilitate the development of shallow hydrocarbon accumulations.

2.2.4 Migration through faults

According to Ligtenberg (2005), faults are in many basins the main conduits for fluids. Considering that displacement across a fault may be significant and extensive, fault conduits have the potential to transmit fluids over long vertical distances (Cartwright et al., 2007). The most common practice in interpreting faults as fluid conduits has been to define them as either conductive (open) or non-conductive (sealing). However, the inherent characteristics of fault

zones, such as complexity, fault plane irregularities and fault intersections, suggests that potential fluid flow through such a zone is equally complex; it is more likely that fluid flow is concentrated and focused to local and weaker sections of the fault zones (Ligtenberg, 2005). Faults may be sealing due to the presence of fault gouge, a low-permeability, fine-grained rock formed by tectonic forces, usually in areas of high shear strain. The production of fault gouge, or the lack thereof, governs the development of open and weak sections prone to enhanced fluid flow within the fault zone, and determines the extent to which fluid flow may occur (Cartwright et al., 2007; Ligtenberg, 2005). The juxtaposition of lithologies across a fault may also determine whether a fault is sealing or not, regardless of the properties of the actual fault. A sand terminating towards a shale will obviously impair fluid movement, whereas a sand terminating towards a sand may result in sustained fluid flow across the fault (Fossen, 2016).

Individual faults or fault zones have a very limited lateral extent and can therefore be difficult to identify directly on seismic sections. Instead, fault zones are usually represented by discontinuous reflections of great vertical extent and a relative displacement of reflections across the discontinuities (Løseth et al., 2009). As hydrocarbons are rarely observed within the faults themselves, fluid migration is usually represented by other direct hydrocarbon indicators (further described in section 2.4). This includes bright spots on either side of faults, of which fluids have migrated into adjacent permeable zones and changed the acoustic properties of the strata (Ligtenberg, 2005; Løseth et al., 2009). Pockmarks and mud volcanoes may also be observed in association with faults and are indications of fluid leakage, often occurring on the seabed or as paleo-features along structural trends (Ligtenberg, 2005).

2.3 Seismic reflection theory

The studies carried out in this thesis relies primarily on the interpretation of seismic data, and it is therefore necessary to account for the main geophysical principles substantiating the seismic reflection method. Seismic surveying and acquisition have long been important tools for mapping the subsurface, also revealing important physical properties of subsurface strata. Continuous improvement of the acquisition process, including further development of equipment and data processing tools, have resulted in better quality, resolution and versatility of the method (Keary et al., 2002).

2.3.1 Basic principles

The seismic reflection method is based on the generation of seismic waves or pulses from a controlled source, and the recording of the reflected pulses by receivers distributed near or at the surface (Keary et al., 2002; Nanda, 2016). During propagation, the seismic pulses interact

with the subsurface strata and its internal boundaries, causing some of the energy to be reflected back towards the surface (Nanda, 2016). The characteristics of the recorded reflected pulse depends mainly on two physical properties; the compressional wave velocity (V_p , m/s) and the density (ρ , kg/m³) of the medium of which the pulse propagates through. The product of these properties is known as *acoustic impedance* (Z)(Keary et al., 2002), and can be expressed as:

Eq. 2.8: Acoustic impedance

$$Z = V_p \cdot \rho$$

A significant change in acoustic impedance (i.e. impedance contrast) usually occur at layer interfaces in the subsurface, resulting in the generation of a seismic reflection (Nanda, 2016; Veeken, 2013). The strength or amplitude of the generated reflection can be quantified in terms of the *reflection coefficient* (RC), which is expressed as:

Eq. 2.9: Reflection coefficient

$$R = \frac{Z_2 - Z_1}{Z_2 + Z_1} = \frac{V_2\rho_2 - V_1\rho_1}{V_2\rho_2 + V_1\rho_1}$$

where Z_1 and Z_2 are the acoustic impedances of the upper and lower layer, respectively (Keary et al., 2002). It follows from eq. 2.9 that $-1 \leq R \leq +1$, where RC = -1 or 1 indicates that all energy is reflected. In the case of RC = 0, all energy is transmitted, occurring whenever there is no acoustic impedance contrast across an interface (Keary et al., 2002).

2.3.2 Seismic response and polarity

Seismic pulses reflected and recorded by receivers are visually presented as *seismic traces*, representing the response of the elastic wave to impedance contrasts across interfaces in the subsurface (Keary et al., 2002). The seismic traces consist of wavelets that are plotted as a function of time and are usually described in terms of polarity or phase. There are several polarity conventions available, the two most common being the convention of Badley (1985) and that of Sheriff (2002). For the purpose of this thesis, the Society of Exploration Geophysicists (SEG) polarity convention after Sheriff (2002) has been applied (illustrated in fig. 2.10). For a minimum-phase, normal polarity wavelet, an increase in acoustic impedance results in a deflection to the left (trough, white) right below the interface, followed by a deflection to the right (peak, black). In the case of reversed polarity, a deflection to the right (peak, black) is followed by a deflection to the left (trough, white). For a zero-phase, normal polarity wavelet, an increase in acoustic impedance results in a central peak at the interface and

two side-troughs. The opposite, a central trough at the interface and two side-peaks, occurs in the case of reversed polarity.

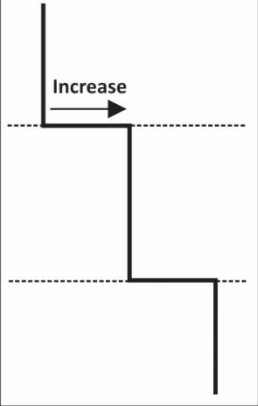
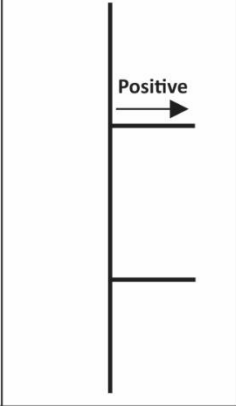
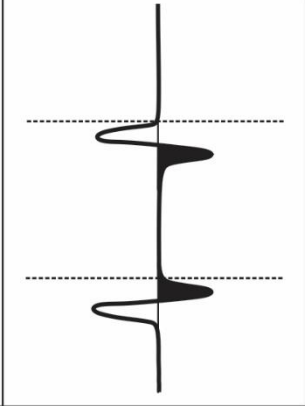
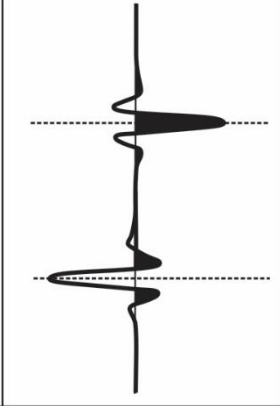


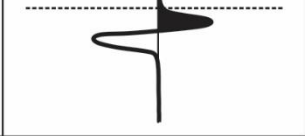
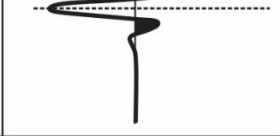
Convention after Sheriff (2002)				
Polarity	Acoustic impedance	Reflection coefficient	Minimum phase signal	Zero-phase signal
Normal				
Reversed				

Figure 2.10: Polarity convention after Sheriff (2002), used in this master thesis.

2.3.3 Resolution

Seismic resolution constitutes the greatest constraint on seismic interpretation and subsurface mapping, ultimately defining the quality and level of detail attained during a survey. As a quantification of the greatest achievable precision, resolution is defined by the size of the smallest features that have the potential to be detected by the seismic pulse, both in time and space (Keary et al., 2002; Nanda, 2016). The resolution is dependent on the acquisition and processing systems and comprises both a vertical and horizontal aspect (Brown, 2004; Nanda, 2016). Both the vertical and horizontal resolution is determined mainly by the dominant wavelength (λ , m) of the seismic pulse, which in turn is dependent on the frequency (f , Hz) and the velocity (v , m/s) of the signal (Brown, 2004; Nanda, 2016). The relationship between these parameters can be expressed as:

Eq. 2.10: Relationship between wavelength, velocity and frequency

$$\lambda = \frac{v}{f}$$

It follows from eq. 2.10 that any change in any of these parameters will affect the resolution of the survey (relationship illustrated in fig. 2.11). In general, velocity tend to increase with depth due to the effects of sediment compaction and diagenesis, and subsequent density increase (Brown, 2004; Nanda, 2016). As higher frequencies attenuate faster due to absorption of energy by frictional losses, deeper-travelling waves tend to have lower dominant frequencies, ultimately resulting in the lengthening of the pulse (Brown, 2004; Nanda, 2016). Thus,

frequency decreases whereas wavelength increases with increasing depth. During propagation of a seismic pulse, the energy originating from the source becomes distributed over an expanding spherical cell known as the *wavefront*. As the same amount of energy becomes distributed over a successively larger area, the energy attenuates due to geometrical spreading, resulting in poorer resolution with depth (Brown, 2004; Keary et al., 2002; Nanda, 2016; Veeken, 2013). Other causes of energy loss and hence poorer resolution include scattering/dispersion of energy and wave conversions at subsurface interfaces (Keary et al., 2002; Nanda, 2016).

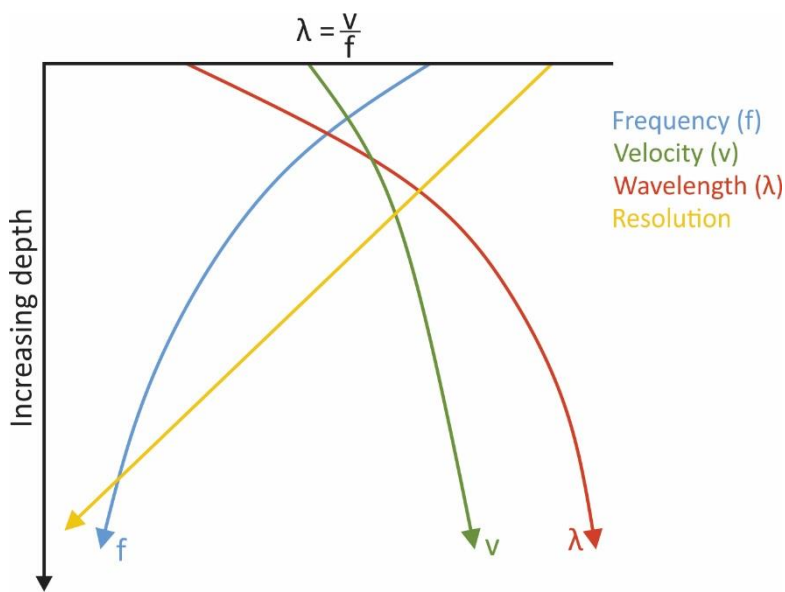


Figure 2.11: Relationship between velocity, wavelength, frequency and resolution. Inspired by fig. 1-3 in Brown (2004).

2.3.3.1 Vertical resolution

A multi-layered subsurface tend to produce a number of reflectors given sufficient impedance contrasts across the vertically adjacent interfaces. The ability to recognize and separate these superimposed, individual reflection events is measured in terms of the vertical resolution (Keary et al., 2002; Nanda, 2016; Veeken, 2013). According to Brown (2004), the vertical resolution has two main limits; the limit of separability and the limit of visibility. The *limit of separability* (also known as tuning thickness) defines whether two superimposed interfaces may be distinguished from one another on a seismic section or not; it is equal to $\frac{\lambda}{4}$ and is the bed thickness corresponding to the closest separation between two wavelets of a given seismic pulse (Brown, 2004). Below this limit, amplitudes progressively interfere until the *limit of visibility* is reached. The interval may still be present in the subsurface but is too thin to be resolved seismically (Brown, 2004). The concept of vertical resolution is summarized in fig. 2.12, a wedge model in which amplitudes from the upper and lower interface progressively interfere.

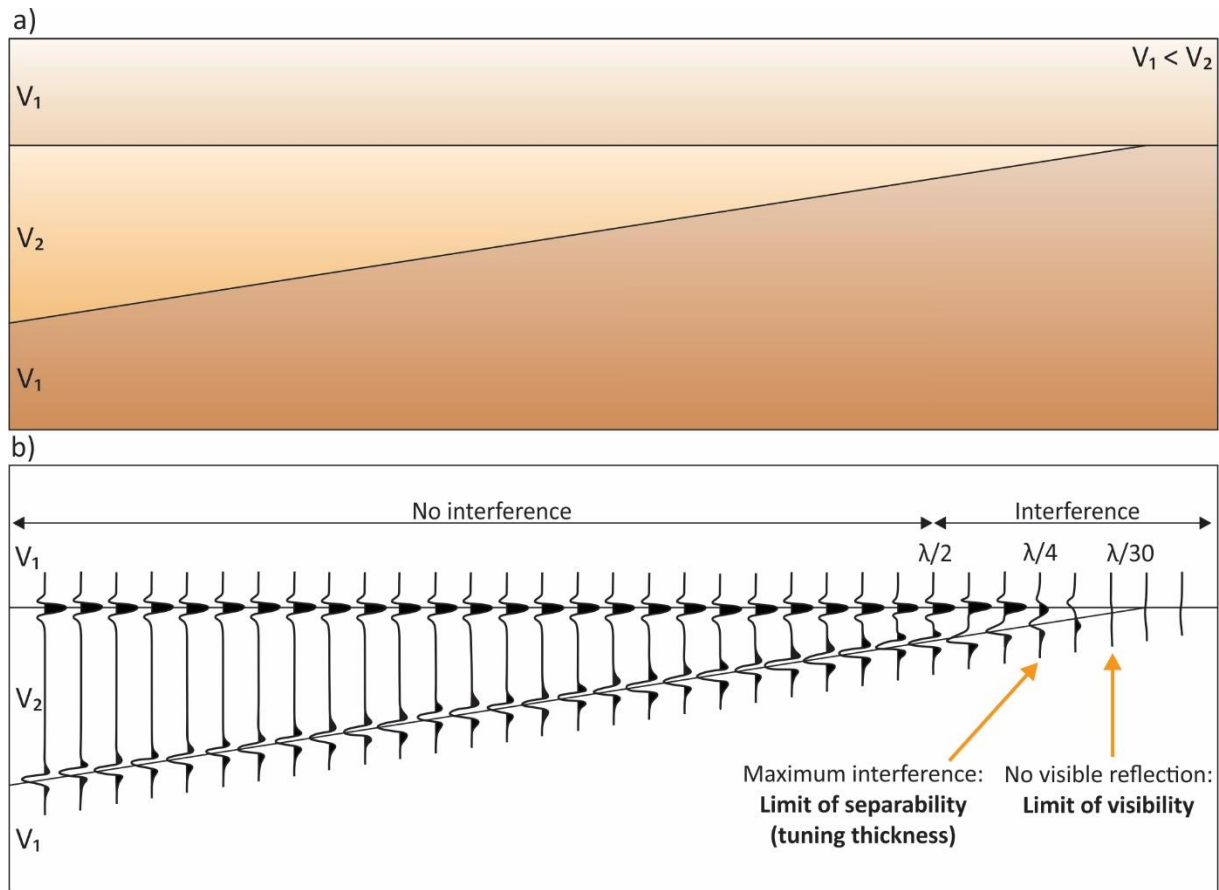


Figure 2.12: Wedge model showing the concept of vertical resolution. a) Cross-section through the subsurface, with an incised higher-velocity wedge. b) Seismic response (zero-phase, normal polarity wavelet) and interference effects. Inspired by fig. RES1 and RES3 in Badley (1985).

2.3.3.2 Horizontal resolution

The horizontal resolution measures the ability to recognize and separate individual features that are laterally adjacent to one another (Nanda, 2016). There are mainly two constraints on the horizontal resolution; the detector spacing of the seismic array and the actual reflection process of a seismic pulse (Keary et al., 2002). The energy generated by a source propagates as a three-dimensional wavefront, of which a considerable area of the wavefront interacts with the interface, as illustrated in fig. 2.13a (Keary et al., 2002; Nanda, 2016). The wavefront first tangents the reflector, producing the initial reflected arrival recorded by the receivers from one reflection point. As the wavefront propagates, an infinite number of reflection points in a given area contributes energy to the recorded reflected signal. This area, known as the Fresnel Zone, is limited by the extent of the wavefront interacting with the reflector one-quarter of a wavelength later, arriving within one-half of a wavelength at the receiver (due to two-way travel time). Hence, the radius of the Fresnel Zone represents the absolute limit on the horizontal resolution of unmigrated seismic data (Keary et al., 2002). This implies that features with a lateral extent exceeding the Fresnel Zone may be observed in the seismic data, whereas features with a lesser lateral extent is non-detectable (fig. 2.13a).

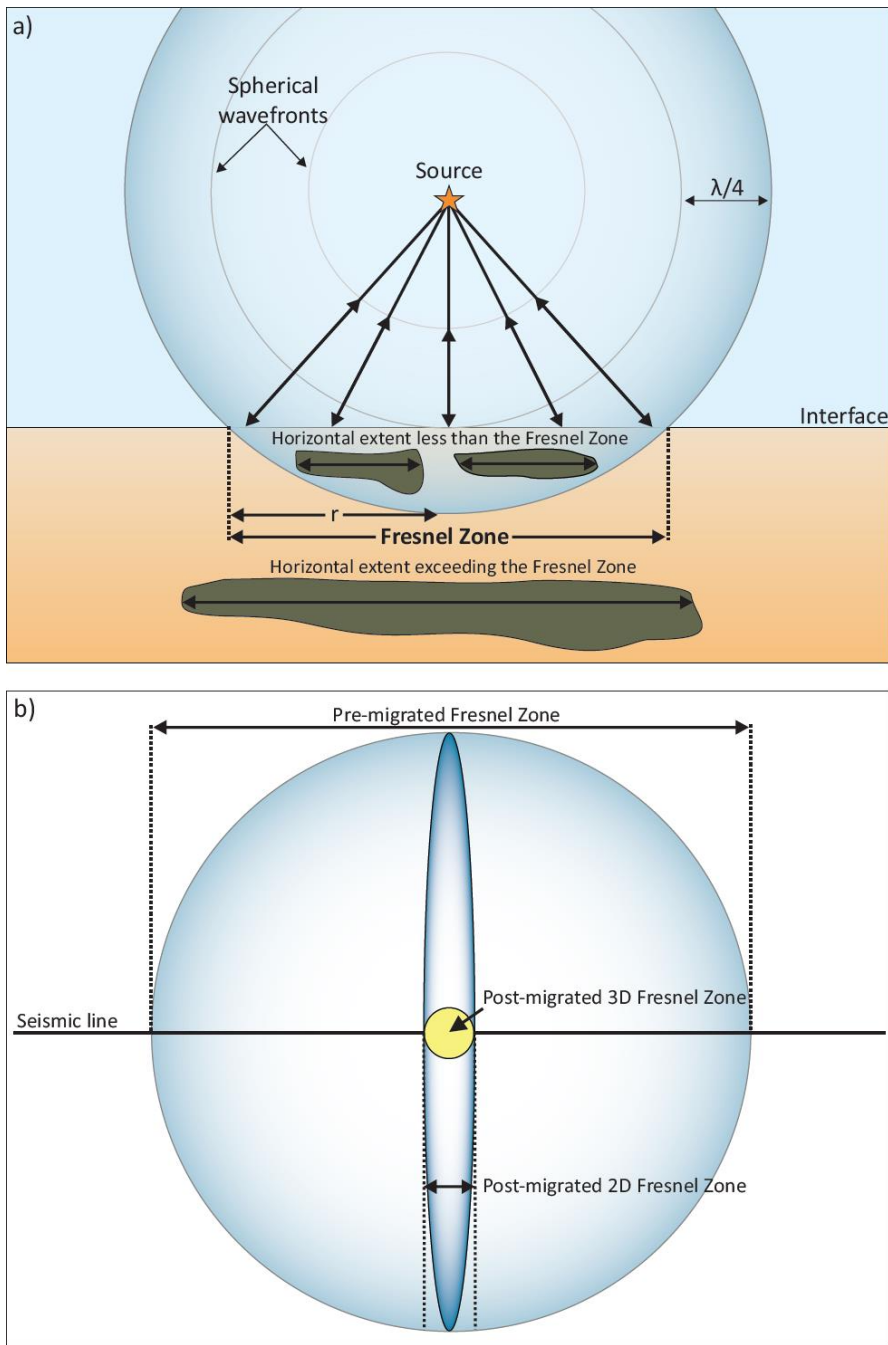


Figure 2.13: a) The concept of horizontal resolution and the Fresnel Zone. Inspired by fig. 4.11 in Keary et al. (2002). b) The concept of seismic migration, enhancing the horizontal resolution by collapsing energy into an ellipse for 2D data and a circle for 3D data. Inspired by fig. 1-5 in Brown (2004).

The radius (r , m) of the Fresnel Zone can be expressed as a function of the average seismic velocity (v , m/s), two-way travel time (t , s) and frequency (f , Hz)(Brown, 2004):

Eq. 2.11: Horizontal resolution (radius of the Fresnel Zone)

$$r_f = \frac{v}{2} \sqrt{\left(\frac{t}{f}\right)}$$

It follows from eq. 2.11 that the width of the Fresnel Zone increases with increasing depth and velocity and with lower frequencies. Horizontal resolution may be improved by using the

process of seismic migration, which encompasses (1) repositioning of reflectors to their original position, (2) focusing energy distributed over the Fresnel Zone and (3) collapsing diffraction patterns from points and edges (Brown, 2004; Nanda, 2016). The energy spread over the Fresnel Zone is focused to an ellipse for 2D data and to a small circle for 3D data (illustrated in fig. 2.13b). This results in a more concentrated and interpretable seismic signal, hence an enhanced horizontal resolution (Brown, 2004; Nanda, 2016).

2.4 Fluid flow features

Indicators of fluids and fluid flow can be observed as morphologically distinct features on the seabed (surface indicators) as well as seismic anomalies in the subsurface (subsurface indicators). Confidence in interpretation of potential fluid flow processes comes from integrated studies of both surface and subsurface features, and thus the most common features will be accounted for in the following sections.

2.4.1 Surface indicators

Fluids moving through poorly consolidated sediments may cause alterations and disturbances of the primary sedimentary structures when moving towards and eventually reaching the seabed surface (Judd & Hovland, 2007). Fluid expulsion near or at the surface may cause the development of distinct surface features, of which the actual expulsion of fluids may be observed as bubble plumes rising above the seabed.

2.4.1.1 Pockmarks

The most common indicators of focused fluid flow and expulsion are *pockmarks* (fig. 2.14a-b), which are erosive, circular to sub-circular depressions or craters on the seabed (Hovland et al., 2002; Judd & Hovland, 2007). They are morphologically diverse features found in marine or lacustrine environments, and the fluids expelled may be gas or liquid, originating from microbial, thermogenic, hydrothermal or volcanic processes, or from groundwater (Hovland et al., 2002). The distribution of pockmarks on the seabed is largely controlled by the underlying geology, fluid flux and the nature of the seabed sediments (Hovland et al., 2002). Pockmarks are thought to form in response to fluid eruption in low-permeability, fine grained sediments, of which each eruption episode is followed by an extended period of recurring fluid escape (Hovland et al., 2002; Judd & Hovland, 2007).

Due to the large variations in dimensions, location and character, Hovland et al. (2002) subdivides pockmarks into six morphological classes; unit pockmarks, normal pockmarks, elongated pockmarks, eyed pockmarks, strings of pockmarks and complex pockmarks. Depending on the resolution of seismic data and the size of the pockmarks, the craters can be

observed on both the seabed reflection and as buried paleo-pockmarks on deeper reflections (Ligtenberg, 2005).

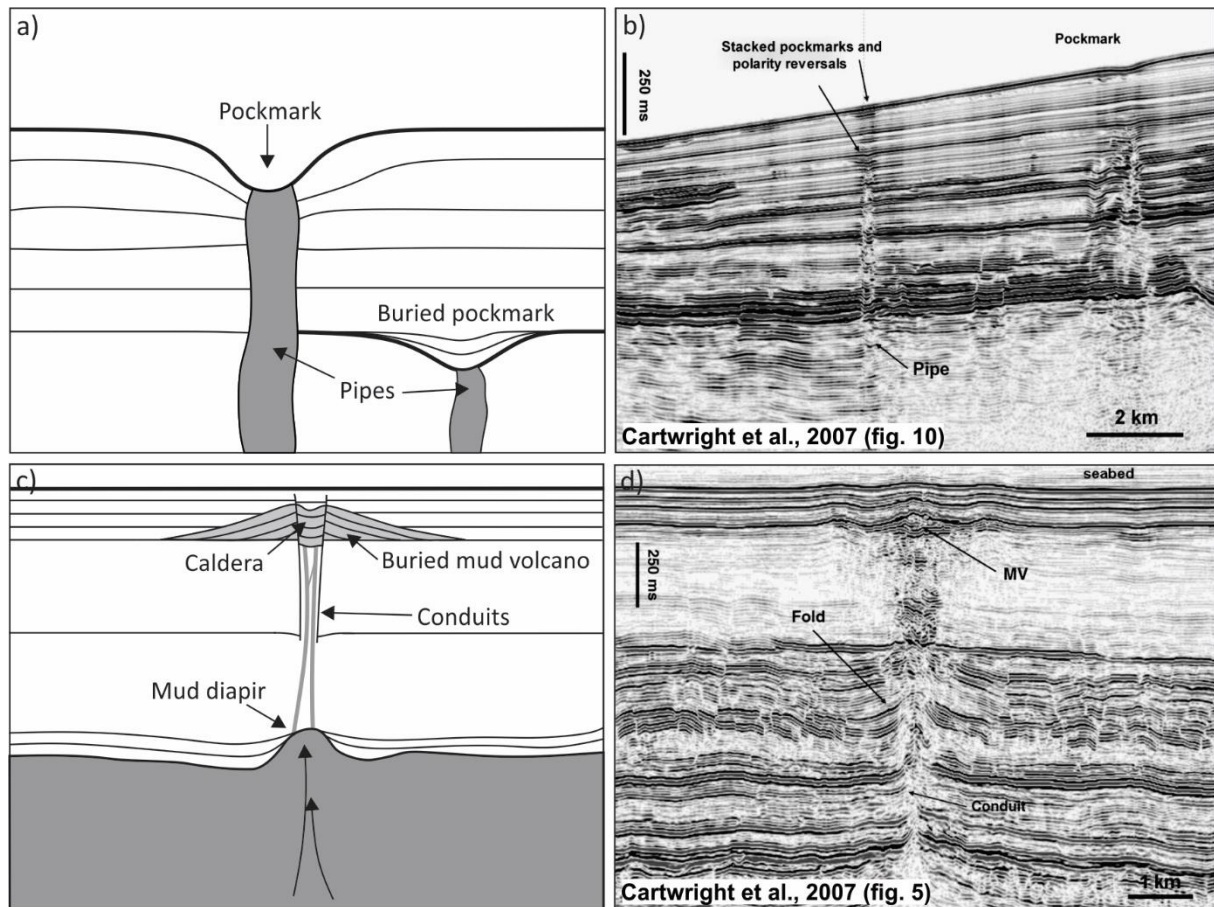


Figure 2.14: a) Illustration of pockmarks and buried pockmarks and associated pipes. b) Seismic section showing vertically stacked pockmarks and associated pipes (left) and a pockmark occurring on the seabed (right). Modified from Cartwright et al. (2007). c) Illustration of a buried mud volcano and associated mud diapir and conduits connecting the two features. d) Seismic expression of a buried mud volcano. Modified from Cartwright et al. (2007).

2.4.1.2 Mud volcanoes and dipairs

In contrast to pockmarks, *mud volcanoes* (fig. 2.14c-d) are positive topographic features which periodically or continuously release fluids and liquid sediments (Judd & Hovland, 2007; Ligtenberg, 2005). They are characterized as conical hills with a central crater or vent, representing the region of fluid/sediment expulsion. The diameter of mud volcanoes ranges from a few centimeters to over 1000 m, and their height may be ten to hundreds of meters (Judd & Hovland, 2007). *Mud diapirs* are features rising through and deforming surrounding and younger strata (fig. 2.14c). Diapirs are usually restricted as a subsurface feature, but if they reach the seabed and expel fluids/sediment, they are termed mud volcanoes. The vertical extent of the conduits of mud volcanoes and diapirs can reach up to several kilometers, and they are as such commonly deeply rooted (Judd & Hovland, 2007). The formation and development of mud volcanoes and diapirs is related to processes such as rapid sedimentation in e.g. subsiding

basins, deltas and deep-water fans, as well as accumulations of sediments in accretionary wedges (Judd & Hovland, 2007).

2.4.2 Subsurface indicators

As mentioned, the impedance contrasts giving rise to reflections are dependent on the density contrasts across interfaces and the compressional wave velocity (V_p) of the formations. However, the presence of pore fluids usually alters the acoustic properties of subsurface strata. Gas encountered in the sediments may cause dramatic decreases in V_p due to the low density of the gas (reducing the bulk density of the formation); this results in a strong impedance contrast characterized by a negative reflection coefficient (RC) and an amplitude anomaly (Nanda, 2016). With a density closer to that of water, the presence of oil has little to no effect on seismic reflections. It is thus easier to identify potential gas accumulations, and there are several direct hydrocarbon indicators (DHIs) aiding the identification of fluids in the subsurface (Brown, 2004; Nanda, 2016). However, it is important to keep in mind that amplitude anomalies occurring on seismic sections may be an expression of a strong impedance contrast caused by e.g. lithological differences, rather than the presence of hydrocarbons.

2.4.2.1 Bright spots and dim spots

Bright spots (fig. 2.15a and 2.16a) are reflections with local and anomalously high amplitudes resulting from strong acoustic impedance contrasts. Bright spots are usually characterized by negative reflection coefficients, occurring when the hydrocarbon saturated section of a reservoir has a much lower acoustic impedance than the overlying strata (Nanda, 2016). The bright spots are thus phase-reversed with respect to reflections from positive impedance contrasts, such as the seabed reflector (Brown, 2004; Judd & Hovland, 2007).

Dim spots (fig. 2.15b and 2.16a) are, in contrast to bright spots, reflections with local and anomalously low amplitudes. A reservoir with a higher acoustic impedance than the overlying strata will initially cause a strong, positive impedance contrast. However, the presence of hydrocarbons (especially gas) reduces the impedance contrast and consequently the amplitude of the reflection. Hence, dim spots are phase-reversed with respect to bright spots, but has a lower amplitude than e.g. the seabed reflector (Brown, 2004; Nanda, 2016).

2.4.2.2 Flat spots

Stratification of fluids of different densities produces flat fluid contacts that can be identified in seismic sections as flat-lying reflections, often cross-cutting adjacent strata. These reflections are known as *flat spots* (fig. 2.15a-c and 2.16a), usually representing the gas/oil or oil/water contact in a reservoir. As density-dependent stratification involves an increase in density

downwards, the flat spots are always positive as each contact represents an increase in acoustic impedance, e.g. from the gas-filled reservoir to the water-filled. However, flat spots are only visible on seismic sections given sufficient thickness of the hydrocarbon column and acoustic impedance contrast across the contact (Brown, 2004; Nanda, 2016).

2.4.2.3 Polarity/phase reversals

Polarity or phase reversals (phase shift of 180°) occur when there is a change in acoustic impedance contrast along the same and otherwise continuous reflector (Nanda, 2016); a peak becomes a trough and a trough becomes a peak (fig. 2.15c and 2.16a). This may occur in areas of which the surrounding strata have a higher acoustic impedance than the hydrocarbon-bearing part of the formation, and lower acoustic impedance than the water-bearing part of the formation (Brown, 2004). Phase reversal is a common feature of bright spots.

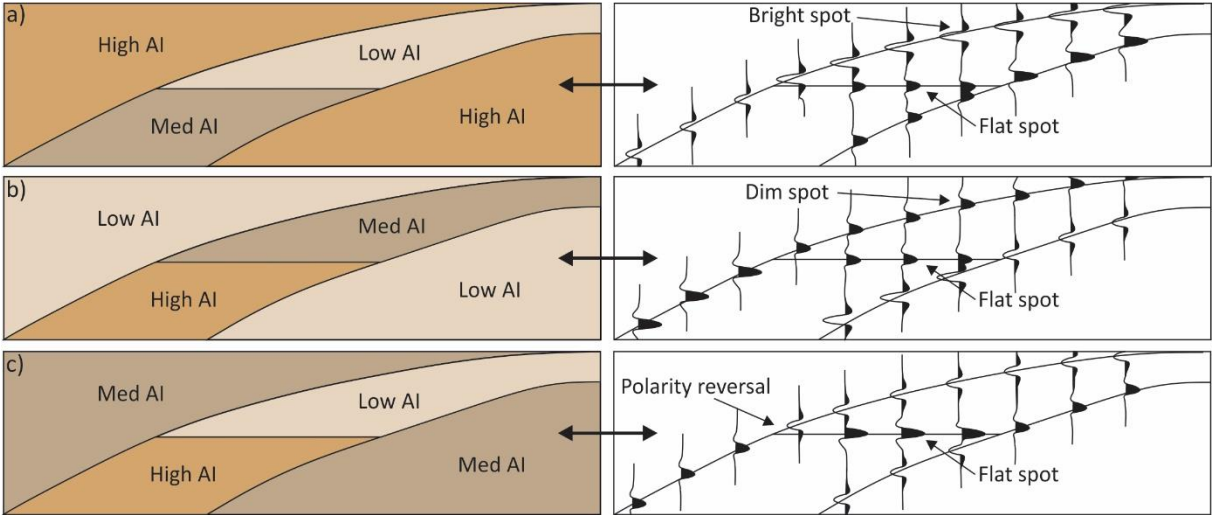


Figure 2.15: a) Geological model for generation of bright spots and subsequent seismic expression. AI = acoustic impedance. b) Geological model for generation of dim spots and associated seismic expression. c) Geological model for generation of polarity/phase reversal and associated seismic expression. Inspired by fig. 5-5 in Brown (2004).

2.4.2.4 Velocity effects

As mentioned, the presence of gas in sediments reduces the compressional wave velocity of the gas-bearing interval. It thus follows that the reflected arrival will be delayed as the seismic pulse travels slower, and given a sufficient thickness of the interval, underlying reflections may appear as deflected downwards (Judd & Hovland, 2007; Nanda, 2016). This effect is known as a *push-down* (fig. 2.16b), and commonly appear beneath gas-bearing formations. The opposite effect, known as *pull-up*, occur below high-velocity intervals (Judd & Hovland, 2007).

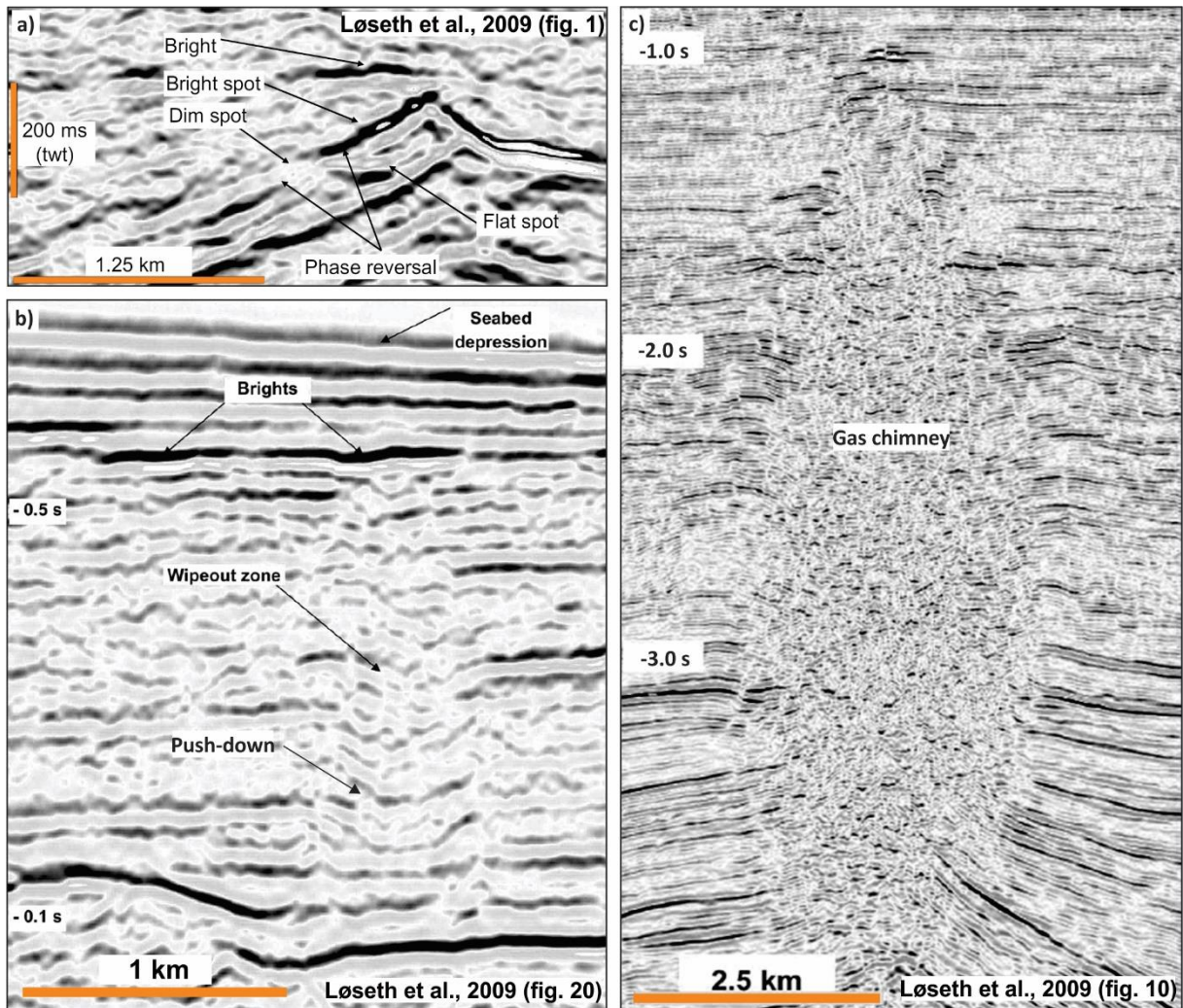


Figure 2.16: a) Seismic expression of bright spot, dim spot, flat spot and phase reversal. Modified from Løseth et al. (2009). b) Seismic expression of wipe-out zone (acoustic masking) and velocity effects (push-down). Modified from Løseth et al. (2009). c) Seismic expression of vertical wipe-out zone (gas chimney). Modified from Løseth et al. (2009).

2.4.2.5 Acoustic masking and pipes

Acoustic masking (also known as wipe-outs) refers to areas on seismic sections of highly distorted and obscured seismic signals of low amplitudes (fig. 2.16b-c). Reflections within these areas are usually characterized as chaotic and discontinuous, resulting from acoustic energy being absorbed and scattered by interstitial gas bubbles within the sediments (Judd & Hovland, 2007; Ligtenberg, 2005). On seismic sections, acoustic masking may occur in all shapes and sizes, of different orientations and extent. Although commonly occurring in soft, fine-grained sediments, similar effects may be caused by e.g. gravels scattering energy or peat absorbing energy (Judd & Hovland, 2007). *Acoustic pipes* refer to near-vertical zones of acoustic masking with very limited lateral extent. The pipes can be recognized in areas of which the continuity of reflections is disrupted over a longer vertical extent, often in association with adjacent bright spots (Andreassen, Nilssen, et al., 2007). Observations of acoustic masking in association with

bright spots or push-down of underlying reflections are strong indications of the presence of gas in the sediments.

2.5 Gas hydrates

Gas hydrates, also known as clathrates, are crystalline solids with an ice-like structure, consisting of water and gas (Judd & Hovland, 2007; Sloan et al., 1998). The gas molecules (any constituent of natural gas) are trapped in a framework of hydrogen-bonded water molecules, and there are three naturally occurring hydrate structures; I, II and H (Judd & Hovland, 2007; Sloan et al., 1998). Structure I usually contain molecules smaller than propane (e.g. methane), whereas structure II encapsulates molecules smaller than pentane (e.g. ethane and butane). Structure H encapsulates even larger molecules, usually pentanes and hexanes (Sloan et al., 1998).

Gas hydrates remain stable in very specific temperature and pressure conditions, given a sufficient supply of both water and gas (usually methane). The Gas Hydrate Stability Zone (GHSZ) defines the region of which gas hydrates form and remain stable, and is a function of bottom water temperature, the geothermal gradient, fluid pressure within sediments (water depth), pore water salinity, gas composition and the physical and chemical properties of the host rock (Bünz et al., 2003; Judd & Hovland, 2007). Conditions favorable for gas hydrate formation and accumulation are found in permafrost regions on land and in the marine environment in areas of low temperature and high pressures, usually the upper few hundred meters of the subsurface (Bünz et al., 2003; Judd & Hovland, 2007).

Changes in the stability parameters of the GHSZ may cause gas hydrates to dissociate. Changes in the pressure-temperature (P-T) conditions, such as heating or depressurizing, may cause the release of large volumes of gas and fresh water (Judd & Hovland, 2007). Gas hydrate dissociations typically affect sediment properties and stability and is thus considered a significant geohazard; the process may contribute to submarine landslides and massive blow-outs of greenhouse gases (Andreassen et al., 2017; Judd & Hovland, 2007; Vadakkepuliambatta et al., 2017).

The base of the GHSZ can be geophysically detected in seismic reflection data and is commonly represented by bottom-simulating reflectors (BSRs)(Bünz et al., 2003; Judd & Hovland, 2007). Due to the pressure-temperature dependence of gas hydrate occurrence and hence the level of the BSR, the latter usually mimics the seafloor and tends to cross-cut stratigraphic horizons (Bünz et al., 2003). The presence of gas hydrates in sediments may substantially impair the

movement of free gas towards the seafloor. The BSR is thus usually characterized by high seismic amplitudes and reversed polarity (relative to the seafloor) due to the high acoustic impedance contrast between hydrate-bearing sediments and underlying sediments containing accumulations of free (shallow) gas (Bünz et al., 2003; Vadakkepuliambatta et al., 2017). However, hydrate-bearing sediments may still exist even without a distinctive BSR, usually indicating that no free gas has been trapped beneath the gas hydrates (Bünz et al., 2003).

3 Geological framework

The Barents Sea (fig. 3.1) is a wide epicontinental sea covering the northwestern corner of the Eurasian continental shelf (Faleide et al., 2015; Faleide et al., 1984). The sea is bounded by the landmasses of the Svalbard Archipelago and Franz Josef Land to the north, Novaya Zemlya to the east, and the Kola peninsula and Norwegian Coast to the south (Faleide et al., 1984; Smelror et al., 2009). The Barents Sea defines one of the largest areas of continental shelf on Earth, covering approximately 1.3 million km², with an average water depth of usually less than 500 m (Smelror et al., 2009; Worsley, 2008).

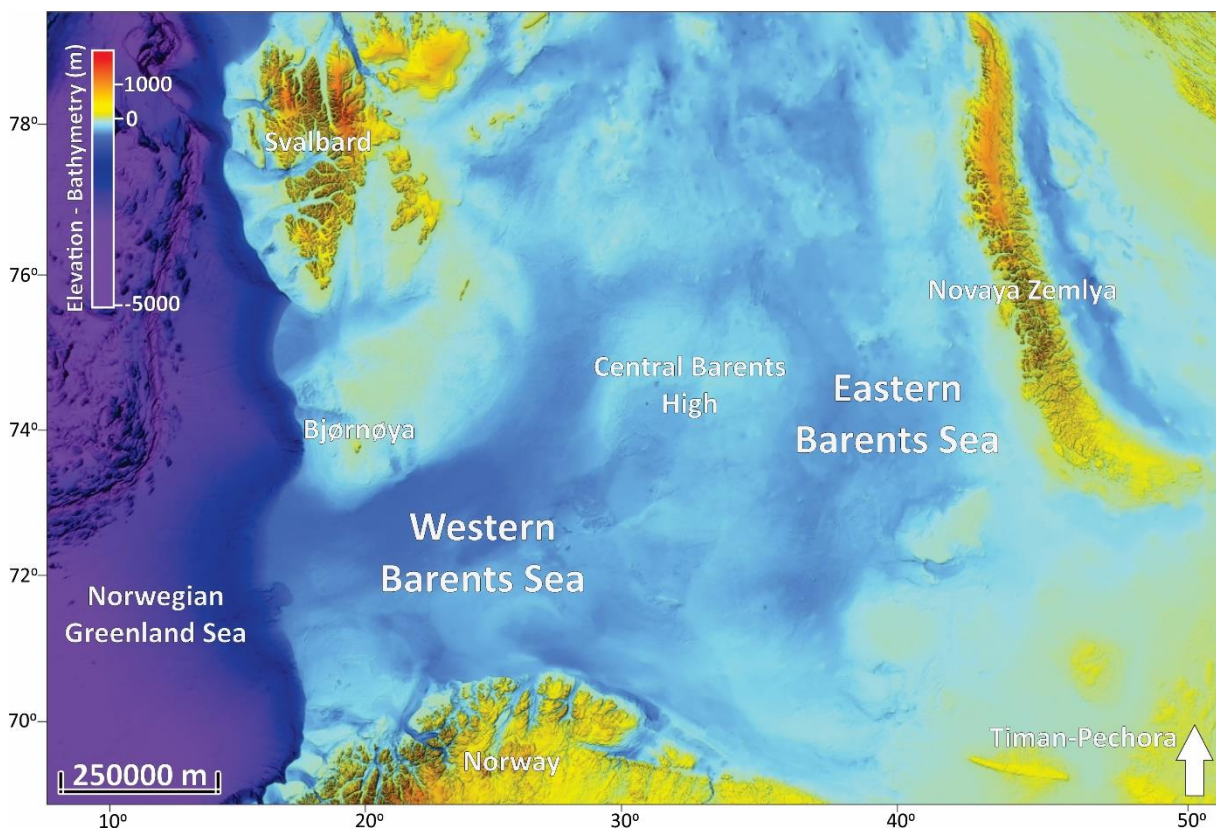


Figure 3.1: Overview of the Barents Sea, with its surrounding landmasses and subdivision into western and eastern provinces.

The present-day geology of the Barents Sea reflects a complex tectonic history and varying climatic conditions, ultimately contributing to the wide variety of depositional environments that have occurred through time across the shelf (Smelror et al., 2009). The main events related to the geological development of the Barents Sea are outlined in fig. 3.2, and will be accounted for in the following sections. Onland exposures surrounding the Barents Shelf has proven to display a comprehensive overview of the regional geology, in areas such as the Svalbard Archipelago, northern Norway, Timan-Pechora, Novaya Zemlya and Franz Josef Land (Worsley, 2008). Such exposures have been an important correlation tool for outlining the geological evolution of the Barents Sea region.

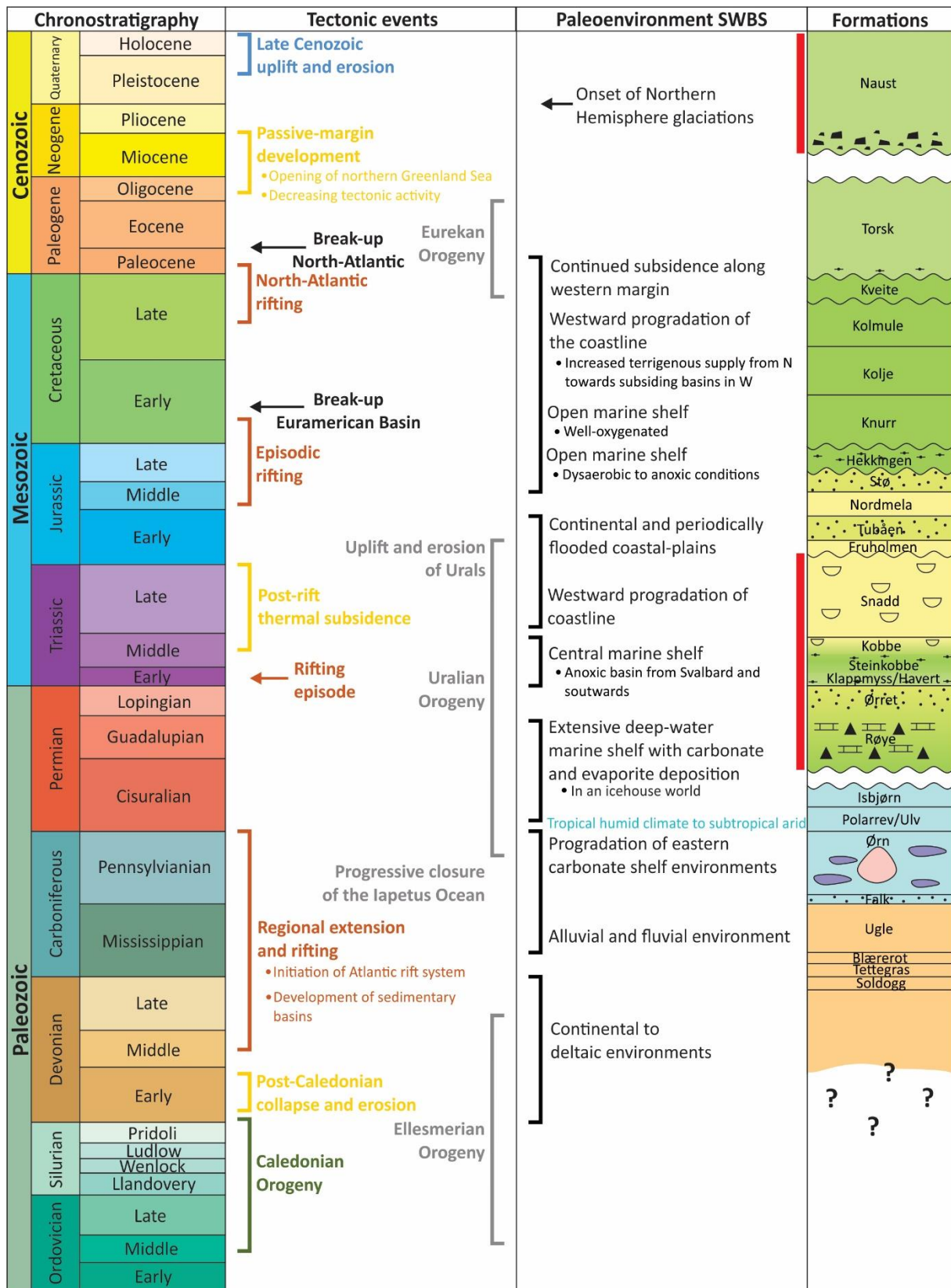


Figure 3.2: Summary of the most important events in the geological development of the Barents Sea, with emphasis on the SW region. Events of the eastern Barents Sea are colored grey. Vertical red lines indicates formations present in the study area. Inspired by fig. on p. 48 in Smelror et al. (2009).

3.1 Tectonic and structural development of the SW Barents Sea

The Barents Shelf can be subdivided into a western and an eastern province, separated by a north-south trending monoclinical structure, known as the Central Barents Arch (Henriksen, Ryseth, et al., 2011; Smelror et al., 2009). The composite mosaic of basins, platforms and highs characterizing the shelf reflects the interplay between the several phases of large-scale tectonic processes that have occurred through time (Doré, 1995; Henriksen, Ryseth, et al., 2011; Worsley, 2008). The western province has been the most tectonically active region throughout the Mesozoic and Cenozoic, with its geological development closely linked to the Caledonian Orogeny, complex post-Caledonian rifting, continental break-up and the formation of the Norwegian-Greenland Sea and Arctic Ocean (Gabrielsen et al., 1990; Smelror et al., 2009). The eastern province has experienced less pronounced tectonic activity and has been characterized by relatively stable platforms since the Late Paleozoic, with its geological development closely related to the Uralian Orogeny and the tectonic histories of the Novaya Zemlya and Timan-Pechora areas (Gabrielsen et al., 1990; Smelror et al., 2009; Worsley, 2008). As the current study area, Loppa High, is located in the western province, emphasis is placed on the geological development of the southwestern Barents Sea.

3.1.1 Paleozoic

From Ordovician times, the geological development of the western Barents Sea was directly linked to the Caledonian Orogeny. Caledonian deformation commenced in Middle Ordovician times, reaching its maximum during the Silurian (Henriksen, Ryseth, et al., 2011). The Caledonian Orogeny culminated in Early Devonian times (approximately 400 Ma (million years ago)), as the Laurentian (Greenland and North America) and the Baltican (Scandinavia and western Russia) plates consolidated into the Laurasian continent following the closure of the Iapetus Ocean (Doré, 1995; Smelror et al., 2009). By Late Devonian, extensive land areas covered most of the western Barents Sea, and post-Caledonian rifting and collapse was accompanied by extensive erosion of the hinterland (Henriksen, Ryseth, et al., 2011). The main structural trend (the Barents Sea Caledonides) follows the north-easterly axis between Laurentia and Baltica, covering most of the southwestern Barents Sea and continuing towards the northeast. A northerly oriented trend (the Svalbard Caledonides) underlies the northwestern Barents Sea (Henriksen, Ryseth, et al., 2011; Smelror et al., 2009). The fracture system originating from the Caledonian Orogeny and older tectonic events may have set the premises for the following structural development of the region (Gudlaugsson et al., 1998; Smelror et al., 2009).

During Carboniferous, regional extension and rifting dominated the western Barents Sea, exemplified by the development of a 300 km wide rift zone (Barents Sea rift), extending approximately 600 km towards the northeast (Gudlaugsson et al., 1998; Smelror et al., 2009). Related tectonic activity and rifting have been regarded as related to the initiation of the Atlantic rift system between Norway and Greenland, leading to the development of interconnected half-grabens and highs along old, inherited structures from the Barents Sea Caledonides (Gudlaugsson et al., 1998; Henriksen, Ryseth, et al., 2011; Smelror et al., 2009). Development of the major sedimentary basins of the western Barents Sea, e.g. the Tromsø, Bjørnøya, Nordkapp, Fingerdjupet, Maud and possibly Hammerfest basins, may have been initiated at this time. Fault-bounded subsidence became more prevalent as basin development intensified in Middle Carboniferous (Henriksen, Ryseth, et al., 2011). The pattern of subsidence observed in the western Barents Sea was probably related to the development of a regional sag basin encompassing the entire Barents Shelf. Its development has been inferred as partially thermally driven and a result of lithospheric extension, possibly related to the closure of the Uralian Ocean along the eastern Baltican margin (Gudlaugsson et al., 1998; Henriksen, Ryseth, et al., 2011).

Although decreasing, continued crustal extension and rifting caused the development of regional seaways around Baltica and the western margins in the Early to Late Permian transition. The marine connections dramatically changed the basin physiography and the oceanic circulation pattern, causing a shift in depositional regime as cooler water from the east flowed across the Barents Shelf (Henriksen, Ryseth, et al., 2011; Smelror et al., 2009; Worsley, 2008)

3.1.2 Mesozoic

The Triassic period has generally been considered a tectonically quiescent period, characterized by passive regional subsidence and only minor tectonic movements along the western Barents Shelf margin (Gabrielsen et al., 1990; Henriksen, Ryseth, et al., 2011). During this period, halokinetic movements of the Late Paleozoic salt was initiated in the Nordkapp Basin, continuing until the Late Triassic (Henriksen, Ryseth, et al., 2011; Smelror et al., 2009). The Middle to Late Triassic post-rift thermal subsidence was followed by a significant change in the paleogeography with the initiation of progressive uplift in areas to the north, east and south of the region (Gernigon et al., 2014; Smelror et al., 2009). From Late Triassic to Early Jurassic, the North Atlantic and Arctic regions experienced renewed tectonic activity (Gernigon et al., 2014; Smelror et al., 2009).

Middle to Late Jurassic was characterized by regional extension and minor strike-slip movements along older structural trends (Faleide et al., 1993). Continued extension led to progressive subsidence, and from Middle Jurassic to Early Cretaceous, the North Atlantic rift basins extended into the southwestern Barents Sea, representing the northwards progradation of the Atlantic rift system. This eventually led to the development of marine connections across the Barents Shelf (Faleide et al., 1993; Smelror et al., 2009). To the north, tectonic activity was related to the early stages of the opening of the Arctic Ocean, represented by extension in the Amarasia Basin (Smelror et al., 2009).

The progressive break-up of the supercontinent Pangaea and related tectonic activity intensified from Late Jurassic to Early Cretaceous (Henriksen, Ryseth, et al., 2011; Smelror et al., 2009), culminating with the establishment of the structural architecture of basins and highs in the present-day Barents Sea (Henriksen, Ryseth, et al., 2011). Continued uplift and subsequent erosion of the northern Barents Sea was associated with volcanic eruptions occurring on Franz Josef Land, Kong Karls Land and adjacent offshore areas, also coinciding with sill intrusions in other regions of the Barents Sea (Faleide et al., 2015; Smelror et al., 2009). This suggests a regional rather than local extent of volcanic activity, and the tectonomagmatic events have been inferred as related to the opening of the Arctic Ocean/Euramerican Basin and associated seafloor spreading (Henriksen, Ryseth, et al., 2011; Smelror et al., 2009; Worsley, 2008). Successive rifting events during the Cretaceous caused rapid subsidence along the southwestern Barents Shelf and development of basins such as the Harstad, Tromsø, Bjørnøya and Sørvestnaget basins, which subsequently became major depocenters for Late Cretaceous strata (Faleide et al., 1993; Henriksen, Ryseth, et al., 2011; Smelror et al., 2009). Continued uplift to the north eventually led to most of the Barents Shelf being uplifted by Late Cretaceous. As the rifting phase between Norway and Greenland intensified from Late Cretaceous to Paleocene, subsequent strike-slip movements and deformation within the De Geer Zone led to the development of subsiding pull-apart basins in the western Barents Sea (Faleide et al., 1993; Smelror et al., 2009).

3.1.3 Cenozoic

The Cenozoic tectonic development of the Barents Sea is closely related to the opening of the Norwegian-Greenland Sea around the Paleocene-Eocene transition (55-54 Ma) and subsequent development of a sheared continental margin (Faleide et al., 1993; Henriksen, Ryseth, et al., 2011; Smelror et al., 2009). The ocean-continent boundary, represented by the Senja Fracture Zone, experienced significant shearing as the spreading ridge of the North Atlantic propagated

northwards, and seafloor spreading in the Norwegian-Greenland Sea and Arctic Ocean commenced in Early Eocene (Faleide et al., 1996; Henriksen, Ryseth, et al., 2011). Prior to the opening, a narrow fold-and-thrust belt along the western coast of Spitsbergen developed in response to compression along the transform fault zone connecting the spreading centres in the newly formed oceans (Faleide et al., 1984), of which the crustal shortening has been estimated to approximately 30 km (Smelror et al., 2009; Worsley, 2008). Following a shift in the orientation of the rift axis in Early - Middle Oligocene, opening of the northern Greenland Sea began and the western shelf margin developed into a passive margin as tectonic activity decreased (Faleide et al., 1984; Faleide et al., 1993; Smelror et al., 2009). Continued seafloor spreading eventually led to the separation of the Barents Shelf and Greenland/North America and the subsequent establishment of the Fram Strait and a North Atlantic-Arctic marine connection in Miocene (Smelror et al., 2009).

The Late Cenozoic was characterized by glacially induced subsidence and uplift, and extensive differential glacial erosion, with continued subsidence of the western marginal basins (Faleide et al., 1984; Smelror et al., 2009; Worsley, 2008). Estimations of uplift and erosion varies greatly throughout the Barents Shelf area; from 3000 m on Stappen High and Svalbard, to 0 m in the Sørvestnaget Basin (Ktenas et al., 2018; Lasabuda, 2018; Ohm et al., 2008; Vorren et al., 1991).

3.2 Stratigraphy and paleoenvironment of the SW Barents Sea

The term *basement* refers to the deeper crystalline bedrocks, which are usually overlain by a number of sedimentary sequences originating from a variety of depositional environments. *Top basement* refers to the horizon separating the basement and the overlying sedimentary succession, also representing the base of the sedimentary basins. Throughout the Barents Sea, the depth to top basement and hence the thickness of overlying sedimentary strata varies greatly on both a local and regional scale, reflecting the different depositional environments that have occurred through time. For the western Barents Sea, the changing depositional regimes has caused thickness variations from 8 km in sedimentary basins to 6 km and less on platforms and highs, respectively (Smelror et al., 2009).

3.2.1 Paleozoic

In Early to Late Devonian, the formation and subsequent denudation of the contemporaneous Caledonian Orogeny largely controlled the sedimentation pattern in the northern and western Barents Sea (Smelror et al., 2009). Extensive continental areas covered most of the western Barents Sea, being gradually eroded and peneplaned (Henriksen, Ryseth, et al., 2011; Smelror

et al., 2009). Major deltaic systems prograding from the west developed and provided siliciclastic input to the marine carbonate environments dominating the eastern Barents Sea. Hence, continental to deltaic and shallow marine environments passed eastwards into the fully marine environments characterizing the eastern shelf (Henriksen, Ryseth, et al., 2011; Smelror et al., 2009; Worsley, 2008).

In Early Carboniferous, the climate was tropically humid and the post-Caledonian depositional regime on the western shelf transitioned into a complex system of highlands, alluvial and fluvial plains and marshes (Smelror et al., 2009). Uplift and rifting were accompanied by horst and graben development (e.g. Ottar, Tromsø, Bjørnøya and Nordkapp basins), partly controlling the developing sedimentary systems in the area (Smelror et al., 2009; Worsley, 2008). Following the northwards continental drift of Pangaea, the climate transitioned into subtropically arid, which combined with decreasing tectonic activity and an overall transgression in Late Carboniferous, led to the expansion of the carbonate shelf environments dominating the eastern shelf. Warm-water carbonate environments subsequently prevailed over the entire Barents Sea – Kara Sea region, with extensive evaporite deposition in deep basins and in shallower salinas and sabkhas (Henriksen, Ryseth, et al., 2011; Smelror et al., 2009; Worsley, 2008).

The Early Permian paleogeography and -environment encompassed extensive carbonate shelves dissected by shallow basins and highs (Henriksen, Ryseth, et al., 2011; Smelror et al., 2009). Warm-water carbonate deposition occurred in a climate characterized by high frequency and high amplitude eustatic sea level changes reflecting the various phases of the contemporaneous Gondwanan (southern hemisphere) glaciations (Henriksen, Ryseth, et al., 2011; Smelror et al., 2009; Worsley, 2008). During sea level highstands, the entire shelf was flooded and shallow-water platform carbonates with stacked organic build-ups developed on structural highs, whereas carbonate mudstones accumulated in deeper basins. During sea level lowstands, structural highs became subaerially exposed, and basins were predominantly filled by evaporites (Henriksen, Ryseth, et al., 2011; Smelror et al., 2009; Worsley, 2008).

Warm-water carbonate deposition was replaced by cold- and deep-water carbonate deposition following the development of a marine seaway between Norway and Greenland in late Early Permian (Henriksen, Ryseth, et al., 2011; Worsley, 2008). By Mid-Permian, major transgressions had caused the development of an extensive marine shelf covering the Barents Sea and Kara regions, and carbonate deposition was replaced by a siliciclastic regime (Smelror et al., 2009; Worsley, 2008). This drastic depositional change can be attributed to the development of the Ural Mountains and the closure of the marine connection to the south

(Henriksen, Ryseth, et al., 2011; Worsley, 2008). By Late Permian, deep-water shelf environments prevailed to the west, whereas near-shore marine environments existed to the east (Smelror et al., 2009).

3.2.2 Mesozoic

In the Early Triassic, the Barents region received sediments from several provenance areas, including the uplifted Novaya Zemlya and Uralian hinterland in the east, and the Fennoscandian Shield in the south (Henriksen, Ryseth, et al., 2011; Smelror et al., 2009; Worsley, 2008). While marine conditions prevailed in the west, the emergent Uralides caused the development of non-marine depositional conditions in the east, characterized by lacustrine and flood-plain environments (Smelror et al., 2009). By Mid-Triassic, the Barents Sea encompassed a central marine shelf surrounded by continental areas to the east, south and northwest, with a southwestern marine link into the North Atlantic rift system (Smelror et al., 2009). A restricted and anoxic basin extending from SW to NE on the western shelf developed, of which the organic-rich mudstones and siltstones of the Botnheia (Svalbard)/Kobbe (SW Barents Sea) formations accumulated, constituting prolific hydrocarbon source rocks (Smelror et al., 2009; Worsley, 2008). Further south, similar deposits have been attributed to the Steinkobbe Formation (Smelror et al., 2009). Continued uplift and erosion in the eastern Barents Sea – Kara region in Late Triassic led to an overall regression and westward progradation of the coastline. Continental and coastal-plain environments were subsequently established over major parts of the Barents Sea, while marine conditions became restricted to the west (Smelror et al., 2009; Worsley, 2008).

Following the Late Triassic to Early Jurassic uplift and erosion, major parts of the Barents Sea comprised periodically flooded, wide continental lowlands with shallow-marine environments restricted to small basins in the west (Henriksen, Ryseth, et al., 2011; Smelror et al., 2009). The extensive erosion has left a depositional gap in the sedimentary succession over large parts of the region (Smelror et al., 2009). The Jurassic was generally characterized by transgressive-regressive cycles, with flooding of continental lowlands during maximum transgression (e.g. Toarcian) and subaerial exposure and erosion during maximum regression (e.g. Bajocian). The Late Jurassic (Tithonian) maximum transgression resulted in the establishment of marine environments over most of the Barents Shelf. Dysaerobic to anoxic conditions gave way for the dark shales of the prolific Hekkingen Formation, one of the most significant source rocks in the Barents Sea (Henriksen, Ryseth, et al., 2011; Smelror et al., 2009; Worsley, 2008).

By Early Cretaceous, most of the Barents Shelf comprised an open marine shelf environment, characterized by well-oxygenated bottom-water conditions (Smelror et al., 2009; Worsley, 2008). Fine, siliciclastic sediments were deposited over much of the region, whereas condensed carbonate deposits were restricted to platforms and structural highs (Smelror et al., 2009; Worsley, 2008). The latest Jurassic overall regression continued into the Cretaceous, and tectonic uplift of the northern Barents Shelf reinforced the process. Continental conditions were subsequently established over large parts of the northern shelf margin, leading to a westward deltaic progradation and an increased terrigenous supply from the north to the rapidly subsiding basins in the west (Henriksen, Ryseth, et al., 2011; Smelror et al., 2009). Open marine shelf conditions still prevailed in the western and central parts of the Barents Shelf (Smelror et al., 2009). Late Cretaceous was characterized by continued subsidence along the western shelf margin, proven by thick Late Cretaceous strata in e.g. Tromsø and Sørvestnaget basins (Henriksen, Ryseth, et al., 2011).

3.2.3 Cenozoic

Subsidence of the western marginal basins continued into the Paleogene, of which large amounts of sediments continued to accumulate. The eastern Barents Shelf was uplifted, and represented either continental hinterlands or shallow-marine seas with limited net deposition (Smelror et al., 2009). Paleocene and Lower Eocene strata is preserved in the Hammerfest and Nordkapp basins, but Cenozoic strata is absent below the base Quaternary in surrounding platform areas and highs, also documented in eastern and northern shelf areas (Henriksen, Ryseth, et al., 2011; Smelror et al., 2009). The major unconformities between Miocene and overlying strata can be attributed to Northern Hemisphere glaciations initiated in Late Pliocene – Pleistocene. Repeated glaciations and subsequent alternations between uplift and subsidence, caused extensive erosion of the eastern shelf and subsidence to the west, and hence a limited distribution of Cenozoic strata (Henriksen, Ryseth, et al., 2011; Smelror et al., 2009). The erosional products were deposited as thick sedimentary wedges in and beyond the subsiding basins along the western margin, of which the largest accumulations are found in trough mouth fans such as the Bjørnøya and Storfjorden fans (Smelror et al., 2009; Worsley, 2008). Svalbard and the northern platform areas experienced maximum uplift and erosion, where 2-3 km of sediments have been removed. Further south, uplift and erosion was less extensive (Smelror et al., 2009; Worsley, 2008).

3.3 Loppa High

Loppa High is one of the major structural elements of the southwestern Barents Sea, situated between $71^{\circ}50'N$, $20^{\circ}E$ and $71^{\circ}55'N$, $22^{\circ}40'E$, and $72^{\circ}55'N$, $24^{\circ}10'E$ and $73^{\circ}20'N$, $23^{\circ}E$ (fig. 3.3). The structural high is bounded to the south by the Asterias Fault Complex, and to the west by the Ringvassøy-Loppa and Bjørnøyrenna Fault complexes. To the east, Loppa High grades into the Bjarmeland Platform, whereas the Svalis Dome and Maud Basin marks the northeastern limit (Gabrielsen et al., 1990).

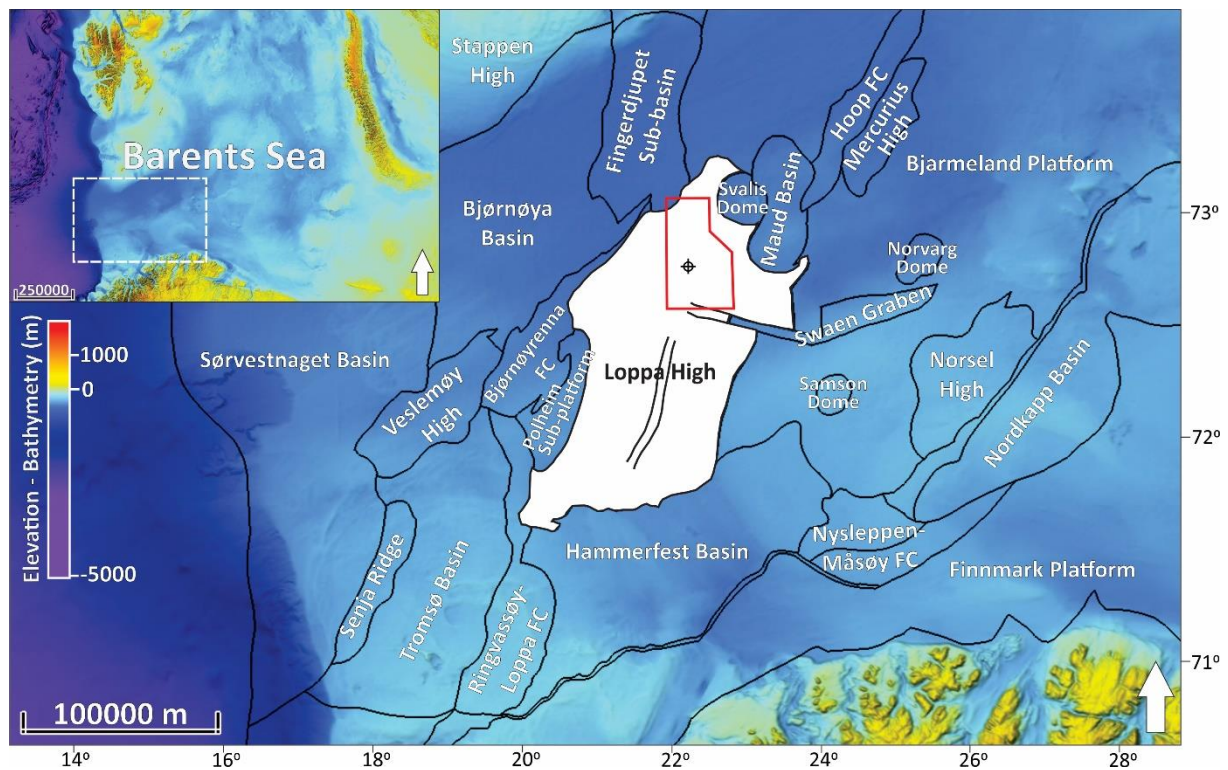


Figure 3.3: Overview of the study area (red outline), Loppa High and surrounding structural elements. Approximate position of well 7222/1-1 is indicated in black.

The structural complexity of Loppa High results from several phases of uplift, tilting, erosion and subsidence. The high exhibits a Mid-Carboniferous rift topography, possibly developed during the initiation of the Atlantic rift system between Norway and Greenland (Henriksen, Ryseth, et al., 2011; Larssen et al., 2002). Upper Paleozoic sediments have subsequently filled and draped the structural relief of the high (Larssen et al., 2002). Loppa High was initially uplifted and tilted during Early Triassic, but rapid subsidence during Middle to Late Triassic caused Loppa High to become a significant depocentre, proven by the almost complete Upper Triassic succession (Henriksen, Ryseth, et al., 2011; Worsley, 2008). Following increased tectonic activity from Late Jurassic to Early Cretaceous, the structure became reactivated as a high and exposed to erosion (Gabrielsen et al., 1990; Henriksen, Ryseth, et al., 2011). Due to extensive glacial erosion of Cenozoic strata, Loppa High mainly comprises Quaternary

sediments resting unconformably on Late Triassic strata (Henriksen, Ryseth, et al., 2011; Smelror et al., 2009).

3.4 Stratigraphic units

The structural and stratigraphic configuration of the present day Loppa High is a result of several phases of uplift, tilting and extensive erosion. Erosion is clearly recorded by the extensive stratigraphic gap between Upper Triassic and Neogene strata, especially in the northern parts of Loppa High. The following sections thus accounts for and is limited to the lithostratigraphic units present in the study area, of which the division and nomenclature is mainly based on Dallmann (1999) and Larssen et al. (2002).

3.4.1 Tempelfjorden Group

The Tempelfjorden Group is an Early/Middle to Late Permian lithostratigraphic unit, deposited in a temperate to cold, shallow to deep marine environment during an overall transgression (Blomeier et al., 2011; Worsley, 2008). The group overlies the Gipsdalen and Bjarmeland Groups, representing the transition from warm-water carbonate deposition to mixed siliciclastic-carbonate deposition in the Barents Sea (Blomeier et al., 2011; Worsley, 2008). In general, the group thins over structural highs and platforms, whereas thicker deposits are recognized in the western marginal basins. In the Barents Sea, the group can be subdivided into two formations; the underlying Røye Formation and the overlying Ørret Formation (Larssen et al., 2002).

3.4.1.1 Røye Formation

The Røye Formation (?Kungurian to Kazanian age), the approximate age-equivalent of the Kapp Starostin Formation on Svalbard, comprises fine-grained silicified mudstones and limestones (Ehrenberg et al., 2010; Larssen et al., 2002). During and after a major initial transgression, the lower part of the formation was deposited in a distal marine, deep shelf to basinal environment, whereas the upper part reflects distal marine, moderate to deep shelf environments affected by storm reworking. On structural highs, carbonate platforms and ramp conditions prevailed (Larssen et al., 2002).

3.4.1.2 Ørret Formation

The Ørret Formation (?Kungurian - ?Tatarian age) comprises mainly coarser siliciclastic sediments, including sandstones, siltstones and shales (Larssen et al., 2002). Contrasting to the Røye Formation, the deposits of the Ørret Formation show much less silification. The depositional environment of the formation ranges from deltaic and lower coastal-plain, to deep shelf environments, and in the deeper shelf settings to the east, anoxic conditions occurred

locally. Hence, from Loppa High and eastward, organic-rich shales become progressively more important (Larssen et al., 2002). Henriksen, Ryseth, et al. (2011) have listed the Ørret Formation as one of the significant petroleum source rocks in the greater Barents Sea, characterized by kerogen type II/III.

3.4.2 Sassendalen Group

The Sassendalen Group is an Early to Middle Triassic lithostratigraphic unit, representing a group of stacked transgressive-regressive successions deposited during an overall transgression (Dallmann, 1999; Worsley, 2008). The group can be subdivided into mainly four formations (Havert, Klappmyss, Steinkobbe and Kobbe formations), each of which was initiated by a significant and regional transgression (Dallmann, 1999; Henriksen, Ryseth, et al., 2011). The successions consist of both reservoir and source rocks, with the former deposited during maximum regressions and the latter during maximum transgressions and seabed anoxia (Henriksen, Ryseth, et al., 2011). On western Spitsbergen, coastal, deltaic to shallow shelf deposits have been recorded, whereas shallow to deep shelf deposits dominates in the southwestern Barents Sea (Dallmann, 1999).

3.4.2.1 Havert Formation

The Havert Formation (Induan age) comprises predominantly shales, with minor interbedded siltstones and sandstones. The sediments were deposited in a shallow marine to open marine setting, of which coastal environments were located to the south and southeast of the Barents Sea region (Dalland et al., 1988; Dallmann, 1999).

3.4.2.2 Klappmyss Formation

The Klappmyss Formation (Olenekian age) generally comprises shales passing upwards into interbedded siltstones and sandstones (Dalland et al., 1988; Dallmann, 1999). The formation show great similarities to the Havert Formation in terms of depositional setting; a shallow to open marine setting, with renewed coastal progradation following the Olenekian transgression (Dallmann, 1999).

3.4.2.3 Steinkobbe Formation

The Steinkobbe Formation (Spathian – Anisian age) comprises organic-rich and phosphatic mudstones and calcareous siltstones, deposited in a deep restricted, open shelf environment with anoxic conditions (Dallmann, 1999; Smelror et al., 2009). The Steinkobbe Formation is the equivalent of the prolific Kobbe and Botnheia formations, with a total organic carbon (TOC) content between 1.5 and 9%. The formation thus constitutes a prolific hydrocarbon source rock (Dallmann, 1999; Smelror et al., 2009).

3.4.2.4 *Kobbe Formation*

The Kobbe Formation (Anisian age) comprises organic-rich and phosphatic shales, passing upwards into siltstones and sandstones (Dallmann, 1999; Smelror et al., 2009). The depositional environment was initially a restricted, anoxic basin extending eastward on Svalbard and southwards on the Barents Shelf, and TOC values up to 12% have been recorded (Smelror et al., 2009). The uppermost sandstones of the Kobbe Formation reflects a build-out of clastic and marginal marine regimes from southern coastal areas, with sediments supplied from the Fennoscandian hinterland (Dallmann, 1999; Henriksen, Ryseth, et al., 2011).

3.4.3 *Kapp Toscana Group*

The Kapp Toscana Group is a Late Triassic to Middle Jurassic lithostratigraphic unit deposited in a nearshore, deltaic environment, of which deltaic and fluviodeltaic sediments were exposed to marine and coastal reworking (Dallmann, 1999). The group can be subdivided into the Realgrunnen and Storfjorden subgroups, comprising a total of five formations; Snadd, Fruholmen, Tubåen, Nordmela and Stø (Dallmann, 1999). Due to extensive erosion on Loppa High, the sedimentary succession from this time mainly comprises the Middle to Late Triassic Storfjorden Subgroup with the Snadd Formation.

3.4.3.1 *Snadd Formation (Storfjorden Subgroup)*

The Snadd Formation (Ladinian – Early Norian age) consists of basal shales passing upwards into siltstone and immature sandstones (Dallmann, 1999). The lower (Ladinian) succession represents distal marine environments with deposition of prodelta shales, whereas the upper (Carnian) succession reflects the large-scale, progradational deltaic systems that developed over most of the province at this time (Dallmann, 1999; Worsley, 2008). The formation show similarities to the Tschermakfjellet and De Geerdalen formations on Svalbard (Dallmann, 1999).

3.4.4 *Nordland Group*

The Nordland Group (Miocene – Pleistocene age) is a lithostratigraphic unit deposited in a bathyal to glaciomarine environment, generally comprising sands, clays, cobbles and boulders, reflecting glacial erosion and transportation. The sand content generally increases upwards in the succession (Dalland et al., 1988). Deposition of the Nordland Group was mainly restricted to the western shelf margins, of which up to 5 km of fine-grained deposits have accumulated (Faleide et al., 1996; Worsley, 2008).

3.5 Petroleum systems in the SW Barents Sea

3.5.1 Plays and source rocks

The Barents Sea constitutes a fairly unexplored and immature area compared to the North Sea and Norwegian Sea; according to the Norwegian Petroleum Directorate's fact pages, the number of exploration wells in the Norwegian Barents Sea is only 167, compared with the North Sea's 1399 and the Norwegian Sea's 373 (NPD, 2020). Several hydrocarbon discoveries have been made in the Barents Sea, albeit most of them being rather small. At present, only three commercial fields are in production or approved for production; Goliat (Tromsøflaket), Snøhvit (Hammerfest Basin) and Johan Castberg (Polhem Subplatform/Bjørnøyrenna Fault Complex) (NP, 2020; NPD, 2020). Several plays, i.e. areas where producible petroleum could be proven, of Carboniferous to Paleocene age have been identified in the southwestern Barents Sea, the most extensive ones being of Triassic and Lower to Middle Jurassic age (NPD, 2019).

The SW Barents Sea encompasses several source rocks ranging from Silurian to Cretaceous age, with varying potential of generating hydrocarbons (Henriksen, Ryseth, et al., 2011; Ohm et al., 2008). Accounting for the effects of uplift and erosion, Ohm et al. (2008) have carried out a study of the many source rocks of the Norwegian Barents Sea to better understand their distribution and generative potential. The Upper Jurassic Hekkingen Formation is by far the most prolific source rock in the SW Barents Sea, with a high total organic carbon content (TOC), hydrocarbon generative potential (S₂) and hydrogen index (HI) (Ohm et al., 2008). However, the complex geological development of the Loppa High has led to constraints on the presence, distribution and maturity of source rocks potentially feeding hydrocarbon accumulations in the area. For instance, the Hekkingen Formation is deeply buried and overmature in the Tromsø Basin but mature in the Hammerfest basin. On the Loppa High and Finnmark Platform, the formation is completely eroded (Ohm et al., 2008).

Based on geochemical analyses and vitrinite reflectance data, Ohm et al. (2008) have compiled a tentative uplift and maturity map (fig. 3.4) indicating the area of which different source rocks might have been oil mature prior to uplift and erosion (pre-uplift maturity). The figure shows that the western flank of the Loppa High does not encompass strata that has occurred within the oil window. However, Triassic oil mature strata appears to occur within the study area, located towards the northeastern flank of the high. The maturity process is irreversible, meaning that the generation potential of formations occurring within the oil and gas window (75-170°C and 170-230°C, respectively) will change and eventually cease according to decreasing temperatures during uplift. Formations that have previously expelled hydrocarbons at their

maximum burial depth will not be able to generate and expel hydrocarbons at shallower depths (Henriksen, Bjørnseth, et al., 2011). Burial depth is thus an important parameter, especially in the Barents Sea, that must be accounted for when evaluating the source rock potential of different formations.

According to the maturity map after Ohm et al. (2008), Late Permian source rocks are overmature in most of the Norwegian Barents Sea, except for a narrow zone on the Loppa High and along the margins of the Finnmark Platform. Triassic source rocks are oil mature along the western margin, including the northeastern flank of the Loppa High, and the central and southern parts of the Bjarmeland Platform as well as the Nordkapp Basin. The Late Jurassic source rock (Hekkingen Formation) is oil mature in the Hammerfest Basin and the northern parts of the Bjarmeland Platform (Henriksen, Ryseth, et al., 2011; Ohm et al., 2008). Paleozoic source rocks are still oil mature in the Timan-Pechora Basin in the eastern Barents Sea, suggesting that progressively older sequences enter the oil window in an eastward direction from the Hammerfest Basin, Loppa High and Finnmark platform (Henriksen, Ryseth, et al., 2011; Ohm et al., 2008).

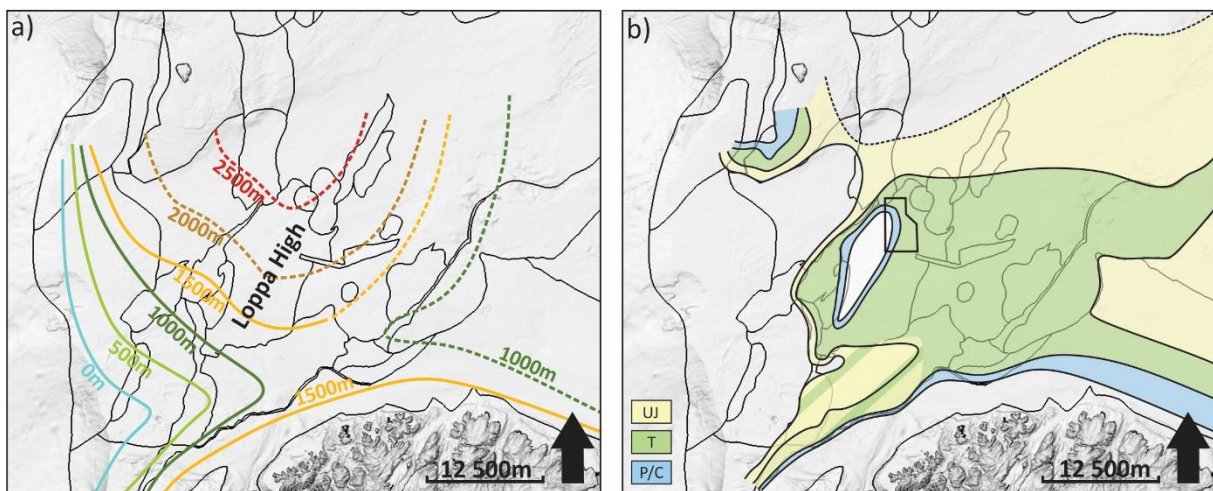


Figure 3.4: a) Tentative uplift map, based on fig. 6 in Ohm et al. (2008). b) Tentative maturity map of Upper Jurassic (UJ, Hekkingen fm.), Triassic (T, Snadd, Kobbe, Klappmyss and Havert fms.) and Permian/Carboniferous (P/C) source rocks, based on fig. 10 in Ohm et al. (2008). Approximate location of the study area (black outline) is indicated on the Loppa High.

3.5.2 Effects of uplift on maturity and migration

Erosion estimates from the SW Barents Sea suggest that 2000-2500 m of sediments have been eroded from the study area (Ktenas et al., 2018; Ohm et al., 2008). Uplift and erosion has thus most likely affected the potential petroleum systems in the SW Barents Sea and northern Loppa High. The most significant consequence is changes in the maturation process of source rock intervals, and the maturity trends observed in the SW Barents Sea can largely be attributed to the various amounts of uplift and erosion in the region. As the hydrocarbon generation process

depends on specific temperature intervals, and hence burial depth, uplift and subsequently decreasing temperatures may cause cessation of hydrocarbon generation (Ohm et al., 2008), as source rock intervals previously subjected to temperatures sufficient for hydrocarbon generation may have been lifted out of the oil and/or gas window.

Even though generation may cease, migration of hydrocarbons may continue. Gas in hydrocarbon accumulations will expand and exsolve in response to decreasing pressures during uplift and decreasing sediment load due to erosion. This can in turn result in lateral oil spill, given that the trap has been filled to spill and cause fracturing of sealing lithologies (Doré & Jensen, 1996; Henriksen, Bjørnseth, et al., 2011; Nyland et al., 1992), facilitating remigration both laterally and vertically. Similar effects can be triggered by glacial loading and unloading (Lerche et al., 1997), and may together explain why gas discoveries seem to outnumber oil discoveries in the SW Barents Sea; oils have been more or less forced to remigrate (Nyland et al., 1992). Consequently, long-range remigration into distal traps may occur and in a multisource area such as the Barents Sea, this process may also facilitate mixing of oils from different source rocks (Ohm et al., 2008). The more positive effects of uplift and erosion include i.a. shallow mature source rocks, methane exsolution from formation water and light oil/condensate exsolution from gas, fracture enhancement of reservoirs and remigration from deep to shallower reservoirs (see e.g. Doré and Jensen (1996)).

4 Data and methods

4.1 Datasets and wells

For the purpose of this thesis, three 3D seismic datasets located on the northern margin of Loppa High (location and extent indicated in fig. 4.1a) constitutes the main database. In addition to these, five 2D datasets have also been used for interpretations (fig 4.1b), and details concerning individual datasets are summarized in tables 4.1 – 4.4. Well data from well 7222/1-1 was used for correlation and stratigraphic delineation across all eight datasets, and for formation thicknesses and calculated interval velocities. The delineation of the study area, with an areal coverage of 1645 km², has been based on the 3D data coverage and 2D lines connecting the 3D datasets.

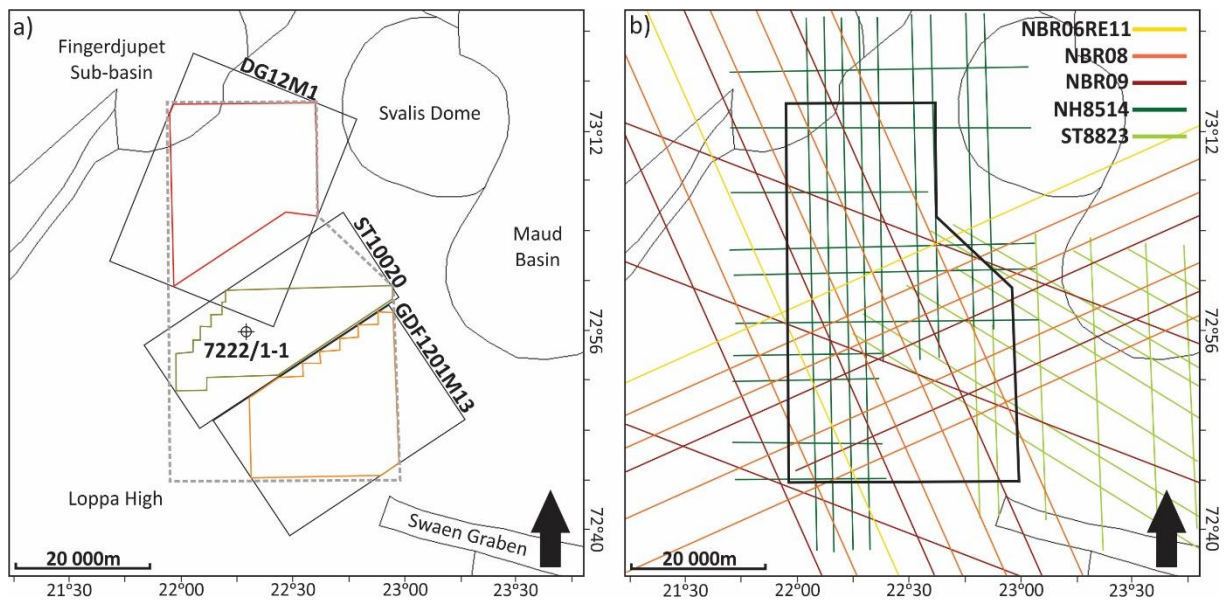


Figure 4.1: a) Location and coverage of the 3D datasets used in this thesis. Study area outline indicated by grey dotted line. b) Location of the 2D datasets used in this thesis. Note that the seismic lines extend well beyond the study area outline (black); only data within the defined study area has been interpreted (also shown in fig. 4.5).

Table 4.1: General information about the 3D datasets.

Survey	Survey type	Responsible company	Gathered by	Coverage (km ²)	Polarity	Inline orientation
DG12M1	3D	DONG E&P Norge AS	CGG	446	Zero-phase, normal (SEG)	S/SW - N/NE
ST10020	3D	Statoil AS	Fugro-Geoteam AS	289	Zero-phase, normal (SEG)	SW - NE
GDF1201M13	3D	GDF SUEZ E&P Norge AS	Dolphin AS	395	Zero-phase, normal (SEG)	SW - NE

The array parameters for each individual dataset are summarized in tables 4.3. and 4.4. The processing flow of each dataset is somewhat different, but common operations include positioning, noise attenuation and filtering, binning, time migration and stacking, and for several of the 2D datasets, zero-phase conversion.

Table 4.2: General information about the 2D datasets.

Survey	Survey type	Responsible company	Year acquired	No. of lines (total)	No. of lines (used)	Polarity	Length (km)
NH8514	2D	Norsk Hydro Produksjon AS	1985	26	26	Minimum-phase, normal (SEG)	907
ST8823	2D	Den Norske Stats Oljeselskap AS	1988	16	16	Zero-phase, normal (SEG)	742
NBR06RE11	2D	Fugro-Geoteam AS	2006	23	2	Zero-phase, normal (SEG)	5136
NBR08	2D	Fugro-Geoteam AS	2008	63	8	Zero-phase, normal (SEG)	19458
NBR09	2D	Fugro-Geoteam AS	2009	50	8	Zero-phase, normal (SEG)	10990

Table 4.3: Seismic array of the 3D datasets.

Survey	No. of inlines	No. of crosslines	Inline interval (m)	Crossline interval (m)	Sampling rate (ms)	Bandwidth (Hz)	Frequency (main, Hz)
DG12M1	1399	1779	18.75	18.75	4	6 - 75	12 - 30
ST10020	1201	2853	12.50	12.50	4	4 - 85	19 - 38
GDF1201M13	823	2513	25.00	12.50	4	5 - 80	15 - 35

Survey	Length (m)	No. of cables	No. of groups	Group interval (m)	Source (in ³)	Shot interval (m)	Record length (ms)
DG12M1	6000	10	480	12.50	2 x 3460	18.75	7060
ST10020	5400	10	432	12.50	2 x 3440	18.75	6600
GDF1201M13	6000	10	480	12.50	2 x 3460	18.75	6560

Table 4.4: Seismic array of the 2D datasets. – indicates no available data for the datasets.

Survey	Source (in ³)	Sample interval (ms)	Shot interval (m)	Group interval (m)	Record length (s)	Bandwidth (Hz)	Frequency (main, Hz)
NH8514	5570	4	25	25.0	–	5 - 77	8 - 27
ST8823	–	–	–	–	–	6 - 70	10 - 30
NBR06RE11	3410	2	25	12.5	10.3	5 - 83	5 - 40
NBR08	3400/4258	2	25	12.5	10.2	7 - 85	7 - 24
NBR09	4258	2	25	12.5	10.3	5 - 83	5 - 40

4.1.1 Frequencies

The frequency spectra in fig. 4.2, showing the relationship between power (or energy, dB) and frequencies (Hz), have been retrieved using the spectral analysis tool in Petrel E&P. The main frequency range for the individual datasets is characterized by a relatively flat curve, indicative of a relatively uniform resolution. Peak frequencies are thus somewhat harder to determine, but approximate values are indicated in fig. 4.2a and b. Inaccuracy in determination of peak frequencies can have a major impact on e.g. calculations of the resolution of the datasets. Note

that no vertical window for frequency retrieval has been specified, for neither the 2D nor the 3D datasets; frequencies are thus based on entire seismic sections.

A single inline from each 3D dataset has been used as a reference for the frequency range characterizing the datasets, although there are variations from one inline or crossline to the next. The spectra and peak frequencies in fig. 4.2a have therefore been used as an approximation to the frequencies characterizing the individual datasets. Fig 4.2a shows that the frequency range is near equal for all three datasets, and the comparison of observations between datasets thus becomes easier and more reliable, increasing confidence in interpretations. Similarly, a single line from each of the 2D datasets has been used as a reference for the frequencies of the respective datasets, shown in fig. 4.2b. In this case, variations between different datasets are greater than for the 3D datasets, most likely caused by the different size of seismic/acoustic sources and the layout of the surveys.

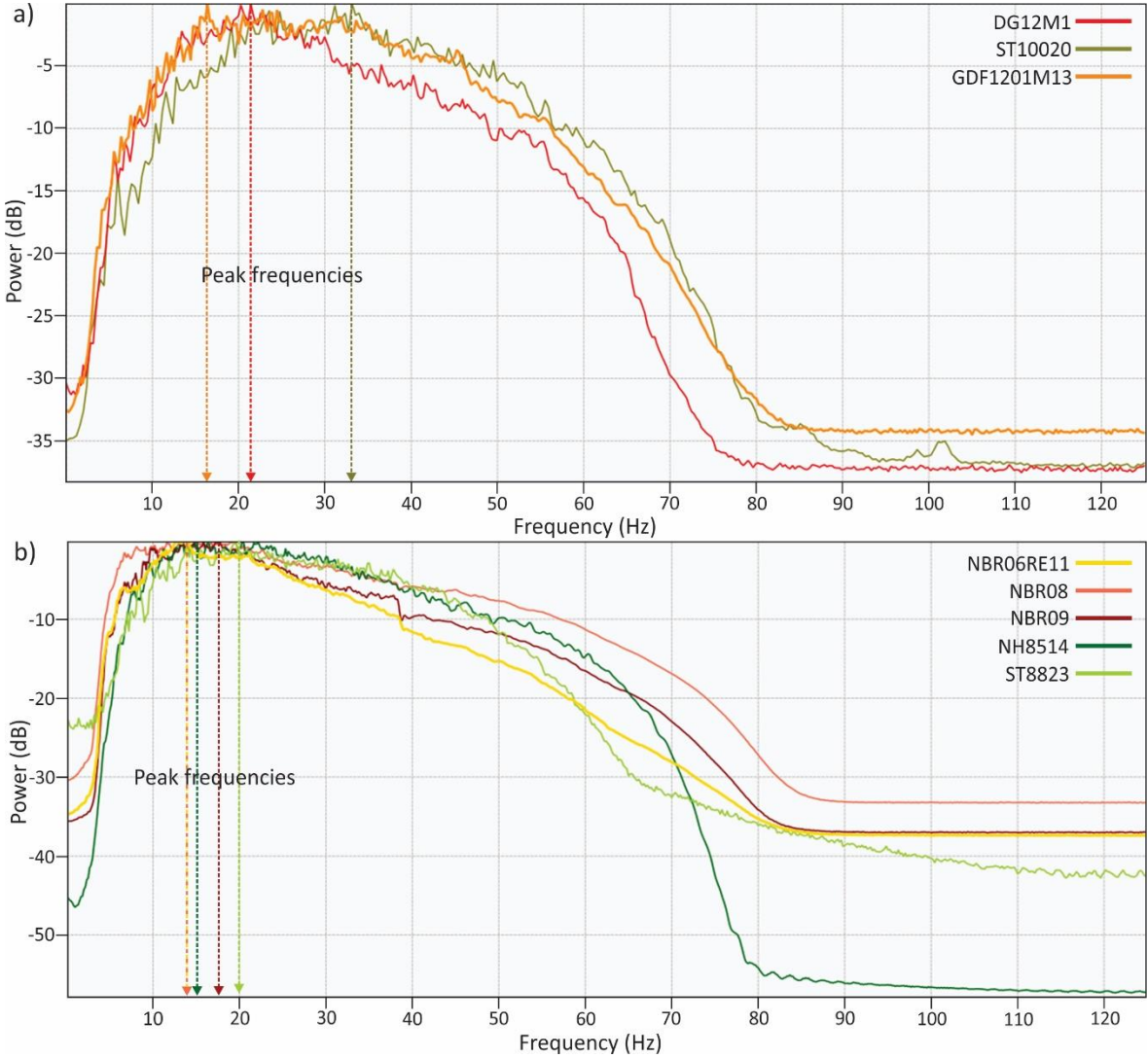


Figure 4.2: a) Frequency spectra (energy (dB) vs. frequency (Hz)), based on a single inline from each of the 3D datasets. b) Frequency spectra based on a single line from each of the 2D datasets.

4.1.2 Velocities

The average velocity of the water column is assumed to be approximately 1500 m/s (Ktenas et al., 2018). Due to an incomplete sonic log in the well data, the interval velocity of each formation (table 4.5) was calculated based on the thicknesses of each formation and their interval travel time (Keary et al., 2002):

Eq. 4.1: Interval velocity

$$V_{int} = \frac{z_{int}}{t_{int}}$$

where V_{int} = interval velocity (m/s), z_{int} = interval thickness (m) and t_{int} = one way travel time (OWTT, s) through the formation. The thicknesses and two way travel time (TWTT) for each formation were obtained from well 7222/1-1.

Table 4.5: Calculated interval velocities for the formations in the study area.

Formation	Depth to top formation, m (ms)	Interval thickness (z_{int} , m)	Interval TWTT (s)	Interval OWTT (t_{int} , s)	Interval velocity (V_{int} , m/s)
Nordland Gp.	424 (562.8 ms)	81	0.0988	0.0494	1640
Snadd fm.	505 (661.6 ms)	925	0.6464	0.3232	2862
Kobbe fm.	1430 (1308.7 ms)	229	0.1427	0.0714	3207
Steinkobbe fm.	1659 (1451.4 ms)	276	0.1706	0.0853	3236
Klappmyss fm.	1935 (1622.0 ms)	226	0.1114	0.0557	4057
Røye fm.	2161 (1733.4 ms)	–	–	–	–

Velocity inversion analysis in the SW Barents Sea, carried out by Ktenas et al. (2018), shows that velocities of the Triassic and Cenozoic succession on the western Loppa High lie in the range of 1600 – 4800 m/s. These observations correspond well with the calculated interval velocities for the formations present in the study area. Note, however, that the velocities calculated are specific for the formations penetrated by the well and that variations across the study area occur due to differences in interval thicknesses. Values obtained are thus used as an average or approximation to velocities occurring across the study area, for e.g. calculations of resolution. A complete sonic log would provide an even greater accuracy in calculations.

4.1.3 Resolution

The horizontal resolution of unmigrated data is usually defined by the width of the Fresnel Zone (accounted for in section 2.3.3.2). However, considering that all three 3D datasets are processed and migrated, the horizontal resolution is determined by the bin spacing (inline and crossline

intervals) of the 3D data, which is the minimum area encompassing common depth points (CDP) for stacking (Bulat, 2005; Keary et al., 2002; Nanda, 2016). The bin spacing or inline/crossline interval for each dataset has been retrieved from Petrel (statistics) and is 18.75m × 18.75m (DG12M1), 12.5m × 12.5m (ST10020) and 25.0m × 12.5m (GDF1201M13). The horizontal resolution (table 4.6) was calculated for the different 2D datasets, using eq. 2.11 for pre-migration resolution. Peak frequencies and velocities are retrieved from fig. 4.2b and table 4.5, respectively. According to Brown (2004), horizontal resolution post-migration corresponds to the calculated vertical resolution; $H_r = V_r = \frac{\lambda}{4}$ (table 4.7).

Table 4.6: Horizontal resolution (pre-migration) for 2D datasets.

Survey	Peak frequency (Hz)	Horizontal resolution (m)					
		Seabed ($V_p = 1500$ m/s)	Nordland Gp. ($V_p = 1640$ m/s)	Snadd fm. ($V_p = 2862$ m/s)	Kobbe fm. ($V_p = 3207$ m/s)	Steinkobbe fm. ($V_p = 3236$ m/s)	Klappmyss fm. ($V_p = 4057$ m/s)
NBR06RE11	13	156.0	185.0	454.0	535.8	571.5	740.7
NBR08	13	156.0	185.0	454.0	535.8	571.5	740.7
NBR09	18	132.6	157.2	385.9	455.3	485.7	629.5
NH8514	15	145.3	172.2	422.7	498.8	532.1	689.6
ST8823	20	125.8	149.1	366.1	432.0	460.8	597.2

The vertical resolution (table 4.7) of each dataset was calculated based on eq. 2.10 and $V_r = \frac{\lambda}{4}$, and peak frequencies and velocities from fig. 4.2a and b, and table 4.5, respectively.

Table 4.7: Vertical resolution for 3D and 2D datasets. Also correspond to horizontal resolution post-migration for 2D data.

Survey	Peak frequency (Hz)	Vertical resolution (m)					
		Seabed ($V_p = 1500$ m/s)	Nordland Gp. ($V_p = 1640$ m/s)	Snadd fm. ($V_p = 2862$ m/s)	Kobbe fm. ($V_p = 3207$ m/s)	Steinkobbe fm. ($V_p = 3236$ m/s)	Klappmyss fm. ($V_p = 4057$ m/s)
DG12M1	22	17.1	18.6	32.5	36.4	36.8	46.1
ST10020	33	11.4	12.4	21.7	24.3	24.5	30.7
GDF1201M13	17	22.1	24.1	42.1	47.2	47.6	59.7
NBR06RE11	13	28.8	31.5	55.1	61.7	62.2	78.0
NBR08	13	28.8	31.5	55.1	61.7	62.2	78.0
NBR09	18	20.8	22.8	39.8	44.6	44.9	56.3
NH8514	15	25.0	27.3	47.7	53.5	53.9	67.6
ST8823	20	18.8	20.5	35.8	40.1	40.5	50.7

4.2 Seismic artefacts

Seismic data initially encompass both signals (wanted response) and noise (unwanted response), and the main goal of processing is to increase the signal-to-noise ratio (Nanda, 2016). However, noise may still remain even after extensive processing of the data. Seismic artefacts are features without a true geological origin, occurring as coherent noise in the seismic data. Identification of such artefacts is important as they can obscure real features and interfere with the interpretation of the data. Two of the 3D datasets, DG12M1 and ST10020, exhibit a common case of seismic artefacts, known as a survey footprint (Brown, 2004; Bulat, 2005). This coherent noise appears as lines oriented parallel to the inline direction in each dataset, as illustrated in fig. 4.3.

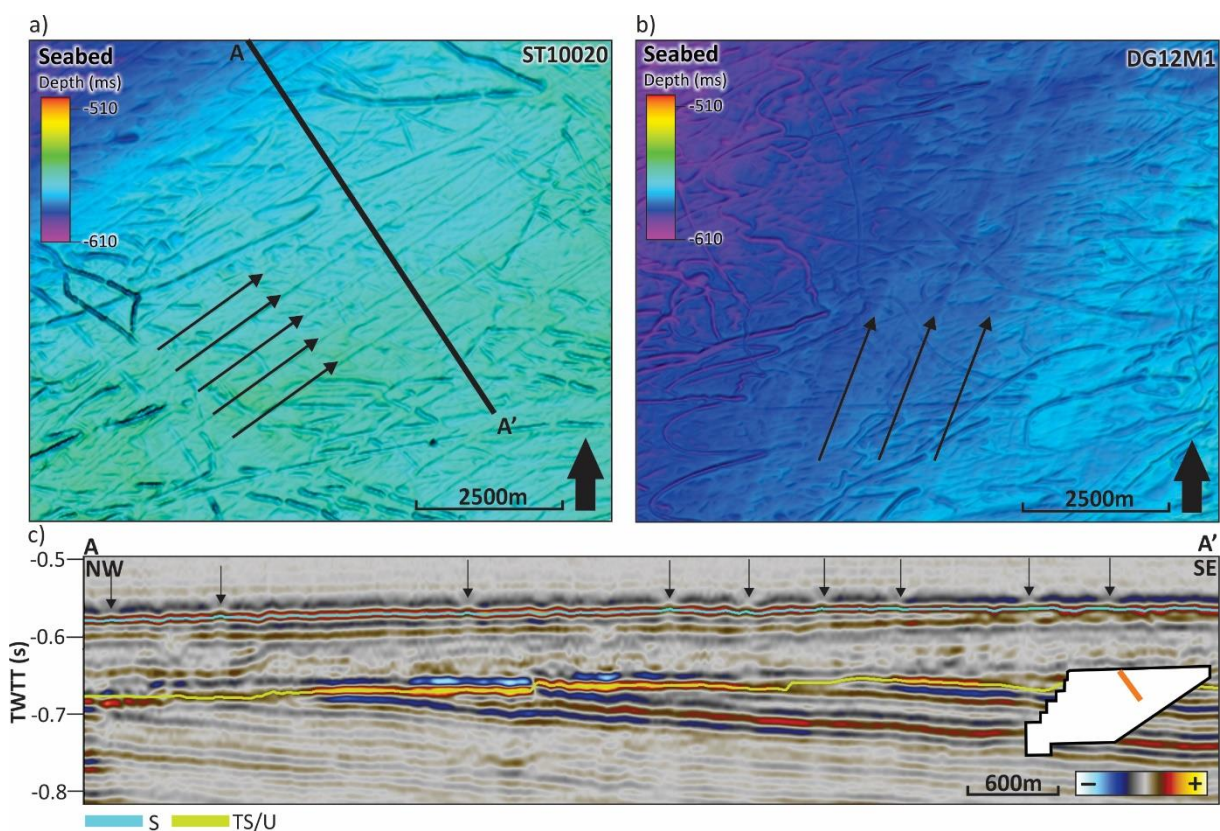


Figure 4.3: a) Seismic artefacts (survey footprint) in the ST10020 dataset, observed on the seabed surface. Vertical exaggeration (VE): 10. b) Seismic artefacts (survey footprint) in the DG12M1 dataset, observed on the seabed surface. VE: 10. c) Seismic section corresponding to A-A' in a), showing the seismic expression of the artefacts. S = Seabed and TS/U = Top Snadd/URU.

4.3 Methods

4.3.1 Software

Seismic interpretation and analysis in this study have been carried out using the Schlumberger software Petrel E&P (2019). Figures and illustrations have been created using CorelDraw (2017). The workflow and approach are summarized in fig. 4.4.

Workflow	Tools/method	Objectives
1) Seismic interpretation → Well correlation and horizon interpretation ↓ 2) Identification and characterization of structural trends → Faults ↓ 3) Identification and characterization of fluid flow indications → Amplitude anomalies, Acoustic masking, Paleo-depressions and exposed depressions ↓ 4) Integrated interpretation of structural development → Conceptual model for the structural development of the study area ↓ 5) Integrated interpretation of fluid flow indications → Conceptual models for fluid flow processes in the study area	2D seeded autotracking 3D seeded autotracking 2D and 3D seismic Variance attribute (volumes/time slices) 2D and 3D seismic RMS amplitude attribute (volumes/time slices) Dip angle attribute Analysis of structural trends in the study area and comparison with established tectonic development of the SW Barents Sea (literature) Analysis of fluid flow indications and relationship to structural trends, comparison with observations from SW Barents Sea (literature)	Establish seismic stratigraphy and depositional trends across different datasets Gain better understanding of the structural trends in the area Map individual fluid flow indications for further analysis and basis for delineating potential relationship to structural trends Establish the structural framework by correlating with major tectonic events Gain better understanding of the potential fluid flow processes in the study area

Figure 4.4: Figure of the workflow and approach used in this thesis, with the tools and methods used, and the objectives of using them.

4.3.2 Seismic interpretation

Stratigraphic delineation and seismic interpretation (1 in fig. 4.4) have been based on correlation with well 7222/1-1, located within the ST10020 dataset. Individual reflectors were interpreted using mainly the 3D seeded autotracking tool for 3D data, of which the choice of tool was based on reflector continuity and relatively strong amplitudes. Autotracking was carried out with a dip of 2.00 samples/trace and a correlation quality of 0.8 (default setting). Due to the uncertainties associated with the 3D autotracking tool (e.g. across larger discontinuities such as faults), each interpreted reflector has been carefully examined to ensure that the correct reflector was interpreted.

Even though there is a geometric overlap between the different 3D surveys (black squares in fig. 4.1a), lack of data coverage between the datasets has constituted a challenge in terms of correlation of reflectors across the study area. Thus, interpretation of 2D lines covering the gaps (fig. 4.5) and careful examination of reflector characteristics, facies and relationship to underlying and overlying units has been important in order to continue the interpretation across the entire study area. 2D seeded

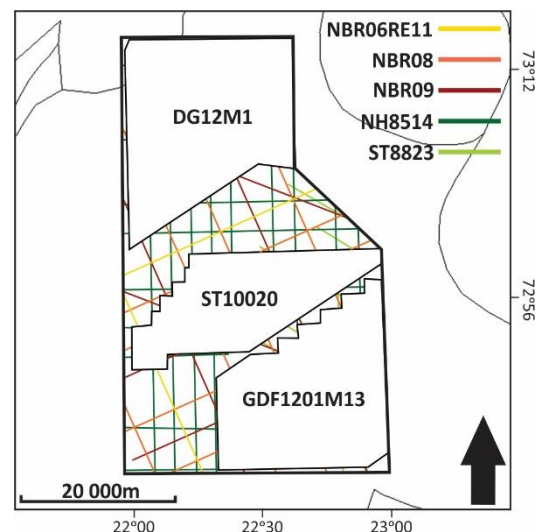


Figure 4.5: Study area with the basis for interpretation; 3D datasets and the 2D lines covering the gaps between them.

autotracking was the preferred tool for interpretation of 2D data, carried out with a correlation quality of 0.8 (default setting).

Horizon interpretation based on 2D and 3D data becomes merged when producing horizon surfaces in Petrel E&P. The surfaces were produced with a 25×25 grid increment using convergent interpolation, with the study area outline as boundary and basis for grid size and position. The large variations in surface expression between areas covered by 2D and 3D data can be attributed to the preferred autotracking tool (2D vs. 3D, respectively), the resolution and areal coverage of the respective datasets.

4.3.3 Seismic attributes

One of the main advantages of using 3D seismic data is the possibility of using seismic attributes, which quantify and extract certain properties of the seismic data/signals. These properties may not be seen on actual seismic sections, and seismic attributes may thus improve the geological and geophysical interpretation of the data (Nanda, 2016). For the purpose of this thesis, several attributes were used for identification and characterization of both structural trends and fluid flow features (2 and 3 in fig. 4.4).

4.3.3.1 Variance/coherence

The variance attribute is based on the similarity or coherency between neighboring traces or waveforms. The degree of coherency defines the continuity of reflections; high coherency (low variance) signifies lateral continuity, whereas low coherency (high variance) signifies discontinuity (Nanda, 2016). As such, the variance attribute is commonly used to analyze and map subsurface stratigraphic or structural discontinuities, such as faults, fractures, channels and pockmarks (Nanda, 2016). In this study, the variance attribute has been extracted mainly from 3D volumes, using the volume attributes tool in Petrel E&P, in order to delineate the structural trends and to identify fluid flow features such as faults and pockmarks. The main parameters set include inline and crossline range of 3, vertical smoothing of 15 and no dip correction.

4.3.3.2 RMS amplitude

The RMS amplitude attribute calculates the root mean square (RMS) of both positive and negative single-trace samples (Nanda, 2016). The subsequent enhancement of seismic amplitudes facilitates the identification of high amplitude anomalies characteristic for shallow gas accumulations and as indications of other fluid flow features (Nanda, 2016). Similar to the variance attribute, the RMS amplitude attribute has been extracted mainly from 3D volumes, using the volume attributes tool in Petrel E&P, in order to identify amplitude anomalies

indicative of gas accumulations. RMS amplitudes were retrieved from a 32 ms window for all three datasets.

4.3.3.3 Dip angle and azimuth

The dip angle and azimuth defines the magnitude and direction of dip (both measured in degrees) with respect to a reference, usually north. Dip angle and azimuth are useful attributes for determining the size, shape and orientation of subsurface and surface features (Nanda, 2016). In this study, the dip angle has mostly been used to determine the orientation and dip of seabed surface depressions, generated based on the interpreted seabed horizon and corresponding surface.

4.3.3.4 Time slices

Time slices are horizontal displays at given arrival times (in ms) cutting through volumes of seismic data, such as the 3D datasets. Time slices are useful for preliminary evaluations of different seismic attributes, e.g. seismic amplitudes and coherence/variance, revealing subtle depositional and structural features such as channels and faults (Nanda, 2016). Note that time slices cutting through volumes may result in a false representation of the true lateral extent of given features. Unlike horizon slices, representing a specific reflection event or depositional surface, the horizontality of time slices does not account for depth and dip variations of subsurface strata (illustrated in fig. 4.6).

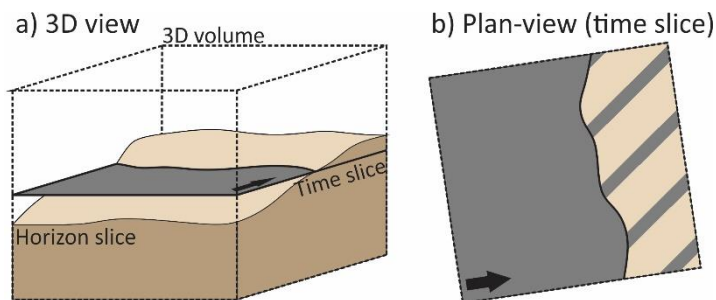


Figure 4.6: a) 3D view showing both a horizon slice and time slice. b) Time slice in plan-view.

4.3.4 Integrated interpretation

Based on the observations made during seismic interpretation and analysis, results were subsequently correlated to tectonic and depositional events, and compared with established literature (4 and 5 in fig. 4.4). Integrated interpretation allows the development of conceptual models for the tectonic development and structural framework of the area, accounting mainly for the timing of faulting in a regional-scale setting. Conceptual models for the fluid flow processes and their relationship to the structural development were also produced, accounting for the fluid origin, potential migration pathways and accumulations in the study area.

5 Results

The following chapter will account for the main observations and preliminary interpretations of stratigraphy, structural trends (faults), fluid flow indications (high-amplitude anomalies and acoustic masking) and the seabed morphology. Even though the study area has proven to consist of numerous fluid flow indications, only a selection will be presented in detail. Emphasis will accordingly be placed on the location, general characteristics and potential relationship to structural trends and other fluid flow indications in the study area.

5.1 Seismic stratigraphy

The main focus of this thesis is fluid flow features and not seismic stratigraphy per se. However, the different stratigraphic intervals are used as reference levels for the occurrence of fluid flow features in the subsurface strata. Stratigraphic delineation is thus necessary, and a short characterization of the reflectors and units identified is sufficient. Six horizons are interpreted based on well tops from well 7222/1-1, dividing the stratigraphy into mainly six units ranging from Permian to Pleistocene age (fig. 5.1). The surfaces produced based on interpretation are presented in fig. 5.2.

Unit 1 encompasses the Røye Formation of the Tempelfjorden Group, and its upper limit is defined by a low-amplitude, semi-continuous and positive reflector, interpreted as Top Røye (TR). The reflector depth varies across the study area, from -2.5 s to the north to -1.6 s in the central areas. No thickness trend is identified, as the Top Røye reflector is the deepest reflector interpreted and the lower limit is somewhat uncertain. The unit is generally characterized by semi-parallel and semi-continuous reflectors of low amplitudes. Several faults terminate within the unit or against the Top Røye horizon, and some extend into shallower levels.

Due to low continuity of the reflector and the effects of interference, the Havert Formation (Sassendalen Group) has not been interpreted individually, but incorporated into Unit 2 with the Klappmyss Formation (Sassendalen Group). Unit 2, lying unconformably on top of the Røye Formation, is defined by a low-amplitude, semi-continuous and positive reflector interpreted as Top Klappmyss (TKM). The reflector depth varies in the same manner as the Top Røye reflector, with the deepest and shallowest levels recorded to the north (-2.3 s) and central areas (-1.6 s), respectively. Unit 2 is characterized by semi-parallel and semi-continuous reflectors of generally low amplitudes. The thickness increases from S to N, and the faults identified generally dissect the unit and extends into shallower depths.

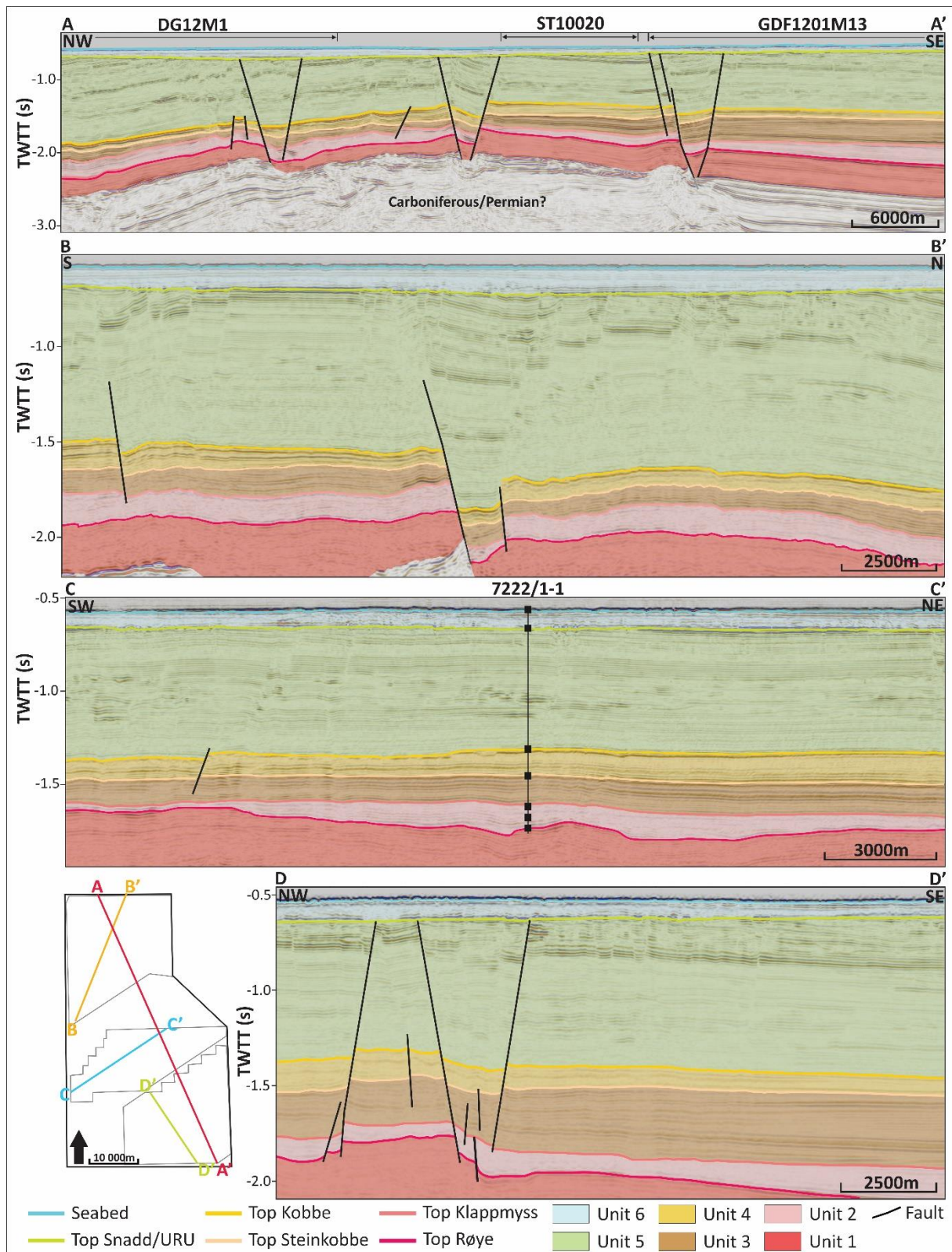


Figure 5.1: Stratigraphic units and horizons interpreted. Position of the seismic sections indicated in the study area outline. Only faults displacing the main stratigraphic units have been included.

Unit 3, encompassing the Steinkobbe Formation (Sassendalen Group), lies conformably on top of the Klappmyss Formation, and its upper limit is defined by a high-amplitude, semi-continuous and negative reflector, interpreted as Top Steinkobbe (TSK). The reflector depth is

rather consistent in the southern and central areas (-1.5 s), but deepens towards the north (-2.2 s). The unit is characterized by semi-parallel to parallel and semi-continuous to continuous reflectors of which amplitudes appear to vary. The thickness of the unit increases towards the SE, and the faults identified dissect the unit and extends into shallower depths.

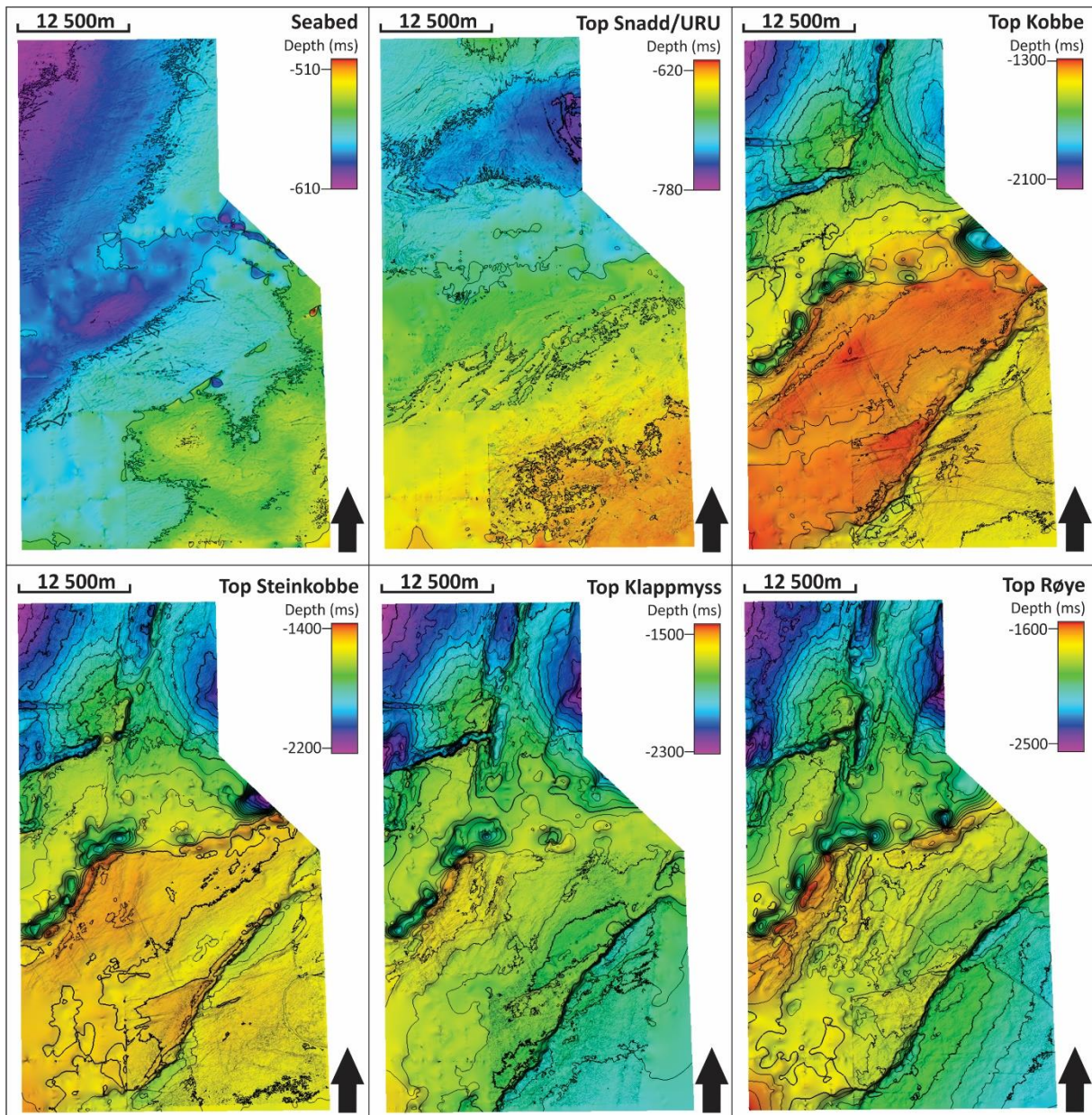


Figure 5.2: Surfaces produced based on interpreted horizons in the study area. Vertical exaggeration (VE): 10. Seabed contour increment (CI): 25. Top Snadd/URU CI: 30. Top Kobbe – Top Røye CI: 50.

The upper limit of Unit 4, encompassing the Kobbe Formation (Sassendalen Group), is defined by a high-amplitude, continuous and negative reflector, interpreted as Top Kobbe (TK). The reflector depth is shallowest in the central areas (-1.3 to -1.4 s) and deepens towards the north (-2.1 s), similar to the other units described. Unit 4 is characterized by parallel and semi-continuous to continuous reflectors, of which amplitudes appear to vary. Lying conformable on

top of the Steinkobbe Formation, the unit thickens towards the central parts of the study area. Faults are observed dissecting the unit, some extending into shallower depths and some terminating near the Top Kobbe reflector.

The Top Snadd/URU (TS/U) reflector defines the upper limit of Unit 5, encompassing the vertically extensive, but partially incomplete, Snadd Formation (Kapp Toscana Group). URU (the Upper Regional Unconformity) is a laterally extensive and regional erosional boundary originating from Late Pliocene-Pleistocene glaciations (Faleide et al., 1996; Vorren et al., 1991). The interpreted horizon is represented by a high-amplitude, semi-continuous to continuous and positive reflector, and is largely affected and truncated by underlying reflectors. The reflector occurs -0.1 to -0.17 s below the seabed, with a rather constant depth of -0.6 to -0.8 s. The lower part of the unit is characterized by parallel and continuous reflectors of low amplitudes, followed by semi-continuous and semi-parallel reflectors with local amplitude variations. The seismic facies of the upper part is similar to the lowermost Snadd Formation, but amplitudes appear to increase towards the Top Snadd/URU horizon. Unit 5 thickens towards the NW and is extensively faulted.

Unit 6 encompasses the glacial Nordland Group, and its upper limit is defined by the high-amplitude, continuous and positive seabed (S) reflector. Reflector depth is rather consistent (-0.5 to -0.6 s) throughout the whole study area, and the unit is characterized by contorted and discontinuous reflectors of low amplitudes. Unit 6 thickens towards the NE and lies unconformably on top of the Kapp Toscana Group, as proven by the erosional boundary represented by URU.

5.2 Faults

The tectonic history of the SW Barents Sea and Loppa High has given rise to numerous faults and larger fault zones of different character. Faults are identified in seismic sections as vertically extensive discontinuities, with a relative displacement of reflectors across the discontinuities. Even though previous studies from the SW Barents Sea have identified and interpreted polygonal faults as potential fluid conduits (e.g. Ostanin et al. (2012)), no such faults are identified in the study area. The following account of faults is based on the stratigraphic level of occurrence and vertical extent of the faults, and thus a three-fold division into Permian, Permian-Triassic and Triassic faults. Nomenclature for describing the structural trends is based on Peacock et al. (2016). Based on variance time slices through 3D volumes, inlines/crosslines from 3D datasets and 2D lines, the main structural trends in the study area have been summarized in fig. 5.3, based on level of occurrence.

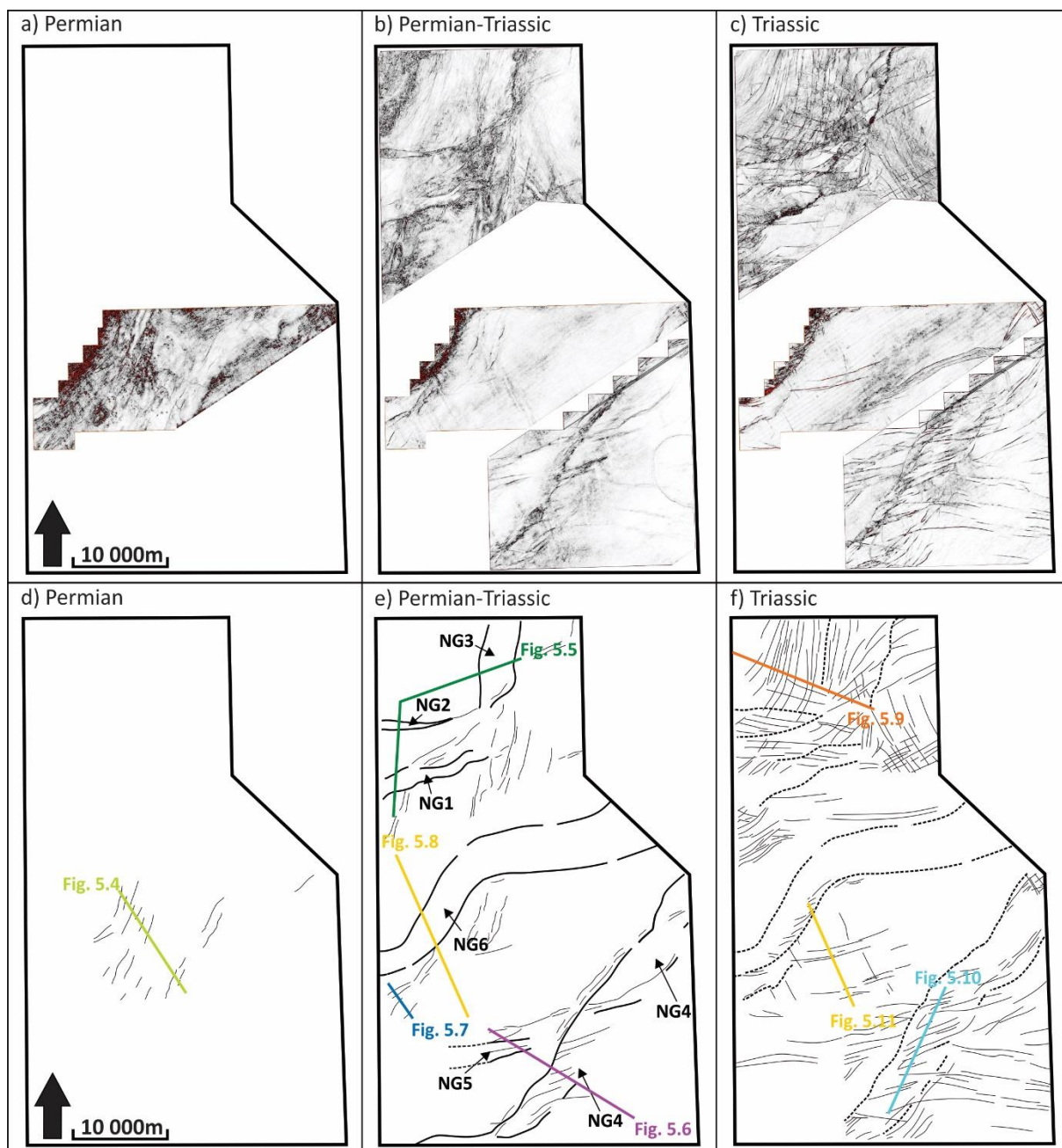


Figure 5.3: a) Permian faults identified on variance time slice at -1804 ms (ST10020). b) Permian-Triassic faults identified on variance time slices at -1848 ms (DG12M1), -1532 ms (ST10020) and -1480 ms (GDF1201M13). c) Triassic faults identified on variance time slices at -860 ms (all three datasets). d) Permian faults identified in the study area, and location of seismic section in fig. 5.4. e) Permian-Triassic faults identified in the study area and location of seismic sections in figs. 5.5-5.8. f) Triassic faults identified in the study area and the location of seismic sections in figs. 5.9-5.11. The dotted lines in f) represent the location of the Permian-Triassic faults, extending all the way up to the Top Snadd/URU horizon.

5.2.1 Permian faults

The Permian faults in the study area are those limited below and terminating against the Top Røye horizon. Poor resolution with increasing depths and deteriorated data have resulted in identification of Permian faults only in the central parts of the study area (the ST10020 dataset). The faults identified have a dominating strike orientation from SW to NE, and a varying lateral extent, ranging from 1300 to 5000 m. The exact vertical extent is somewhat masked by deteriorated data, but appears to range from 120 to 270 ms, with throws ranging from 14 to 32 ms. Some of the faults seem to constitute horst-and-graben structures (seen in fig. 5.4), initially indicative of normal faulting and an extensional tectonic regime.

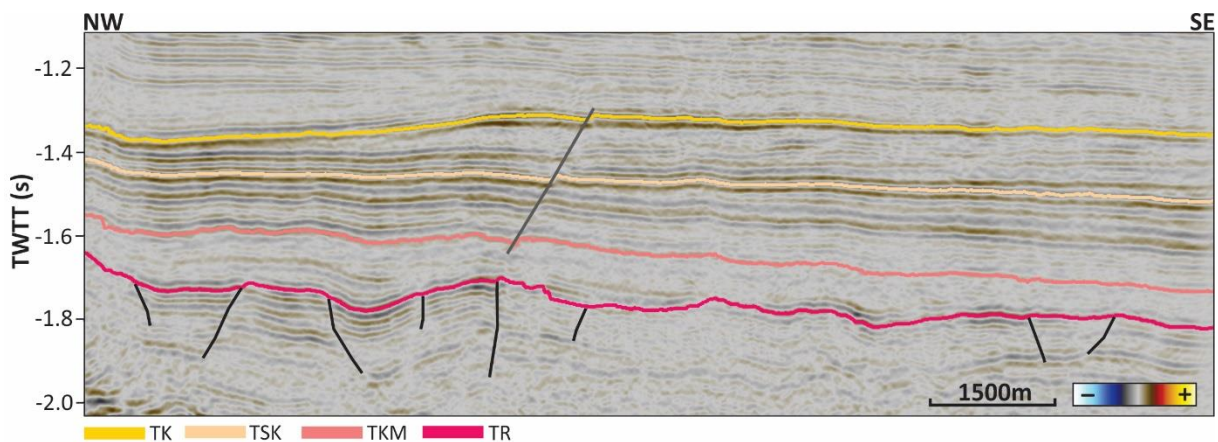


Figure 5.4: Seismic section from the ST10020 dataset (position shown in fig. 5.3d), showing Permian faults terminating against the Top Røye (TR) reflector. Permian faults are colored black. Fault pattern appears to constitute horst-and-graben structures, indicative of normal faulting.

5.2.2 Permian-Triassic faults

The Permian-Triassic faults are those extending from Permian into Triassic strata, and in some cases all the way up to the Top Snadd/URU horizon. The Permian-Triassic faults in the northern and southern regions of the study area mainly constitutes narrow grabens (NGs), delineating larger horst blocks. To the north (the DG12M1 dataset), three possibly related and intersecting grabens are identified (NG1-3 in fig. 5.5), and the lateral extent ranges from 7000 to 11 500 m. Observed in plan-view, NG1 and NG2 appear to die out towards the NE and E, respectively (fig. 5.3e). The strike orientation varies from SW to NE (NG1), W to E (NG2) and S to N (NG3). The delineating faults have throws ranging from 23 to 200 ms, and internal fault blocks appear downfaulted, having throws ranging from 20 to 66 ms. Throws generally appear to decrease with increasing depths.

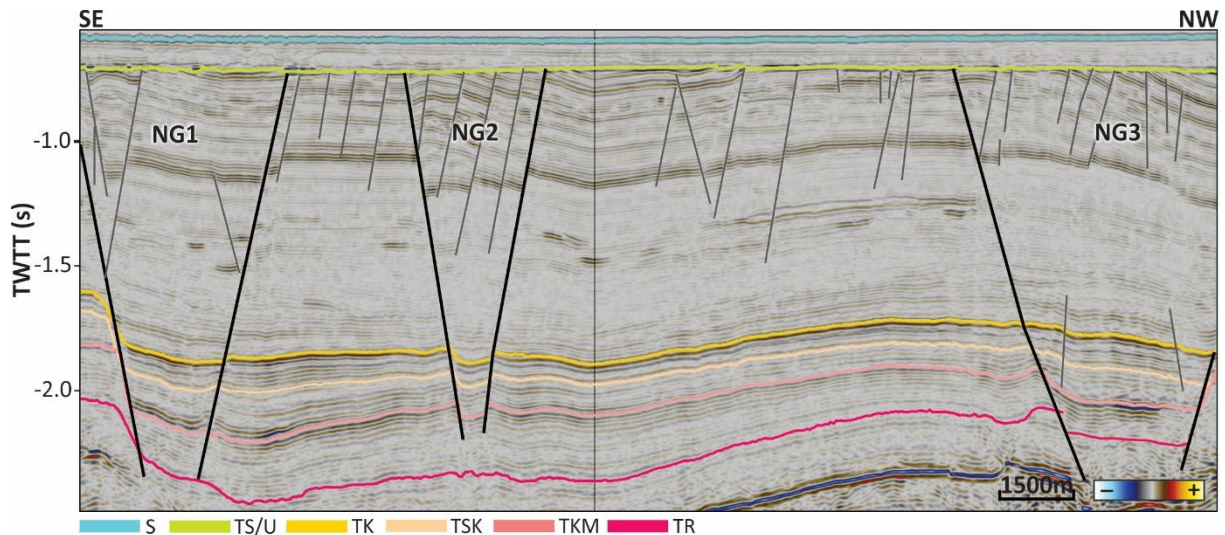


Figure 5.5: Seismic section from the DG12M1 dataset (position shown in fig. 5.3e), showing three narrow grabens (NG1-3) terminating against the Top Snadd/URU horizon (TS/U). Permian-Triassic faults are colored black, whereas other faults are colored grey. The lateral extent of the NGs increases with decreasing depth and displacement within them appears to be downwards. The grabens separate several horst blocks of larger lateral extent.

In the southern part of the study area (the GDF1201M13 dataset), one of the narrow grabens observed (NG4 in fig. 5.6) extends 32 000 m from SW to NE across the entire area, and is represented by an anastomosing fault pattern in plan-view (fig. 5.3b-c, e-f).

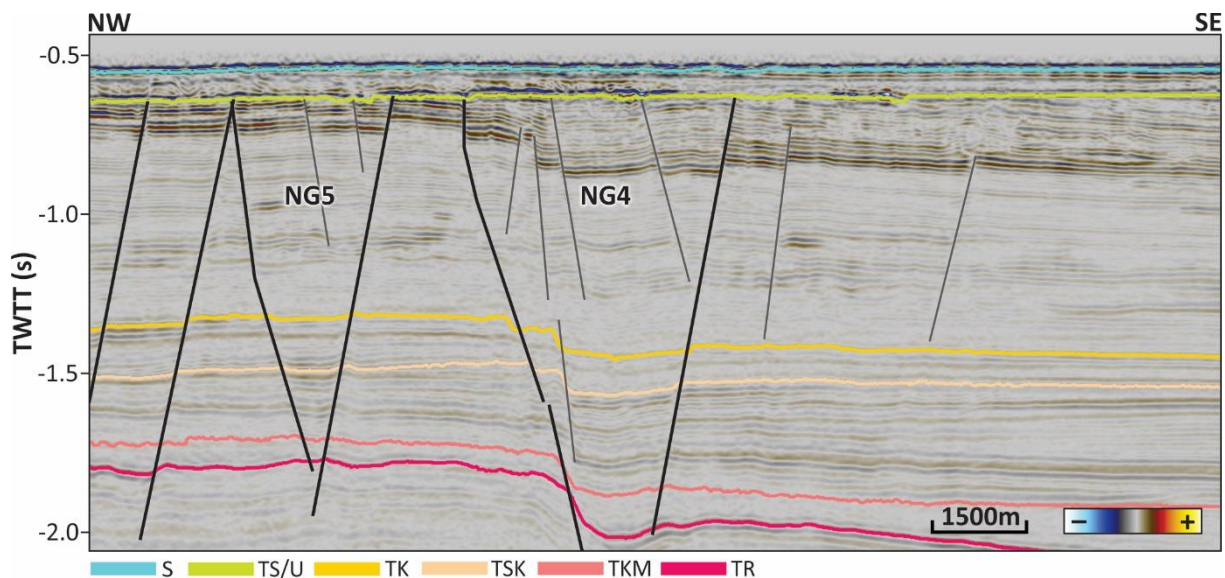


Figure 5.6: Seismic section from GDF1201M13 (position shown in fig. 5.3e), showing two narrow grabens (NG4-5) terminating against the Top Snadd/URU (TS/U) horizon. Permian-Triassic faults are colored black, whereas others are colored grey. Both grabens, separated by horst blocks, widens with decreasing depths and internal fault blocks appear to be downfaulted. The general displacement across NG4 is down towards the SE.

The throw of the delineating faults of NG4 ranges from 24 to 41 ms, of which internal fault blocks have throws ranging from 7 to 71 ms. NG5 (fig. 5.6) is a smaller graben located NW of NG4, having a lateral extent of approximately 6400 m. However, 3D data coverage towards the SE of GDF1201M13 is limited, and the termination of the structure against the outline of the dataset initially suggests a continuation of the structure further to the SE. The throw of the

delineating and internal faults of NG5 ranges from 15 to 28 ms and 11 to 23 ms, respectively. All five graben structures (NG1-5) terminate against the Top Snadd/URU horizon, and as seen in fig. 5.5 and 5.6, the delineating faults of the grabens converge with increasing depths. Internal fault blocks appear to be delineated by synthetic and antithetic faults, and are displaced downwards within the graben structures, with respect to surrounding strata.

In the central parts of the study area (the ST10020 and northern GDF1201M13 datasets), the Permian-Triassic faults observed have a dominating strike orientation from SW to NE, with a varying lateral extent ranging from 1700 to 15 000 m (fig. 5.3e and 5.7). The vertical extent of the faults ranges from 450 to 1800 ms, and the throws recorded range from 14 to 33 ms. Although on a much smaller scale, some of these faults also appear to constitute horst-and-graben structures, indicative of normal faulting. Narrow grabens on the scale of those previously described are not identified in this particular area.

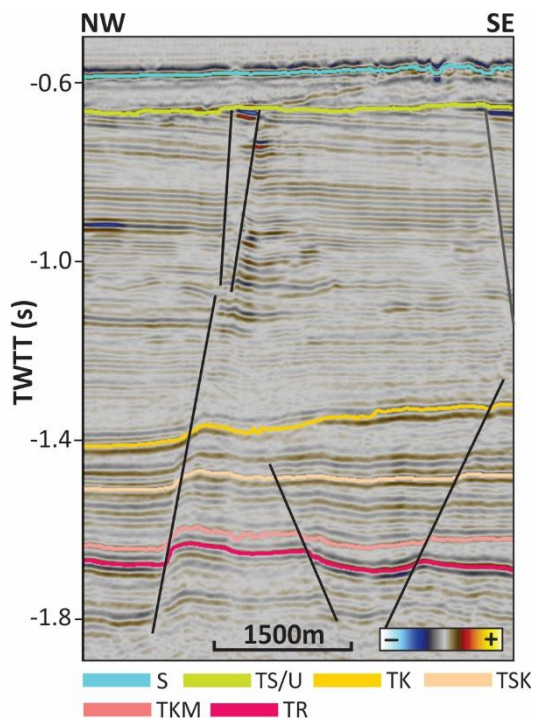


Figure 5.7: Seismic section from ST10020 (position shown in fig. 5.3e), showing the Permian-Triassic faults with dominating strike orientation from SW to NE. Some of the faults appear to constitute horst-and-graben structures.

Two larger faults located to the east and west in the ST10020 dataset stand out due to their superiorly greater lateral and vertical extent. The western fault appears to be related to a narrow graben (NG6 in fig. 5.3e and 5.8), extending from SW to NE between the ST10020 and DG12M1 datasets. The delineating faults of NG6 have throws ranging from 104 to 266 ms, whereas internal fault blocks have throws ranging from 15 to 117 ms. The eastern fault appears to be a continuation of NG4 observed in the GDF1201M13 dataset. The narrow grabens identified are delineated by normal faults of opposite dips, converging with increasing depths,

and are characterized by a down-faulted interior. These characteristics indicates that the narrow grabens (NG1-6) in fact might be classified as negative flower structures, associated with strike-slip faulting and transtensional releasing bends (Fossen, 2016).

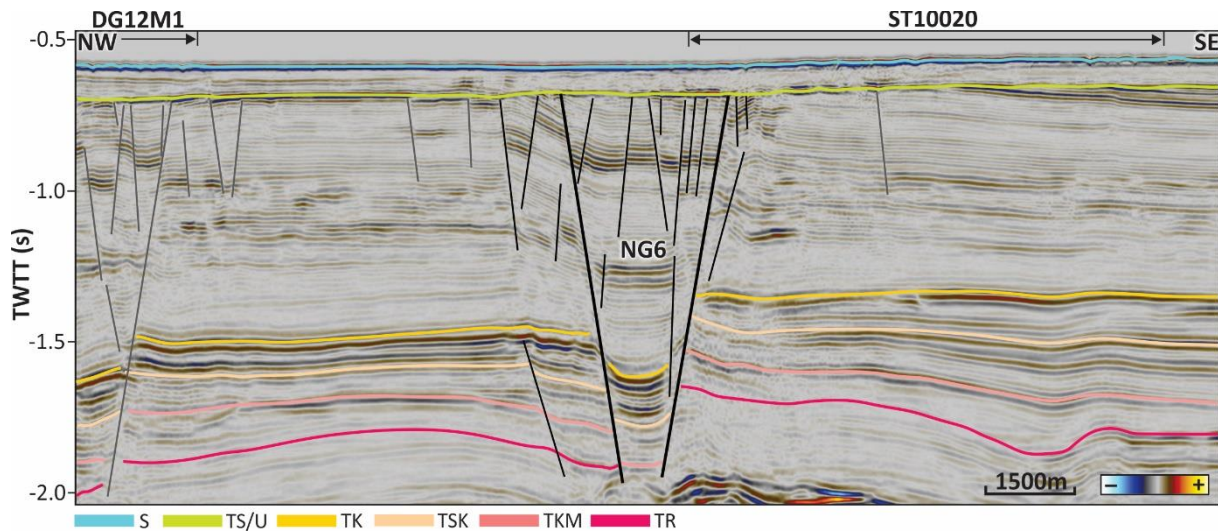


Figure 5.8: 2D line (NBR09-240736, position shown in fig. 5.3e) covering a substantial area between the DG12M1 and ST10020 datasets, showing the narrow graben (NG6) extending from SW to NE between the datasets. Western fault identified in ST10020 appears to be one of delineating faults of the NG6. NG6 also appear to separate two larger fault blocks.

5.2.3 Triassic faults

The Triassic faults are those limited to Triassic strata, and in this area exclusively in the Snadd Formation. The number and density of Triassic faults vary across the entire study area; the southern and northern regions (DG12M1 and GDF1201M13 datasets) are extensively faulted, whereas the central region (ST10020) only comprises a few faults (fig. 5.3f, 5.9-5.11). Some of the Triassic faults are related to several of the narrow grabens characterizing the area, but are still classified as Triassic due to their level of occurrence and limited vertical extent. In plan-view, the strike orientation of the Triassic faults seems somewhat arbitrary, but three trends are observed; SE to NW, E to W and S to N. Fault pattern can thus be classified as intersecting, possibly abutting and random. The exact lateral extent of each individual fault is difficult to determine as they cross-cut and intersect each other, and seismic sections show that the dip angle is variable. Although some of the faults seem to constitute horst-and-graben structures indicative of normal faulting, the density and variability of the faults may suggest a more complex tectonic regime. The vertical extent of the faults ranges from 230 to 960 ms, and the throws recorded range from 7 to 98 ms. All Triassic faults terminate at or near the Top Snadd/URU horizon.

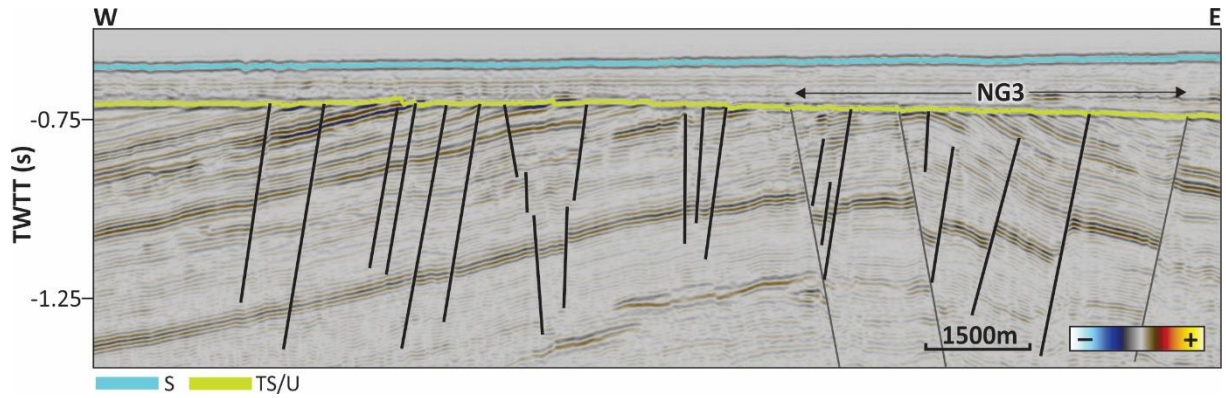


Figure 5.9: Seismic section from the DG12M1 dataset (position shown in fig. 5.3f), showing several Triassic faults dissecting the Snadd Formation. Triassic faults are colored black, others grey. Several faults appear to have the same dip direction, while others appear to constitute horst-and-graben structures. Some of the Triassic faults are antithetic and synthetic faults related to NG3.

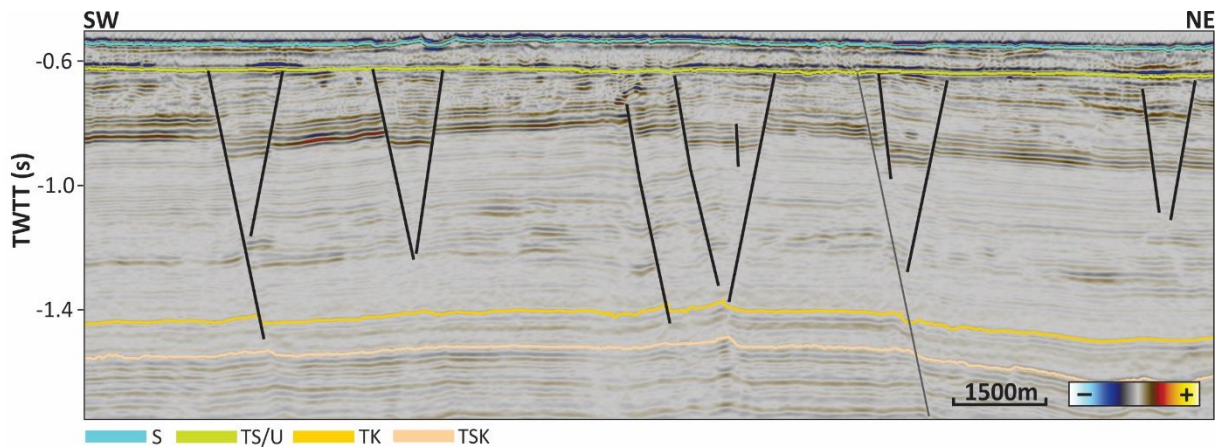


Figure 5.10: Seismic section from the GDF1201M13 dataset (position shown in fig. 5.3f), showing several Triassic faults dissecting the Snadd Formation. Triassic faults are colored black, others grey. The majority of the faults in this section appear to constitute smaller-scale horst-and-graben structures.

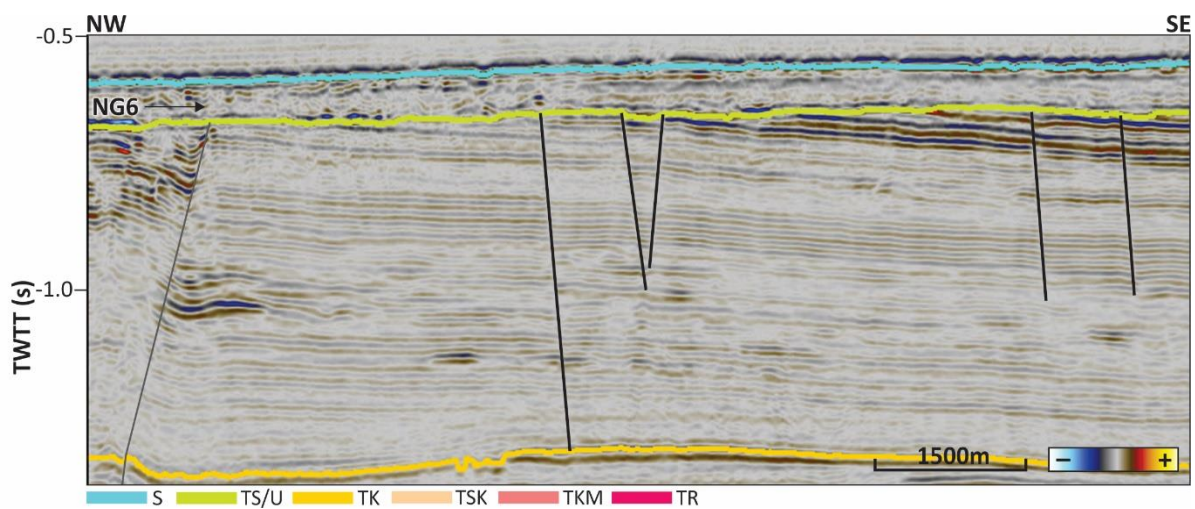


Figure 5.11: Seismic section from the ST10020 dataset (position indicated in fig 5.3f), showing the Triassic faults with a dominating strike orientation from SW to NE, of which some appear to constitute horst-and-graben structures.

5.3 Fluid flow indications

5.3.1 Amplitude anomalies

The term *amplitude anomaly* refers to all amplitude deviations from a standard in a given dataset, thus including both abnormally high and abnormally low amplitudes. During exploration for subsurface fluids, especially shallow accumulations, emphasis is placed on high amplitude anomalies (bright spots) indicative of strong impedance contrasts and the presence of gas. Thus, the amplitude anomalies described in this section are local amplitude increases with respect to normal amplitude variations within individual datasets, and color scales are adjusted in order to highlight these anomalies. The anomalies have been categorized according to their level of occurrence (Permian, Triassic and Cenozoic strata), of which their location and distribution is presented in fig. 5.12. The majority of the amplitude anomalies identified (AA3-AA10) are interpreted as gas accumulations, evidenced by enhanced amplitudes, reversed polarities and in some cases push-down effects. Similar observations have been made in the SW Barents Sea, by e.g. Andreassen, Nilssen, et al. (2007), Rajan et al. (2013) and Vadakkepuliambatta et al. (2013).

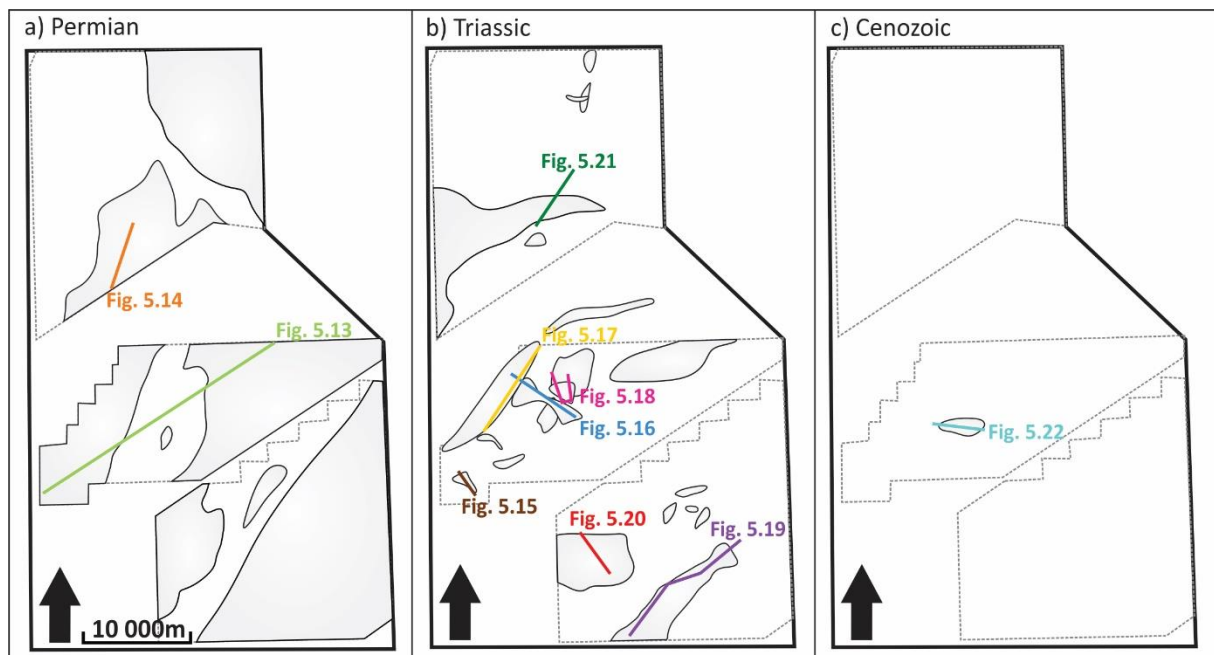


Figure 5.12: a) Amplitude anomalies in Permian strata and approximate location of figs. 5.13-5.14. b) Amplitude anomalies in Triassic strata and location of figs. 5.15-5.21. c) Amplitude anomalies in Cenozoic strata and location of fig. 5.22. Outline of anomalies roughly corresponds to their extent, and in several cases include several smaller anomalies.

5.3.1.1 Amplitude anomalies within Permian strata

5.3.1.1.1 Amplitude Anomaly 1 and 2 (AA1 and AA2)

AA1 encompasses two large anomalies extending from SW to NE in the ST10020 dataset (fig. 5.12a and 5.13), of which amplitudes appear to be reversed with respect to the seabed. The anomalies occur approximately 300 ms below the Top Røye horizon, and approximately 2000

ms below the seabed. Being two of the largest anomalies identified in the study area, the areal extent of the western and eastern anomaly measures to 122.8 km² and 193.7 km², respectively. As seen from the seismic section in fig. 5.13c, the anomalies are separated by an area of very low amplitudes, possibly a result of acoustic masking or representing lateral geological variations. Furthermore, several small discontinuities cross-cutting the anomalies can be observed, initially thought to represent smaller faults with rather small throws. However, in plan-view (fig. 5.13a-b), these discontinuities correspond to several elongated and circular to sub-circular features.

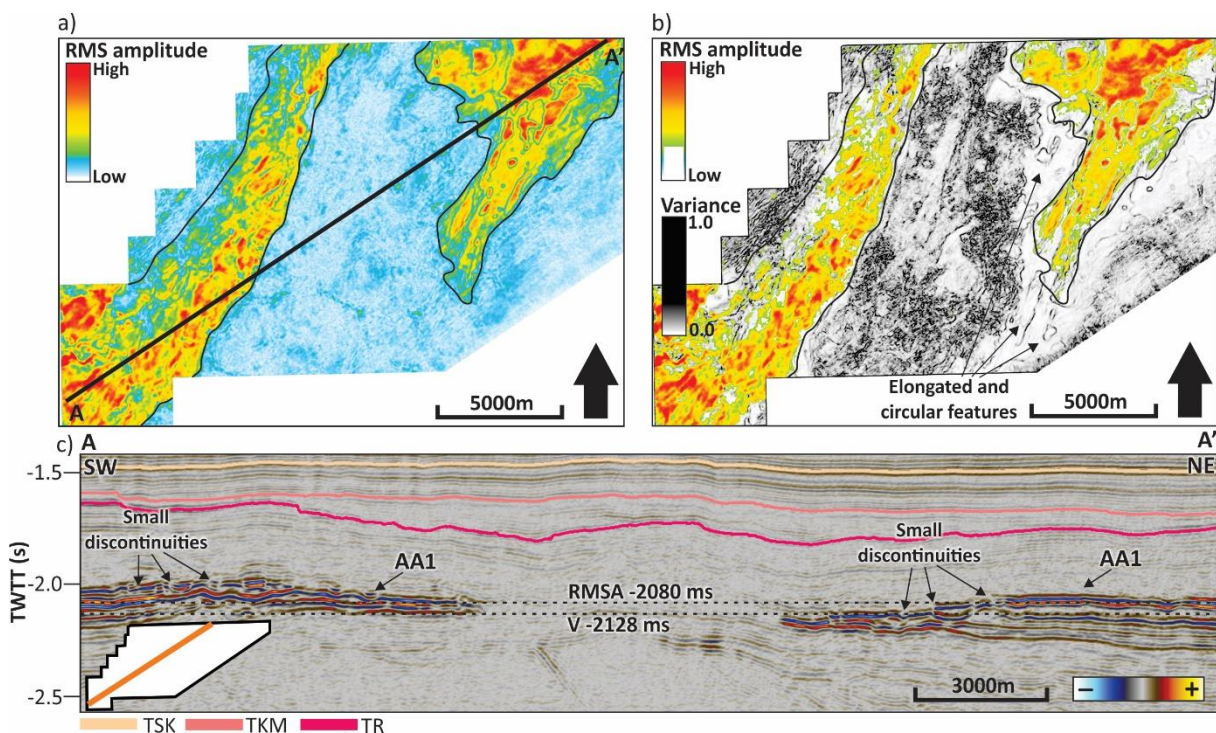


Figure 5.13: a) RMS amplitude (RMSA) time slice showing the extent of AA1 in the ST10020 dataset, and variations in amplitude, at -2080 ms. b) RMSA time slice (-2080 ms, adjusted opacity) superimposed on a variance (V) time slice (-2128 ms), showing the relationship between amplitude anomalies and structural trends in the ST10020 dataset. c) Seismic section across AA1 (location shown in fig. 5.12a and in the dataset outline), with RMSA and V time slices indicated. Small discontinuities observed in seismic section correspond to elongated and circular to sub-circular features seen in b).

AA2 (fig. 5.14) is a large amplitude anomaly, observed to extend across large parts of the DG12M1 dataset, showing great similarities to AA1. The anomaly is located well below the Top Røye horizon (220-300 ms) and the seabed (1550-2070 ms), and has a large areal extent covering the entire region. In fig. 5.14 a-b, only a smaller part of the anomaly is cut by time slice -2104 ms, due to large variations in the level of occurrence. Amplitudes are reversed with respect to the seabed, and the variance time slice (5.14b) shows the same elongated and sub-circular features seen in the ST10020 dataset.

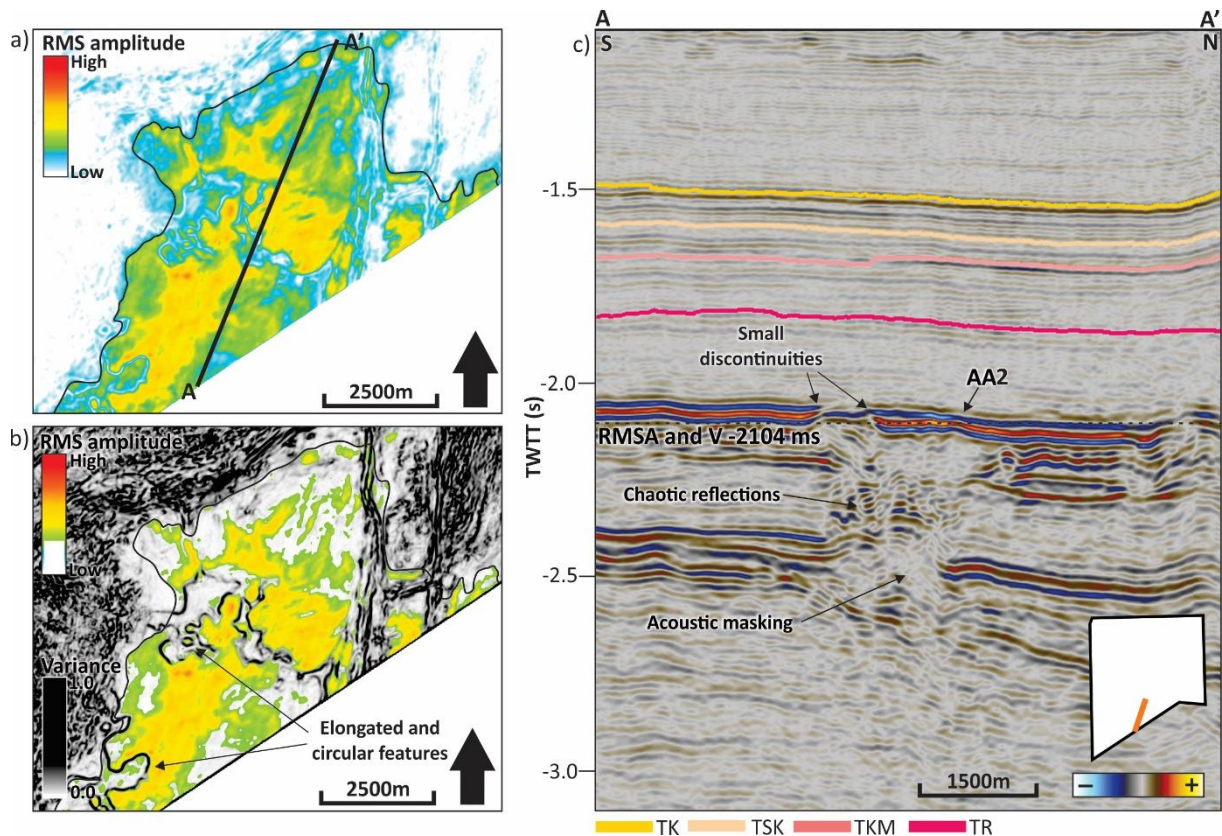


Figure 5.14: a) RMS amplitude (RMSA) time slice showing the extent and amplitude variation of AA2 in the DG12M1 dataset, at -2104 ms. b) RMSA time slice (-2104 ms, adjusted opacity) superimposed on variance (V) time slice (-2104 ms) showing the relationship between amplitude anomalies and structural trends in the DG12M1 dataset. c) Seismic section showing AA2 (location shown in fig. 5.12a and in the dataset outline), and the similar discontinuities observed in AA1.

Unlike the following amplitude anomalies, AA1 and 2 are not interpreted as hydrocarbon accumulations. AA1 appear to correspond to the Fafner succession (Gipsdalen Group) described by Ahlborn et al. (2014), a sequence restricted to the eastern downdip margin of the Loppa High. Resting unconformably on eroded Ørn sediments, the succession is described as composed by several sequences consisting of a basal evaporite unit overlain by carbonates and/or dolomites. Several of these sequences show evidence of subaerial exposure and karstification, demonstrated by the presence of breccia-pipes and collapse features (Ahlborn et al., 2014), corresponding to the discontinuities identified in this study. AA2 show similarities to AA1, but the smaller number of discontinuities and the limited extent of the Fafner succession suggests that AA2 might correlate to the Ørn Formation (Top Gipsdalen Group), which can be identified on a regional scale (Ahlborn et al., 2014). As eroded and karstified carbonate deposits, both anomalies may represent significant reservoir intervals rather than actual accumulations.

5.3.1.2 Amplitude anomalies within Triassic strata

5.3.1.2.1 Amplitude Anomaly 3 (AA3)

AA3 is located to the SW in the ST10020 dataset (fig. 5.12b), occurring within the Triassic Snadd Formation, approximately 300 ms below the seabed (fig. 5.15). The anomaly encompasses two superimposed reflectors, and occur within a 30 ms window. It is characterized by a reversed polarity with respect to the seabed, suggesting a decrease in acoustic impedance. From the seismic section (fig. 5.15c) it is apparent that the amplitude of the reflectors decreases laterally towards the SE and the anomaly terminates against a larger fault towards the NW; the areal extent of the anomaly thus measures to approximately 0.81 km². The delineating fault extends vertically from the Top Snadd/URU horizon, down to below -1800 ms, penetrating both the prolific Kobbe and Steinkobbe formations. The Triassic Snadd Formation is known for its channel structures and deposits (see e.g. Klausen et al. (2015) and Arntzen (2018)), and the amplitude anomaly appears to coincide with such a structure extending from the SE to NW.

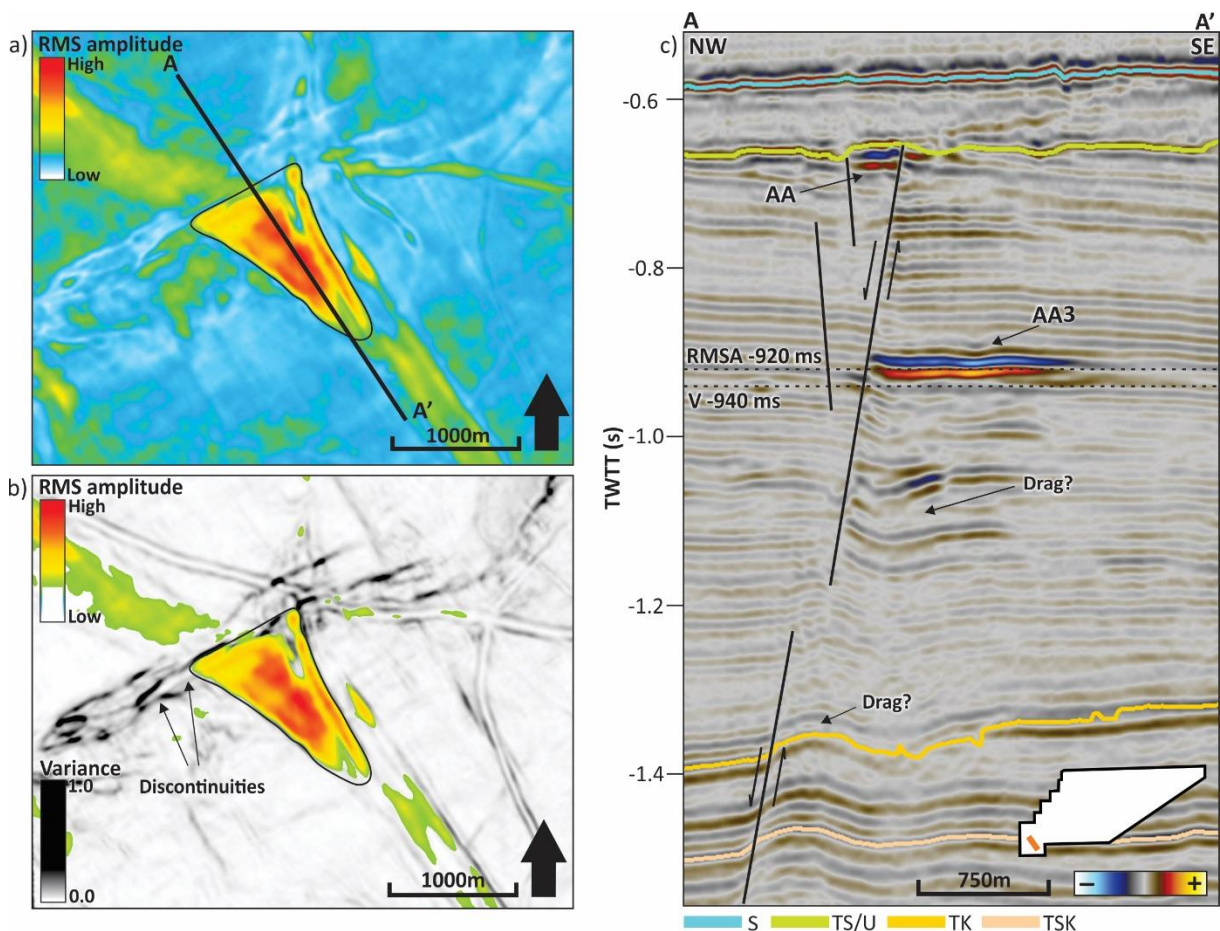


Figure 5.15: a) RMS amplitude (RMSA) time slice showing the extent and amplitude variations of AA3 in the ST10020 dataset, at -920 ms. b) RMSA time slice (-920 ms, adjusted opacity) superimposed on variance (V) time slice (-940 ms) showing the relationship between AA3 and structural trends. Note how the anomaly continues across the discontinuity observed in b). c) Seismic section (location shown in fig. 5.12b and the dataset outline) showing AA3 terminating against a fault and overlying smaller amplitude anomalies located along Top Snadd/URU. SW-NE oriented discontinuity in b) corresponds to the delineating fault in c).

5.3.1.2.2 Amplitude Anomaly 4 (AA4)

AA4 is located to the N in the ST10020 dataset, occurring within the Triassic Snadd Formation (fig. 5.12b and 5.16). The anomaly is located approximately 350 ms below the seabed and encompasses mainly two superimposed reflectors occurring in a 45 ms window. The amplitude of AA4 appears to be reversed with respect to the seabed, and decreases laterally towards the SE. Similar to AA3, the anomaly terminates against a vertically extensive fault to the NW, extending from below -1600 ms and all the way up to the Top Snadd/URU horizon. The fault in question appears to be the SE delineating fault of NG6, which has previously been described as extending way below the Top Røye horizon. AA4 measures to approximately 0.42 km², and appears to coincide with an apparent channel structure, much like AA3. Several amplitude anomalies have also been identified directly below AA4.

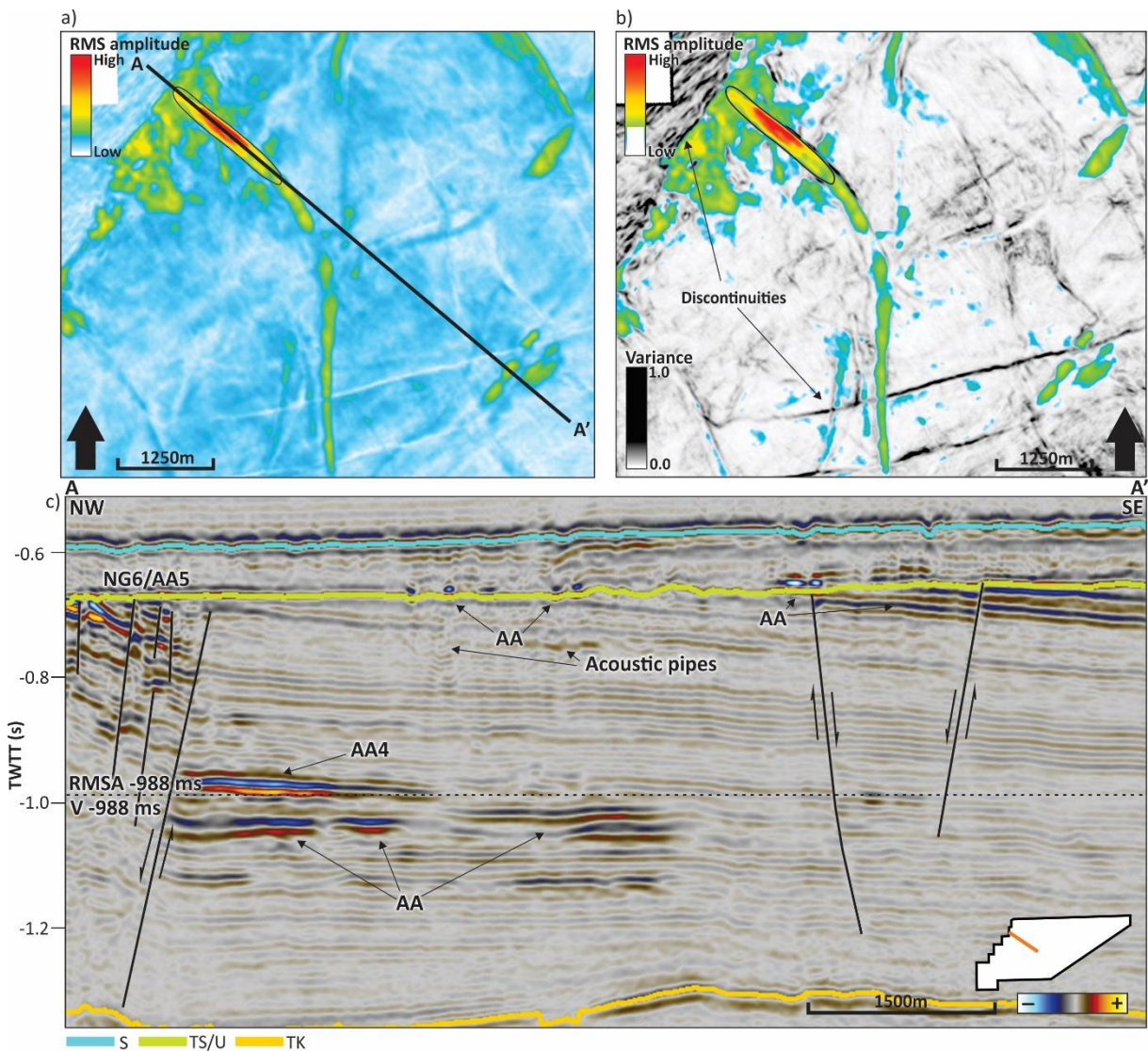


Figure 5.16: a) RMS amplitude (RMSA) time slice showing the extent and amplitude variations of AA4 in the ST10020 dataset, at -988 ms. b) RMSA time slice (-988 ms, adjusted opacity) superimposed on variance (V) time slice (-988 ms), showing the relationship between structural trends and AA4. Note the continuation of enhanced amplitudes, related to AA4, towards the south. c) Seismic section showing AA4 terminating against NG6, as well as underlying amplitude anomalies.

5.3.1.2.3 Amplitude Anomaly 5 (AA5)

AA5 is located to the NW in the ST10020 dataset, encompassing a larger area of several smaller anomalies occurring near or at the Top Snadd/URU horizon (fig. 5.12b and 5.17). The top of the identified anomalies is located approximately 80 ms below the seabed, occurring within a 100 ms window. All anomalies have a reversed polarity with respect to the seabed, suggesting a decrease in acoustic impedance. The areal extent of AA5, all anomalies included, measures to approximately 15.5 km². The zone of amplitude anomalies occurs above an extensively faulted zone related to the vertically extensive NG6 described in section 5.2.2, penetrating both the Kobbe and Steinkobbe formations. The tilted fault blocks observed on the seismic section are delineated by the associated antithetic and synthetic faults and the amplitudes of some of the reflectors within the internal fault blocks appear to increase updip.

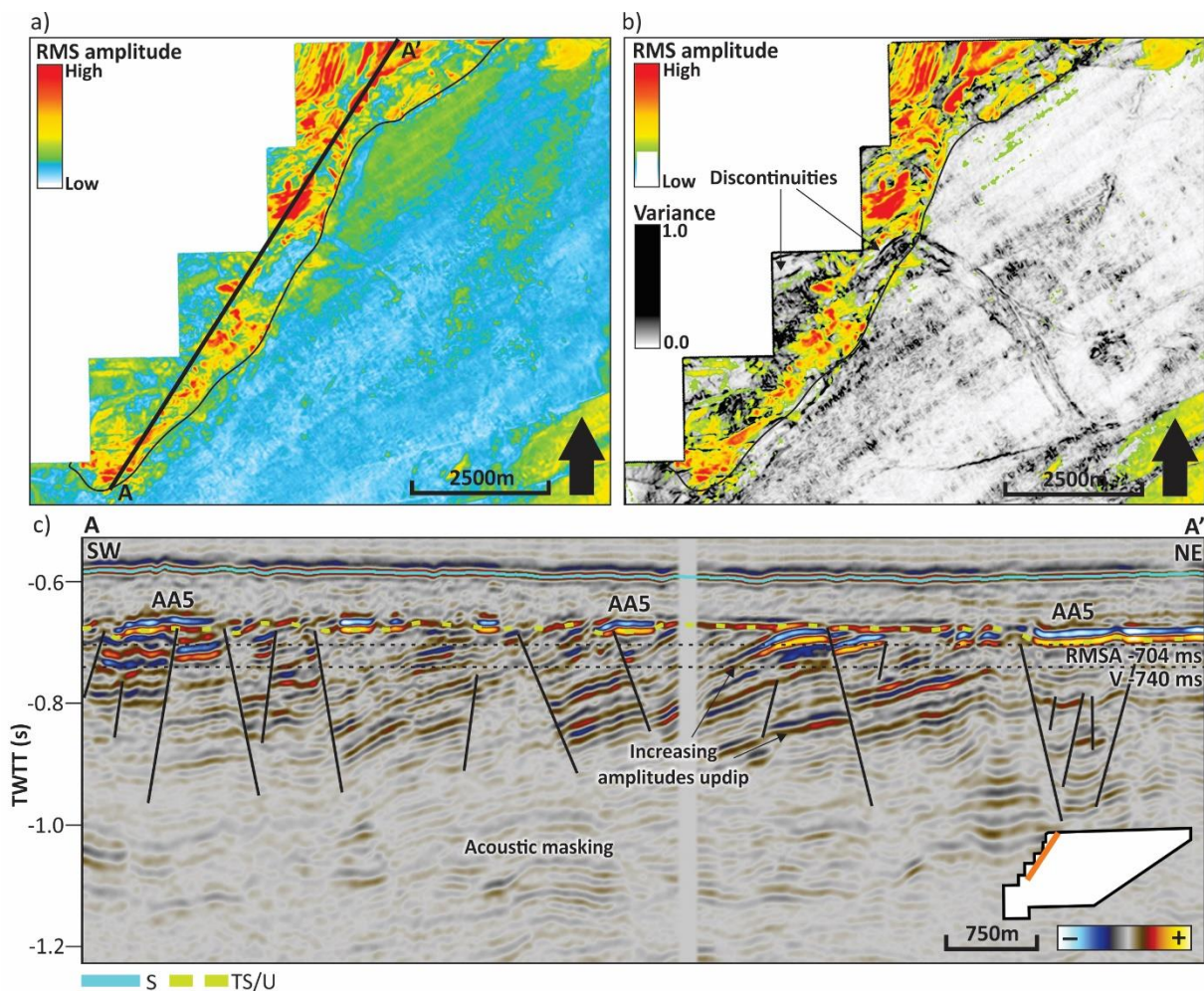


Figure 5.17: a) RMS amplitude (RMSA) time slice showing the extent and amplitude variation of AA5 in the ST10020 dataset, at -704 ms. b) RMSA time slice (-704 ms, adjusted opacity) superimposed on variance (V) time slice (-740 ms) showing the relationship between AA5 and structural trends. c) Seismic section (location shown in fig. 5.12b and in the dataset outline), showing how AA5 encompasses numerous smaller amplitude anomalies covering a larger area above an extensively faulted zone. Several anomalies have increasing amplitudes updip and some are bounded by faults.

5.3.1.2.4 Amplitude Anomaly 6 (AA6)

AA6 is located in the central part of the ST10020 dataset (fig. 5.12b), encompassing three anomalies (annotated AA6-1 to AA6-3 in fig. 5.18), occurring along the Top Snadd/URU horizon. The anomalies are located approximately 70 ms below the seabed, in a 40 ms window. The three anomalies have reversed polarities with respect to the seabed, suggesting a decrease in acoustic impedance, and amplitudes appear to decrease laterally. AA6-1, AA6-2 and AA6-3 have areal extents of approximately 0.18 km², 0.36 km² and 0.17 km², respectively. A single fault is identified approximately 180 ms below the anomalies, continuing into a narrow zone of acoustic masking located below AA6-2. Below both AA6-1 and AA6-2, push-down effects in narrow pipes have been recorded.

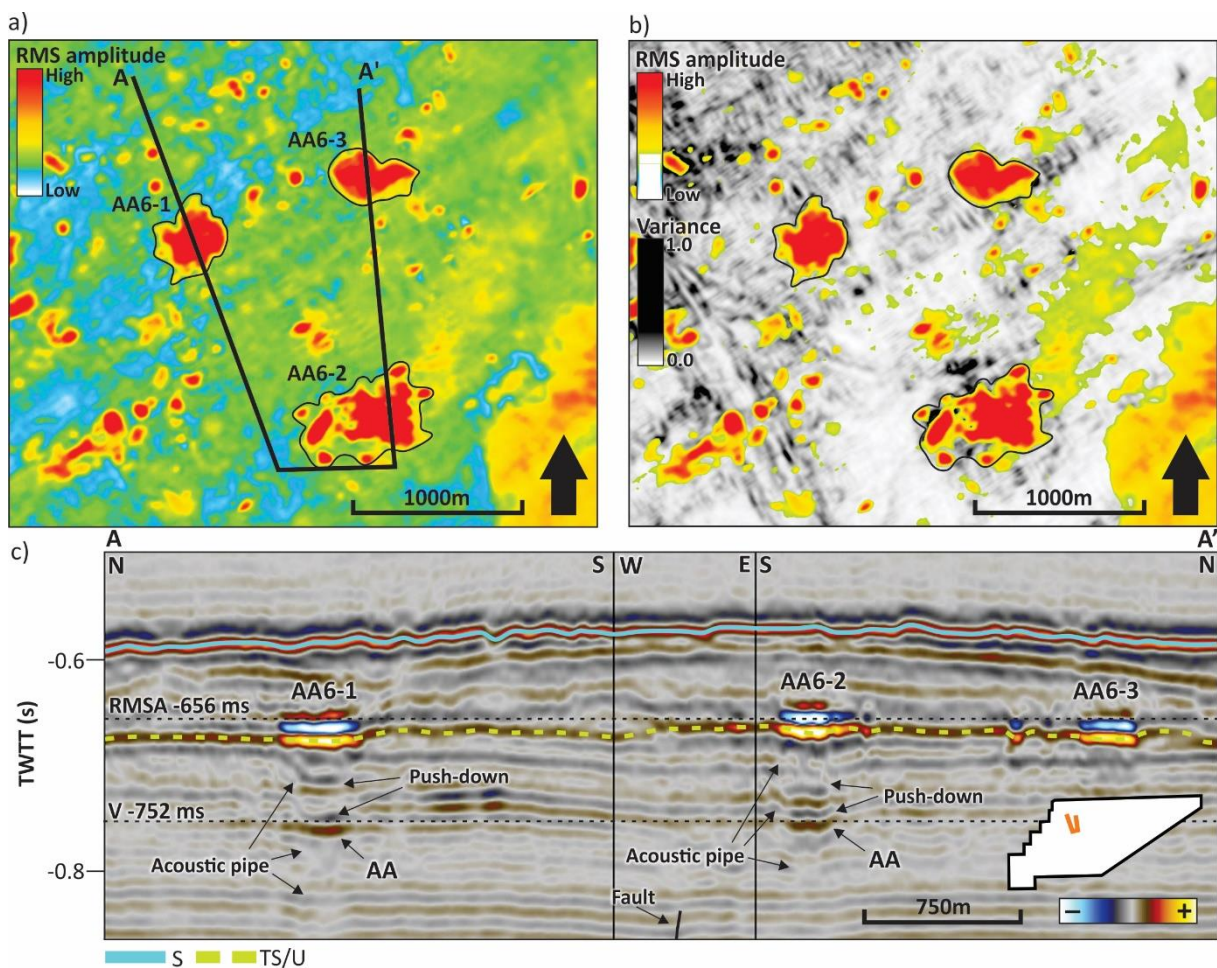


Figure 5.18: a) RMS amplitude (RMSA) time slice showing the extent and amplitude variations of AA6 in the ST10020 dataset, at -656 ms. Note that intermediate amplitudes surrounding AA6-1-3 can be attributed to the strong URU reflector. b) RMSA time slice (-656 ms, adjusted opacity) superimposed on variance (V) time slice (-752 ms), showing the relationship between amplitude anomalies and structural trends in the area. Note how no discontinuities have been identified directly below AA6 in this interval, but on a much deeper level. c) Seismic section (location shown in fig. 5.12b and the dataset outline), showing AA6-1-3 located along the Top Snadd/URU horizon, and associated push-down effects in acoustic pipes.

5.3.1.2.5 Amplitude Anomaly 7 (AA7)

AA7 is located to the S in the GDF1201M13 dataset (fig. 5.12b), occurring at the Top Snadd/URU horizon approximately 60-80 ms below the seabed, in a 30-45 ms window. All anomalies have reversed polarities with respect to the seabed, and amplitudes decrease laterally along the Top Snadd/URU horizon. Surrounded by several smaller ones, the anomalies in question (annotated AA7-1 to AA7-4 in fig. 5.19) are the largest in the area, with areal extents of 0.9 km², 0.27 km², 0.45 km² and 1.2 km², respectively. The anomalies identified are located directly above some of the Triassic faults described in section 5.2.3, also seen on the variance time slice in fig. 5.19b. Despite the high density of faults located below the anomalies, only a few penetrate potential source rocks such as the Kobbe and Steinkobbe formations.

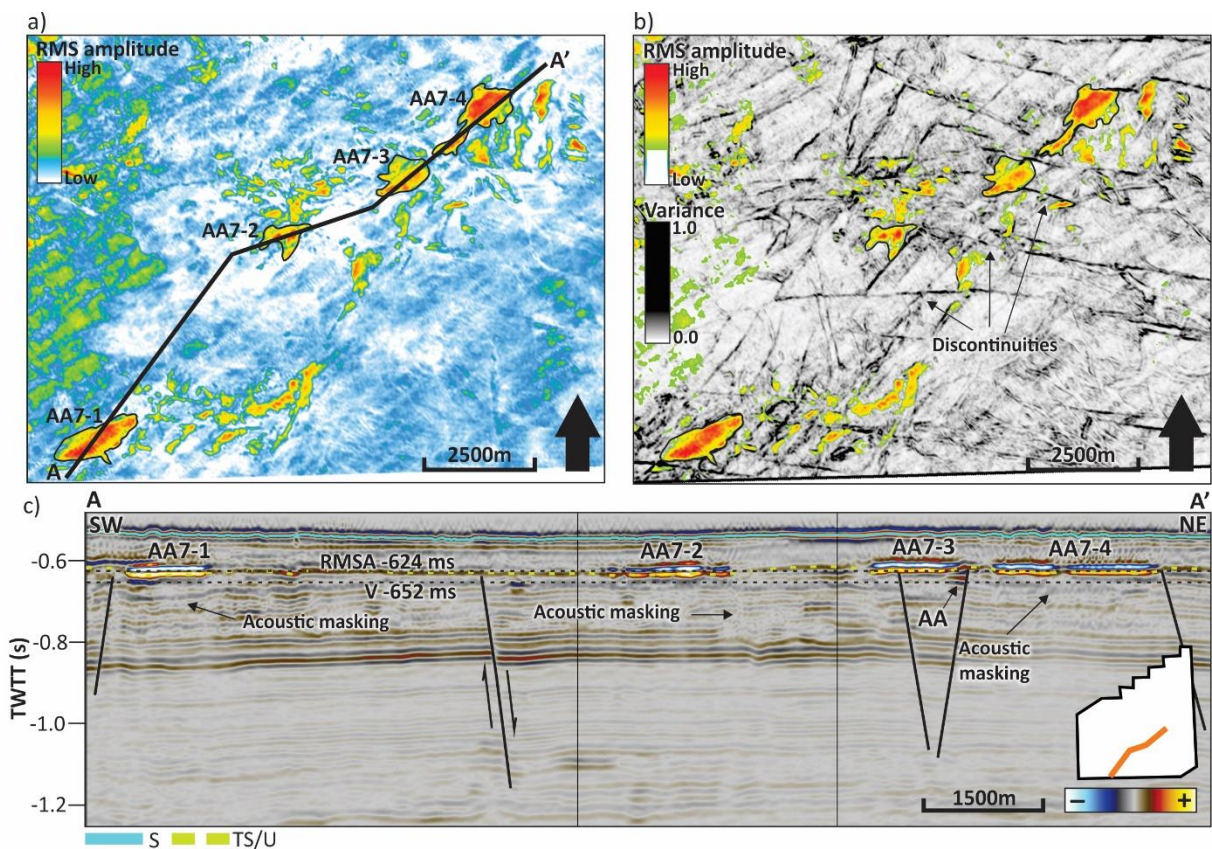


Figure 5.19: a) RMS amplitude (RMSA) time slice showing the extent and amplitude variations of AA7 in the GDF1201M13 dataset, at -624 ms. b) RMSA time slice (-624 ms, adjusted opacity) superimposed on variance (V) time slice (-652 ms) showing the relationship between amplitude anomalies and structural trends, mainly Triassic faults. Note the high density of discontinuities identified on the variance time slice and the location of amplitude anomalies in association with these. c) Seismic section (location shown in fig. 5.12b and in the dataset outline) showing AA7 located along the Top Snadd/URU horizon. Note also the location of the Triassic faults.

5.3.1.2.6 Amplitude Anomaly 8 (AA8)

AA8 is located to the W in the GDF1201M13 dataset (fig. 5.12b), occurring along the Top Snadd/URU horizon. Several anomalies are identified, of which the two larger ones described in this section (annotated AA8-1 and AA8-2 in fig. 5.20) are surrounded by several smaller. The amplitudes appear to be reversed with respect to the seabed, again indicating a decrease in acoustic impedance. The anomalies occur 65-75 ms below the seabed, in a 30-35 ms window. AA8-1 measures to approximately 5.0 km² and AA8-2 to approximately 5.5 km². The anomalies are located above several faults, some of which extend down to below -1800 ms, penetrating both the Kobbe and Steinkobbe formations. The anomalies show large similarities with the anomalies identified along the Top Snadd/URU horizon in the ST10020 dataset.

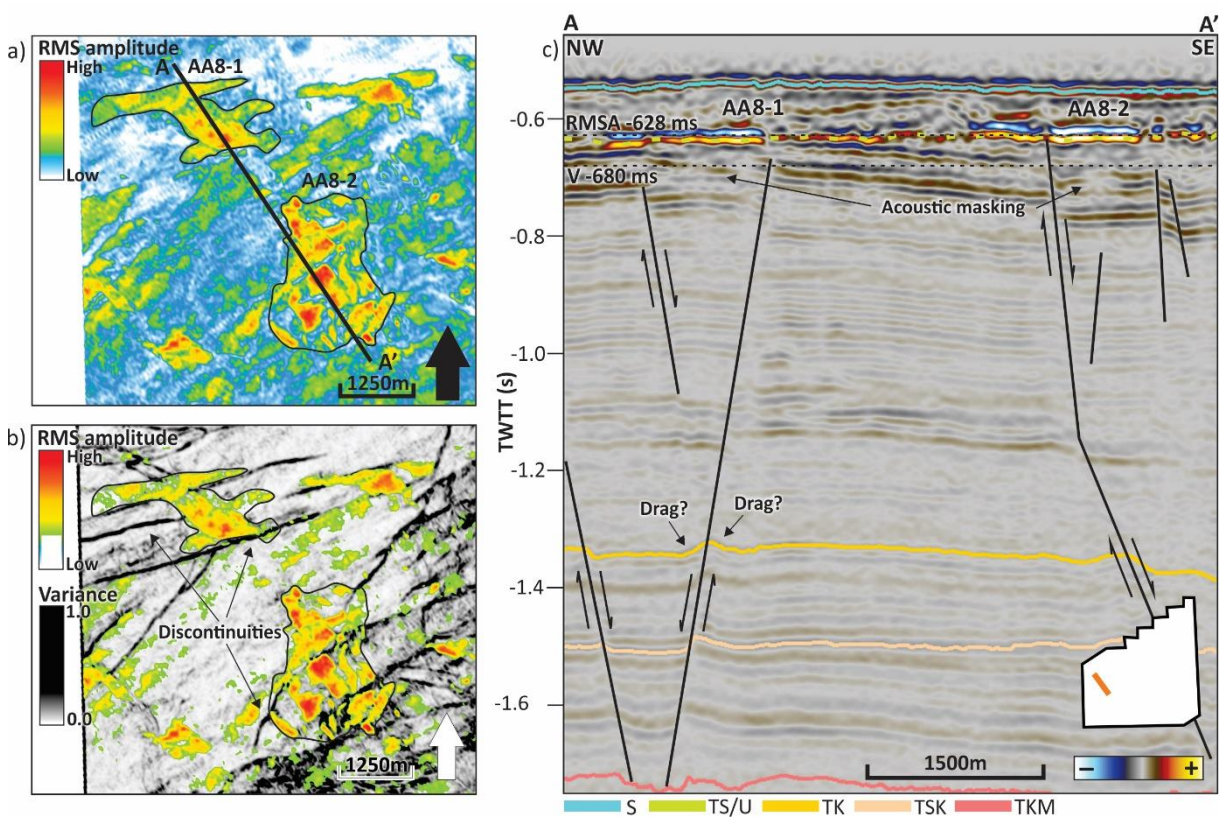


Figure 5.20: a) RMS amplitude (RMSA) time slice showing the extent and amplitude variation of AA8 in the GDF1201M13 dataset, at -628 ms. b) RMSA time slice (-628 ms, adjusted opacity) superimposed on variance (V) time slice (-680 ms) showing the relationship between AA8 and structural trends. Note how the anomalies are located above several discontinuities. c) Seismic section (location shown in fig. 5.12b and in the dataset outline) showing AA8 located along the Top Snadd/URU horizon and associated areas of acoustic masking. Note the location of amplitude anomalies in close proximity to faults, both Triassic and Permian-Triassic.

5.3.1.2.7 Amplitude Anomaly 9 (AA9)

AA9 encompasses a larger area of several smaller anomalies (AA9-1 to AA9-4 in fig. 5.21), located to the SW in the DG12M1 dataset (fig. 5.12b). All of the anomalies occur along the Top Snadd/URU horizon, approximately 120-140 ms below the seabed, in a 30-40 ms window. Similar to the other identified anomalies, amplitudes appear to be reversed with respect to the seabed. The areal extents of AA9-1 to AA9-4 measure to approximately 1.24 km², 0.29 km², 0.16 km² and 0.31 km², respectively. The anomalies are located directly above one of the larger narrow grabens in the area (NG1), and their distribution largely corresponds to the smaller faults delineating internal fault blocks. The larger faults defining the lateral extent of the graben extends from the Top Snadd/URU horizon, down to below -2000 ms, penetrating both the Kobbe and Steinkobbe formations.

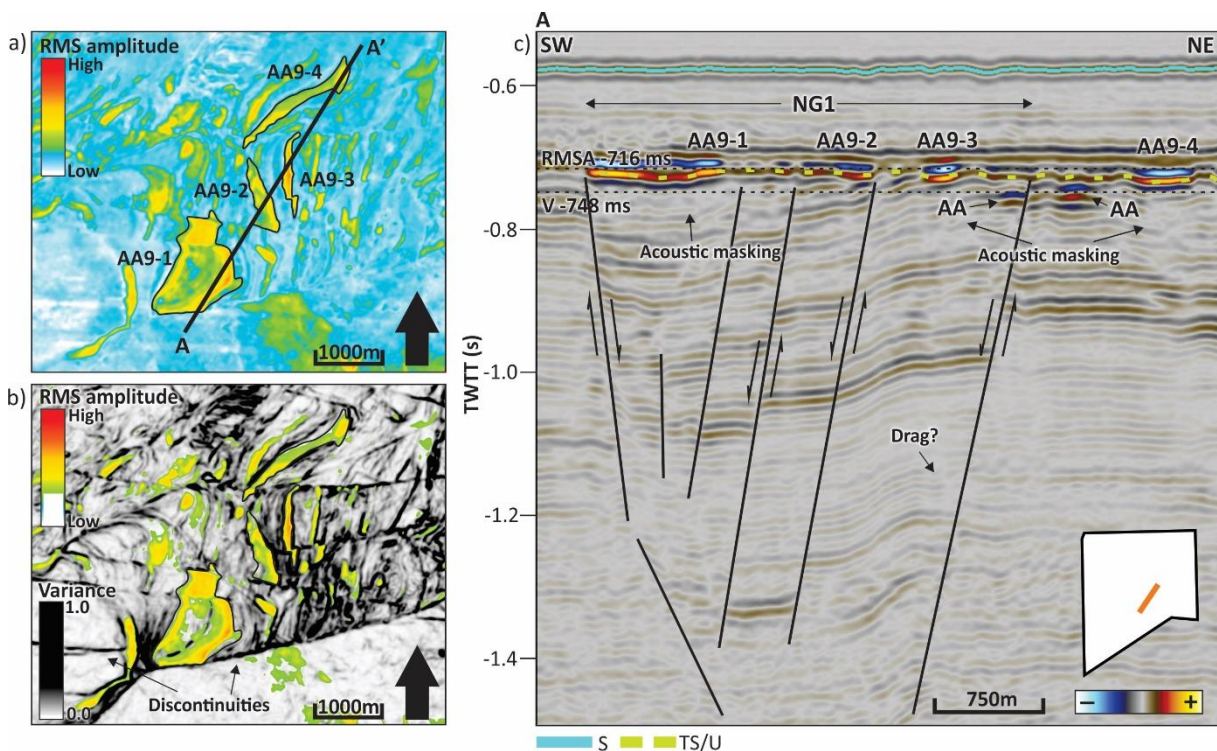


Figure 5.21: a) RMS amplitude (RMSA) time slice showing the extent and amplitude variation of AA9 in the DG12M1 dataset, at -716 ms. Note the other amplitude anomalies located in close proximity to those included in AA9. b) RMSA time slice (-716 ms, adjusted opacity) superimposed on variance (V) time slice (-748 ms) showing the relationship between amplitude anomalies and structural trends. c) Seismic section (location shown in fig. 5.12b and in the dataset outline) showing AA9 located along the Top Snadd/URU horizon and associated areas of acoustic masking. Note their relationship to several faults.

5.3.1.3 Amplitude anomalies within Cenozoic strata

5.3.1.3.1 Amplitude Anomaly 10 (AA10)

AA10 encompasses an area of several smaller anomalies (annotated AA10-1 to AA10-3 in fig. 5.22), located in the central parts of the ST10020 dataset (fig. 5.12c). The anomalies are located within the Nordland Group, approximately 45 ms below the seabed and 20-30 ms above the Top Snadd/URU horizon. Amplitudes appear to be reversed with respect to the seabed, and decrease laterally. AA10-1, AA10-2 and AA10-3 have areal extents of approximately 0.14 km², 0.14 km² and 0.25 km², respectively. All of the anomalies lie directly above or in close proximity to two faults oriented from W to E, extending from the Top Snadd/URU horizon down to approximately -1200 ms. Based on the seismic section in fig. 5.22c, no prolific source rock seems to be penetrated by the faults.

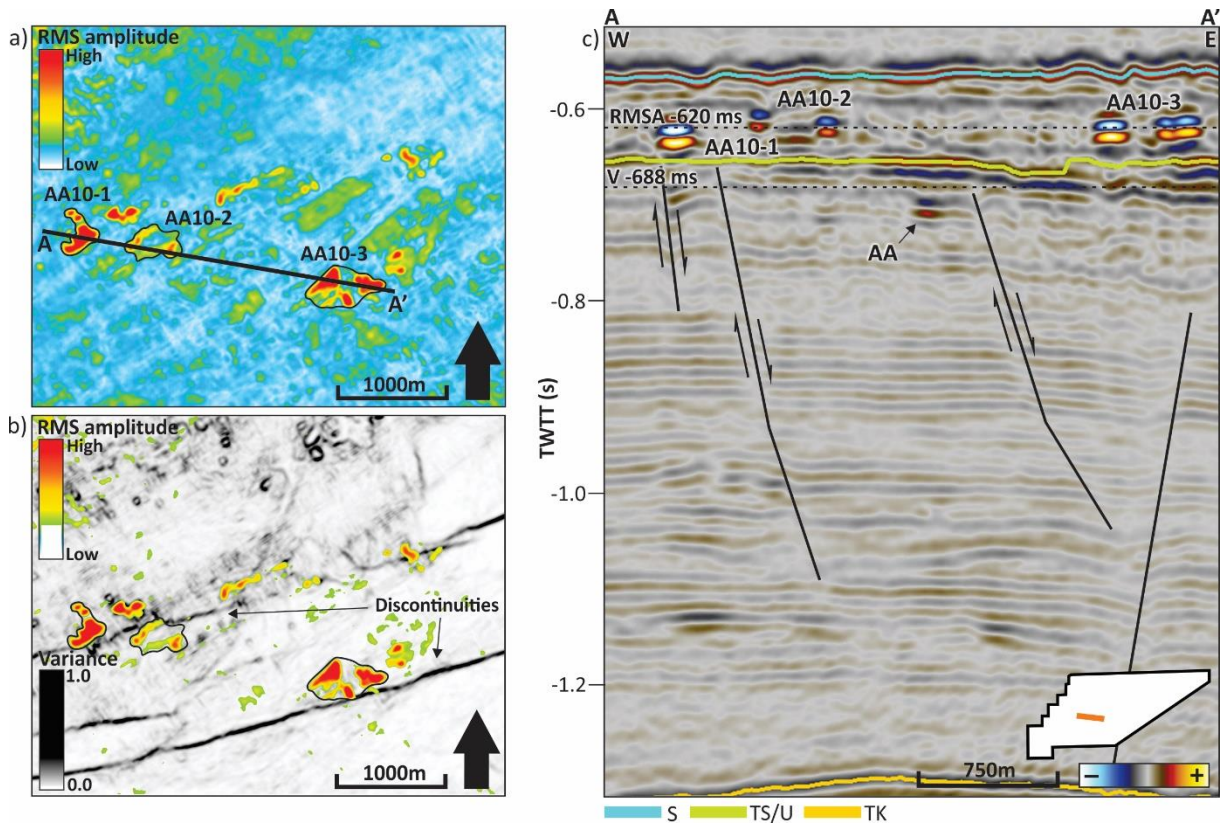


Figure 5.22: a) RMS amplitude (RMSA) time slice showing the extent and amplitude variations of AA10 in the ST10020 dataset, at -620 ms. b) RMSA time slice (-620 ms, adjusted opacity) superimposed on variance (V) time slice (-688 ms), showing the relationship between amplitude anomalies and structural trends. c) Seismic section (location shown in fig. 5.12c and in the dataset outline), showing the location of AA10 along the Top Snadd/URU horizon. Note the faults terminating against the Top Snadd/URU horizon and the deeper amplitude anomaly in close proximity to one of them.

5.3.2 Larger zones of acoustic masking

Despite the large number of amplitude anomalies identified in the study area as a whole, associated zones of acoustic masking are generally small and local. However, three larger, vertically extensive zones of acoustic masking or disturbance are observed in the study area, one of which is associated with NG4, the other two associated with NG6 (fig. 5.23 and 5.24). The zones of acoustic disturbance, hereinafter abbreviated to DZs (disturbance zones), are characterized by chaotic reflections of generally low amplitudes, disrupting otherwise continuous or semi-continuous reflectors. All of the disturbance zones identified have seismic expressions similar to those of gas chimneys, as described by Løseth et al. (2009), but only two of them (DZ2 and 3) are interpreted as potential gas chimneys. Similar features, though more clearly defined by e.g. high-amplitude upper terminations, have been identified and interpreted as gas chimneys by e.g. Vadakkepuliyaambatta et al. (2013) and Rajan et al. (2013). The current depth of the gas chimneys and relationship to larger fault zones suggest deeply-rooted fluid flow.

DZ1 is located to the NW in the ST10020 dataset, directly below AA5 and in close proximity to NG6. Measured on the seismic section in fig. 5.23, the zone extends 1600 ms vertically, from below the Top Røye horizon and all the way up to the Top Snadd/URU horizon. The true areal extent of DZ1 is difficult to determine due to lack of 3D data towards the NW. However, 2D lines between the DG12M1 and ST10020 datasets reveal that DZ1 in fact is a narrow zone of acoustic masking located along the full extent of the SE delineating fault of NG6. DZ2 and DZ3 (fig. 5.24) are located in the central parts of the study area, approximately 11 km apart. DZ2 is located directly below NG6, extending 1500 ms vertically. Several 2D lines between the ST10020 and DG12M1 datasets reveal that the zone is present below the entire SW-NE extent of NG6, mainly occurring within Carboniferous/Permian strata. The zone is characterized by a distinct obelisk shape, with possible push-down effects and local amplitude increases. DZ2 has no distinct upper termination, possibly caused by the faults of NG6. DZ3 is associated with NG4, extending 700 ms vertically, also occurring within Carboniferous/Permian strata. In contrast to DZ2 and NG6, the zone is located laterally adjacent to NG4, and not directly below. No apparent push-down effects are recorded, and the only amplitude anomalies identified occur along the NW delineating fault of NG4, within the Snadd Formation. No distinct upper termination is recorded for DZ3.

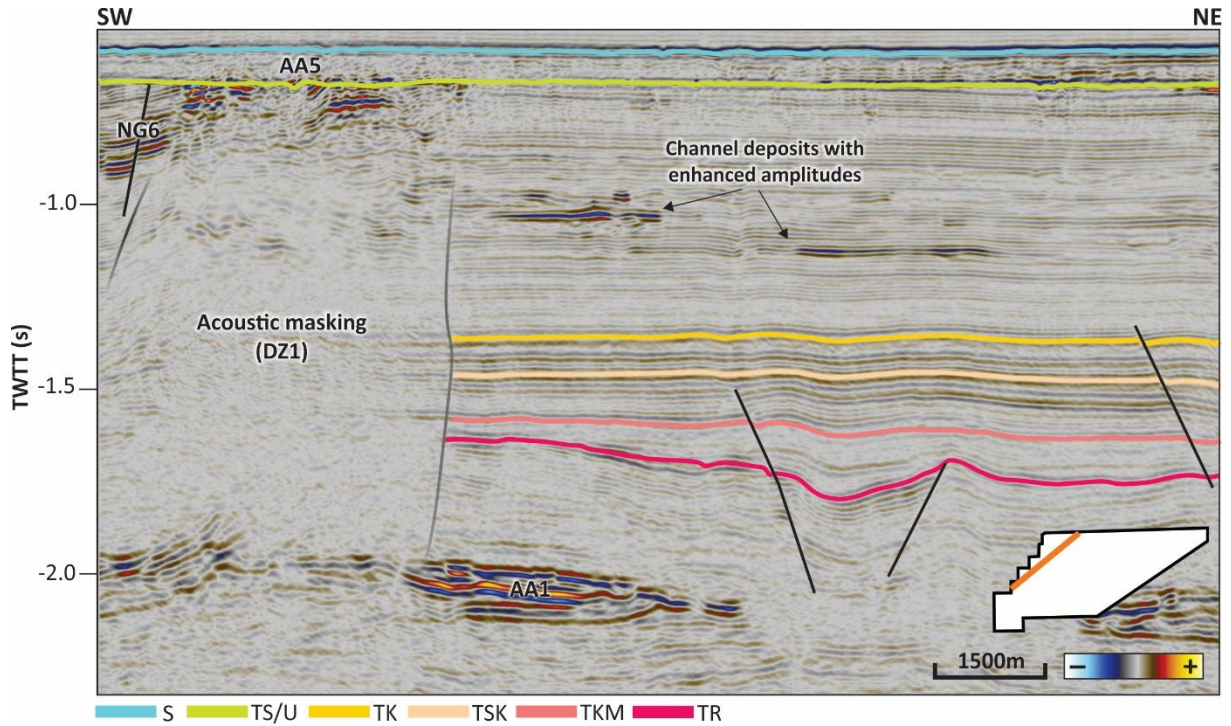


Figure 5.23: Seismic section (location indicated in dataset outline), showing a larger zone of acoustic disturbance in close proximity to NG6, below AA5. Note the chaotic reflectors of low amplitudes within DZ1.

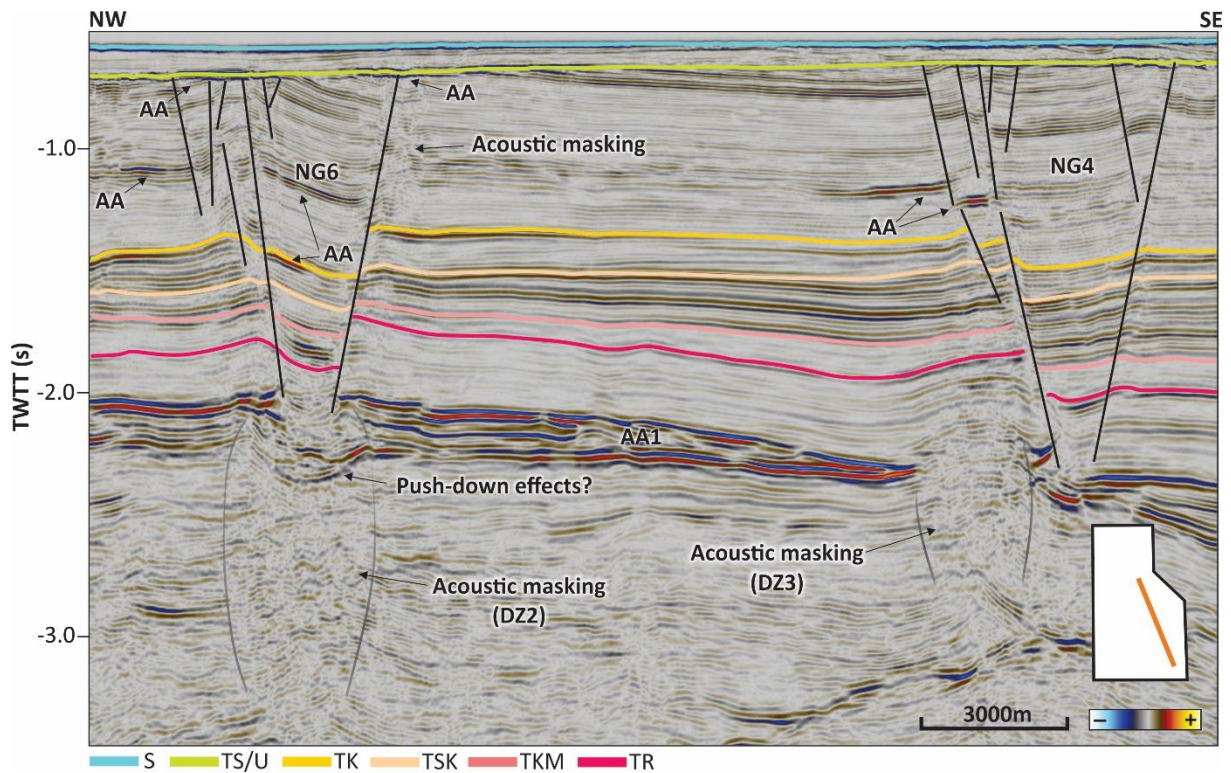


Figure 5.24: Seismic section (NBR09-242200, location indicated in study area outline), showing two larger zones of acoustic disturbance below NG6 (left) and close to NG4 (right).

5.3.3 Morphological features on the seabed

5.3.3.1 Elongated depressions

Common features observed on the seabed surface generated based on 3D seismic are numerous elongated and mostly randomly oriented, both linear and curvilinear depressions (fig. 5.25a-c). These features are known as plough and scour marks, originating from icebergs scouring the seabed during the Late Weichselian deglaciation of the Fennoscandian ice sheet (Andreassen, Rafaelsen, et al., 2007). As no clear trends have been identified, the orientation of the scour and plough marks appears arbitrary, and several of them intersect and cut each other off. Furthermore, some of these features reach up to 8.9 km in length, and the scour depths range from 8 to 25 ms, corresponding to 6-19 m ($V_p = 1500$ m/s, fig. 5.25 and 5.26).

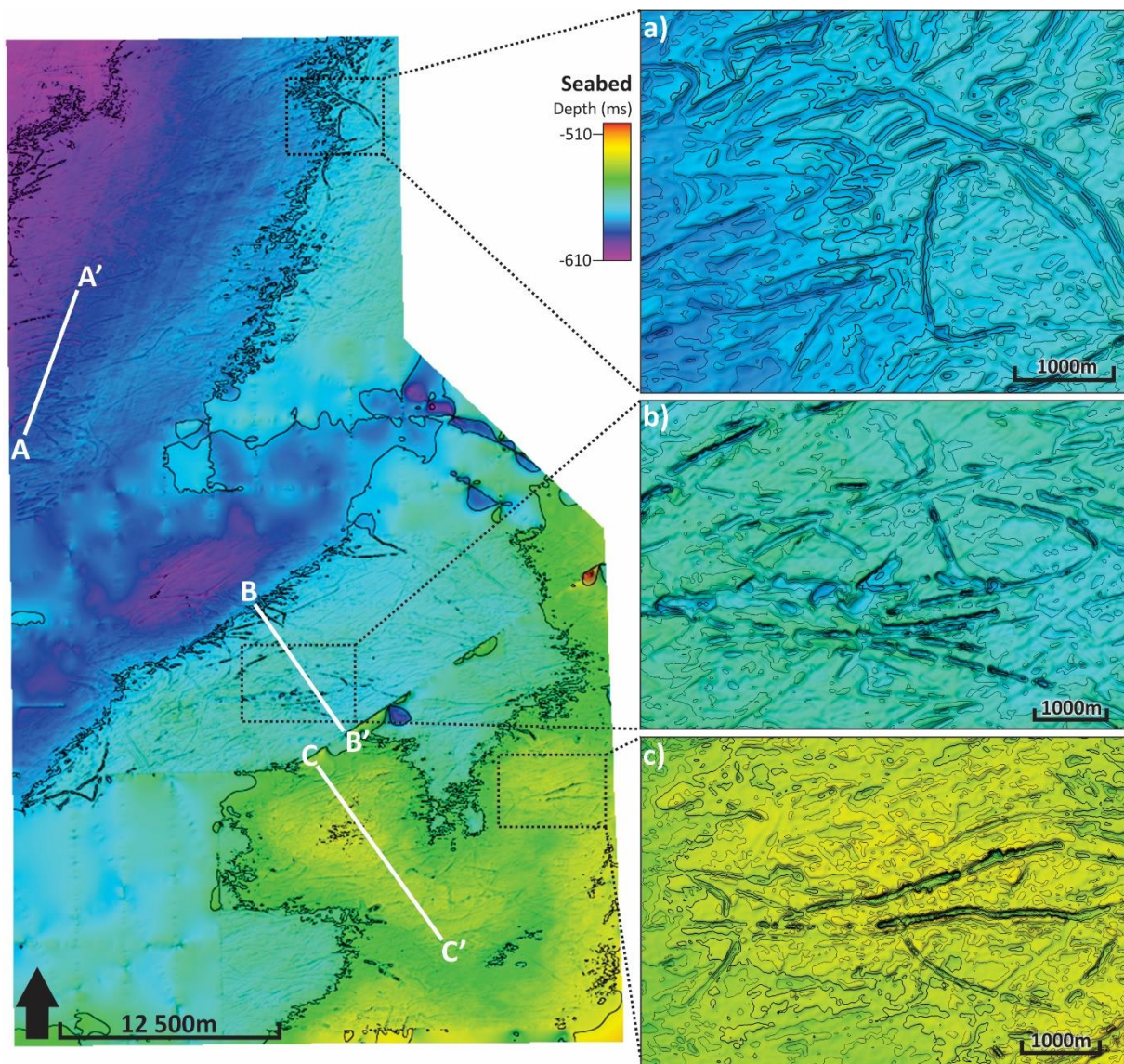


Figure 5.25: Overview of the seabed surface. Vertical exaggeration (VE): 10. Contour increment (CI): 25. A-A', B-B' and C-C' correspond to seismic sections in fig. 5.26. a) Ploughmarks from the DG12M1 dataset. CI: 2.5. b) Ploughmarks from the ST10020 dataset. CI: 5. c) Ploughmarks from the GDF1201M13 dataset. CI: 2.5.

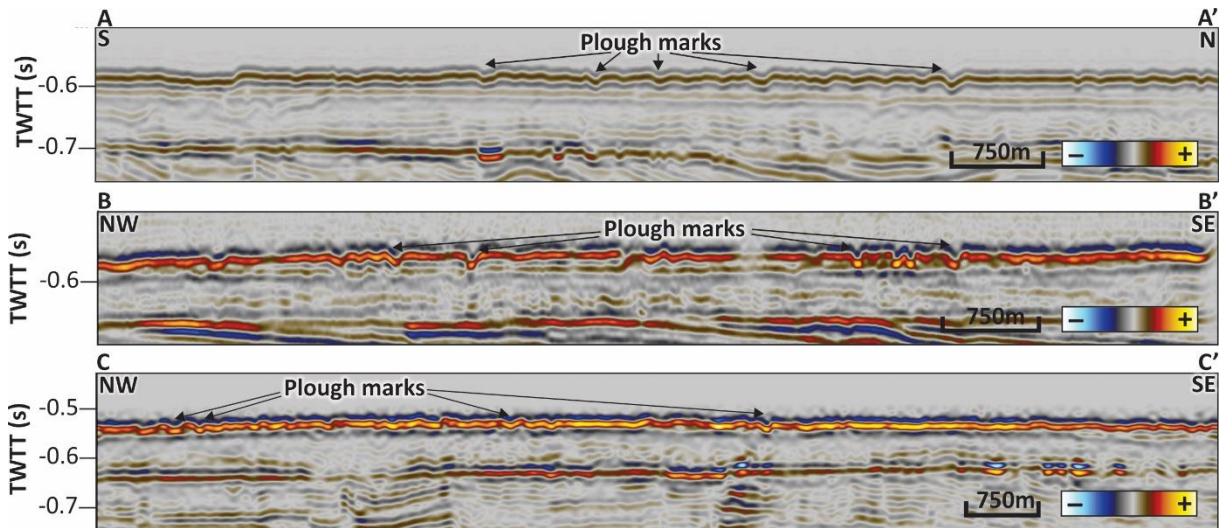


Figure 5.26: Seismic sections (location indicated in fig. 5.25) showing the seabed morphology, with several depressions originating from icebergs (plough and scourmarks).

5.3.3.2 Exposed circular depressions

As previously mentioned, the seabed is largely affected by plough and scour marks originating from the deglaciation in Late Weichselian. The presence and density of such marks largely conceal other potential geomorphological features, and the mapping of these has thus been more challenging. However, several sub-circular to circular depressions are identified on the seabed, hereinafter referred to as exposed depressions (EDs, fig. 5.27).

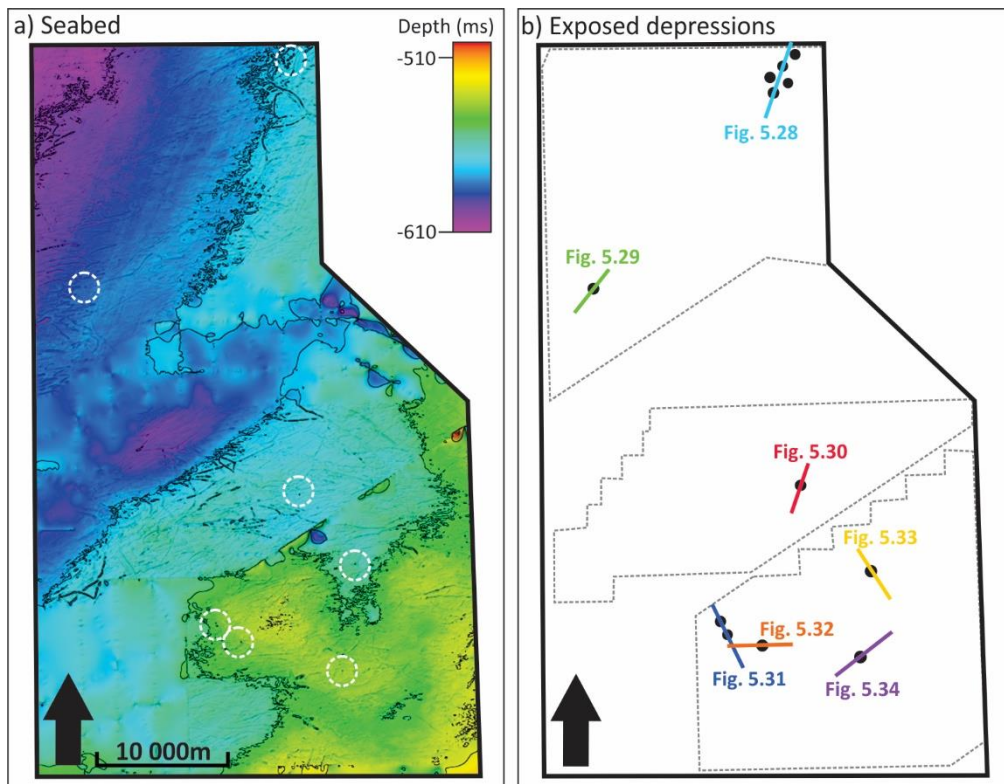


Figure 5.27: a) Seabed surface with exposed depressions indicated by white circles. Vertical exaggeration (VE): 10. b) Approximate location of exposed depressions in the 3D datasets and position of seismic section in c) in figs. 5.28-5.34. The size of depressions is not to scale.

Sub-circular and circular depressions on the seabed are common features of the SW Barents Sea seabed, many of which have been interpreted as pockmarks indicative of fluid expulsion (e.g. Chand et al. (2012), Pau et al. (2014) and Tasianan et al. (2018)). The exposed depressions identified may have the same origin, but lack of seismic evidence to support this interpretation (e.g. acoustic pipes, push-down effects) possibly suggests a different mechanism of formation rather than fluid expulsion, and will be further discussed in section 6.4.2.

5.3.3.2.1 Exposed depression 1-6 (ED1-6)

Six sub-circular to circular depressions are identified in the DG12M1 dataset (fig. 5.28 and 5.29), of which five are located to the NE (ED1-5) and a single depression is located to the SW (ED6).

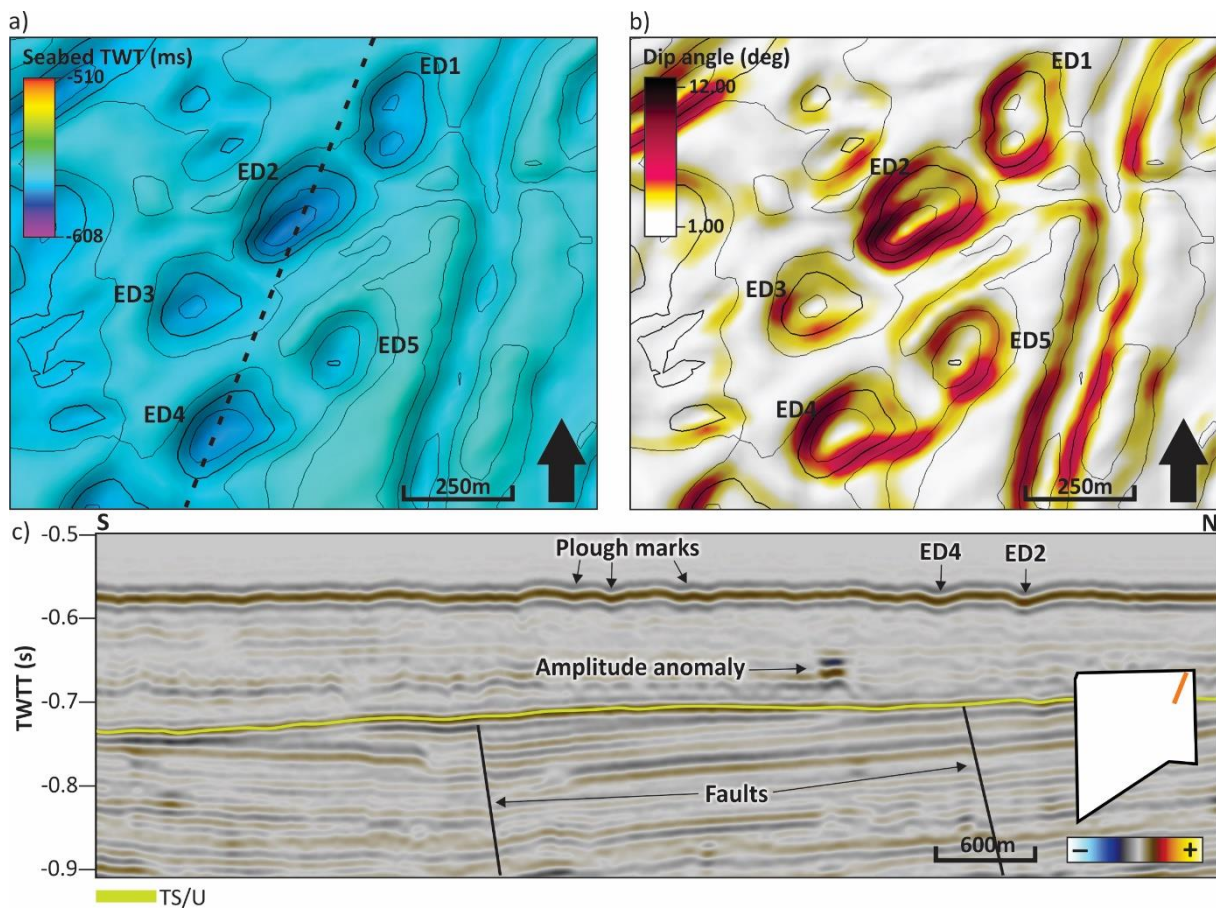


Figure 5.28: a) ED1-5 located on the seabed in the DG12M1 dataset, VE: 10. Black dotted line indicates the orientation of the seismic section in c). b) Dip angle map showing increasing dips towards the center of each depression, and then a general flattening in c). c) Seismic section (location shown in fig. 5.27 and in the dataset outline), showing ED4 and ED2 on the seabed, and adjacent plough marks. Note the faults terminating against the Top Snadd/URU horizon.

The depressions to the NE (ED1-5, fig. 5.28) occur in a cluster, and are surrounded by several plough or scour marks. The long axes of the depressions range from 242 to 319 m, and the depth ranges from 12 to 18 ms, corresponding to 9-13.5 m ($V_p = 1500$ m/s). The dip angle of the depressions ranges from 1° - 9° and all of them appear to flatten towards their center. The

distance between the depressions ranges from 27 to 73 m. Based on the seismic section in fig. 5.28c, a single Triassic fault is identified just below the depressions, terminating against the Top Snadd/URU horizon. The closest amplitude anomaly is a small anomaly occurring within the Nordland Group, located to the S of the depressions.

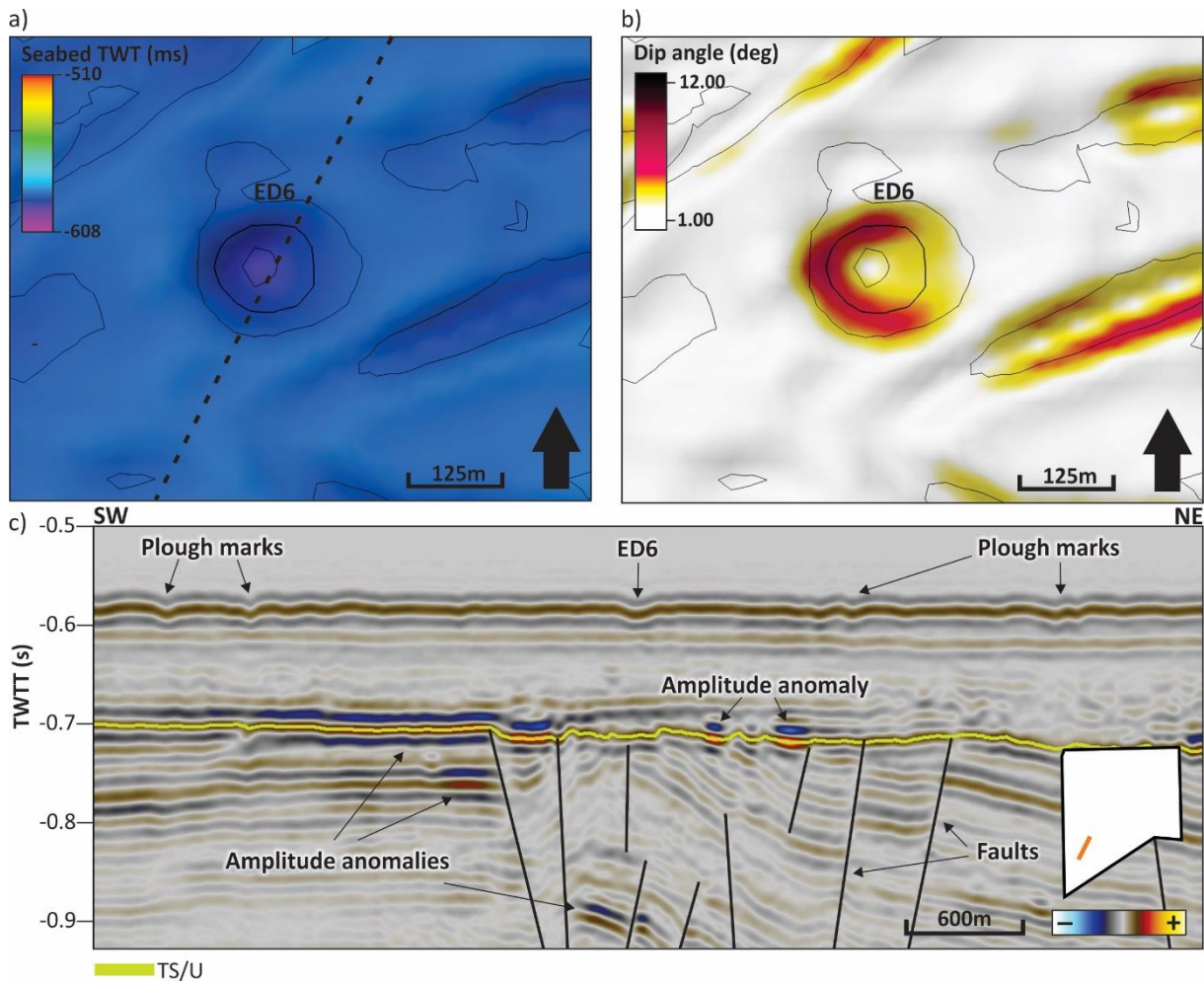


Figure 5.29: a) ED6 located on the seabed in the DG12M1 dataset, VE: 10. Black dotted line indicates the orientation of seismic section in c). b) Dip angle map showing increasing dips towards the center of ED6, and subsequent flattening. c) Seismic section (location indicated in fig. 5.27 and in the dataset outline) showing ED6 on the seabed. Note the location of several faults terminating against the Top Snadd/URU horizon, directly below the depression, and the associated amplitude anomaly.

The single depression to the SW is annotated ED6 in fig. 5.29 and occurs alone in an area of extensive reworking by icebergs. The long and short axis of the depression measures to 204 and 194 m, respectively. The depth of the depression is 17 ms, corresponding to approximately 12.8 m ($V_p = 1500$ m/s), and the dip angle ranges from 1° to 6° , with a decreasing dip towards its center. Depressions of similar size and character are not observed in relation to the depression, but an area of what appears to be somewhat smaller circular depressions is located approximately 2.5 km towards E. The depression is located directly above one of the larger grabens in the area (NG1), extending from W to E, of which all faults terminate against the Top

Snadd/URU horizon, and several of them extend down to below -2000 ms. Furthermore, the depression is located above an amplitude anomaly possibly associated with AA9.

5.3.3.2.2 Exposed depression 7 (ED7)

Only one circular depression (annotated ED7 in fig. 5.30) is identified to the E in the ST10020 dataset. The depression occurs within a plough mark with a large lateral extent (approximately 8.9 km), and the long and short axis of the depression measures to 147 and 122 m, respectively. Unlike the previously described depressions, the dip angle of ED7 ranges from 5° to 23°, thus constituting one of the steepest depressions identified. There are also no indications of flattening towards the center of the depression. The depth of ED7 is approximately 28 ms, corresponding to 21 m ($V_p = 1500$ m/s). In contrast to the other depressions, no faults or amplitude anomalies are identified in close proximity to the depression.

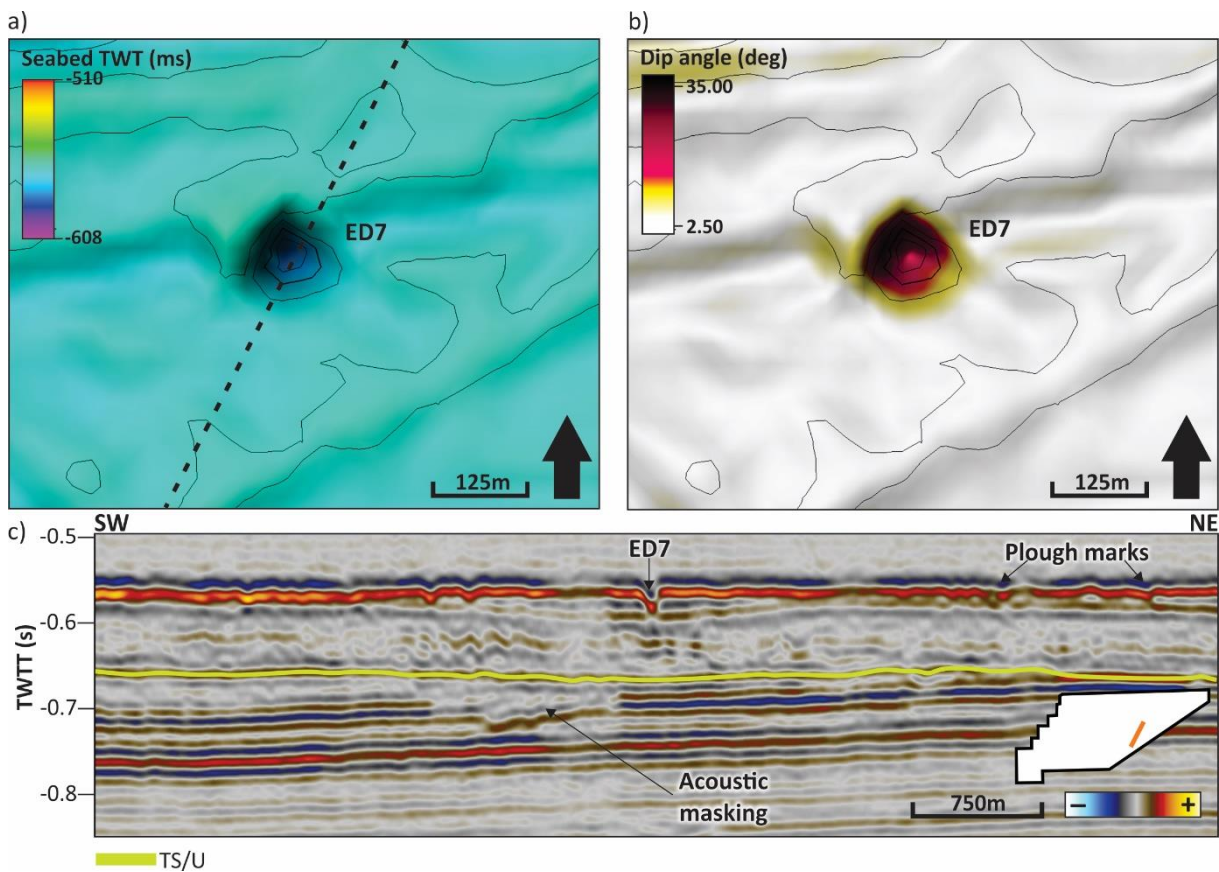


Figure 5.30: a) ED7 located on the seabed in the ST10020 dataset, VE: 10. Black dotted line indicates the orientation of the seismic section in c). b) Dip angle map showing increasing dips towards the center of the depression. c) Seismic section (location shown in fig. 5.27 and in the dataset outline) showing ED7 on the seabed, and adjacent plough marks. No faults have been identified in close proximity to the depression, but an area of acoustic masking is located towards the SW, occurring below the Top Snadd/URU horizon.

5.3.3.2.3 Exposed depression 8-12 (ED8-12)

Five sub-circular to circular depressions are identified in the GDF1201M13 dataset (figs. 5.31 – 5.34). ED8 and 9 (fig. 5.31) are located towards the NW and 104 m apart, of which the long

axes of the depressions measure to 110 and 160 m, respectively. The depth of ED8 and 9 is approximately 20.5 and 23 ms, corresponding to 15.4 and 17.3 m ($V_p = 1500$ m/s). The dip angle of the depressions ranges from 2.5° to 15° , and ED9 appears to flatten towards its center. While ED8 appears symmetric, ED9 is characterized by an asymmetric morphological expression. ED8 and 9 are located in an area of which Permian-Triassic faults terminating against the Top Snadd/URU horizon extend down to below -2000 ms. The only amplitude anomaly identified in the area occurs approximately 2 km towards the SE of the depressions.

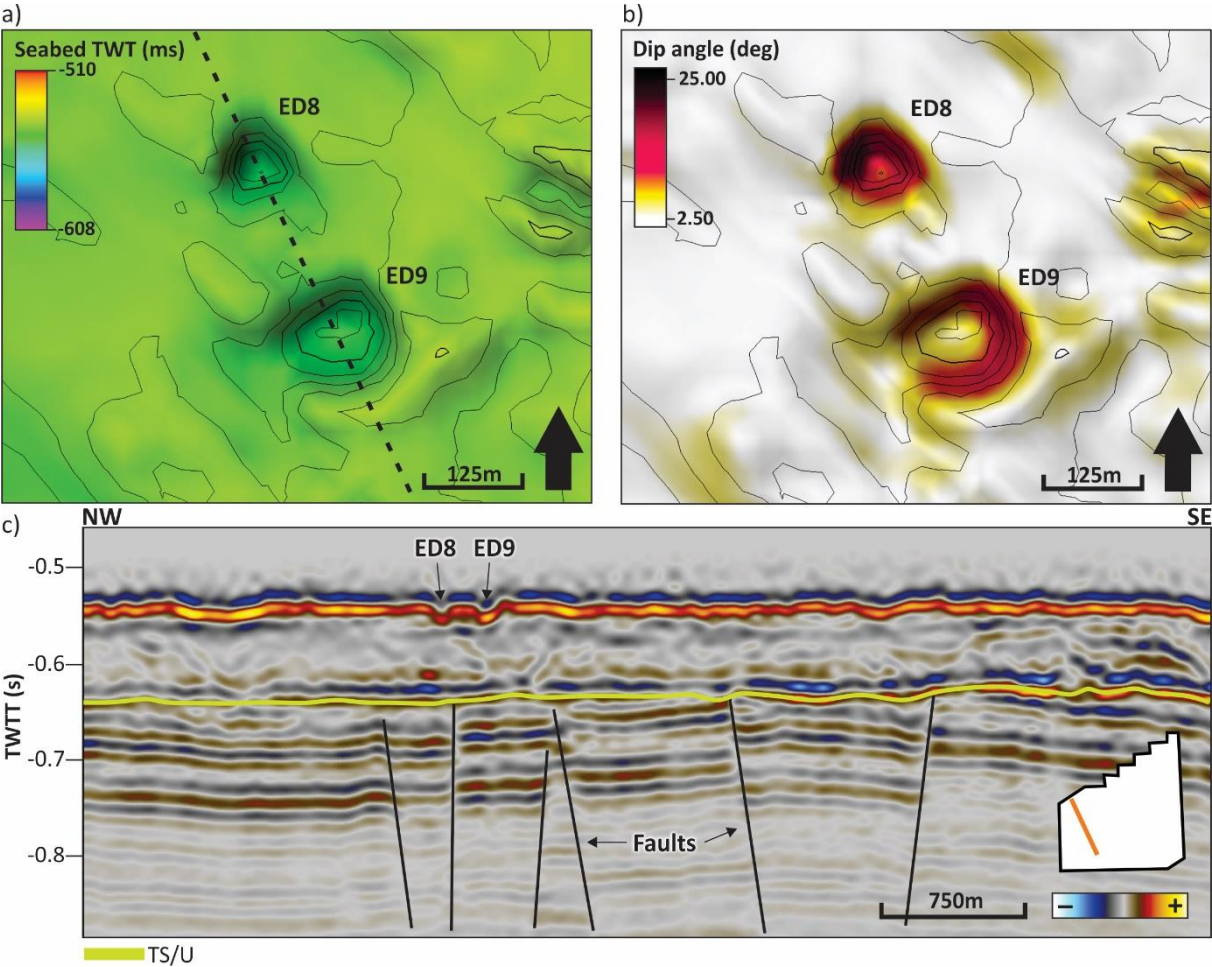


Figure 5.31: a) ED8 and 9 located on the seabed in the GDF1201M13 dataset, VE: 10. Black dotted line indicates the orientation of the seismic section in c). b) Dip angle map showing increasing dips towards the center of the depression, and the apparent flattening of ED9. c) Seismic section (location shown in fig. 5.27 and in the dataset outline) showing ED8 and 9 on the seabed. Note the faults terminating against the Top Snadd/URU horizon below the depressions.

ED10 (fig. 5.32) is located approximately 2 km to the SE of ED8 and 9, and is similar to ED9 characterized by an asymmetric morphological expression. The long and short axis of the depression measure to 178 m and 107 m, and the depth of ED6 is approximately 26 ms, corresponding to 19.5 m ($V_p = 1500$ m/s). The dip angle of the depression ranges from 2.5° to 21° and it appears to flatten towards its center. In contrast to the other depressions, ED10 also encompasses an elevated rim extending approximately 10 ms (7.5 m) above the seabed.

Furthermore, the depression is located in close proximity to NG4 extending across the entire dataset, of which the faults terminating against the Top Snadd/URU horizon extend down to below approximately -1800 ms. ED10 is located directly above an amplitude anomaly occurring along the Top Snadd/URU horizon.

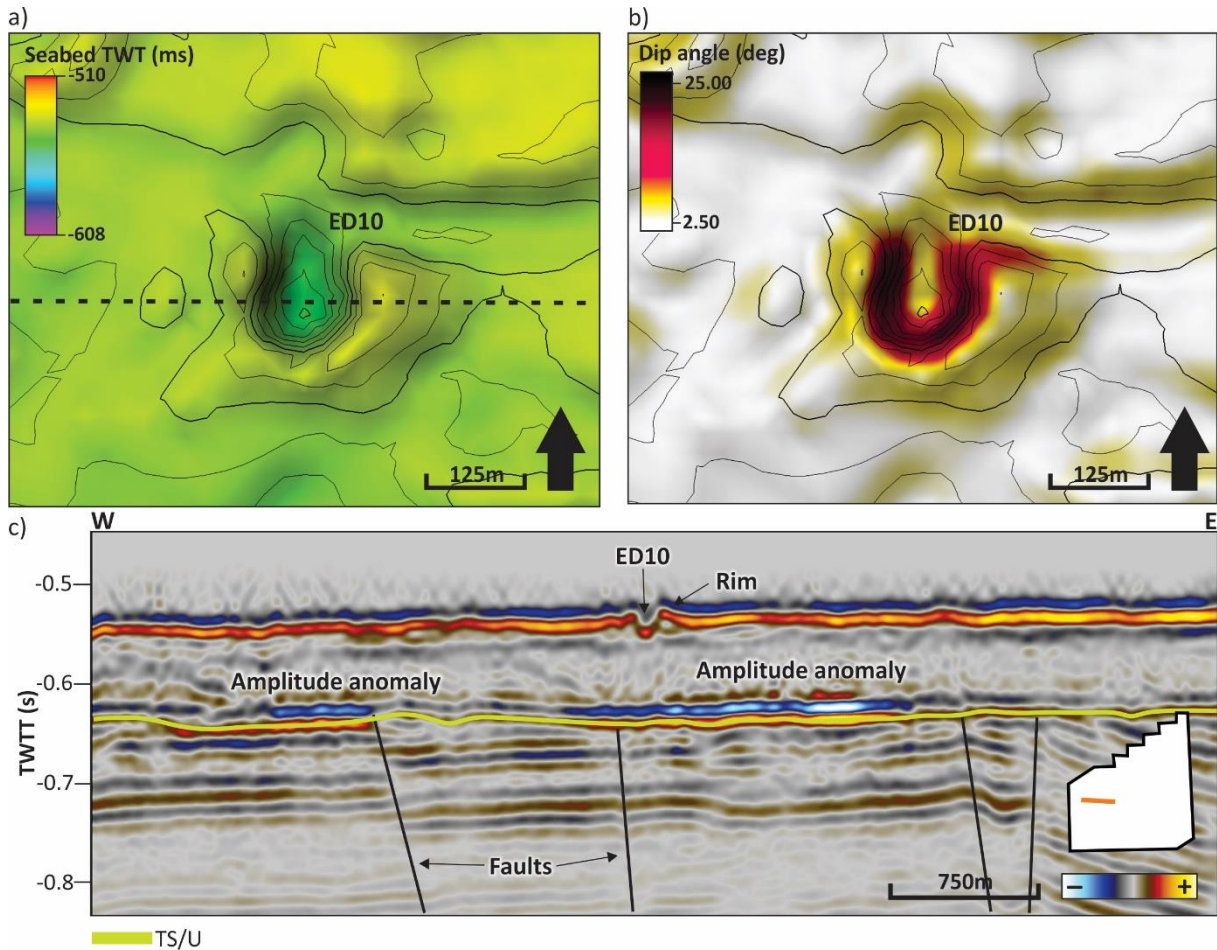


Figure 5.32: a) ED10 located on the seabed in the GDF1201M13 dataset, VE: 10. Black dotted line indicates the orientation of the seismic section in c). b) Dip angle map showing increasing dips towards the center of the depression, and the elevated rim surrounding it. c) Seismic section (location shown in fig. 5.27 and in the dataset outline) showing ED10 on the seabed, and the associated elevated rim. Note the amplitude anomalies occurring along the Top Snadd/URU horizon and faults terminating below the depression.

ED11 (fig. 5.33) is located to the N in the dataset, occurring alone in an area greatly affected by icebergs. The long and short axis of the depression measure to 169 m and 110 m, respectively. The depth of the depression is approximately 21 ms (15.8 m, $V_p = 1500$ m/s), and dip angle ranges from 3° to 24° . Similar to ED10, ED11 is located directly above the laterally extensive graben (NG4) and associated faults, but no amplitude anomalies are identified in close proximity to the depression.

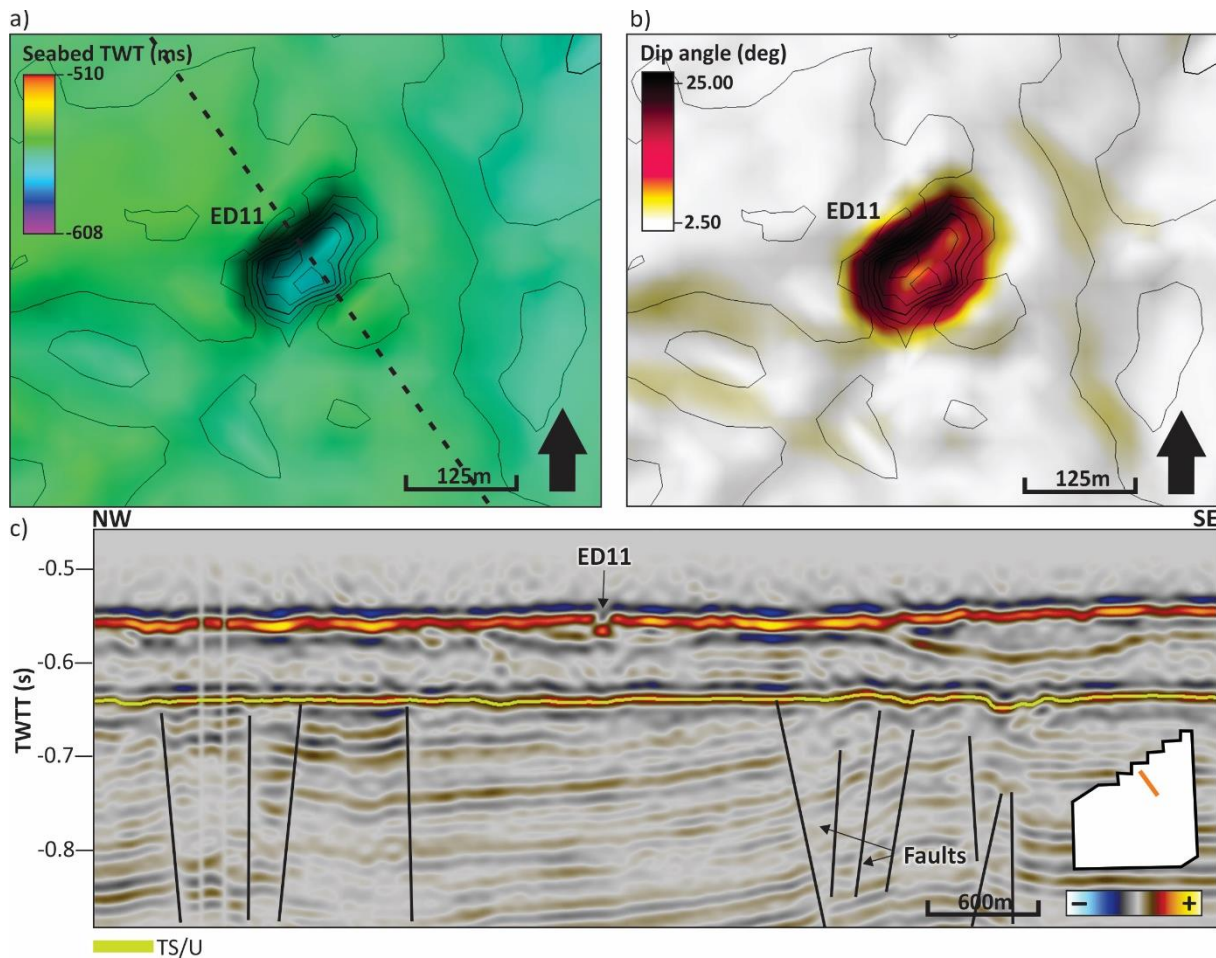


Figure 5.33: a) ED11 located on the seabed in the GDF1201M13 dataset, VE: 10. Black dotted line indicates the orientation of the seismic section in c). b) Dip angle map showing increasing dips towards the center of the depression. c) Seismic section (location shown in fig. 5.27 and in the dataset outline), showing ED11 on the seabed, and underlying faults terminating against the Top Snadd/URU horizon.

ED12 (fig. 5.34) is located in the central parts of the dataset, of which the long and short axis of the depression measure to 147 m and 122 m, respectively. The depth of the depression is approximately 28 ms (21 m, $V_p = 1500$ m/s) and the dip angle ranges from 5° to 23° . As seen from the seismic section in fig. 5.34c, several Triassic faults terminating against the Top Snadd/URU horizon can be observed, as well as amplitude anomalies located along the same horizon.

5.3.3.3 Paleo-depressions

In addition to depressions exposed on the seabed, variance volumes and time slices reveal circular features of similar character occurring below the seabed, mainly within the Nordland Group and down to the Top Snadd/URU horizon. These features are subsequently referred to as paleo-depressions (PDs). Despite the large number of PDs, especially in the DG12M1 dataset, only a selection from the study area as a whole is described in detail. The location of the following figures, as well as the paleo-depressions identified, are summarized in fig. 5.35.

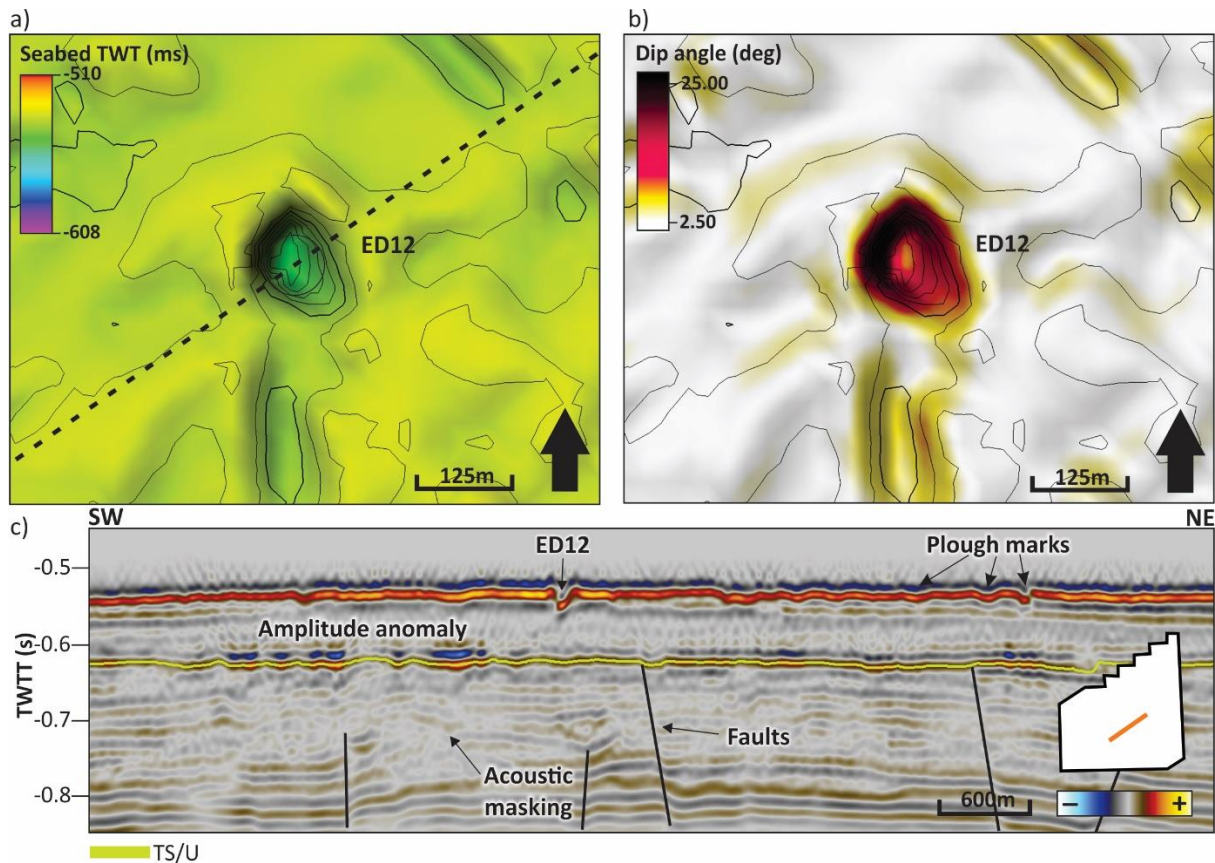


Figure 5.34: a) ED12 located on the seabed in the GDF1201M13 dataset, VE: 10. Black dotted line indicates the orientation of the seismic section in c). b) Dip angle map showing increasing dips towards the center of the depression. c) Seismic section (location shown in fig. 5.27 and in the dataset outline) showing ED12 on the seabed, and an amplitude anomaly along the Top Snadd/URU horizon. Note also the faults terminating against the same horizon.

The number of depressions indicated in fig. 5.35b only illustrates the differences between the datasets, and does not reflect the actual number of paleo-depressions in the study area. In contrast to the exposed depressions identified on the seabed, seismic evidence of vertical fluid migration is identified in relation to the paleo-depressions, thus supporting a theory of them being paleo-pockmarks formed as a result of fluid expulsion.

5.3.3.3.1 Paleo-depression 1-3 (PD1-3)

PD1-3 (fig. 5.36) are located towards the W in the DG12M1 dataset, occurring 41 m apart and approximately 40 ms below the seabed. The depths of the depressions are 16 ms and 18 ms, corresponding to 13.1 m and 14.8 m ($V_p = 1640$ m/s). The long axes of PD1 and 2 measure to 163 m and 147 m, whereas the short axes measure to 133 m and 80 m, respectively. PD3 is located approximately 3 km towards the SE from PD2, occurring approximately 28 ms below the seabed. The depression is approximately 33 ms deep (27 m), with a long and short axis measuring to 309 m and 195 m, respectively. In contrast to PD1 and 2, both an amplitude anomaly and several faults are identified below PD3. The amplitude anomaly correspond to

those observed in close proximity to AA9, and the faults are related to the graben structure extending from W to E in the dataset (NG1).

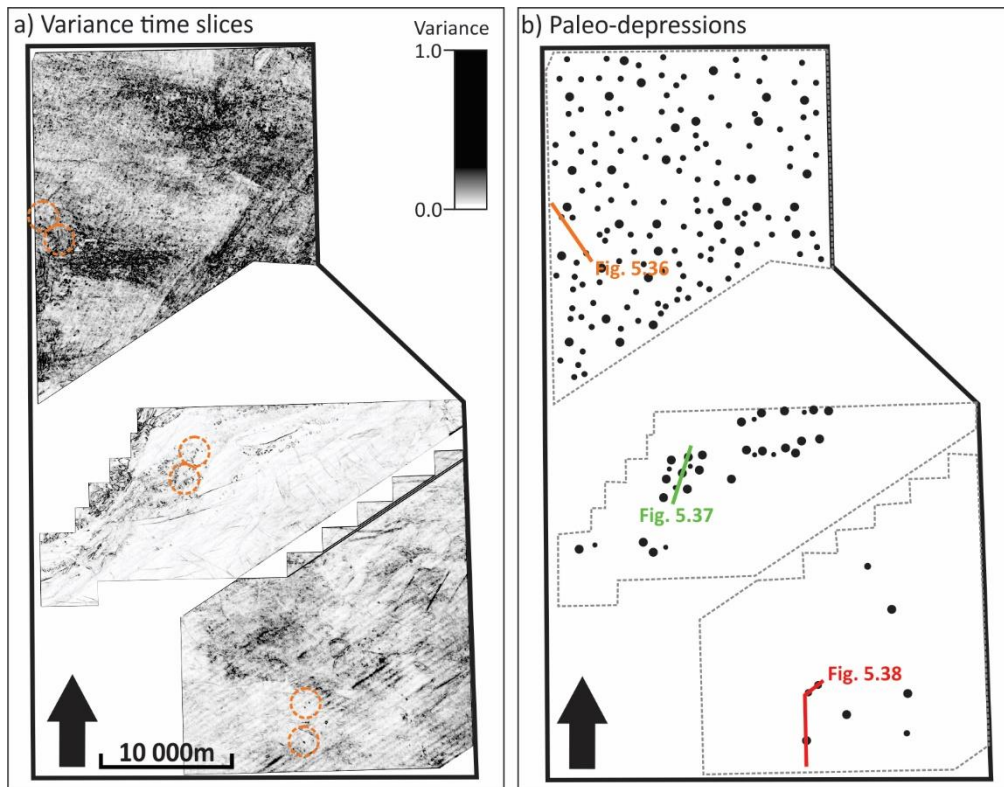


Figure 5.35: a) Variance time slices at -664 ms (DG12M1), -672 ms (ST10020) and -572 ms (GDF1201M13) showing paleo-depressions within the Nordland Group. b) Approximate location of paleo-depressions in the 3D datasets and seismic sections in b) in figs. 5.37-5.39. Note that the size of the paleo-depressions is not to scale.

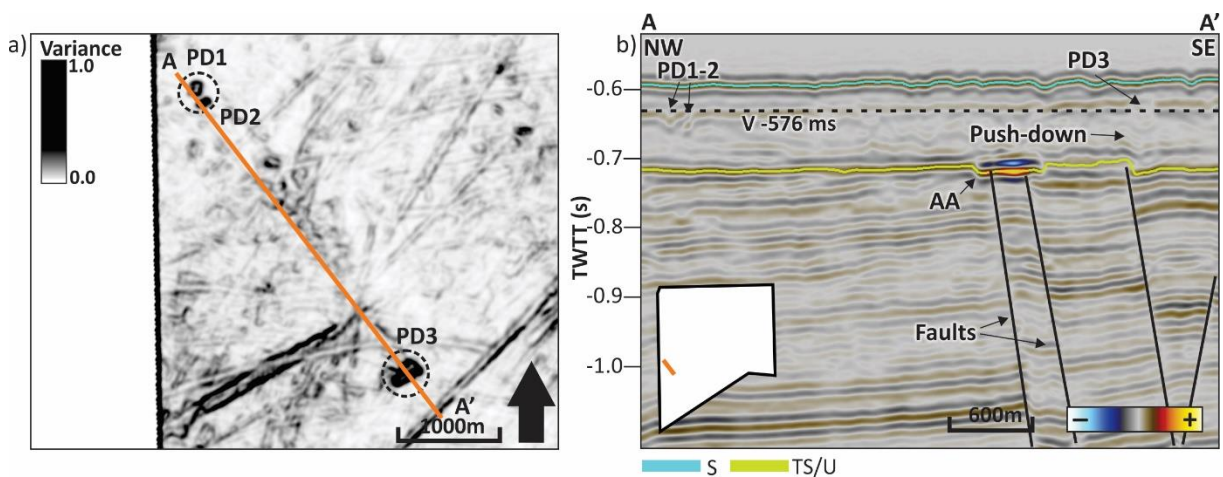


Figure 5.36: a) Variance (V) time slice (-576 ms) showing the location of PDI-3 in the DG12M1 dataset. b) Seismic section (location indicated in fig 5.35 and in the dataset outline) showing the location of PDI-3 within the Nordland Group. Note the amplitude anomaly and faults terminating against the Top Snadd/URU horizon, and the apparent push-down effects below PD3.

5.3.3.3.2 Paleo-depression 4-10 (PD4-10)

Several paleo-depressions are identified in the ST10020 dataset, and PD4-10 are located towards the NE in an area of several depressions (fig. 5.37). PD4-10 occur 83 to 94 ms below the seabed, with depths ranging from 9 to 16 ms, corresponding to 7.4 to 13.1 m ($V_p = 1640$ m/s). The long axes of the depressions range from 89 to 249 m, and short axes from 76 to 129 m. The distance between the depressions ranges from 24 to 230 m. PD4-10 are located in close proximity to AA6-2 and AA6-3, occurring at the same level along the Top Snadd/URU horizon, and amplitudes appear to increase laterally towards each individual depression. Several acoustic pipes with push-down effects can be identified below the amplitude anomalies and depressions, and the vertical extent of these pipes ranges from 26 to 260 ms (37.2 m to 372 m, $V_p = 2859$ m/s). Additionally, a Triassic fault extending from -800 ms to approximately -1300 ms is located directly below AA6-2.

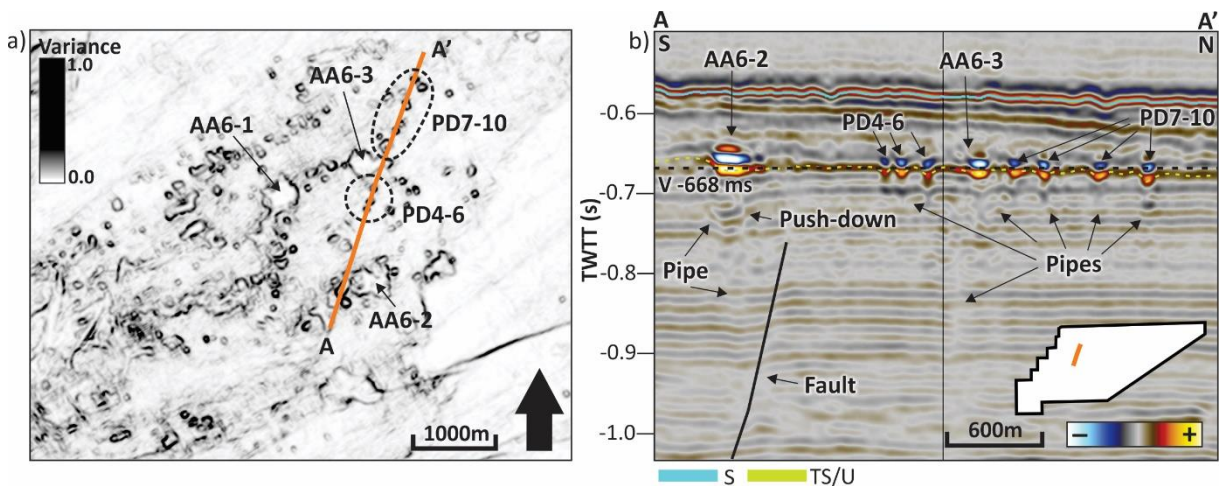


Figure 5.37: a) Variance (V) time slice (-668 ms) showing an area of several PDs located in close proximity to AA6 in the ST10020 dataset. Black circles indicate the location of PD4-10. b) Seismic section (location shown in fig. 5.35 and the dataset outline) showing PD4-10 occurring along the Top Snadd/URU horizon. Note the location of AA6-2 and AA6-3 in close proximity to the depressions, and the associated acoustic pipes and push-down effects. Note also the location of the fault just below the Top Snadd/URU horizon.

5.3.3.3.3 Paleo-depression 11-13 (PD11-13)

PD11-13 (fig. 5.38) is located towards the S in the GDF1201M13 dataset. PD11 is the southernmost depression, and is approximately 15 ms deep, corresponding to 12.3 m ($V_p = 1640$ m/s). The long and short axis of the depression measure to 176 m and 107 m, respectively. PD12 and 13 occur 385 m apart, located approximately 2.8 km away from PD11. The depth of PD12 and 13 are 22 ms and 18 ms, corresponding to 18.0 and 14.8 m ($V_p = 1640$ m/s). The long axes of the depressions measure to 124 m and 146 m, and short axes to 118 m and 99 m, respectively. The depressions are located in close proximity to amplitude anomalies associated with AA7, and above Triassic faults extending from the Top Snadd/URU horizon, down to approximately -1600 ms.

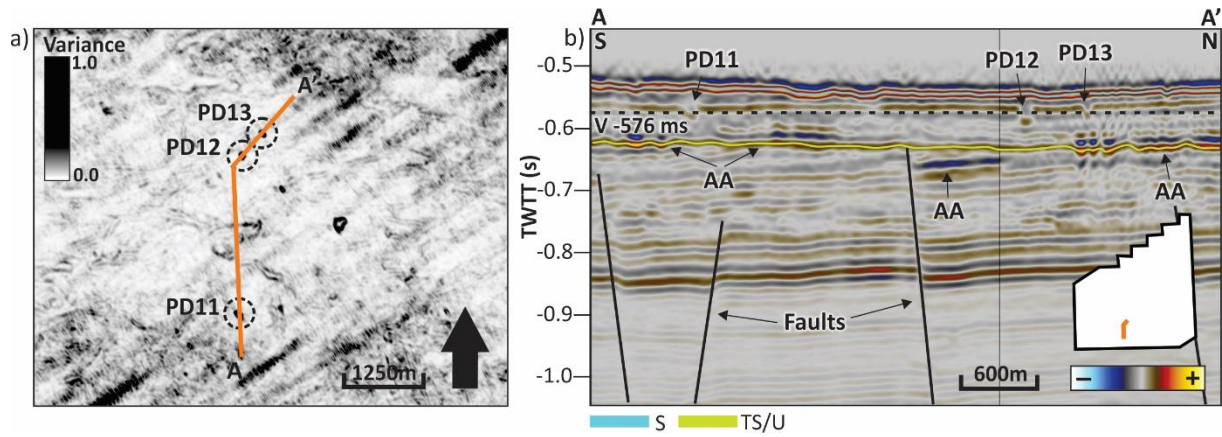


Figure 5.38: a) Variance (V) time slice (-576 ms) showing PD11-13 in the GDF1201M13 dataset. b) Seismic section (location indicated in fig. 5.35 and in the dataset outline) showing the location of PD11-13 within the Nordland Group, right below the seabed. Note the amplitude anomalies occurring along the Top Snadd/URU horizon and the faults located directly below the depressions.

6 Discussion

The following chapter discusses the structural trends in the area and the occurrence of fluid flow indications, and their potential relationship to one another. The discussion is based on presented theory and the results from the current study, and comparison to previous studies in the same field of research. The discussion is concluded with a conceptual model for the fluid flow processes in the study area, focusing on the relationship between structural elements and fluid flow indications, fluid origin, migration mechanisms and timing of fluid flow.

6.1 Faults and correlation with tectonic events

The diamond-shaped outline of the Loppa High was established in response to rifting and the break-up of Pangaea, during the Late Jurassic to Early Cretaceous (Gabrielsen et al., 1990; Henriksen, Ryseth, et al., 2011). The faults identified in the study area, in the interior of the Loppa High, largely reflects the tectonic regimes that have controlled the geological development of the SW Barents Sea. Reactivation of faults in response to several phases of subsidence and uplift have also resulted in inversion structures, especially along the western and southwestern margins of the high (e.g. Gabrielsen et al. (1993) and Indrevær et al. (2016)), but identification of these in the study area is beyond the scope of this thesis. The following discussion of faults thus focuses on the correlation between faults identified in the study area, with major tectonic events potentially responsible for their formation. The structural development of the study area is summarized in fig. 6.1.

6.1.1 Permian faults

The faults identified within Permian strata are limited to the ST10020 dataset, but this does not mean that they are only present in this area. Identification of deeper faults may have been limited by increasing depths of Permian strata, and hence poorer resolution, in both the northern and southern part of the study area. Thus, the number of faults and limited distribution of those identified may not be representative for the actual structural trend of Carboniferous-Permian strata. The limited vertical extent of the faults and the apparent draping between local highs and depressions indicates erosion of Permian deposits prior to Triassic deposition. The exact nature of the Late Permian – Triassic transition is still debated, and it has been suggested that the Permian-Triassic transition is either conformable, marking a condensed succession (Ehrenberg et al., 2010) or might represent Late Permian subaerial exposure (Ehrenberg et al., 1998; Stemmerik & Worsley, 2005).

Basements trends established during the Precambrian to Early Paleozoic orogenies have probably affected the subsequent structural development of the SW Barents Sea and the Loppa

High (Elvebakk et al., 2002; Gudlaugsson et al., 1998). The Permian faults identified have a clear SW-NE trend, possibly correlating to the Caledonian structural grain paralleling the Nordkapp, Hammerfest and Tromsø basins, and hinge faults developed during Carboniferous – Permian rifting (Elvebakk et al., 2002; Gudlaugsson et al., 1998). Late Paleozoic rifting affecting the Loppa High has been divided into three main rift phases (Early Carboniferous, Late Carboniferous and mid-late Permian), most likely related to an early attempt of propagation of the NE Atlantic rift system into the SW Barents Sea (Elvebakk et al., 2002; Gudlaugsson et al., 1998; Henriksen, Ryseth, et al., 2011). These rifting events resulted in a highly segmented shelf and gradual eastward tilting, faulting and differential subsidence of the Loppa High (Elvebakk et al., 2002). The Permian faults identified in the study area might thus be related to Late Paleozoic rifting events, largely controlled by the structural grain of the Barents Sea Caledonides (Gudlaugsson et al., 1998).

6.1.2 Permian-Triassic faults

The majority of faults extending from Permian into Triassic strata constitutes narrow grabens (NG1-6), and the larger-scale structural geology of the study area is characterized by narrow grabens/negative flower structures delineating rather extensive horst blocks. Large similarities between the narrow grabens identified in the study area suggests a relationship between the structures. According to Gabrielsen et al. (1990), a narrow graben on the Loppa High, possibly corresponding to NG6 in this thesis, constitutes the southern segment of the Hoop Fault Complex, which is located further to the NE of the study area. Furthermore, both Gabrielsen et al. (1993) and Indrevær et al. (2016) describes the Swaen Graben, located to the SE of the study area, as linking up with narrow grabens extending along the central Loppa High, possibly including NG4 described in this thesis. The narrow grabens characterizing the interior of the Loppa High might thus be genetically linked to both the Hoop Fault Complex in the NE and the Swaen Graben in the SE.

The Hoop Fault Complex represents an old zone of weakness, characterized by periods of reactivation in Middle Triassic, Late Jurassic to Cretaceous and possibly Paleogene/Neogene (Gabrielsen et al., 1990). The development of the extensional Swaen Graben was initiated during the Jurassic to Early Cretaceous, with a subsequent phase of strike-slip movements from the Late Cretaceous, possibly continuing into Early Paleogene (Omosanya et al., 2017). Both structures are thus related to the rifting episodes characterizing the Jurassic and Cretaceous – Paleocene periods, of which the North-Atlantic rift system extended into the SW Barents Sea and strike-slip movements and rifting between Norway and Greenland intensified (Faleide et

al., 1993; Smelror et al., 2009). Given a genetic link between these structures and the system of narrow grabens in the study area, the NGs identified were probably formed in response to rifting during the same time period. This theory is further substantiated by the large vertical extent of the fault zones, narrowing down the time of formation; faults extend from the Permian Røye Formation into the Triassic Snadd Formation, terminating against the Top Snadd/URU horizon.

6.1.3 Triassic faults

The Triassic faults identified have a limited vertical extent, almost exclusively occurring within the Snadd formation and terminating against the Top Snadd/URU horizon. As previously stated, the number of Triassic faults varies greatly throughout the study area, of which the highest number and density of faults are limited to the northern and southern parts. While the central region resembles a platform area, the northern and southern horst blocks appear to be down-faulted with respect to the central horst blocks, possibly facilitating and explaining the development and distribution of Triassic faults in the study area. Even though the Triassic faults appear to be normal faults, and some appear to constitute horst-and-graben structures, the plan-view fault pattern is so complex that it is difficult to determine the exact tectonic regime. However, according to Klausen et al. (2015), the post-depositional history of the Snadd Formation include Late Jurassic to Cretaceous rifting, corresponding to North-Atlantic rifting and the progressive opening of the Norwegian-Greenland Sea and possibly the development of the large-scale framework of the narrow grabens and extensive horsts. Thus, the faults are most likely extensional.

The Triassic faults show similarities to the first- and second-order faults in the Hammerfest Basin, described by Ostanin et al. (2012). The first-order faults dissect the Triassic to Early Eocene successions, whereas the second-order faults mainly dissect Triassic to Lower Cretaceous successions, not affecting Cenozoic strata (Ostanin et al., 2012). The faults identified in the study area terminates against URU, suggesting that the faults have initially extended into even younger strata and been active prior to Plio-Pleistocene glaciations. However, considering that the Upper Triassic to Miocene strata has been eroded on the Loppa High, the true extent and timing of the Triassic faults cannot be determined accurately. Based on the observations made by Ostanin et al. (2012) and descriptions from Klausen et al. (2015), the Triassic faults in the study area might have developed in response to tectonic readjustments during Jurassic-Cretaceous rifting related to the North-Atlantic rift system and the opening of the Norwegian-Greenland Sea. An alternative formation mechanism include tectonic readjustments and development of additional faults during Late Cenozoic uplift and erosion.

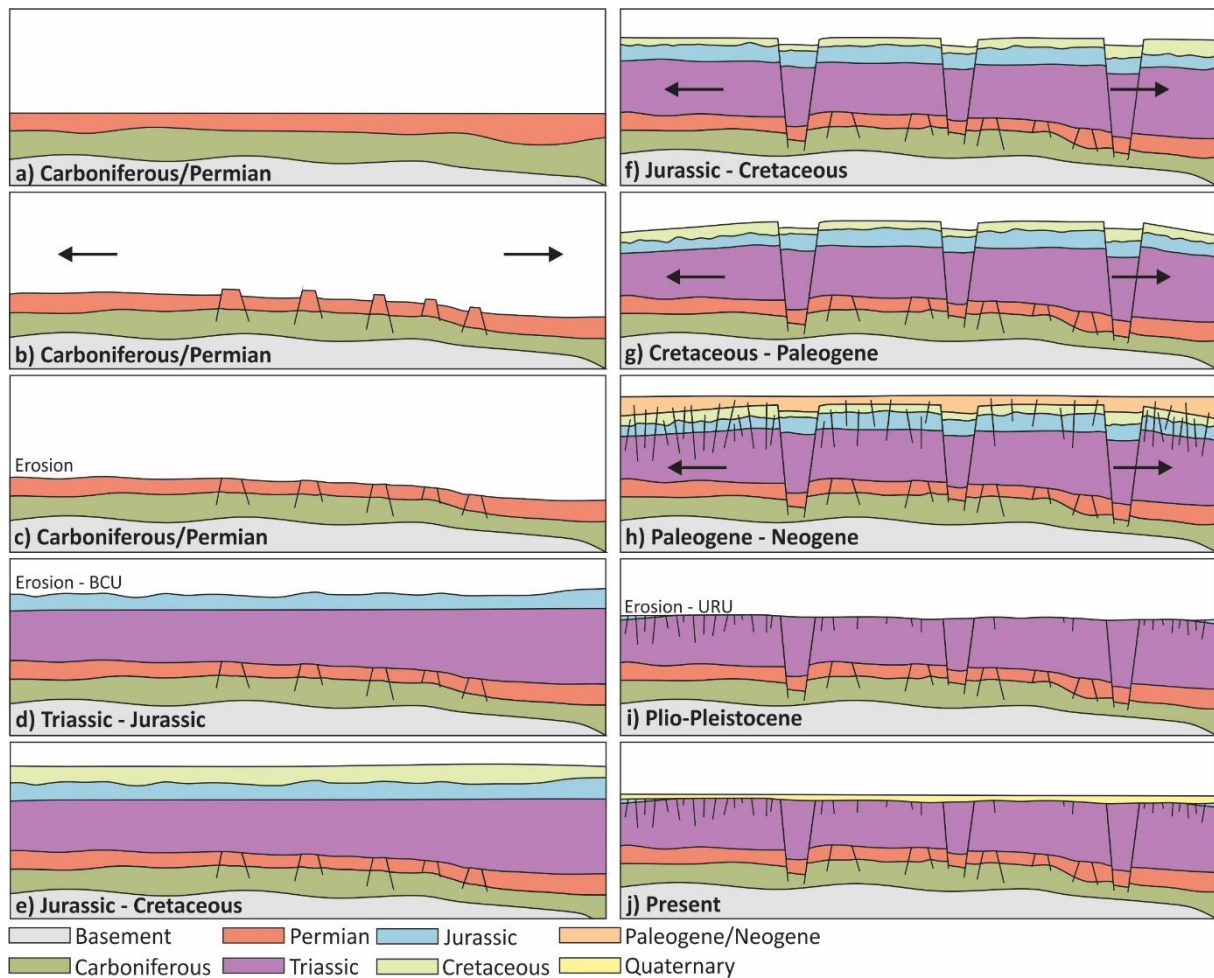


Figure 6.1: Conceptual model of the tectonic development of the study area, and inferred time of fault generation. Cross-section through the study area is based on seismic section A-A' in fig. 5.1. a) Deposition of Carboniferous/Permian strata. b) Permian faults developed in response to Carboniferous-Permian rifting. c) Subaerial exposure and erosion of the high. d) Deposition of Triassic to Jurassic strata, erosion and development of the Base Cretaceous Unconformity (BCU). e) Deposition of Cretaceous strata. f-h) Development of narrow grabens and extensive horsts, and possibly shallower faults in response to rifting and propagation of the North-Atlantic rift system during the Jurassic and Cretaceous. i) Extensive erosion in response to uplift and glacial influence, development of the Upper Regional Unconformity (URU). j) Present-day structural configuration of the study area.

6.2 Fluid origin

According to the tentative maturity map after Ohm et al. (2008), illustrated in fig. 3.4, the study area coincides with areas where Carboniferous/Permian and Triassic source rocks have been mature pre-uplift. Henriksen, Ryseth, et al. (2011) describes the Triassic petroleum system as the most effective on the Loppa High, but the Triassic source rock intervals (e.g. Snadd, Kobbe, Klappmyss and Havert formations) are at present thought to lack generative potential due to shallow burial (Ohm et al., 2008). Fluid flow indications (e.g. gas chimneys and gas accumulations along vertically extensive faults) identified at all stratigraphic levels in the study area suggests source rock intervals of both Carboniferous/Permian and Triassic age. These observations appear to correspond to the distribution of previously mature source rock intervals in the tentative maturity map. However, these are already identified, established and proven

source rock intervals, but other source rocks that are not initially considered to be prolific may also have generative potential, being potential sources for migrating fluids in the study area. Several of the fluid flow indications are also interpreted as gas accumulations, which is initially generated at greater depths than oil. Thus, the previously oil mature source rock intervals might not explain the abundance of gas in the SW Barents Sea and study area. However, gas expansion and exsolution from oils is a likely consequence of uplift and erosion, and glacial loading and unloading (Doré & Jensen, 1996; Henriksen, Bjørnseth, et al., 2011; Lerche et al., 1997; Nyland et al., 1992). Without additional information it is therefore difficult to accurately determine the sources for fluids in the study area, only based on the level of occurrence of fluid flow indications. Furthermore, geochemical analyses from wells on the Loppa High suggest mixtures of hydrocarbons generated from different source rocks at different times (Ohm et al., 2008), suggesting multiple mature intervals in and around the study area. The alternating episodes of uplift/erosion and glacial cycles during the Cenozoic, and the subsequent effects on maturity and migration (see section 3.5.2) may have contributed to and/or controlled the type of fluids and pattern of leakage of hydrocarbons in the study area and hence the fluid flow systems in the SW Barents Sea (Vadakkepuliyambatta et al., 2013).

6.3 Fluid migration and accumulation

Vertical and lateral migration is driven by the interaction between different fluid and subsurface pressures, and is governed by weaker zones of higher permeability and porosity (see section 2.1.4). Fluid flow indications have been recorded occurring both vertically adjacent to one another, along e.g. faults and potential gas chimneys, but also laterally, confined to specific stratigraphic intervals or horizons. Faults and gas chimneys both represent zones of weakness, as can porous and laterally extensive strata. As fluids tend to move according to the path of least resistance, these features may constitute the main fluid migration pathways in the study area. Potential gas accumulations have been identified on several stratigraphic levels within the study area, mainly within Triassic reservoir intervals and along the Top Snadd/URU horizon. Common for them all is the apparent spatial relationship to structural trends in the area, both larger-scale, vertically extensive graben structures and smaller-scale, shallow Triassic faults.

6.3.1 Vertical migration along faults

Several high-amplitude anomalies/bright spots and other fluid flow features have been identified in close proximity to faults, which are, according to Ligtenberg (2005), the main conduits for fluids in many basins. In deeper subsurface strata, fluids tend to migrate along weaker sections within the fault zone rather than the surrounding, highly consolidated strata

(Ligtenberg, 2005). When moving into shallower strata, the rocks usually become progressively less consolidated, allowing fluids to migrate into laterally adjacent porous and permeable zones along the fault plane. Bright spots/amplitude anomalies, zones of acoustic masking and pipes occurring both along and above faults strongly suggest that the faults have been able to transmit fluids. Similarly, the lack of such fluid flow indications suggest non-conductive (sealing) faults (Tasianas et al., 2018). The relationship between fluid flow indications and faults in the study area is summarized in fig. 6.2.

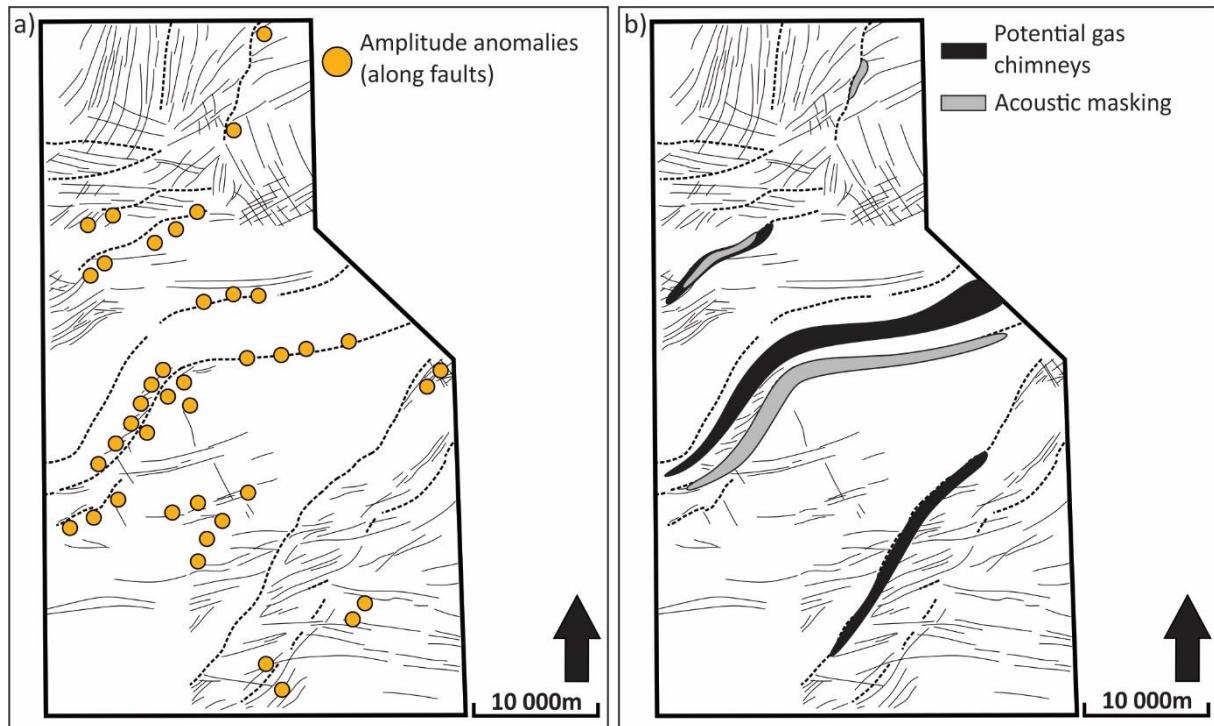


Figure 6.2: a) Location of amplitude anomalies related to faults in the study area. b) Location of potential gas chimneys/zones of acoustic masking and their relationship to faults in the study area.

AA3-5 and AA8-9 are all associated with vertically extensive faults, extending into and beyond several of the prolific source rock intervals (Havert, Klappmyss, Steinkobbe, Kobbe and Snadd formations) in the study area, suggesting open and conductive faults able to transmit fluids and subsequent accumulation of gas along and above them (fig. 6.3a). Gas chimneys, formed in response to fractured cap rocks and irregularly distributed gas zones (Løseth et al., 2009), have also been observed occurring in close proximity to the roots of several of the narrow grabens, mainly NG4 and NG6. The highest density of gas chimneys in the SW Barents Sea have been reported occurring along structural trends, such as the fault complexes delineating the Loppa High (Rajan et al., 2013; Vadakkepuliambatta et al., 2013), thus pointing to a spatial relationship between faults and gas chimneys. Vertically extensive faults penetrating deeper source rock intervals may thus facilitate migration between deep and shallow reservoirs, of

which fluids may migrate in chimneys and subsequently branch along fault planes into shallower strata (fig. 6.3b), a process also proposed by Vadakkepuliambatta et al. (2013). An increasing number of faults, and hence potential migration pathways, associated with the internal fault blocks of the NGs may also facilitate enhanced fluid flow in the upper subsurface strata and thus a greater distribution of amplitude anomalies representing gas accumulations along URU. Vadakkepuliambatta et al. (2013) have suggested i.a. the Carboniferous shales or the Late Carboniferous/Early Permian Ørn Formation as potential sources for fluids in the SW Barents Sea. These in addition to the previously discussed source rock intervals are thus plausible sources for fluids and potential accumulations related to the vertically extensive faults and deeply-rooted gas chimneys in the study area.

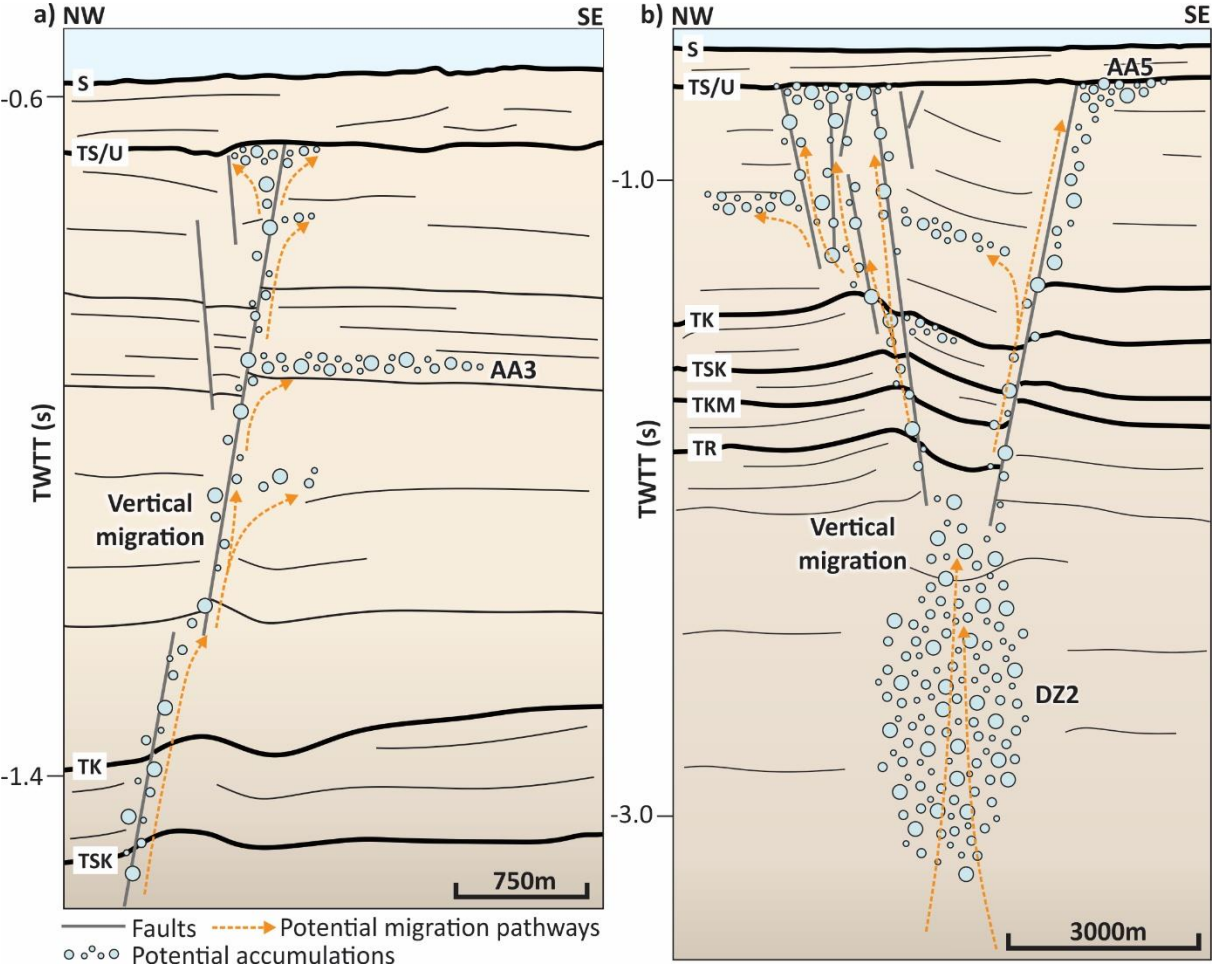


Figure 6.3: a) Conceptual model for migration and accumulation related to AA3. Cross-section corresponds to seismic section in fig. 5.15c. b) Conceptual model for migration and accumulation related to NG6 and DZ2. Cross-section corresponds to NW part of seismic section in fig. 5.24.

AA5, AA8 and AA9, occurring along the Top Snadd/URU horizon, are in this area located directly below the Nordland Group, consisting of glacial diamicton (Sættem et al., 1992). With a high clay content and very low permeability (Sættem et al., 1992), fluid migration through the Nordland Group may be limited, causing URU to essentially act as a permeability

barrier and fluids to accumulate beneath (Rajan et al., 2013). AA6-7 and AA10 are, similar to AA5 and AA8-9, located along the Top Snadd/URU horizon, but are associated with much shallower faults, most of them with their lower termination within the Snadd Formation (fig. 6.4). There appears to be a close spatial relationship between these amplitude anomalies and the faults, initially suggesting conductive faults able to transmit fluids vertically. However, none of the major source rock intervals have been penetrated by these faults, suggesting a component of lateral migration prior to vertical, or less known source rock intervals within the Triassic succession/Snadd Formation. As also noted by Rajan et al. (2013), tuning between the beds truncating URU and the strong URU reflector cannot be excluded as a possible cause of amplitude anomalies.

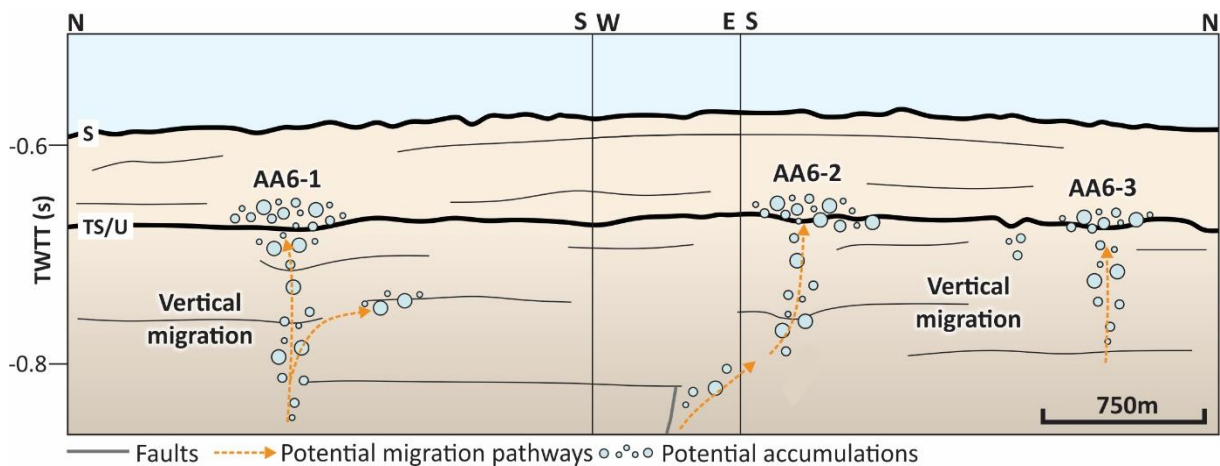


Figure 6.4: Conceptual model for migration and accumulation related to AA6. Cross-section corresponds to seismic section in fig. 5.18c.

After formation, faults may be inherently conductive, allowing fluids to migrate along the weaker section of the fault plane. On the contrary, faults may be initially sealing, preventing vertical fluid migration. The pre-Cenozoic distribution of fluid flow systems and hydrocarbon accumulations in the study area has probably been related to the distribution of conductive and non-conductive faults in the study area. However, according to Henriksen, Bjørnseth, et al. (2011), fault-bounded traps are more sensitive to the effects of uplift and erosion than stratigraphic or anticlinal traps, of which their sensitivity is largely attributed to the subsequent seal capacity and integrity. During uplift and tectonic readjustments, reservoir tilting and subsequent hydrocarbon spill can be substantial, and the development of additional faults breaching the sealing lithologies, hence reducing the seal capacity, may provide additional potential migration pathways through the subsurface strata. A high density and number of faults hence increases the probability of fluid migration, especially at fault intersections (Doré & Jensen, 1996; Ligtenberg, 2005; Vadakkepuliambatta et al., 2013). Furthermore, initially

sealing fault planes may become conductive, so that fluids initially trapped against bounding faults may leak along the fault plane and into shallower strata. Faults may also become exposed at the surface given sufficient exhumation, allowing fluids to escape completely from the subsurface (Doré & Jensen, 1996). The structural development, both prior to but especially in response to Late Cenozoic uplift and erosion, may thus have contributed to the nature of the fluid flow systems in the study area, strongly suggesting a structural control on vertical migration.

6.3.2 Lateral migration in reservoir intervals

Evidence of lateral migration usually includes enhanced amplitudes and possible phase reversals along laterally extensive reflectors. The only indication of lateral migration identified in the study area are laterally adjacent bright spots in the lower Snadd Formation (e.g. AA3 and AA4), all of which are located in close proximity to vertically extensive faults, such as those associated with NG6. Several Triassic formations encompass both potential cap rocks and reservoir intervals, which fluids may migrate along and within. However, the reservoir potential of the Triassic formations is variable, and largely affected by diagenetic alterations related to deep burial (Henriksen, Ryseth, et al., 2011). This subsequently affects the porosity and permeability of the formations, limiting both migration distances and potential migration pathways.

The Triassic Snadd Formation reflects several different depositional environments, and alternating episodes of transgression and regression during the Middle to Late Triassic have given rise to alternating shales and silt-/sandstone deposits within the formation. Low-permeability source or cap rocks are usually deposited during transgressions and landward translation of the shoreline, whereas porous and permeable reservoir rocks are deposited during regressions with progradation of the shoreline (Henriksen, Ryseth, et al., 2011). Several stages of regression during the Ladinian and Carnian caused the progradation of deltaic systems across the shelf, and sediments deposited during this time included coastal plain and fluvial deposits, evidenced by channel sand bodies with significant reservoir potential identified at several levels in the Snadd Formation (Klausen et al., 2015). Several amplitude anomalies (e.g. AA3 and AA4, fig. 6.5) have been identified within channel deposits, suggesting sufficient porosities and permeabilities allowing fluid migration and accumulation. Cross-cutting, converging and stacked channel structures may constitute a larger network of porous and permeable deposits, potentially constituting important fluid migration pathways. A high connectivity between channel deposits may cause them to serve as lateral carrier beds, facilitating long-range lateral

migration, limited by the geometry of the respective channel deposits and degree of interference with other channel structures (Osborne & Swarbrick, 1997; Selley & Sonnenberg, 2015).

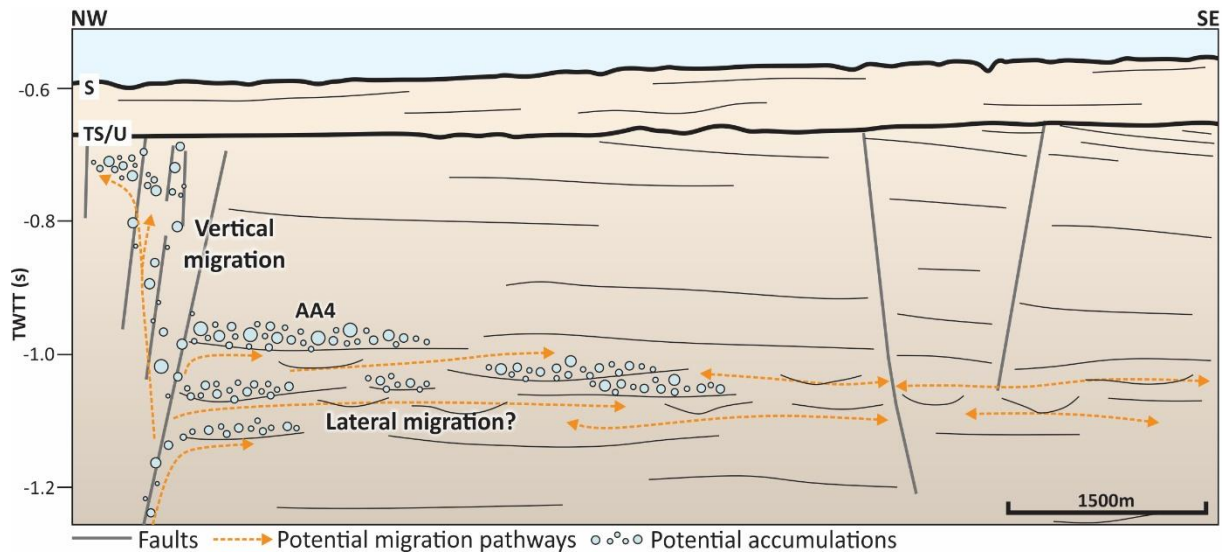


Figure 6.5: Conceptual model for migration and accumulation related to AA4. Cross-section corresponds to seismic section in fig. 5.16c.

Several of the shallow Triassic faults dissect the channel deposits of the lower Snadd Formation, which is generally characterized by low amplitudes in large parts of the study area. Amplitude anomalies associated with these faults (e.g. AA6-7 and AA10, fig 6.6) may originate from fluids that initially migrated vertically through extensive faults (e.g. the faults of NG6/NG4), and subsequently laterally through high-connectivity channel deposits in the lower Snadd Formation. However, low connectivity between the deposits would imply filling of traps proximal to the vertically extensive faults, and limited potential of filling distal traps (also illustrated in fig. 6.5). This might explain the many amplitude anomalies located along the faults of e.g. NG6 and lack of amplitude anomalies with increasing distance away from the fault zone. In this case, AA6-7 and AA10 must have a different origin.

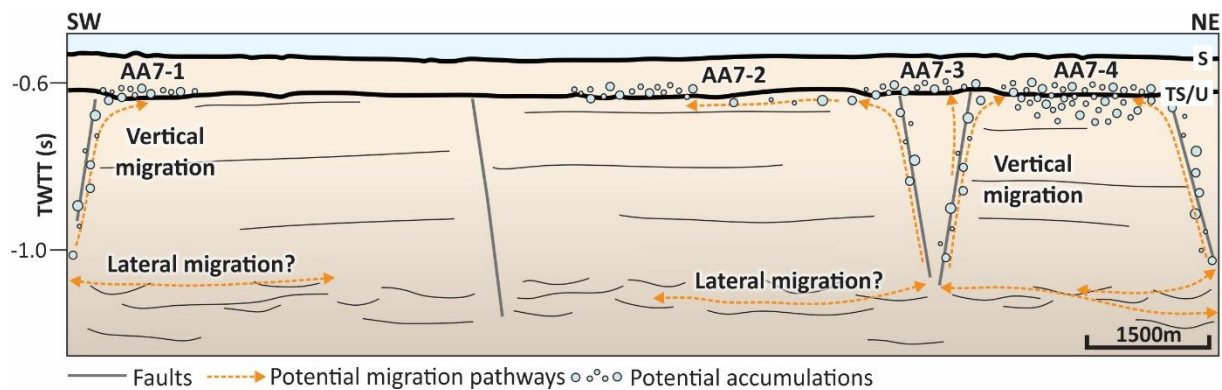


Figure 6.6: Conceptual model for migration and accumulation related to AA7. Cross-section corresponds to seismic section in fig. 5.19c.

6.3.3 Lateral migration in dipping strata

According to the principle of initial horizontality, dipping or tilted strata is caused by deformation (faulting and/or folding), occurring after initial deposition of the sediments (Brookfield, 2004). Dipping strata has been recorded several places in the study area, reflecting the extensive faulting and tilting of the Loppa High. As mentioned, the only evidence of intermediate-scale lateral migration is identified in channel deposits within the Snadd Formation, and not in the gently dipping strata characterizing the high. However, lateral migration in tilted reservoir intervals is possible, given sufficient porosities and permeabilities, and the correct pressure conditions (see section 2.1.4).

Smaller-scale lateral migration in dipping strata is indicated by increasing amplitudes updip in the internal and tilted fault blocks of NG6, culminating in the high-amplitude anomalies of AA5 (fig. 6.7). As fluids tend to accumulate in the highest point of a trap, dipping beds pinching out or terminating against faults will have enhanced amplitudes where hydrocarbons, especially gas, have accumulated and lower amplitudes where they have not. The lower termination of such an accumulation is ideally represented by a flat-spot cross-cutting the dipping strata, but the production of such a flat spot is dependent on the height of the fluid column and sufficient acoustic impedance contrast across the contact (Brown, 2004; Nanda, 2016). The seismic expression along NG6, with high-amplitude anomalies indicative of shallow gas, suggests that the deeper-penetrating faults of the fault zone are conductive and able to transmit fluids vertically from deeper source rock intervals. These fluids may subsequently branch along the internal and tilted fault blocks of NG6 and into laterally adjacent permeable zones below URU.

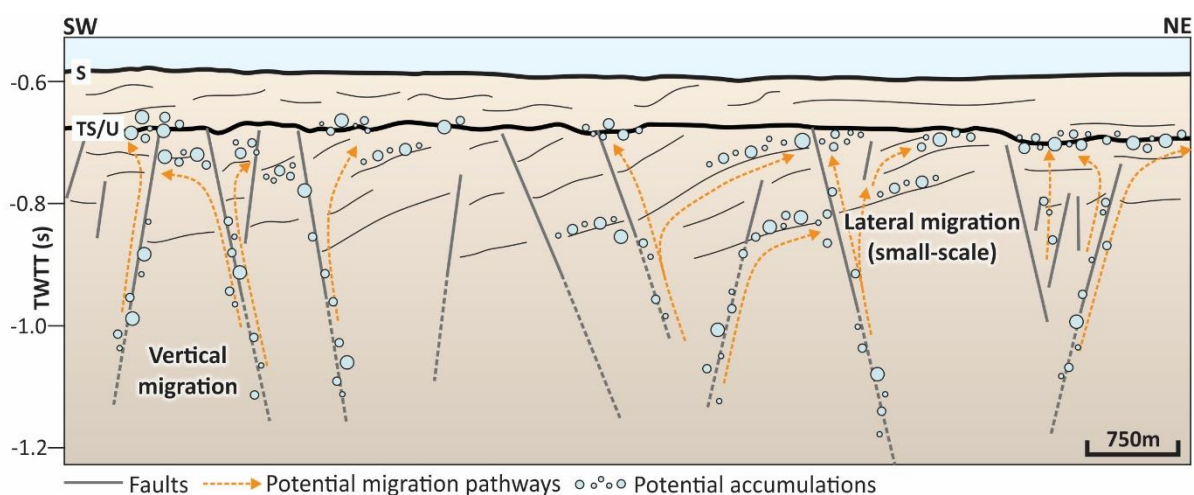


Figure 6.7: Conceptual model for migration and accumulation related to AA5. Cross-section corresponds to seismic section in fig 5.17c.

6.4 Morphological indications of gas seepage

Circular depressions on the seabed have been recorded several places in the SW Barents Sea, and in close proximity to the western Loppa High (Chand et al., 2012; Pau et al., 2014; Rise et al., 2014; Tasianan et al., 2018). These depressions have been interpreted as pockmarks, which are common morphological expressions of gas seepage. Pockmarks and associated gas are sometimes identified in seismic by acoustic pipes characterized by stacked bright spots and/or push-down effects, extending from the depression on the seabed, and down into the subsurface strata (Løseth et al., 2009). However, if gas is absent below the pockmarks, such features may not be observed.

Only twelve circular depressions have been identified on the seabed, which is largely affected by extensive iceberg reworking. The depressions identified mainly occur as isolated features, except for ED1-5, which appear to occur in a cluster, and ED7, which is located within a ploughmark. Compared to the depressions observed on the seabed, the number of paleo-depressions is extremely high, and they are clearly distinguishable as circular features occurring mainly within the Nordland Group. The diameter of exposed and buried depressions ranges from 76 to 319 m, and the depths from 7.4 to 27 m. Some of the paleo-depressions (e.g. PD4-10) are also associated with acoustic pipes, push-down effects and amplitude anomalies.

6.4.1 Depression/pockmark distribution

The exposed depressions identified in the study area occur at water depths ranging from -510 to -610 ms, corresponding to 383 – 458 m ($V_p = 1500$ m/s). According to Hovland et al. (2002), the density of pockmarks on the seabed is largely dependent on the underlying geology, fluid flux and the nature of the seabed sediments. Not only do they require a mature source for fluids, but also a recording medium (soft sediments) of sufficient thickness for their formation and actual occurrence on the seabed (Chand et al., 2009; Pau et al., 2014; Rise et al., 2014).

The number of exposed depressions varies from six in the northern, one in the central and five in the southern part of the study area, a number initially indicating a density of only 0.0073 potential pockmarks/km². Previous studies on the occurrence of pockmarks in the SW Barents Sea have revealed pockmark densities of several hundred pockmarks/km² (e.g. Chand et al. (2012), Rise et al. (2014) and Tasianan et al. (2018)), largely deviating from the current observations from the study area. The density of potential pockmarks occurring on the seabed in the study area may thus reflect the environment in which they have formed, e.g. lack of soft sediments and/or migrating fluids. Several of the exposed depressions are located in close proximity to or directly above faults and fault zones, such as ED1-5 above the eastern flank of

NG3, ED8-9 above shallow Triassic faults and ED10 above NG4 (fig. 6.8a). Given that these features are pockmarks indicative of fluid expulsion, faults may have acted as fluid conduits transferring fluids into shallower strata.

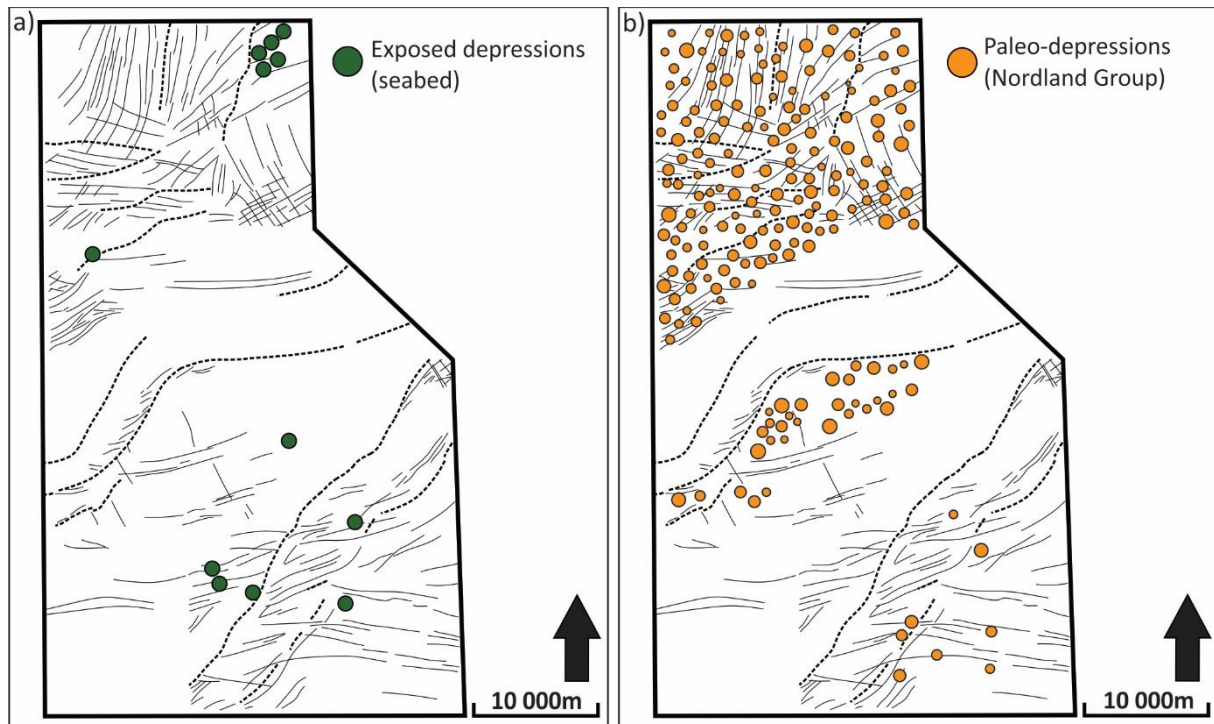


Figure 6.8: a) Relationship between exposed depressions and faults in the study area. b) Relationship between paleo-depressions and faults in the study area.

Variance time slices cutting through the Nordland Group and down to the Top Snadd/URU horizon reveal that the density of paleo-depressions becomes progressively higher from the S/SE to N/NW, as evidenced by only a few PDs in the GDF1201M13 dataset and countless PDs in the DG12M1 dataset. Thus, the density of potential paleo-pockmarks is far greater than the density of potential exposed pockmarks (fig. 6.8b). A concurrent distribution of faults and paleo-depressions has also been observed in the northern and central parts of the study area, substantiating a theory of a relationship between the two. The most obvious example can be observed in the northern part, which is characterized by several Permian-Triassic faults and numerous Triassic faults, and countless paleo-depressions located at several levels within the Nordland Group. Fewer faults and hence potential migration pathways also correlates to the lower number of paleo-depressions in the central parts of the study area. In these cases, conditions appear to have been favorable for the formation of potential pockmarks, with sufficient fluid flux and relatively soft sediments. However, a large discrepancy can be observed further to the south, which is characterized by both Permian-Triassic and Triassic faults, but very few paleo-depressions. Fluid expulsion might thus have been less extensive, possibly due

to the lack of conductive faults or migrating fluids, or significant variations in the seabed sediment lithology.

Amplitude anomalies have also been recorded occurring in close proximity to both exposed and buried depressions. ED6 and ED10 are located directly above amplitude anomalies associated with vertically extensive faults, and might thus represent shallow gas accumulations feeding potential pockmarks. However, acoustic pipes connecting these features would in this case be expected, and has not been directly observed. PD4-10 are associated with AA6, all occurring along the Top Snadd/URU horizon. In this case, fluids may have migrated from deeper sources towards URU, causing fluid expulsion and pockmark formation on the paleo-seabed. Accumulations as those indicated by AA6 suggests fluids migrating in the same pipes, but instead of escaping becomes trapped below the impermeable sediments deposited above URU.

6.4.2 Depression/pockmark origin

The exact formation mechanism of pockmarks and pockmark-like depressions has long been debated, and several mechanisms have been proposed. Common for many of them is the general assumption that their formation is related to fluid escape, but the type of fluids, their origin and manner of fluid migration differs. Seismic evidence related to the paleo-depressions, e.g. acoustic pipes and push-down effects, supports a theory of them being pockmarks related to vertical fluid expulsion. However, lack of similar evidence related to the exposed depressions might suggest a different origin (summarized in fig. 6.9).

The most important theories for the formation of pockmarks include i.a. seepage of pore water/gas bubbles, dewatering of sediments and sediment rafting by buoyant solid phases such as gas hydrates and frozen freshwater (Harrington, 1985; King & MacLean, 1970; Paull et al., 1999). However, venting of and winnowing by thermogenic and biogenic gas originating from degradation of subsurface organic material (Chand et al., 2012; Hovland, 1981; Tasianan et al., 2018) appears to be the most accepted mechanism of pockmark formation in the SW Barents Sea. Chand et al. (2012) have proposed two different processes accounting for the formation of the now active and inactive pockmarks observed on the seabed on the Loppa High; the former related to active gas seepage from the seabed, the latter related to gas hydrate formation and subsequent destabilization. Gas flares observed close to the seabed testify to active gas seepage, most likely related to open fluid conduits such as faults and leakage along stratigraphic boundaries. Continued seepage may cause winnowing of sediments and the formation of active pockmarks on the seabed, representing the first process of pockmark formation. This is, however, dependent on soft sediments able to record the seepage of fluids from the seabed. Gas

flares occurring without any relationship to seabed depressions are commonly attributed to harder and less deformable glaciogenic sediments (Chand et al., 2012). The Barents Sea has been largely affected by the glacial cycles characterizing the Plio-Pleistocene (Knies et al., 2009; Laberg et al., 2010), and one of the main consequences of glacial activity has been the changing pressure and temperature regimes of the uppermost subsurface strata. Gas migrating through open migration pathways, e.g. faults, have most likely encountered pressure and temperature conditions favorable for gas hydrate formation below the concurrent ice sheet. Subsequent glacial retreat, pressure reduction and rapid deposition of glaciomarine sediments may then have contributed to gas hydrate destabilization and release of gas to form the now inactive pockmarks on the seabed, thus representing the second process of pockmark formation (Chand et al., 2012; Lerche et al., 1997; Pau et al., 2014; Tasianan et al., 2018).

Gas hydrate destabilization and melting may not necessarily cause the development of vertical pipes and bright spots below pockmarks, as it does not require an active supply of gas at the time of destabilization. Missing pipes may also be attributed to the fact that gas may no longer exist in the sediments below pockmarks, and hence not result in scattering and vertical zones of acoustic masking. Gas hydrate destabilization is therefore a possible formation mechanism for both the paleo-depressions and exposed depressions identified in the study area. The formation of pockmark-like depressions have also been proposed as glacially induced by scouring icebergs (Bass & Woodworth-Lynas, 1988), and a result of seabed collapse in response to liquefaction (Judd & Hovland, 2007). The depressions are in these cases not representative for active fluid migration from the deeper subsurface. Given the glacial history of the SW Barents Sea, the occasionally concurrent distribution of ploughmarks and depressions, and lack of seismic evidence below several of the depressions, a glacial origin is possible. Pockmarks or depressions occurring within iceberg ploughmarks initially suggest a synchronous time of formation (Tasianan et al., 2018), and can either be directly related to iceberg scouring, gas hydrate destabilization or weaker zones within ploughmarks allowing the easy escape of gas.

The concurrent distribution of faults, fluid flow indications and paleo-depressions suggest extensive migration through an open and conductive fault network during the last glaciation, and release of shallow gas at the paleo-seabed. Paleo-depressions occurring along URU and at several levels within the Nordland Group might suggest episodic or syn-depositional fluid expulsion, possibly during episodes of glacial retreat and decreasing pressures. Accumulation of gas hydrates and associated free gas below the concurrent ice sheet, and subsequent

destabilization during retreat may also be a plausible explanation for both paleo- and exposed depressions. However, iceberg reworking through scouring in the SW Barents Sea is extensive, and may together with sparse seismic evidence constitute a third possible explanation for the formation of paleo- and exposed depressions in the area.

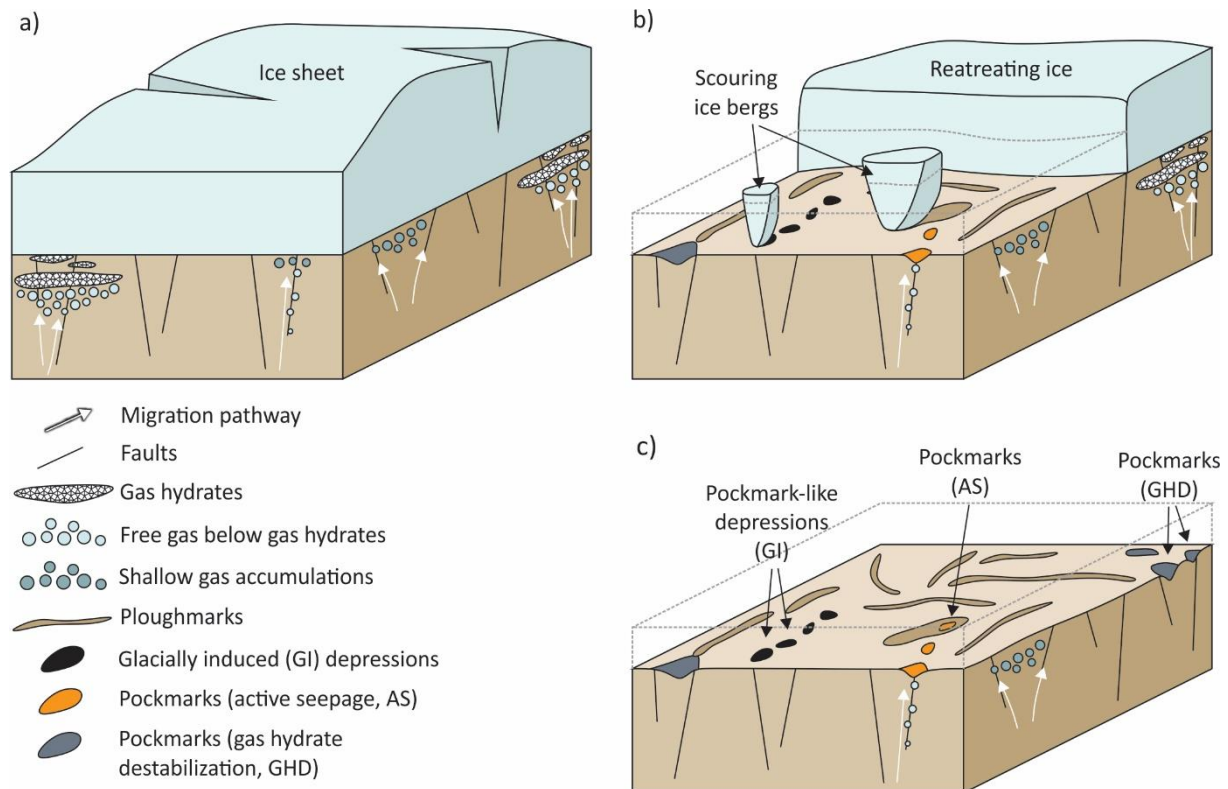


Figure 6.9: Plausible mechanisms for pockmark formation in the study area. a) Gas hydrate development and entrapment of free gas below a concurrent ice sheet, as well as shallow gas migration and accumulation along faults. b) Glacial retreat and gas hydrate destabilization, scouring icebergs and release of gas through open migration pathways (faults). c) Post-glacial seabed morphology with glacially induced depressions and depressions caused by gas hydrate destabilization and seepage.

6.5 Conceptual model and Petroleum System Event Chart

The conceptual model in fig. 6.10 summarizes the main processes discussed in the preceding sections, and the stratigraphic delineation is based on seismic section in fig. 5.24. Modifications have been made in order to incorporate most of the processes discussed into one process-based model for fluid flow and accumulation in the study area. The proposed Petroleum System Event Chart in fig. 6.11 accounts for the time of deposition of known source, reservoir and seal rocks (based on fig. 3.2) and the timing of trap formation and generation, migration and accumulation in the study area. The timing of (structural) trap formation roughly corresponds to the main tectonic events potentially responsible for their formation, and several critical moments refer to several phases of migration and possible remigration in response to rifting and tectonic readjustments from Middle-Late Mesozoic to Late Cenozoic.

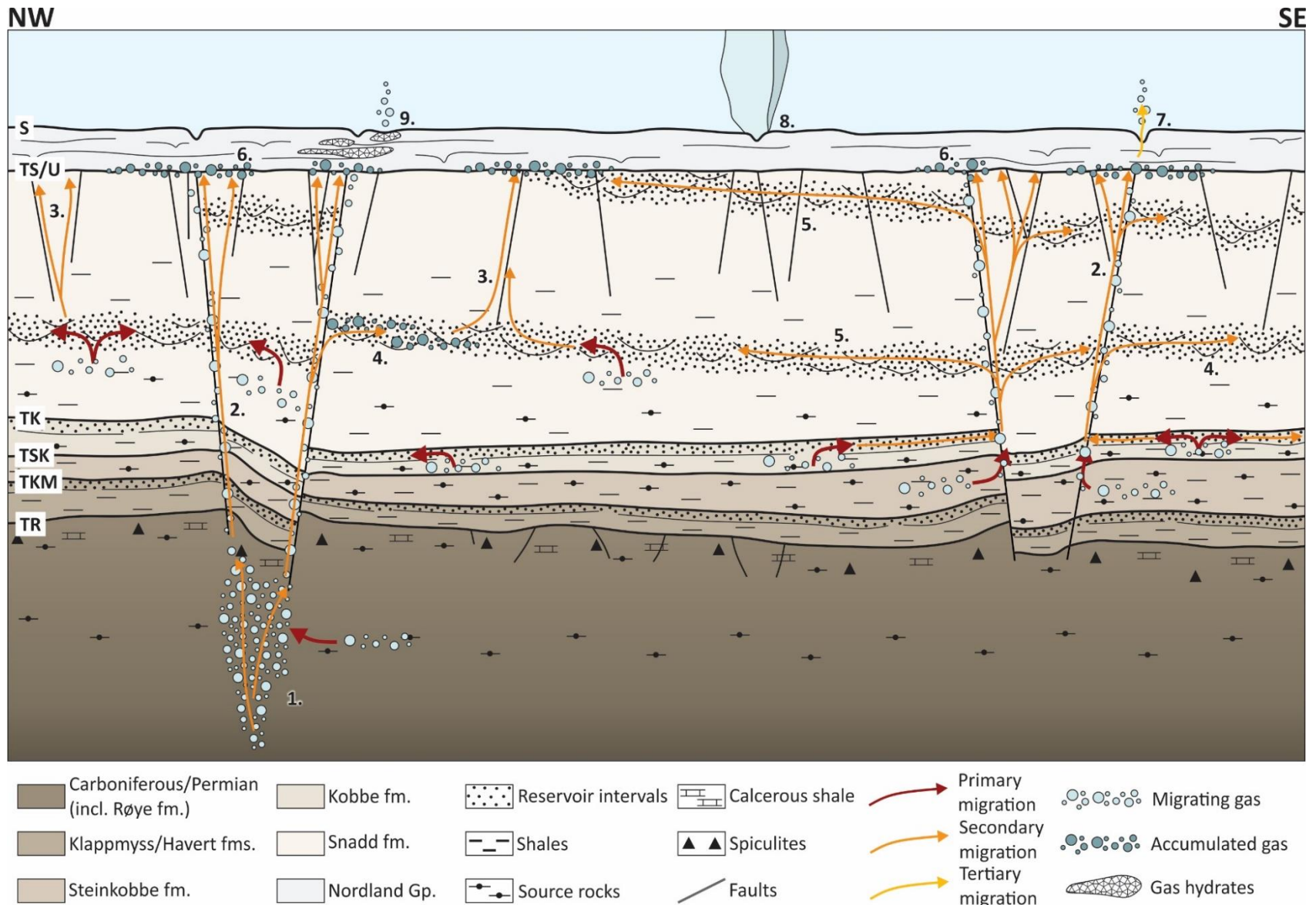


Figure 6.10: Conceptual model for fluid flow, accumulation and the associated processes in the study area. 1. Vertical migration in gas chimneys. 2. Vertical migration and branching along vertically extensive faults. 3. Vertical migration in shallow faults, possible connection to channel deposits. 4. Lateral migration in channel deposits. 5. Lateral migration in reservoir intervals/dipping strata. 6. Shallow gas accumulation along URU. 7. Pockmark formation by active seepage from underlying faults. 8. Pockmark formation by iceberg scouring. 9. Pockmark formation by gas hydrate destabilization.

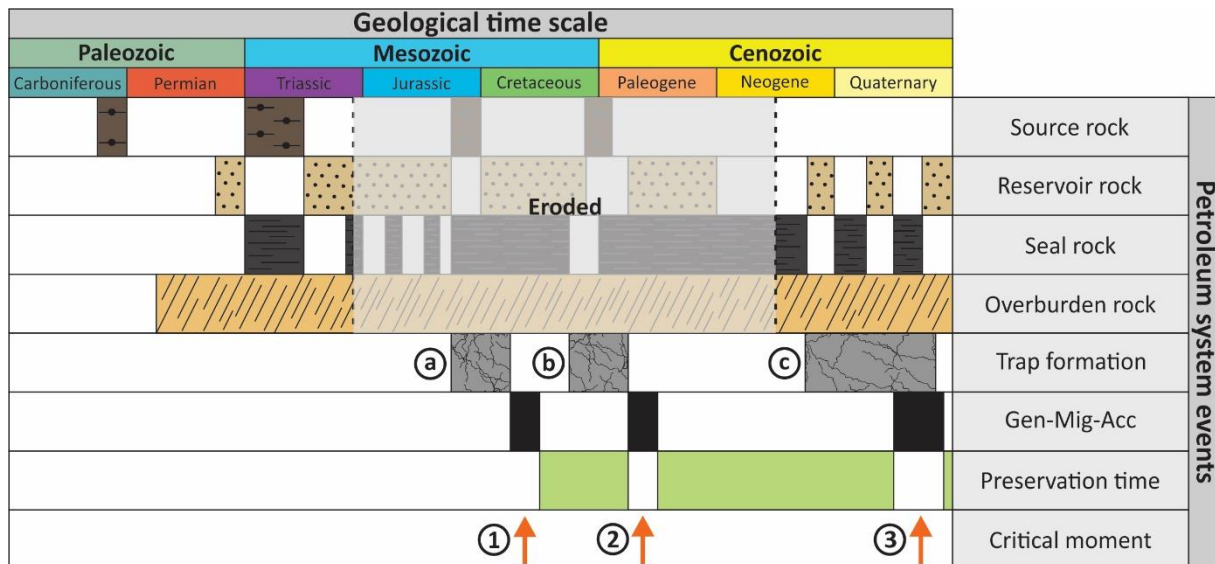


Figure 6.11: Proposed Petroleum System Event Chart for the study area, with the inferred time of source, reservoir, seal and overburden deposition, as well as trap formation, generation, migration and accumulation. Several phases of potential (structural) trap formation is indicated, with a) faulting related to the progradation of the North Atlantic rift system into the SW Barents Sea, b) faulting related to intensified rifting and the progressive opening of the Norwegian-Greenland Sea, and c) faulting related to Late Cenozoic uplift and erosion. Several critical moments refers to several phases of potential migration and remigration, and subsequent accumulation, with 1) generation and migration into structural traps formed during a), 2) generation, migration and possible remigration into structural traps formed during b), and 3) migration and remigration into structural traps formed during c).

7 Conclusion

Interpretation and analysis of both 2D and 3D seismic datasets covering the northern margin of the Loppa High has allowed stratigraphic delineation and identification of fluid flow indications such as leaking faults, shallow gas accumulations and gas chimneys, as well as morphological indications of gas seepage such as depressions on the seabed. Interpretation of individual features and correlation with the structural development and the denudation history of the area have provided a better insight to the controlling mechanisms for fluid flow and accumulation in the study area and resulted in the following conclusions:

- The faults characterizing the northern Loppa High include deep-seated Permian faults, vertically extensive Permian-Triassic faults and shallow Triassic faults, all of which appear to be extensional features.
- The structural configuration of the study area is believed to reflect Carboniferous-Permian rifting episodes, followed by extensional faulting related to the proto-Atlantic rift system and later rifting events associated with the opening of the Norwegian-Greenland Sea.
- Fluid flow indications have been identified in several places in the study area, testifying to vertical and lateral migration from deeper source rock intervals, shallow accumulation and episodes of potential gas release at the seabed.
- Vertical migration appears to have been governed by open and conductive faults, penetrating prolific source rock intervals ranging from Carboniferous to Triassic age. Gas chimneys may reflect deeply-rooted fluid flow, which have subsequently reached and branched along vertically extensive faults.
- Lateral migration appears to have been restricted mostly to the Snadd Formation, occurring in laterally adjacent channel sand bodies close to major faults and possibly in dipping and alternating reservoir intervals within the formation.
- The majority of potential gas accumulations appear to be concentrated along URU, of which fluids may have been impaired from further migration due to the low permeability and porosity of the overlying Nordland Group.
- The high density and distribution of paleo-depressions may suggest extensive migration through an open fault network prior to and during the last glacial cycles, but variations in density may reflect differences in seabed sediment lithology, fluids available for migration and remigration and/or the number of conductive vs. non-conductive faults. A low density of exposed depressions may suggest much poorer

conditions for pockmark formation, but may also suggest a glacial origin or reflect episodes of post-glacial gas hydrate destabilization.

- There is overwhelming evidence suggesting that migration may have been structurally controlled, as evidenced by potential gas accumulations and other fluid flow indications along and above laterally and vertically extensive Permian-Triassic and shallow Triassic faults. Tectonic readjustments and possible reactivation of faults may have altered the pre-Cenozoic distribution of fluid flow systems, accumulations and affected the type of fluids available for migration, and resulted in the present day distribution of fluid flow systems in the study area.

8 Further research

Further investigations and analyses of the faults identified may provide a better insight to their time of formation and their potential of being conductive fluid conduits, and consequently a better understanding of their role in fluid migration in the study area. Furthermore, as resolution poses the greatest constraint on interpretation, acquisition of high-resolution 3D seismic from the upper subsurface strata will provide much better means of analyzing the seabed morphology. This can subsequently contribute to a better understanding of the occurrence, density and distribution of seabed depressions, and the determination of whether they might reflect vertical fluid migration or result from other formation mechanisms

References

- AHLBORN, M., STEMMERIK, L., & KALSTØ, T.-K. (2014). 3D seismic analysis of karstified interbedded carbonates and evaporites, Lower Permian Gipsdalen Group, Loppa High, southwestern Barents Sea. *Marine and Petroleum Geology*, 56, 16-33. doi:10.1016/j.marpetgeo.2014.02.015
- ANDERSON, E. M. (1951). *The dynamics of faulting and dyke formation with applications to Britain*. Edinburgh: Oliver and Boyd.
- ANDREASSEN, K., HUBBARD, A., WINSBORROW, M., PATTON, H., VADAKKEPULIYAMBATTA, S., PLAZA-FAVEROLA, A., . . . BÜNZ, S. (2017). Massive blow-out craters formed by hydrate-controlled methane expulsion from the Arctic seafloor. *Science*, 356 (6341), 948-953. doi:10.1126/science.aal4500
- ANDREASSEN, K., NILSSEN, E., & ØDEGAARD, C. (2007). Analysis of shallow gas and fluid migration within the Plio-Pleistocene sedimentary succession of the SW Barents Sea continental margin using 3D seismic data. *Geo-Marine Letters*, 27 (2), 155-171. doi:10.1007/s00367-007-0071-5
- ANDREASSEN, K., RAFAELSEN, B., & ØDEGAARD, C. M. (2007). Imprints of former ice streams, imaged and interpreted using industry three-dimensional seismic data from the south-western Barents Sea. In R. J. Davies, H. W. Posamentier, L. J. Wood, & J. A. Cartwright (Eds.), *Seismic Geomorphology: Applications to Hydrocarbon Exploration and Production* (pp. 151-169). London: The Geological Society of London.
- ARNTZEN, M. (2018). *Triassic Channel Systems on the northern Loppa High, SW Barents Sea*. UiT - The Arctic University of Norway, Tromsø.
- BADLEY, M. E. (1985). *Practical Seismic Interpretation*. Boston: International Human Resources Development Corporation.
- BASS, D. W., & WOODWORTH-LYNAS, C. (1988). Iceberg crater marks on the sea floor, Labrador Shelf. *Marine Geology*, 79 (3), 243-260. doi:10.1016/0025-3227(88)90041-2
- BEAUMONT, E. A., & FIEDLER, F. (1999). Chapter 5: Formation Fluid Pressure and Its Application. In E. A. Beaumont & N. H. Foster (Eds.), *Exploring for Oil and Gas Traps* (pp. 1150): AAPG.
- BERNDT, C. (2005). Focused fluid flow in passive continental margins. *Philosophical transactions: Mathematical, physical, and engineering sciences*, 363 (1837), 2855-2871. doi:10.1098/rsta.2005.1666
- BLOMEIER, D., DUSTIRA, A., FORKE, H., & SCHEIBNER, C. (2011). Environmental change in the Early Permian of NE Svalbard: from a warm-water carbonate platform (Gipshuken Formation) to a temperate, mixed siliciclastic-carbonate ramp (Kapp Starostin Formation). *Facies*, 57 (3), 493-523. doi:10.1007/s10347-010-0243-z
- BROOKFIELD, M. E. (2004). *Principles of Stratigraphy*. Malden, Massachusetts: Blackwell Publishing.
- BROWN, A. R. (2004). *Interpretation of Three-Dimensional Seismic Data* (6th ed. Vol. 42). Tulsa, Oklahoma: AAPG and SEG.
- BULAT, J. (2005). Some considerations on the interpretation of seabed images based on commercial 3D seismic in the Faroe-Shetland Channel. *Basin Research*, 17 (1), 21-42. doi:10.1111/j.1365-2117.2005.00253.x
- BULLER, A., BJØRKUM, P. A., NADEAU, P. H., & WALDERHAUG, O. (2005). Distribution of hydrocarbons in sedimentary basins: The importance of temperature. *R&D Memoir*, 7, 1-15.
- BÜNZ, S., MIENERT, J., & BERNDT, C. (2003). Geological controls on the Storegga gas-hydrate system of the mid-Norwegian continental margin. *Earth and Planetary Science Letters*, 209 (3-4), 291-307. doi:10.1016/S0012-821X(03)00097-9

- CARTWRIGHT, J. (2007). The impact of 3D seismic data on the understanding of compaction, fluid flow and diagenesis in sedimentary basins. *Journal of the Geological Society*, 164 (5), 881-893. doi:10.1144/0016-76492006-143
- CARTWRIGHT, J. (2011). Diagenetically induced shear failure of fine-grained sediments and the development of polygonal fault systems. *Marine and Petroleum Geology*, 28 (9), 1593-1610. doi:10.1016/j.marpetgeo.2011.06.004
- CARTWRIGHT, J., & DEWHURST, D. (1998). Layer-bound compaction faults in fine-grained sediments. *Geological Society of America Bulletin*, 110 (10), 1242-1257.
- CARTWRIGHT, J., HUUSE, M., & APLIN, A. C. (2007). Seal bypass systems. *AAPG Bulletin*, 91 (8), 1141-1166. doi:10.1306/04090705181
- CARTWRIGHT, J., & LONERGAN, L. (2003). Volumetric contraction during the compaction of mudrocks: A mechanism for the development of regional-scale polygonal fault systems. *Basin Research*, 8 (2), 183-193. doi:10.1046/j.1365-2117.1996.01536.x
- CHAND, S., RISE, L., OTTESEN, D., DOLAN, M. F. J., BELLEC, V., & BØE, R. (2009). Pockmark-like depressions near the Goliat hydrocarbon field, Barents Sea: Morphology and genesis. *Marine and Petroleum Geology*, 26 (7), 1035-1042. doi:10.1016/j.marpetgeo.2008.09.002
- CHAND, S., THORSNES, T., RISE, L., BRUNSTAD, H., STODDART, D., BØE, R., . . . SVOLSBRU, T. (2012). Multiple episodes of fluid flow in the SW Barents Sea (Loppa High) evidenced by gas flares, pockmarks and gas hydrate accumulation. *Earth and Planetary Science Letters*, 331-332, 305-314. doi:10.1016/j.epsl.2012.03.021
- DALLAND, A., WORSLEY, D., & OFSTAD, K. (1988). A lithostratigraphic scheme for the Mesozoic and Cenozoic succession offshore mid- and northern Norway. *NPD Bulletin*, no. 4.
- DALLMANN, K. (1999). *Lithostratigraphic lexicon of Svalbard: review and recommendations for nomenclature use. Upper Palaeozoic to Quaternary bedrock*. Tromsø: Norsk Polarinstitutt.
- DAVIES, R. J., & IRELAND, M. T. (2011). Initiation and propagation of polygonal fault arrays by thermally triggered volume reduction reactions in siliceous sediment. *Marine Geology*, 289 (1), 150-158. doi:10.1016/j.margeo.2011.05.005
- DAVIES, R. J., IRELAND, M. T., & CARTWRIGHT, J. A. (2009). Differential compaction due to the irregular topology of a diagenetic reaction boundary: a new mechanism for the formation of polygonal faults. *Basin Research*, 21 (3), 354-359. doi:10.1111/j.1365-2117.2008.00389.x
- DEWHURST, D. N., CARTWRIGHT, J. A., & LONERGAN, L. (1999). The development of polygonal fault systems by syneresis of colloidal sediments. *Marine and Petroleum Geology*, 16 (8), 793-810. doi:10.1016/S0264-8172(99)00035-5
- DORÉ, A. G. (1995). Barents Sea Geology, Petroleum Resources and Commercial Potential. *Arctic*, 48 (3), 207-221. doi:10.14430/arctic1243
- DORÉ, A. G., & JENSEN, L. N. (1996). The impact of late Cenozoic uplift and erosion on hydrocarbon exploration: offshore Norway and some other uplifted basins. *Global and Planetary Change*, 12 (1), 415-436. doi:10.1016/0921-8181(95)00031-3
- EHRENBERG, S. N., MCARTHUR, J. M., & THIRLWALL, M. F. (2010). Strontium isotope dating of spiculitic Permian strata from Spitsbergen outcrops and Barents Sea well-cores. *Journal of Petroleum Geology*, 33 (3), 247-254. doi:10.1111/j.1747-5457.2010.00476.x
- EHRENBERG, S. N., NIELSEN, E. B., SVÅNÅ, T. A., & STEMMERIK, L. (1998). Depositional evolution of the Finnmark carbonate platform, Barents Sea: results from wells 7128/6-1 and 7128/4-1. *Norwegian Journal of Geology*, 78, 185-224.

- ELVEBAKK, G., HUNT, D. W., & STEMMERIK, L. (2002). From isolated buildups to buildup mosaics: 3D seismic shed new light on upper Carboniferous-Permian fault controlled carbonate buildups, Norwegian Barents Sea. *Sedimentary Geology*, 152 (1-2), 7-17.
- ENGLAND, W. A., MACKENZIE, A. S., MANN, D. M., & QUIGLEY, T. M. (1987). The movement and entrapment of petroleum fluids in the subsurface. *Journal of the Geological Society*, 144 (2), 327-347. doi:10.1144/gsjgs.144.2.0327
- FALEIDE, J. I., BJØRLYKKE, K., & GABRIELSEN, R. H. (2015). Chapter 25: Geology of the Norwegian Continental Shelf. In K. Bjørlykke (Ed.), *Petroleum Geoscience: From Sedimentary Environments to Rock Physics* (2nd ed., pp. 603-635). Berlin, Heidelberg: Springer.
- FALEIDE, J. I., GUDLAUGSSON, S. T., & JACQUART, G. (1984). Evolution of the western Barents Sea. *Marine and Petroleum Geology*, 1 (2), 123-150. doi:10.1016/0264-8172(84)90082-5
- FALEIDE, J. I., SOLHEIM, A., FIEDLER, A., HJELSTUEN, B. O., ANDERSEN, E. S., & VANNESTE, K. (1996). Late Cenozoic evolution of the western Barents Sea-Svalbard continental margin. *Global and Planetary Change*, 12 (1-4), 53-74.
- FALEIDE, J. I., VÅGNES, E., & GUDLAUGSSON, S. T. (1993). Late Mesozoic-Cenozoic evolution of the south-western Barents Sea in a regional rift-shear tectonic setting. *Marine and Petroleum Geology*, 10 (3), 186-214.
- FOSSEN, H. (2016). *Structural Geology*. Cambridge: Cambridge University Press.
- GABRIELSEN, R. H., FÆRSETH, R. B., JENSEN, L. N., KALHEIM, J. E., & RIIS, F. (1990). Structural elements of the Norwegian continental shelf. Part 1: The Barents Sea Region. *NPD Bulletin*, no. 6.
- GABRIELSEN, R. H., GRUNNALEITE, I., & OTTESEN, S. (1993). Reactivation of fault complexes in the Loppa High area, southwestern Barents Sea. *Norwegian Petroleum Society Special Publications*, 2, 631-641.
- GERNIGON, L., BRÖNNER, M., ROBERTS, D., OLESEN, O., NASUTI, A., & YAMASAKI, T. (2014). Crustal and basin evolution of the southwestern Barents Sea: From Caledonian orogeny to continental breakup. *Tectonics*, 33 (4), 347-373. doi:10.1002/2013TC003439
- GOULTY, N. R. (2008). Geomechanics of polygonal fault systems: a review. *Petroleum Geoscience*, 14 (4), 389-397. doi:10.1144/1354-079308-781
- GUDLAUGSSON, S. T., FALEIDE, J. I., JOHANSEN, S. E., & BREIVIK, A. J. (1998). Late Palaeozoic structural development of the South-western Barents Sea. *Marine and Petroleum Geology*, 15 (1), 73-102.
- HARRINGTON, P. K. (1985). Formation of Pockmarks by Pore-Water Escape. *Geo-Marine Letters*, 5 (3), 193-197. doi:10.1007/BF02281638
- HEGGLAND, R. (1998). Gas seepage as an indicator of deeper prospective reservoirs. A study based on exploration 3D seismic data. *Marine and Petroleum Geology*, 15, 1-9.
- HENRIET, J. P., DE BATIST, M., & VERSCHUREN, M. (1991). Early fracturing of Paleogene clays, southernmost North Sea: relevance to mechanisms of primary hydrocarbon migration. In A. M. Spencer (Ed.), *Generation, accumulation, and production of Europe's hydrocarbons, Special Publication of the European Association of Petroleum Geoscientists No. 1* (pp. 217-227). Oxford: Oxford University Press.
- HENRIKSEN, E., BJØRNSETH, H. M., HALS, T. K., HEIDE, T., KIRYUKHINA, T., KLØVJAN, O. S., . . . STOUPAKOVA, A. V. (2011). Chapter 17: Uplift and erosion of the greater Barents Sea: impact on prospectivity and petroleum systems. In A. M. Spencer, A. F. Embry, D. L. Gautier, A. V. Stoupakova, & K. Sørensen (Eds.), *Arctic Petroleum Geology* (Vol. 35, pp. 271-281). London: The Geological Society of London.

- HENRIKSEN, E., RYSETH, A. E., LARSSSEN, G. B., HEIDE, T., RØNNING, K., SOLLID, K., & STOUPAKOVA, A. V. (2011). Chapter 10: Tectonostratigraphy of the greater Barents Sea: implications for petroleum systems. In A. M. Spencer, A. F. Embry, D. L. Gautier, A. V. Stoupakova, & K. Sørensen (Eds.), *Arctic Petroleum Geology* (Vol. 35, pp. 163-195). London: The Geological Society of London.
- HINDLE, A. D. (1997). Petroleum Migration Pathways and Charge Concentration: A Three-Dimensional Model. *AAPG Bulletin*, 81 (9), 1451-1481.
- HOVLAND, M. (1981). Characteristics of pockmarks in the Norwegian Trench. *Marine Geology*, 39 (1), 103-117. doi:10.1016/0025-3227(81)90030-X
- HOVLAND, M., GARDNER, J. V., & JUDD, A. G. (2002). The significance of pockmarks to understanding fluid flow processes and geohazards. *Geofluids*, 2 (2), 127-136. doi:10.1046/j.1468-8123.2002.00028.x
- INDREVÆR, K., GABRIELSEN, R. H., & FALEIDE, J. I. (2016). Early Cretaceous synrift uplift and tectonic inversion in the Loppa High area, southwestern Barents Sea, Norwegian shelf. *Journal of the Geological Society*, 174, 242-254.
- JUDD, A., & HOVLAND, M. (2007). *Seabed fluid flow: the Impact on Geology, Biology, and the Marine Environment*. Cambridge: Cambridge University Press.
- KEARY, P., BROOKS, M., & HILL, I. (2002). *An Introduction to Geophysical Exploration* (3rd ed.). Oxford: Blackwell Science Ltd.
- KING, L. H., & MACLEAN, B. (1970). Pockmarks on the Scotian Shelf. *Geological Society of America Bulletin*, 81 (10), 3141-3148. doi:10.1130/0016-7606(1970)81[3141:POTSS]2.0.CO
- KLAUSEN, T. G., RYSETH, A. E., HELLAND-HANSEN, W., GAWTHORPE, R., & LAURSEN, I. (2015). Regional development and sequence stratigraphy of the Middle to Late Triassic Snadd Formation, Norwegian Barents Sea. *Marine and Petroleum Geology*, 62, 102-122. doi:10.1016/j.marpetgeo.2015.02.004
- KNIES, J., MATTHIESSEN, J., VOGT, C., LABERG, J. S., HJELSTUEN, B. O., SMELROR, M., . . . VORREN, T. O. (2009). The Plio-Pleistocene glaciation of the Barents Sea–Svalbard region: a new model based on revised chronostratigraphy. *Quaternary Science Reviews*, 28 (9-10), 812-829. doi:10.1016/j.quascirev.2008.12.002
- KTENAS, D., MEISINGSET, I., HENRIKSEN, E., & NIELSEN, J. K. (2018). Estimation of net apparent erosion in the SW Barents Sea by applying velocity inversion analysis. *Petroleum Geoscience*, 25 (2), 169-187. doi:10.1144/petgeo2018-002
- LABERG, J. S., ANDREASSEN, K., KNIES, J., VORREN, T. O., & WINSBORROW, M. (2010). Late Pliocene-Pleistocene development of the Barents Sea Ice Sheet. *Geology*, 38 (2), 107-110. doi:10.1130/G30193.1
- LARSSSEN, G. B., ELVEBAKK, G., HENRIKSEN, L. B., KRISTENSEN, S.-E., NILSSON, I., SAMUELSBERG, T. J., . . . WORSLEY, D. (2002). Upper Paleozoic lithostratigraphy of the Southern Norwegian Barents Sea. *NPD Bulletin*, no. 9.
- LASABUDA, A. P. E. (2018). *Cenozoic tectonosedimentary development and erosion estimates for the Barents Sea continental margin, Norwegian Arctic*. UiT - The Arctic University of Norway, Tromsø.
- LERCHE, I., YU, Z., TØRUDBAKKEN, B., & THOMSEN, R. O. (1997). Ice loading effects in sedimentary basins with reference to the Barents Sea. *Marine and Petroleum Geology*, 14 (3), 277-338. doi:10.1016/S0264-8172(96)00059-1
- LIGTENBERG, J. H. (2005). Detection of fluid migration pathways in seismic data: implications for fault seal analysis. *Basin Research*, 17 (1), 141-153. doi:10.1111/j.1365-2117.2005.00258.x

- LØSETH, H., GADING, M., & WENSAAS, L. (2009). Hydrocarbon leakage interpreted on seismic data. *Marine and Petroleum Geology*, 26 (7), 1304-1319. doi:10.1016/j.marpetgeo.2008.09.008
- MAGOON, L. B., & BEAUMONT, E. A. (1999). Chapter 3: Petroleum Systems. In E. A. Beaumont & N. H. Foster (Eds.), *Exploring for Oil and Gas Traps* (pp. 1150): AAPG.
- NANDA, N. C. (2016). *Seismic Data Interpretation and Evaluation for Hydrocarbon Exploration and Production: A Practitioner's Guide* (1st ed.). Cham: Springer International Publishing.
- NP. (2020). Fields on the Norwegian Continental Margin. Retrieved 09.05.2020 from <https://www.norskpetroleum.no/en/facts/field/>
- NPD. (2019). Plays and method for calculating undiscovered petroleum resources: Barents Sea. Retrieved 14.11.2019 from <https://www.npd.no/en/facts/geology/plays/barents-sea/>
- NPD. (2020). FactMaps. Retrieved 09.05.2020 from https://factmaps.npd.no/factmaps/3_0/
- NYLAND, B., JENSEN, L. N., SKAGEN, J., SKARPNES, O., & VORREN, T. O. (1992). Tertiary uplift and erosion in the Barents Sea: Magnitude, Timing and Consequences. In R. M. Larsen, H. Brekke, B. T. Larsen, & E. Talleraas (Eds.), *Structural and Tectonic Modeling and its Application to Petroleum Geology*. (pp. 153-162). Amsterdam: Elsevier.
- OHM, S. E., KARLSEN, D. A., & AUSTIN, T. J. F. (2008). Geochemically driven exploration models in uplifted areas; examples from the Norwegian Barents Sea. *AAPG Bulletin*, 92 (9), 1191-1223. doi:10.1306/06180808028
- OMOSANYA, K. O., ZERVAS, I., MATTOS, N. H., ALVES, T. M., JOHANSEN, S. E., & MARFO, G. (2017). Strike-Slip Tectonics in the SW Barents Sea During North Atlantic Rifting (Swaen Graben, Northern Norway). *Tectonics*, 36 (11), 2422-2446. doi:10.1002/2017TC004635
- OSBORNE, M. J., & SWARBICK, R. E. (1997). Mechanisms for Generating Overpressure in Sedimentary Basins: A Reevaluation. *AAPG Bulletin*, 81 (6), 1023-1041.
- OSTANIN, I., ANKA, Z., DI PRIMIO, R., & BERNAL, A. (2012). Identification of a large Upper Cretaceous polygonal fault network in the Hammerfest basin: Implications on the reactivation of regional faulting and gas leakage dynamics, SW Barents Sea. *Marine Geology*, 332-334, 109-125. doi:10.1016/j.marpetgeo.2012.03.005
- PAU, M., HAMMER, Ø., & CHAND, S. (2014). Constraints on the dynamics of pockmarks in the SW Barents Sea: Evidence from gravity coring and high-resolution, shallow seismic profiles. *Marine Geology*, 355, 330-345. doi:10.1016/j.marpetgeo.2014.06.009
- PAULL, C. K., USSLER III, W., & BOROWSKI, W. S. (1999). Freshwater ice rafting: an additional mechanism for the formation of some high-latitude submarine pockmarks. *Geo-Marine Letters*, 19 (1), 164-168. doi:10.1007/s003670050104
- PEACOCK, D. C. P., NIXON, C. W., ROTEVATN, A., SANDERSON, D. J., & ZULUAGA, L. F. (2016). Glossary of fault and other fracture networks. *Journal of Structural Geology*, 92, 12-29. doi:10.1016/j.jsg.2016.09.008
- RAJAN, A., BÜNZ, S., MIENERT, J., & SMITH, A. J. (2013). Gas hydrate systems in petroleum provinces of the SW-Barents Sea. *Marine and Petroleum Geology*, 46, 92-106. doi:10.1016/j.marpetgeo.2013.06.009
- RISE, L., BELLEC, V., CHAND, S., & BOE, R. (2014). Pockmarks in the southwestern Barents Sea and Finnmark fjords. *Norwegian Journal of Geology*, 94 (4), 263-282.
- SCHOWALTER, T. T. (1979). Mechanics of Secondary Hydrocarbon Migration and Entrapment. *AAPG Bulletin*, 63 (5), 723-760. doi:10.1306/2F9182CA-16CE-11D7-8645000102C1865D
- SELLEY, R. C., & SONNENBERG, S. A. (2015). *Elements of Petroleum Geology* (3rd ed.). San Diego, California: Academic Press.

- SHERIFF, R. E. (2002). *Encyclopedic Dictionary of Applied Geophysics* (4th ed.). Tulsa, Oklahoma: Society of Exploration Geophysics.
- SLOAN, E. D., JR., HENRIET, J. P., & MIENERT, J. (1998). Physical/chemical properties of gas hydrates and application to world margin stability and climatic change. In J. P. Henriet & J. Mienert (Eds.), *Gas Hydrates: Relevance to World Margin Stability and Climate Change*. (Vol. 137, pp. 31-50). London: Geological Society, Special Publications.
- SMELROR, M., BASOV, V. A., LARSEN, G. B., & WERNER, S. C. (2009). *Atlas: Geological History of the Barents Sea*. Trondheim: Geological Survey of Norway.
- SPEIGHT, J. G. (2012). *Shale Oil Production Processes*. Saint Louis: Elsevier Science & Technology.
- STEMMERIK, L., & WORSLEY, D. (2005). 30 years on: Arctic Upper Paleozoic stratigraphy, depositional evolution and hydrocarbon prospectivity. *Norwegian Journal of Geology*, 85, 151-168.
- SÆTTEM, J., RISE, L., & WESTGAARD, D. A. (1992). Composition and properties of Glacigenic sediments in the south-western Barents Sea. *Marine Geotechnology*, 10, 229-255.
- TASIANAS, A., BÜNZ, S., BELLWALD, B., HAMMER, Ø., PLANKE, S., LEBEDEVA-IVANOVA, N., & KRASSAKIS, P. (2018). High-resolution 3D seismic study of pockmarks and shallow fluid flow systems at the Snøhvit hydrocarbon field in the SW Barents Sea. *Marine Geology*, 403, 247-261. doi:10.1016/j.margeo.2018.06.012
- VADAKKEPULIYAMBATTA, S., BÜNZ, S., MIENERT, J., & CHAND, S. (2013). Distribution of subsurface fluid-flow systems in the SW Barents Sea. *Marine and Petroleum Geology*, 43, 208-221. doi:10.1016/j.marpetgeo.2013.02.007
- VADAKKEPULIYAMBATTA, S., CHAND, S., & BÜNZ, S. (2017). The history and future trends of ocean warming-induced gas hydrate dissociation in the SW Barents Sea. *Geophysical Research Letters*, 44 (2), 835-844. doi:10.1002/2016GL071841
- VEEKEN, P. P. (2013). Chapter 2: The seismic reflection method and its constraints. In P. P. Veeken & B. Van Moerkerken (Eds.), *Seismic Stratigraphy and Depositional Facies Models*. Burlington: Elsevier Science.
- VORREN, T. O., RICHARDSSEN, G., KNUTSEN, S. M., & HENRIKSEN, E. (1991). Cenozoic erosion and sedimentation in the western Barents Sea. *Marine and Petroleum Geology*, 8 (3), 317-340. doi:10.1016/0264-8172(91)90086-G
- WORSLEY, D. (2008). The post-Caledonian development of Svalbard and the western Barents Sea. *Polar Research*, 27 (3), 298-317. doi:10.1111/j.1751-8369.2008.00085.x

Table of figures

FIGURE 2.1: PETROLEUM SYSTEM EVENT CHART, SHOWING THE IDEAL COURSE OF EVENTS AND PROCESSES RESULTING IN A HYDROCARBON ACCUMULATION. CRITICAL MOMENT REFERS TO THE TIME OF GENERATION, MIGRATION AND ACCUMULATION, PREFERENTIALLY OCCURRING AFTER TRAP FORMATION. INSPIRED BY FIG. 3-6 IN MAGOON AND BEAUMONT (1999).	2
FIGURE 2.2: VAN KREVELEN DIAGRAM, SHOWING THE ORIGIN OF THE MAIN KEROGEN TYPES AND THEIR POTENTIAL FOR GENERATING OIL AND/OR GAS. INSPIRED BY FIG. 5.15 IN SELLEY AND SONNENBERG (2015).....	3
FIGURE 2.3: THE MOST ESSENTIAL ELEMENTS AND PROCESSES OF A TRAP, REPRESENTED BY THE SIMPLEST ANTICLINAL TRAP. INSPIRED BY FIG. 7.1 IN SELLEY AND SONNENBERG (2015).	4
FIGURE 2.4: RELATIONSHIP BETWEEN THE HYDROSTATIC, LITHOSTATIC, PORE AND FRACTURE PRESSURES. INSPIRED BY FIG. 4.13 IN SELLEY AND SONNENBERG (2015) AND FIG. ON P. 4 IN BULLER ET AL. (2005).	6
FIGURE 2.5: THE CONCEPT OF CAPILLARITY AND THE MENISCUS EFFECT OF AN OIL-WET AND WATER-WET RESERVOIR IN A CAPILLARY TUBE. INSPIRED BY FIG. 6.17 IN SELLEY AND SONNENBERG (2015).	8
FIGURE 2.6: THE MAIN FAULT TYPES.....	10
FIGURE 2.7: ANDERSONS (1951) CLASSIFICATION OF TECTONIC REGIMES, SHOWING THE RELATIONSHIP BETWEEN THE THREE PRINCIPLE STRESSES AND THE RELATIVE MAGNITUDE OF STRESSES. INSPIRED BY FIG. 5.13 IN FOSSEN (2016).....	11
FIGURE 2.8: MOHR'S CIRCLE. STAR REPRESENTS THE FAULT PLANE ORIENTATION, OF WHICH BOTH SHEAR AND NORMAL STRESSES CAN BE OBTAINED. NOTE THAT THE ANGLES IN MOHR'S SPACE ARE DOUBLED. INSPIRED BY FIG. 4.7 IN FOSSEN (2016).	12
FIGURE 2.9: MOHR'S CIRCLE AND COULOMB FAILURE ENVELOPE, AND CORRESPONDING STATES OF STRESS. INSPIRED BY FIG. 7.13 IN FOSSEN (2016).	12
FIGURE 2.10: POLARITY CONVENTION AFTER SHERIFF (2002), USED IN THIS MASTER THESIS.	16
FIGURE 2.11: RELATIONSHIP BETWEEN VELOCITY, WAVELENGTH, FREQUENCY AND RESOLUTION. INSPIRED BY FIG. 1-3 IN BROWN (2004).	17
FIGURE 2.12: WEDGE MODEL SHOWING THE CONCEPT OF VERTICAL RESOLUTION. A) CROSS-SECTION THROUGH THE SUBSURFACE, WITH AN INCASED HIGHER-VELOCITY WEDGE. B) SEISMIC RESPONSE (ZERO-PHASE, NORMAL POLARITY WAVELET) AND INTERFERENCE EFFECTS. INSPIRED BY FIG. RES1 AND RES3 IN BADLEY (1985).....	18
FIGURE 2.13: A) THE CONCEPT OF HORIZONTAL RESOLUTION AND THE FRESNEL ZONE. INSPIRED BY FIG. 4.11 IN KEARY ET AL. (2002). B) THE CONCEPT OF SEISMIC MIGRATION, ENHANCING THE HORIZONTAL RESOLUTION BY COLLAPSING ENERGY INTO AN ELLIPSE FOR 2D DATA AND A CIRCLE FOR 3D DATA. INSPIRED BY FIG. 1-5 IN BROWN (2004).	19
FIGURE 2.14: A) ILLUSTRATION OF POCKMARKS AND BURIED POCKMARKS AND ASSOCIATED PIPES. B) SEISMIC SECTION SHOWING VERTICALLY STACKED POCKMARKS AND ASSOCIATED PIPES (LEFT) AND A POCKMARK OCCURRING ON THE SEABED (RIGHT). MODIFIED FROM CARTWRIGHT ET AL. (2007). C) ILLUSTRATION OF A BURIED MUD VOLCANO AND ASSOCIATED MUD DIAPIR AND CONDUITS CONNECTING THE TWO FEATURES. D) SEISMIC EXPRESSION OF A BURIED MUD VOLCANO. MODIFIED FROM CARTWRIGHT ET AL. (2007).	21
FIGURE 2.15: A) GEOLOGICAL MODEL FOR GENERATION OF BRIGHT SPOTS AND SUBSEQUENT SEISMIC EXPRESSION. AI = ACOUSTIC IMPEDANCE. B) GEOLOGICAL MODEL FOR GENERATION OF DIM SPOTS AND ASSOCIATED SEISMIC EXPRESSION. C) GEOLOGICAL MODEL FOR GENERATION OF POLARITY/PHASE REVERSAL AND ASSOCIATED SEISMIC EXPRESSION. INSPIRED BY FIG. 5-5 IN BROWN (2004).	23
FIGURE 2.16: A) SEISMIC EXPRESSION OF BRIGHT SPOT, DIM SPOT, FLAT SPOT AND PHASE REVERSAL. MODIFIED FROM LØSETH ET AL. (2009). B) SEISMIC EXPRESSION OF WIPE-OUT ZONE (ACOUSTIC MASKING) AND VELOCITY EFFECTS (PUSH-DOWN). MODIFIED FROM LØSETH ET AL. (2009). C) SEISMIC EXPRESSION OF VERTICAL WIPE-OUT ZONE (GAS CHIMNEY). MODIFIED FROM LØSETH ET AL. (2009).....	24
FIGURE 3.1: OVERVIEW OF THE BARENTS SEA, WITH ITS SURROUNDING LANDMASSES AND SUBDIVISION INTO WESTERN AND EASTERN PROVINCES.	27
FIGURE 3.2: SUMMARY OF THE MOST IMPORTANT EVENTS IN THE GEOLOGICAL DEVELOPMENT OF THE BARENTS SEA, WITH EMPHASIS ON THE SW REGION. EVENTS OF THE EASTERN BARENTS SEA ARE COLORED GREY. VERTICAL RED LINES INDICATES FORMATIONS PRESENT IN THE STUDY AREA. INSPIRED BY FIG. ON P. 48 IN SMELROR ET AL. (2009).	28
FIGURE 3.3: OVERVIEW OF THE STUDY AREA (RED OUTLINE), LOPPA HIGH AND SURROUNDING STRUCTURAL ELEMENTS. APPROXIMATE POSITION OF WELL 7222/1-1 IS INDICATED IN BLACK.	36
FIGURE 3.4: A) TENTATIVE UPLIFT MAP, BASED ON FIG. 6 IN OHM ET AL. (2008). B) TENTATIVE MATURITY MAP OF UPPER JURASSIC (UJ, HEKINGEN FM.), TRIASSIC (T, SNADD, KOBBE, KLAPPMYSS AND HAVERT FMS.) AND PERMIAN/CARBONIFEROUS (P/C) SOURCE ROCKS, BASED ON FIG. 10 IN OHM ET AL. (2008). APPROXIMATE LOCATION OF THE STUDY AREA (BLACK OUTLINE) IS INDICATED ON THE LOPPA HIGH.	41

FIGURE 4.1: A) LOCATION AND COVERAGE OF THE 3D DATASETS USED IN THIS THESIS. STUDY AREA OUTLINE INDICATED BY GREY DOTTED LINE. B) LOCATION OF THE 2D DATASETS USED IN THIS THESIS. NOTE THAT THE SEISMIC LINES EXTEND WELL BEYOND THE STUDY AREA OUTLINE (BLACK); ONLY DATA WITHIN THE DEFINED STUDY AREA HAS BEEN INTERPRETED (ALSO SHOWN IN FIG. 4.5).....	43
FIGURE 4.2: A) FREQUENCY SPECTRA (ENERGY (DB) VS. FREQUENCY (HZ)), BASED ON A SINGLE INLINE FROM EACH OF THE 3D DATASETS. B) FREQUENCY SPECTRA BASED ON A SINGLE LINE FROM EACH OF THE 2D DATASETS.	45
FIGURE 4.3: A) SEISMIC ARTEFACTS (SURVEY FOOTPRINT) IN THE ST10020 DATASET, OBSERVED ON THE SEABED SURFACE. VERTICAL EXAGGERATION (VE): 10. B) SEISMIC ARTEFACTS (SURVEY FOOTPRINT) IN THE DG12M1 DATASET, OBSERVED ON THE SEABED SURFACE. VE: 10. C) SEISMIC SECTION CORRESPONDING TO A-A' IN A), SHOWING THE SEISMIC EXPRESSION OF THE ARTEFACTS. S = SEABED AND TS/U = TOP SNADD/URU.	48
FIGURE 4.4: FIGURE OF THE WORKFLOW AND APPROACH USED IN THIS THESIS, WITH THE TOOLS AND METHODS USED, AND THE OBJECTIVES OF USING THEM.....	49
FIGURE 4.5: STUDY AREA WITH THE BASIS FOR INTERPRETATION; 3D DATASETS AND THE 2D LINES COVERING THE GAPS BETWEEN THEM.	49
FIGURE 4.6: A) 3D VIEW SHOWING BOTH A HORIZON SLICE AND TIME SLICE. B) TIME SLICE IN PLAN-VIEW.	51
FIGURE 5.1: STRATIGRAPHIC UNITS AND HORIZONS INTERPRETED. POSITION OF THE SEISMIC SECTIONS INDICATED IN THE STUDY AREA OUTLINE. ONLY FAULTS DISPLACING THE MAIN STRATIGRAPHIC UNITS HAVE BEEN INCLUDED.	53
FIGURE 5.2: SURFACES PRODUCED BASED ON INTERPRETED HORIZONS IN THE STUDY AREA. VERTICAL EXAGGERATION (VE): 10. SEABED CONTOUR INCREMENT (CI): 25. TOP SNADD/URU CI: 30. TOP KOBBE – TOP RØYE CI: 50.	54
FIGURE 5.3: A) PERMIAN FAULTS IDENTIFIED ON VARIANCE TIME SLICE AT -1804 MS (ST10020). B) PERMIAN-TRIASSIC FAULTS IDENTIFIED ON VARIANCE TIME SLICES AT -1848 MS (DG12M1), -1532 MS (ST10020) AND -1480 MS (GDF1201M13). C) TRIASSIC FAULTS IDENTIFIED ON VARIANCE TIME SLICES AT -860 MS (ALL THREE DATASETS). D) PERMIAN FAULTS IDENTIFIED IN THE STUDY AREA, AND LOCATION OF SEISMIC SECTION IN FIG. 5.4. E) PERMIAN-TRIASSIC FAULTS IDENTIFIED IN THE STUDY AREA AND LOCATION OF SEISMIC SECTIONS IN FIGS. 5.5-5.8. F) TRIASSIC FAULTS IDENTIFIED IN THE STUDY AREA AND THE LOCATION OF SEISMIC SECTIONS IN FIGS. 5.9-5.11. THE DOTTED LINES IN F) REPRESENT THE LOCATION OF THE PERMIAN-TRIASSIC FAULTS, EXTENDING ALL THE WAY UP TO THE TOP SNADD/URU HORIZON.	56
FIGURE 5.4: SEISMIC SECTION FROM THE ST10020 DATASET (POSITION SHOWN IN FIG. 5.3D), SHOWING PERMIAN FAULTS TERMINATING AGAINST THE TOP RØYE (TR) REFLECTOR. PERMIAN FAULTS ARE COLORED BLACK. FAULT PATTERN APPEARS TO CONSTITUTE HORST-AND-GRABEN STRUCTURES, INDICATIVE OF NORMAL FAULTING.	57
FIGURE 5.5: SEISMIC SECTION FROM THE DG12M1 DATASET (POSITION SHOWN IN FIG. 5.3E), SHOWING THREE NARROW GRABENS (NG1-3) TERMINATING AGAINST THE TOP SNADD/URU HORIZON (TS/U). PERMIAN-TRIASSIC FAULTS ARE COLORED BLACK, WHEREAS OTHER FAULTS ARE COLORED GREY. THE LATERAL EXTENT OF THE NGs INCREASES WITH DECREASING DEPTH AND DISPLACEMENT WITHIN THEM APPEARS TO BE DOWNWARDS. THE GRABENS SEPARATE SEVERAL HORST BLOCKS OF LARGER LATERAL EXTENT.	58
FIGURE 5.6: SEISMIC SECTION FROM GDF1201M13 (POSITION SHOWN IN FIG. 5.3E), SHOWING TWO NARROW GRABENS (NG4-5) TERMINATING AGAINST THE TOP SNADD/URU (TS/U) HORIZON. PERMIAN-TRIASSIC FAULTS ARE COLORED BLACK, WHEREAS OTHERS ARE COLORED GREY. BOTH GRABENS, SEPARATED BY HORST BLOCKS, WIDENS WITH DECREASING DEPTHS AND INTERNAL FAULT BLOCKS APPEAR TO BE DOWNFAULTED. THE GENERAL DISPLACEMENT ACROSS NG4 IS DOWN TOWARDS THE SE.....	58
FIGURE 5.7: SEISMIC SECTION FROM ST10020 (POSITION SHOWN IN FIG. 5.3E), SHOWING THE PERMIAN-TRIASSIC FAULTS WITH DOMINATING STRIKE ORIENTATION FROM SW TO NE. SOME OF THE FAULTS APPEAR TO CONSTITUTE HORST-AND-GRABEN STRUCTURES.	59
FIGURE 5.8: 2D LINE (NBRO9-240736, POSITION SHOWN IN FIG. 5.3E) COVERING A SUBSTANTIAL AREA BETWEEN THE DG12M1 AND ST10020 DATASETS, SHOWING THE NARROW GRABEN (NG6) EXTENDING FROM SW TO NE BETWEEN THE DATASETS. WESTERN FAULT IDENTIFIED IN ST10020 APPEARS TO BE ONE OF DELINEATING FAULTS OF THE NG6. NG6 ALSO APPEAR TO SEPARATE TWO LARGER FAULT BLOCKS.	60
FIGURE 5.9: SEISMIC SECTION FROM THE DG12M1 DATASET (POSITION SHOWN IN FIG. 5.3F), SHOWING SEVERAL TRIASSIC FAULTS DISSECTING THE SNADD FORMATION. TRIASSIC FAULTS ARE COLORED BLACK, OTHERS GREY. SEVERAL FAULTS APPEAR TO HAVE THE SAME DIP DIRECTION, WHILE OTHERS APPEAR TO CONSTITUTE HORST-AND-GRABEN STRUCTURES. SOME OF THE TRIASSIC FAULTS ARE ANTITHETIC AND SYNTHETIC FAULTS RELATED TO NG3.	61
FIGURE 5.10: SEISMIC SECTION FROM THE GDF1201M13 DATASET (POSITION SHOWN IN FIG. 5.3F), SHOWING SEVERAL TRIASSIC FAULTS DISSECTING THE SNADD FORMATION. TRIASSIC FAULTS ARE COLORED BLACK, OTHERS GREY. THE MAJORITY OF THE FAULTS IN THIS SECTION APPEAR TO CONSTITUTE SMALLER-SCALE HORST-AND-GRABEN STRUCTURES.	61

FIGURE 5.11: SEISMIC SECTION FROM THE ST10020 DATASET (POSITION INDICATED IN FIG 5.3F), SHOWING THE TRIASSIC FAULTS WITH A DOMINATING STRIKE ORIENTATION FROM SW TO NE, OF WHICH SOME APPEAR TO CONSTITUTE HORST-AND-GRABEN STRUCTURES.	61
FIGURE 5.12: A) AMPLITUDE ANOMALIES IN PERMIAN STRATA AND APPROXIMATE LOCATION OF FIGS. 5.13-5.14. B) AMPLITUDE ANOMALIES IN TRIASSIC STRATA AND LOCATION OF FIGS. 5.15-5.21. C) AMPLITUDE ANOMALIES IN CENOZOIC STRATA AND LOCATION OF FIG. 5.22. OUTLINE OF ANOMALIES ROUGHLY CORRESPONDS TO THEIR EXTENT, AND IN SEVERAL CASES INCLUDE SEVERAL SMALLER ANOMALIES.....	62
FIGURE 5.13: A) RMS AMPLITUDE (RMSA) TIME SLICE SHOWING THE EXTENT OF AA1 IN THE ST10020 DATASET, AND VARIATIONS IN AMPLITUDE, AT -2080 MS. B) RMSA TIME SLICE (-2080 MS, ADJUSTED OPACITY) SUPERIMPOSED ON A VARIANCE (V) TIME SLICE (-2128 MS), SHOWING THE RELATIONSHIP BETWEEN AMPLITUDE ANOMALIES AND STRUCTURAL TRENDS IN THE ST10020 DATASET. C) SEISMIC SECTION ACROSS AA1 (LOCATION SHOWN IN FIG. 5.12A AND IN THE DATASET OUTLINE), WITH RMSA AND V TIME SLICES INDICATED. SMALL DISCONTINUITIES OBSERVED IN SEISMIC SECTION CORRESPOND TO ELONGATED AND CIRCULAR TO SUB-CIRCULAR FEATURES SEEN IN B).	63
FIGURE 5.14: A) RMS AMPLITUDE (RMSA) TIME SLICE SHOWING THE EXTENT AND AMPLITUDE VARIATION OF AA2 IN THE DG12M1 DATASET, AT -2104 MS. B) RMSA TIME SLICE (-2104 MS, ADJUSTED OPACITY) SUPERIMPOSED ON VARIANCE (V) TIME SLICE (-2104 MS) SHOWING THE RELATIONSHIP BETWEEN AMPLITUDE ANOMALIES AND STRUCTURAL TRENDS IN THE DG12M1 DATASET. C) SEISMIC SECTION SHOWING AA2 (LOCATION SHOWN IN FIG. 5.12A AND IN THE DATASET OUTLINE), AND THE SIMILAR DISCONTINUITIES OBSERVED IN AA1.	64
FIGURE 5.15: A) RMS AMPLITUDE (RMSA) TIME SLICE SHOWING THE EXTENT AND AMPLITUDE VARIATIONS OF AA3 IN THE ST10020 DATASET, AT -920 MS. B) RMSA TIME SLICE (-920 MS, ADJUSTED OPACITY) SUPERIMPOSED ON VARIANCE (V) TIME SLICE (-940 MS) SHOWING THE RELATIONSHIP BETWEEN AA3 AND STRUCTURAL TRENDS. NOTE HOW THE ANOMALY CONTINUES ACROSS THE DISCONTINUITY OBSERVED IN B). C) SEISMIC SECTION (LOCATION SHOWN IN FIG. 5.12B AND THE DATASET OUTLINE) SHOWING AA3 TERMINATING AGAINST A FAULT AND OVERLYING SMALLER AMPLITUDE ANOMALIES LOCATED ALONG TOP SNADD/URU. SW-NE ORIENTED DISCONTINUITY IN B) CORRESPONDS TO THE DELINEATING FAULT IN C).	65
FIGURE 5.16: A) RMS AMPLITUDE (RMSA) TIME SLICE SHOWING THE EXTENT AND AMPLITUDE VARIATIONS OF AA4 IN THE ST10020 DATASET, AT -988 MS. B) RMSA TIME SLICE (-988 MS, ADJUSTED OPACITY) SUPERIMPOSED ON VARIANCE (V) TIME SLICE (-988 MS), SHOWING THE RELATIONSHIP BETWEEN STRUCTURAL TRENDS AND AA4. NOTE THE CONTINUATION OF ENHANCED AMPLITUDES, RELATED TO AA4, TOWARDS THE SOUTH. C) SEISMIC SECTION SHOWING AA4 TERMINATING AGAINST NG6, AS WELL AS UNDERLYING AMPLITUDE ANOMALIES.	66
FIGURE 5.17: A) RMS AMPLITUDE (RMSA) TIME SLICE SHOWING THE EXTENT AND AMPLITUDE VARIATION OF AA5 IN THE ST10020 DATASET, AT -704 MS. B) RMSA TIME SLICE (-704 MS, ADJUSTED OPACITY) SUPERIMPOSED ON VARIANCE (V) TIME SLICE (-740 MS) SHOWING THE RELATIONSHIP BETWEEN AA5 AND STRUCTURAL TRENDS. C) SEISMIC SECTION (LOCATION SHOWN IN FIG. 5.12B AND IN THE DATASET OUTLINE), SHOWING HOW AA5 ENCOMPASSES NUMEROUS SMALLER AMPLITUDE ANOMALIES COVERING A LARGER AREA ABOVE AN EXTENSIVELY FAULTED ZONE. SEVERAL ANOMALIES HAVE INCREASING AMPLITUDES UPDIP AND SOME ARE BOUNDED BY FAULTS.	67
FIGURE 5.18: A) RMS AMPLITUDE (RMSA) TIME SLICE SHOWING THE EXTENT AND AMPLITUDE VARIATIONS OF AA6 IN THE ST10020 DATASET, AT -656 MS. NOTE THAT INTERMEDIATE AMPLITUDES SURROUNDING AA6-1-3 CAN BE ATTRIBUTED TO THE STRONG URU REFLECTOR. B) RMSA TIME SLICE (-656 MS, ADJUSTED OPACITY) SUPERIMPOSED ON VARIANCE (V) TIME SLICE (-752 MS), SHOWING THE RELATIONSHIP BETWEEN AMPLITUDE ANOMALIES AND STRUCTURAL TRENDS IN THE AREA. NOTE HOW NO DISCONTINUITIES HAVE BEEN IDENTIFIED DIRECTLY BELOW AA6 IN THIS INTERVAL, BUT ON A MUCH DEEPER LEVEL. C) SEISMIC SECTION (LOCATION SHOWN IN FIG. 5.12B AND THE DATASET OUTLINE), SHOWING AA6-1-3 LOCATED ALONG THE TOP SNADD/URU HORIZON, AND ASSOCIATED PUSH-DOWN EFFECTS IN ACOUSTIC PIPES.	68
FIGURE 5.19: A) RMS AMPLITUDE (RMSA) TIME SLICE SHOWING THE EXTENT AND AMPLITUDE VARIATIONS OF AA7 IN THE GDF1201M13 DATASET, AT -624 MS. B) RMSA TIME SLICE (-624 MS, ADJUSTED OPACITY) SUPERIMPOSED ON VARIANCE (V) TIME SLICE (-652 MS) SHOWING THE RELATIONSHIP BETWEEN AMPLITUDE ANOMALIES AND STRUCTURAL TRENDS, MAINLY TRIASSIC FAULTS. NOTE THE HIGH DENSITY OF DISCONTINUITIES IDENTIFIED ON THE VARIANCE TIME SLICE AND THE LOCATION OF AMPLITUDE ANOMALIES IN ASSOCIATION WITH THESE. C) SEISMIC SECTION (LOCATION SHOWN IN FIG. 5.12B AND IN THE DATASET OUTLINE) SHOWING AA7 LOCATED ALONG THE TOP SNADD/URU HORIZON. NOTE ALSO THE LOCATION OF THE TRIASSIC FAULTS.....	69
FIGURE 5.20: A) RMS AMPLITUDE (RMSA) TIME SLICE SHOWING THE EXTENT AND AMPLITUDE VARIATION OF AA8 IN THE GDF1201M13 DATASET, AT -628 MS. B) RMSA TIME SLICE (-628 MS, ADJUSTED OPACITY) SUPERIMPOSED ON VARIANCE (V) TIME SLICE (-680 MS) SHOWING THE RELATIONSHIP BETWEEN AA8 AND STRUCTURAL TRENDS. NOTE HOW THE ANOMALIES ARE LOCATED ABOVE SEVERAL DISCONTINUITIES. C) SEISMIC SECTION (LOCATION SHOWN IN FIG. 5.12B AND IN THE DATASET	

OUTLINE) SHOWING AA8 LOCATED ALONG THE TOP SNADD/URU HORIZON AND ASSOCIATED AREAS OF ACOUSTIC MASKING. NOTE THE LOCATION OF AMPLITUDE ANOMALIES IN CLOSE PROXIMITY TO FAULTS, BOTH TRIASSIC AND PERMIAN-TRIASSIC. .. 70

FIGURE 5.21: A) RMS AMPLITUDE (RMSA) TIME SLICE SHOWING THE EXTENT AND AMPLITUDE VARIATION OF AA9 IN THE DG12M1 DATASET, AT -716 MS. NOTE THE OTHER AMPLITUDE ANOMALIES LOCATED IN CLOSE PROXIMITY TO THOSE INCLUDED IN AA9. B) RMSA TIME SLICE (-716 MS, ADJUSTED OPACITY) SUPERIMPOSED ON VARIANCE (V) TIME SLICE (-748 MS) SHOWING THE RELATIONSHIP BETWEEN AMPLITUDE ANOMALIES AND STRUCTURAL TRENDS. C) SEISMIC SECTION (LOCATION SHOWN IN FIG. 5.12B AND IN THE DATASET OUTLINE) SHOWING AA9 LOCATED ALONG THE TOP SNADD/URU HORIZON AND ASSOCIATED AREAS OF ACOUSTIC MASKING. NOTE THEIR RELATIONSHIP TO SEVERAL FAULTS. 71

FIGURE 5.22: A) RMS AMPLITUDE (RMSA) TIME SLICE SHOWING THE EXTENT AND AMPLITUDE VARIATIONS OF AA10 IN THE ST10020 DATASET, AT -620 MS. B) RMSA TIME SLICE (-620 MS, ADJUSTED OPACITY) SUPERIMPOSED ON VARIANCE (V) TIME SLICE (-688 MS), SHOWING THE RELATIONSHIP BETWEEN AMPLITUDE ANOMALIES AND STRUCTURAL TRENDS. C) SEISMIC SECTION (LOCATION SHOWN IN FIG. 5.12C AND IN THE DATASET OUTLINE), SHOWING THE LOCATION OF AA10 ALONG THE TOP SNADD/URU HORIZON. NOTE THE FAULTS TERMINATING AGAINST THE TOP SNADD/URU HORIZON AND THE DEEPER AMPLITUDE ANOMALY IN CLOSE PROXIMITY TO ONE OF THEM. 72

FIGURE 5.23: SEISMIC SECTION (LOCATION INDICATED IN DATASET OUTLINE), SHOWING A LARGER ZONE OF ACOUSTIC DISTURBANCE IN CLOSE PROXIMITY TO NG6, BELOW AA5. NOTE THE CHAOTIC REFLECTORS OF LOW AMPLITUDES WITHIN DZ1..... 74

FIGURE 5.24: SEISMIC SECTION (NBR09-242200, LOCATION INDICATED IN STUDY AREA OUTLINE), SHOWING TWO LARGER ZONES OF ACOUSTIC DISTURBANCE BELOW NG6 (LEFT) AND CLOSE TO NG4 (RIGHT). 74

FIGURE 5.25: OVERVIEW OF THE SEABED SURFACE. VERTICAL EXAGGERATION (VE): 10. CONTOUR INCREMENT (CI): 25. A-A', B-B' AND C-C' CORRESPOND TO SEISMIC SECTIONS IN FIG. 5.26. A) PLOUGHMARKS FROM THE DG12M1 DATASET. CI: 2.5. B) PLOUGHMARKS FROM THE ST10020 DATASET. CI: 5. C) PLOUGHMARKS FROM THE GDF1201M13 DATASET. CI: 2.5. 75

FIGURE 5.26: SEISMIC SECTIONS (LOCATION INDICATED IN FIG. 5.25) SHOWING THE SEABED MORPHOLOGY, WITH SEVERAL DEPRESSIONS ORIGINATING FROM ICEBERGS (PLOUGH AND SCOURMARKS). 76

FIGURE 5.27: A) SEABED SURFACE WITH EXPOSED DEPRESSIONS INDICATED BY WHITE CIRCLES. VERTICAL EXAGGERATION (VE): 10. B) APPROXIMATE LOCATION OF EXPOSED DEPRESSIONS IN THE 3D DATASETS AND POSITION OF SEISMIC SECTION IN C) IN FIGS. 5.28-5.34. THE SIZE OF DEPRESSIONS IS NOT TO SCALE. 76

FIGURE 5.28: A) ED1-5 LOCATED ON THE SEABED IN THE DG12M1 DATASET, VE: 10. BLACK DOTTED LINE INDICATES THE ORIENTATION OF THE SEISMIC SECTION IN C). B) DIP ANGLE MAP SHOWING INCREASING DIPS TOWARDS THE CENTER OF EACH DEPRESSION, AND THEN A GENERAL FLATTENING. C) SEISMIC SECTION (LOCATION SHOWN IN FIG. 5.27 AND IN THE DATASET OUTLINE), SHOWING ED4 AND ED2 ON THE SEABED, AND ADJACENT PLOUGH MARKS. NOTE THE FAULTS TERMINATING AGAINST THE TOP SNADD/URU HORIZON. 77

FIGURE 5.29: A) ED6 LOCATED ON THE SEABED IN THE DG12M1 DATASET, VE: 10. BLACK DOTTED LINE INDICATES THE ORIENTATION OF SEISMIC SECTION IN C). B) DIP ANGLE MAP SHOWING INCREASING DIPS TOWARDS THE CENTER OF ED6, AND SUBSEQUENT FLATTENING. C) SEISMIC SECTION (LOCATION INDICATED IN FIG. 5.27 AND IN THE DATASET OUTLINE) SHOWING ED6 ON THE SEABED. NOTE THE LOCATION OF SEVERAL FAULTS TERMINATING AGAINST THE TOP SNADD/URU HORIZON, DIRECTLY BELOW THE DEPRESSION, AND THE ASSOCIATED AMPLITUDE ANOMALY (AA9). 78

FIGURE 5.30: A) ED7 LOCATED ON THE SEABED IN THE ST10020, VE: 10. BLACK DOTTED LINE INDICATES THE ORIENTATION OF THE SEISMIC SECTION IN C). B) DIP ANGLE MAP SHOWING INCREASING DIPS TOWARDS THE CENTER OF THE DEPRESSION. C) SEISMIC SECTION (LOCATION SHOWN IN FIG. 5.27 AND IN THE DATASET OUTLINE) SHOWING ED7 ON THE SEABED, AND ADJACENT PLOUGH MARKS. NO FAULTS HAVE BEEN IDENTIFIED IN CLOSE PROXIMITY TO THE DEPRESSION, BUT AN AREA OF ACOUSTIC MASKING IS LOCATED TOWARDS THE SW, OCCURRING BELOW THE TOP SNADD/URU HORIZON..... 79

FIGURE 5.31: A) ED8 AND 9 LOCATED ON THE SEABED IN THE GDF1201M13 DATASET, VE: 10. BLACK DOTTED LINE INDICATES THE ORIENTATION OF THE SEISMIC SECTION IN C). B) DIP ANGLE MAP SHOWING INCREASING DIPS TOWARDS THE CENTER OF THE DEPRESSION, AND THE APPARENT FLATTENING OF ED9. C) SEISMIC SECTION (LOCATION SHOWN IN FIG. 5.27 AND IN THE DATASET OUTLINE) SHOWING ED8 AND 9 ON THE SEABED. NOTE THE FAULTS TERMINATING AGAINST THE TOP SNADD/URU HORIZON BELOW THE DEPRESSIONS. 80

FIGURE 5.32: A) ED10 LOCATED ON THE SEABED IN THE GDF1201M13 DATASET, VE: 10. BLACK DOTTED LINE INDICATES THE ORIENTATION OF THE SEISMIC SECTION IN C). B) DIP ANGLE MAP SHOWING INCREASING DIPS TOWARDS THE CENTER OF THE DEPRESSION, AND THE ELEVATED RIM SURROUNDING IT. C) SEISMIC SECTION (LOCATION SHOWN IN FIG. 5.27 AND IN THE DATASET OUTLINE) SHOWING ED10 ON THE SEABED, AND THE ASSOCIATED ELEVATED RIM. NOTE THE AMPLITUDE ANOMALIES OCCURRING ALONG THE TOP SNADD/URU HORIZON AND FAULTS TERMINATING BELOW THE DEPRESSION. 81

FIGURE 5.33: A) ED11 LOCATED ON THE SEABED IN THE GDF1201M13 DATASET, VE: 10. BLACK DOTTED LINE INDICATES THE ORIENTATION OF THE SEISMIC SECTION IN C). B) DIP ANGLE MAP SHOWING INCREASING DIPS TOWARDS THE CENTER OF THE

DEPRESSION. C) SEISMIC SECTION (LOCATION SHOWN IN FIG. 5.27 AND IN THE DATASET OUTLINE), SHOWING ED11 ON THE SEABED, AND UNDERLYING FAULTS TERMINATING AGAINST THE TOP SNADD/URU HORIZON.	82
FIGURE 5.34: A) ED12 LOCATED ON THE SEABED IN THE GDF1201M13 DATASET, VE: 10. BLACK DOTTED LINE INDICATES THE ORIENTATION OF THE SEISMIC SECTION IN C). B) DIP ANGLE MAP SHOWING INCREASING DIPS TOWARDS THE CENTER OF THE DEPRESSION. C) SEISMIC SECTION (LOCATION SHOWN IN FIG. 5.27 AND IN THE DATASET OUTLINE) SHOWING ED12 ON THE SEABED, AND AN AMPLITUDE ANOMALY ALONG THE TOP SNADD/URU HORIZON. NOTE ALSO THE FAULTS TERMINATING AGAINST THE SAME HORIZON.	83
FIGURE 5.35: A) VARIANCE TIME SLICES AT -664 MS (DG12M1), -672 MS (ST10020) AND -572 MS (GDF1201M13) SHOWING PALEO-DEPRESSIONS WITHIN THE NORDLAND GROUP. B) APPROXIMATE LOCATION OF PALEO-DEPRESSIONS IN THE 3D DATASETS AND SEISMIC SECTIONS IN B) IN FIGS. 5.37-5.39. NOTE THAT THE SIZE OF THE PALEO-DEPRESSIONS IS NOT TO SCALE.	84
FIGURE 5.36: A) VARIANCE (V) TIME SLICE (-576 MS) SHOWING THE LOCATION OF PD1-3 IN THE DG12M1 DATASET. B) SEISMIC SECTION (LOCATION INDICATED IN FIG 5.35 AND IN THE DATASET OUTLINE) SHOWING THE LOCATION OF PD1-3 WITHIN THE NORDLAND GROUP. NOTE THE AMPLITUDE ANOMALY AND FAULTS TERMINATING AGAINST THE TOP SNADD/URU HORIZON, AND THE APPARENT PUSH-DOWN EFFECTS BELOW PD3.	84
FIGURE 5.37: A) VARIANCE (V) TIME SLICE (-668 MS) SHOWING AN AREA OF SEVERAL PDS LOCATED IN CLOSE PROXIMITY TO AA6 IN THE ST10020 DATASET. BLACK CIRCLES INDICATE THE LOCATION OF PD4-10. B) SEISMIC SECTION (LOCATION SHOWN IN FIG. 5.35 AND THE DATASET OUTLINE) SHOWING PD4-10 OCCURRING ALONG THE TOP SNADD/URU HORIZON. NOTE THE LOCATION OF AA6-2 AND AA6-3 IN CLOSE PROXIMITY TO THE DEPRESSIONS, AND THE ASSOCIATED ACOUSTIC PIPES AND PUSH-DOWN EFFECTS. NOTE ALSO THE LOCATION OF THE FAULT JUST BELOW THE TOP SNADD/URU HORIZON.	85
FIGURE 5.38: A) VARIANCE (V) TIME SLICE (-576 MS) SHOWING PD11-13 IN THE GDF1201M13 DATASET. B) SEISMIC SECTION (LOCATION INDICATED IN FIG. 5.35 AND IN THE DATASET OUTLINE) SHOWING THE LOCATION OF PD11-13 WITHIN THE NORDLAND GROUP, RIGHT BELOW THE SEABED. NOTE THE AMPLITUDE ANOMALIES OCCURRING ALONG THE TOP SNADD/URU HORIZON AND THE FAULTS LOCATED DIRECTLY BELOW THE DEPRESSIONS.	86
FIGURE 6.1: CONCEPTUAL MODEL OF THE TECTONIC DEVELOPMENT OF THE STUDY AREA, AND INFERRED TIME OF FAULT GENERATION. CROSS-SECTION THROUGH THE STUDY AREA IS BASED ON SEISMIC SECTION A-A' IN FIG. 5.1. A) DEPOSITION OF CARBONIFEROUS/PERMIAN STRATA. B) PERMIAN FAULTS DEVELOPED IN RESPONSE TO CARBONIFEROUS-PERMIAN RIFTING. C) SUBAERIAL EXPOSURE AND EROSION OF THE HIGH. D) DEPOSITION OF TRIASSIC TO JURASSIC STRATA, EROSION AND DEVELOPMENT OF THE BASE CRETACEOUS UNCONFORMITY (BCU). E) DEPOSITION OF CRETACEOUS STRATA. F-H) DEVELOPMENT OF NARROW GRABENS AND EXTENSIVE HORSTS, AND POSSIBLY SHALLOWER FAULTS IN RESPONSE TO RIFTING AND PROPAGATION OF THE NORTH-ATLANTIC RIFT SYSTEM DURING THE JURASSIC AND CRETACEOUS. I) EXTENSIVE EROSION IN RESPONSE TO UPLIFT AND GLACIAL INFLUENCE, DEVELOPMENT OF THE UPPER REGIONAL UNCONFORMITY (URU). J) PRESENT-DAY STRUCTURAL CONFIGURATION OF THE STUDY AREA.	90
FIGURE 6.2: A) LOCATION OF AMPLITUDE ANOMALIES RELATED TO FAULTS IN THE STUDY AREA. B) LOCATION OF POTENTIAL GAS CHIMNEYS/ZONES OF ACOUSTIC MASKING AND THEIR RELATIONSHIP TO FAULTS IN THE STUDY AREA.	92
FIGURE 6.3: A) CONCEPTUAL MODEL FOR MIGRATION AND ACCUMULATION RELATED TO AA3. CROSS-SECTION CORRESPONDS TO SEISMIC SECTION IN FIG. 5.15C. B) CONCEPTUAL MODEL FOR MIGRATION AND ACCUMULATION RELATED TO NG6 AND DZ2. CROSS-SECTION CORRESPONDS TO NW PART OF SEISMIC SECTION IN FIG. 5.24.	93
FIGURE 6.4: CONCEPTUAL MODEL FOR MIGRATION AND ACCUMULATION RELATED TO AA6. CROSS-SECTION CORRESPONDS TO SEISMIC SECTION IN FIG. 5.18C.	94
FIGURE 6.5: CONCEPTUAL MODEL FOR MIGRATION AND ACCUMULATION RELATED TO AA4. CROSS-SECTION CORRESPONDS TO SEISMIC SECTION IN FIG. 5.16C.	96
FIGURE 6.6: CONCEPTUAL MODEL FOR MIGRATION AND ACCUMULATION RELATED TO AA7. CROSS-SECTION CORRESPONDS TO SEISMIC SECTION IN FIG. 5.19C.	96
FIGURE 6.7: CONCEPTUAL MODEL FOR MIGRATION AND ACCUMULATION RELATED TO AA5. CROSS-SECTION CORRESPONDS TO SEISMIC SECTION IN FIG 5.17C.	97
FIGURE 6.8: A) RELATIONSHIP BETWEEN EXPOSED DEPRESSIONS AND FAULTS IN THE STUDY AREA. B) RELATIONSHIP BETWEEN PALEO-DEPRESSIONS AND FAULTS IN THE STUDY AREA.	99
FIGURE 6.9: PLAUSIBLE MECHANISMS FOR POCKMARK FORMATION IN THE STUDY AREA. A) GAS HYDRATE DEVELOPMENT AND ENTRAPMENT OF FREE GAS BELOW A CONCURRENT ICE SHEET, AS WELL AS SHALLOW GAS MIGRATION AND ACCUMULATION ALONG FAULTS. B) GLACIAL RETREAT AND GAS HYDRATE DESTABILIZATION, SCOURING ICEBERGS AND RELEASE OF GAS THROUGH OPEN MIGRATION PATHWAYS (FAULTS). C) POST-GLACIAL SEABED MORPHOLOGY WITH GLACIALLY INDUCED DEPRESSIONS AND DEPRESSIONS CAUSED BY GAS HYDRATE DESTABILIZATION AND SEEPAGE.	102

FIGURE 6.10: CONCEPTUAL MODEL FOR FLUID FLOW, ACCUMULATION AND THE ASSOCIATED PROCESSES IN THE STUDY AREA. 1. VERTICAL MIGRATION IN GAS CHIMNEYS. 2. VERTICAL MIGRATION AND BRANCHING ALONG VERTICALLY EXTENSIVE FAULTS. 3. VERTICAL MIGRATION IN SHALLOW FAULTS, POSSIBLE CONNECTION TO CHANNEL DEPOSITS. 4. LATERAL MIGRATION IN CHANNEL DEPOSITS. 5. LATERAL MIGRATION IN RESERVOIR INTERVALS/DIPPING STRATA. 6. SHALLOW GAS ACCUMULATION ALONG URU. 7. POCKMARK FORMATION BY ACTIVE SEEPAGE FROM UNDERLYING FAULTS. 8. POCKMARK FORMATION BY ICEBERG SCOURING. 9. POCKMARK FORMATION BY GAS HYDRATE DESTABILIZATION. 103

FIGURE 6.11: PROPOSED PETROLEUM SYSTEM EVENT CHART FOR THE STUDY AREA, WITH THE INFERRED TIME OF SOURCE, RESERVOIR, SEAL AND OVERBURDEN DEPOSITION, AS WELL AS TRAP FORMATION, GENERATION, MIGRATION AND ACCUMULATION. SEVERAL PHASES OF POTENTIAL (STRUCTURAL) TRAP FORMATION IS INDICATED, WITH A) FAULTING RELATED TO THE PROGRADATION OF THE NORTH ATLANTIC RIFT SYSTEM INTO THE SW BARENTS SEA, B) FAULTING RELATED TO INTENSIFIED RIFTING AND THE PROGRESSIVE OPENING OF THE NORWEGIAN-GREENLAND SEA, AND C) FAULTING RELATED TO LATE CENOZOIC UPLIFT AND EROSION. SEVERAL CRITICAL MOMENTS REFERS TO SEVERAL PHASES OF POTENTIAL MIGRATION AND REMIGRATION, AND SUBSEQUENT ACCUMULATION, WITH 1) GENERATION AND MIGRATION INTO STRUCTURAL TRAPS FORMED DURING A), 2) GENERATION, MIGRATION AND POSSIBLE REMIGRATION INTO STRUCTURAL TRAPS FORMED DURING B), AND 3) MIGRATION AND REMIGRATION INTO STRUCTURAL TRAPS FORMED DURING C). 104

Table of equations

Eq. 2.1: OVERBURDEN PRESSURE 5
Eq. 2.2: HYDROSTATIC PRESSURE 5
Eq. 2.3: DARCY’S LAW 6
Eq. 2.4: BUOYANCY PRESSURE 7
Eq. 2.5: CAPILLARY PRESSURE 7
Eq. 2.6: CAPILLARY PRESSURE 8
Eq. 2.7: COULOMB FRACTURE CRITERION 11
Eq. 2.8: ACOUSTIC IMPEDANCE 15
Eq. 2.9: REFLECTION COEFFICIENT 15
Eq. 2.10: RELATIONSHIP BETWEEN WAVELENGTH, VELOCITY AND FREQUENCY 16
Eq. 2.11: HORIZONTAL RESOLUTION (RADIUS OF THE FRESNEL ZONE) 19
Eq. 4.1: INTERVAL VELOCITY 46